Novel Methods and Processes for the Chiral Resolution of Fine Chemicals

José Luis Capdevila Echeverria

Supervisor: Prof. Joop H. ter Horst

Thesis submitted in satisfaction with the requirements of the Strathclyde Institute of Pharmacy and Biomedical Sciences at the University of Strathclyde for the Degree of Doctor of Philosophy

September 2020

DECLARATION

This thesis is the result of the author's original research. It has been composed by the author and has not been previously submitted for examination which has led to the award of a degree.

José Luis Capdevila Echeverria

Lleida, 30th September 2020.

ACKNOWLEDGEMENTS

First of all, I would like to thank Prof. Joop H. ter Horst for accepting me in his research group and supervising me. It has been a challenging and very fruitful opportunity to carry out my PhD in his group. I will always remember our weekly meetings discussions which were of great utility during my PhD. I would also like to thank Prof. Richard Lakerveld to welcome me in his research group during my placement in The Hong Kong University of Science and Technology for the development of our collaboration which resulted in the fourth chapter of the present thesis. Additionally, I would like to thank Dr. Alison Nordon for carefully reading and revising the manuscript. I am deeply thankful to them, without their support, confidence, and direction; this work would not have been possible.

In addition, I would like to acknowledge CMAC Future Manufacturing Research Hub and National Facility supported by UKRPIF (UK Research Partnership Fund) award from the Higher Education Funding Council for England (HEFCE) (grant ref.: HH13054), the International Strategic Partnership between University of Strathclyde and Nanyang Technological University Singapore, the Future Continuous Manufacturing and Advanced Crystallisation Research Hub (grant ref.: EP/P006965/1) to finance my PhD and attendance to scientific conferences and symposiums. I would also like to thank Circa Group Pty Ltd. for the supply of the chiral solvent cyrene used in the experiments. Furthermore, a special appreciation to the International Visiting Internship Student Program from The Hong Kong University of Science and Technology for funding my placement in Hong Kong.

A very warm thanks to Dr. Alan Martin, Dr. Jiayuan Wang, and Dr. Raghunath Venkatramanan for their collaboration with their expertise in X-ray diffraction, process modelling, and process analytical techniques, respectively, that contributed to the development of chapters 3, 4, and 5 of this thesis.

I am also grateful to the assessment committee for their time, care, and consideration for the finalization of my PhD.

Additionally, I would like to thank all the members in Prof. Joop H. ter Horst and Prof. Richard Lakerveld's research groups for their welcome and very useful help and support, and in particular: Carlos, Corin, Raghu, Jiayuan, Kiran, Pramuditha, Junhao, Baggie, and Victor. Also, a special gratitude to Miguel, Pramuditha, and Genís to discover me the very best of Hong Kong.

Finally, a million thanks to my family, Catherine, and friends. Their encouragement and love have gotten me through all the difficult times. I am grateful to them for all the chats, advice, and good moments.

Thank you all for everything!

LIST OF PUBLICATIONS

1. **Temperature and pH-Dependent Solubilities of Enantiopure and Racemic Amino Acids in Complex Aqueous Solutions: a Fast and Accurate Estimation of Phase Diagrams**

   Authors: Jose Capdevila-Echeverria, Joop H. ter Horst

   In preparation

2. **Process Modelling and Optimisation of Continuous Chiral Resolution by Integration of Membrane and Crystallisation Technologies**

   Authors: Jose Capdevila-Echeverria, Jiayuan Wang, Richard Lakerveld, Joop H. ter Horst

   In preparation

3. **Enantioselective Liquid-Liquid Extraction and Crystallisation of Chiral Compounds in a Green Chiral Solvent**

   Authors: Jose Capdevila-Echeverria, Raghunath Venkatramanan, Joop H. ter Horst

   In preparation

ABSTRACT

Chiral molecules occur in left- and right-handed configurations that can be considered as mirror images (enantiomers), and that, like hands, cannot be superimposed onto each other. Despite their similarity, the biological activity of enantiomers inside living organisms can be completely different. While one enantiomer may have a desirable therapeutic effect, the other may induce no response or even be harmful. Most pharmaceuticals and agrochemicals are chiral. The search of this specificity at the molecular level led to the development of many asymmetric syntheses. However, the enantioselective synthetic approach is not always possible and the mixture of equal amounts of both enantiomers (racemate) is obtained instead. Then, the separation of these enantiomers, known as chiral resolution, becomes the alternative pathway. Chiral resolution techniques have already been developed, but they still present some limitations. For that, the aim of this thesis is to develop novel methodologies and processes that integrate membrane filtration, crystallisation, and extraction technologies for the chiral resolution of fine chemical racemates.

In chapter 3, the effects of pH and temperature on the solubility and phase diagrams of three racemic compound-forming systems are described. This preliminary study of effects permits the development of a method to accurately estimate the eutectic points and phase diagrams of these systems. Additionally, the method also gives the possibility to determine the class of crystal lattice (conglomerate, racemic compound, or solid solution) of any chiral compound. The ultimate objective of this chapter is to provide a workflow process to determine fast and accurately the phase diagrams of racemic compounds.

The chiral resolution of conglomerates has been successful by means of crystallisation-based techniques such as preferential crystallisation. Nevertheless, this type of chiral compounds alongside solid solutions are rare with racemic compounds being the most abundant. The latter class requires an initial enantiomeric enrichment which must go beyond the eutectic composition to after being able to selectively crystallise an enantiopure product. The main objective of chapter 4 is to assess if the combination of membrane filtration and crystallisation technologies enables the continuous chiral resolution of racemic compounds. This has been carried out through computerised modelling and optimisation of the integrated

process and has shown potential to further explore and test the process with other chiral systems.

The separation of enantiomers can also be attempted by leveraging the potential distinctive enantiospecific interactions between enantiomers and chiral solvents. In that way, chapter 5 evaluates the chiral recognition capacity of the relatively new chiral solvent cyrene and finds its potential for chiral resolution process applications founded on both enantioselective liquid-liquid extraction and crystallisation.

The work in this thesis has achieved its aim in developing novel methodologies and processes for the chiral resolution of fine chemical racemates by providing a less laborious workflow process for the fast and accurate determination of ternary phase diagrams of racemic compounds, which has served to propose a novel chiral resolution process for this class of chiral compounds that integrates both membrane filtration and crystallisation technologies. In addition, the enantiomeric discrimination power found in the chiral solvent cyrene has made possible to propose this solvent for its use in the separation of enantiomers by means of enantioselective liquid-liquid extraction and crystallisation. The findings described in this text will then facilitate the study, understanding, and characterisation of chiral resolution processes based on enantioselective interactions in separation techniques, such as membrane filtration, crystallisation, and extraction. The new methodologies and processes developed in this thesis have the potential to address current and future challenges in the separation of enantiomers, which is of high interest for the fine chemical industry.

TABLE OF CONTENTS

CHAPTER 1

1. Introduction

1.1. Isomerism, chirality, and chiral resolution

The term isomerism was coined by the Swedish chemist Jöns Jacob Berzelius in the year 1830 to describe the phenomenon in which more than one compound have the same chemical formula but different chemical structures [1,2]. Chemical compounds that have identical chemical formulae but differ in properties and the arrangement of atoms in the molecule are called isomers. Therefore, the compounds that exhibit isomerism are known as isomers. There are two primary types of isomerism, which can be further categorised into different subtypes. These primary types are constitutional isomerism and stereoisomerism. The classification of the different types of isomers is illustrated below (Fig. 1) [2]. Inside this classification, enantiomers are optical isomers that are non-superimposable mirror images by any combination of rotations and translations (Fig. 1). This property is known in chemistry as chirality [2–4]. Enantiomers are designated by classical notations, such as D or L, *R* or *S*, or as (+) or (-) (Fig. 1) [2,5,6]. They have the same chemical properties, except when reacting with other chiral compounds. They also have the same physical properties, except that they have opposite optical activities. A homogeneous mixture of the two enantiomers in equal parts is said to be racemic, and it usually differs chemically and physically from the pure enantiomers.

A document published in 1992 by the U.S. Food and Drug Administration (FDA) created broad and deep impact throughout the world's drug development community [7]. The FDA's Center for Drug Evaluation and Research (CDER) enumerated in this document, for the first time, the proper guidelines for the manufacturing of new stereoisomeric drugs. The CDER informed that, despite drug substances had previously been successfully and safely developed and implemented as racemic mixtures, there had

been several cases in which the enantiomers were found to have distinct pharmacologic and toxicologic effect, producing therapeutic problems [7]. The most well-known instance is the thalidomide case. This drug substance was first marketed in 1956 by the German pharmaceutical company Chemie Grünenthal GmbH (now Grünenthal GmbH) to treat respiratory infections and, later, prescribed in concert with other chemical substances as a sedative and for the therapy of nausea and vomiting of pregnancy [4,8–10]. While the enantiomer *S* was later proven to really produce therapeutic effects, its counter enantiomer *R* was verified to be a teratogen and was consequently associated to physical birth defects [4,8–10].

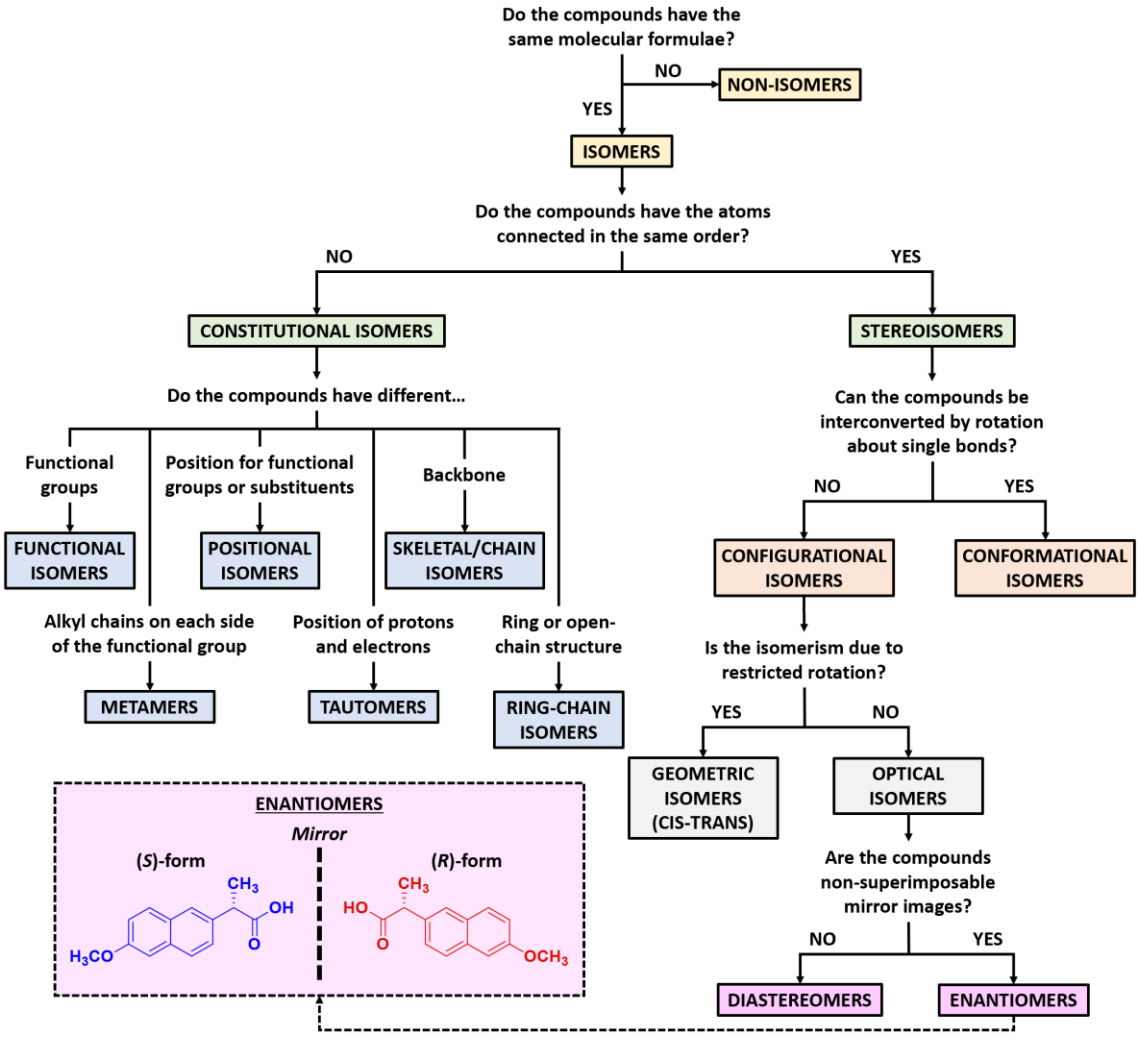

Fig. 1. Flowchart for the classification of the different types of isomers. The molecular example at the left-bottom corner of the flowchart shows the mirror relationship between a couple of enantiomers.

It can be debated that the long-term effects of (*R*)-thalidomide would not have arisen even under the current regulation guidelines for drug acceptance, notably due to the rare interconversion between (*R*)- and (*S*)-thalidomide that occurs in some living organisms such as inside human beings [4,8–10]. Nonetheless, the current FDA's regulation provides the essential level of guarantee against the recurrence of such tragic events [7]. Currently, the FDA's policy requires pharmaceutical manufacturers to quantify the pharmacological and toxicological effects of each enantiomer and produce an enantiopure drug product if the results of either the pharmacokinetics or the toxicology of the enantiomers are considerably different so as to affect drug dosing or secondary effects [7]. Nowadays, the American regulator also requires these assessments to be performed and described thoroughly in the Investigational New Drug (IND) and New Drug Application (NDA) submissions [7].

The purity of chiral pharmaceuticals was an academic issue in the 1990s [8]. This information was important for understanding and classifying the biological transformations of the drug substances. However, it had no great attention in the launch of such products because the manufacturing methodologies of single enantiomers were still limited [8]. Later on, the new policy [7] started having two immediate effects. First, the drug production shifted toward the implementation of single enantiomers [8]. Second, it boosted the development of new techniques for enantioselective synthesis and enantiomeric separations [8]. Thus, this change in regulation required new technology and so created new opportunities for research and development. Between 1992 and 2000, the world market for enantiopure chemical compounds increased from $30 to $100 billion, with almost 24 companies specialising in the separations of chiral compounds in 2001 [8]. Nowadays, enantiomers and their separations find tremendous impact not only in the pharmaceutical sector, but also in the agrochemical, fragrances, and food industries due to their specific and different interaction that they have inside biologic systems and the response they trigger on them [6,11,12].

Since that time, the growth of single enantiomer drug substances has been matched by the growth of asymmetric methods, both in synthesis and separation, which can provide

the required materials. While asymmetric synthesis (or enantioselective synthesis) techniques have improved to allow a variety of compounds to be directly synthesised with high chiral purity, yields of these processes are often low or moderate at best. Conversely, chiral separation (or chiral resolution) techniques can provide near quantitative yields of each enantiomer, however, they are perceived as expensive and inefficient if the undesired enantiomer cannot be utilised in some manner. The main methodologies following these two possible pathways for obtaining enantiopure compounds are described below (Fig. 2) [5,6,8,13–15].

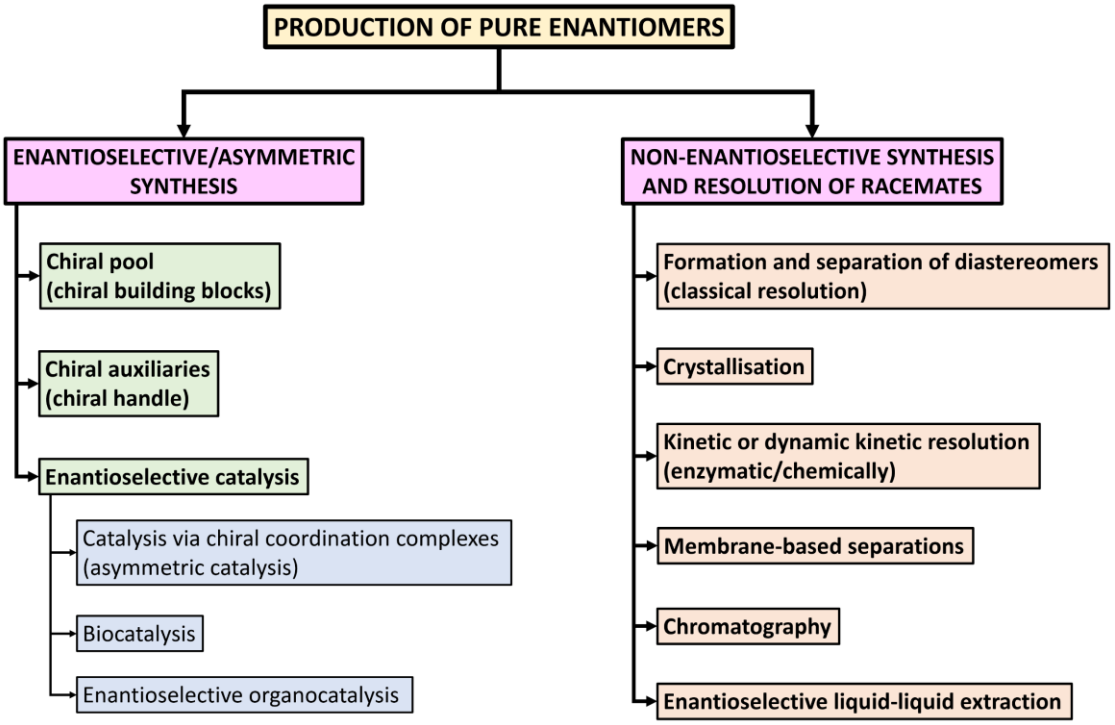

Fig. 2. Possible pathways for producing pure enantiomers.

Inside enantioselective synthesis (Fig. 2), chiral pool synthesis is considered the easiest approach, by means of which available chiral starting materials are manipulated through successive reactions using achiral reagents to obtain the desired chiral target molecules. This pathway results appealing to target molecules with similar chirality to that of more affordable naturally occurring building blocks such as a sugar or an amino acid [6,16,17]. Nevertheless, the chemical transformations of these molecules are often limited, and long complex synthetic routes may be needed. Chiral pool syntheses can become costly in some

cases due to the level of enantiopurity required in the starting materials. This is the case of the synthesis of epothilones [18].

A typical methodology in enantioselective synthesis is the asymmetric induction to convert enantiomers into diastereomers, which present distinct reactivities. An example of this is the use of a chiral auxiliary (Fig. 2) to form an adduct with the starting material which leaves only the desired trajectory open and physically blocks the other one [2,6,16,17]. The reaction pathways thus become often different and lead to different products, especially when this chiral auxiliary presents a specific chirality. This way of proceeding needs two reaction steps to add and remove the chiral auxiliary. The latter translates into a rise in costs and decreasing yields [19].

Enantioselective catalysis (Fig. 2) describes how small amounts of optically active catalysts can promote desired reactions and lead to the formation of larger amounts of enantiomerically pure or enriched products [6,16,17]. It can be mainly divided in three categories: asymmetric catalysis, biocatalysis, and chiral organocatalysis (Fig. 2). An example of metal-ligand complex asymmetric catalysis is the synthesis of naproxen with a chiral phosphine ligand in a hydrocyanation reaction [20]. A case of a catalysed biotransformation is the production of L-lysine by fermentation using *Corynebacterium glutamicum* [6,21]. Finally, an instance of chiral organocatalysis is the asymmetric alkylation or benzylation of glycine derivatives [22].

Regarding non-enantioselective synthesis followed by resolution of racemates, several chiral separations approaches are available (Fig. 2). One of them is classical resolution (Fig. 2) in which the racemate to be separated is converted, with a suitable enantiomerically pure resolving agent, into two diastereomeric salts which present different solubilities and, consequently, become separable by crystallisation [6,14]. This technique is robust and simple to operate. On the other hand, the yields are limited to only 50% if no additional racemization is performed. This resolution technique is still the most applied for the separation of enantiomers at industrial scale. It has also shown a lot of application in the manufacturing of active pharmaceutical ingredients [23]. For instance, thousands of tons of (*S*)-naproxen, D-phenylglycine, and D-4-hydroxyphenylglycine are

produced per year by the formation and separation of diastereomeric salts [24]. Other examples of commercially available pharmaceutical products manufactured by classical resolution are Frovatriptan, Duloxetine, and Eszopiclone [23].

The direct crystallisation of the desired enantiomer from its racemic mixture is also possible for some chiral compounds (Fig. 2). Typically, enantioselective crystallisation occurs after the seeding of a supersaturated solution of the racemic mixture with a crystal of the desired enantiomer. Selective enantiomeric nucleation and crystal growth can occur without seeding under certain conditions for some systems. In 1997, estimations predicted that enantioselective crystallisation accounted for roughly one-fifth of the enantioseparations performed at scales equal or exceeding 1 kg of product [8]. The widespread acceptance of crystallisation is because of the ease of operation and low manufacturing expense. This is the chiral resolution methodology of choice when the technique is available and efficient. Nonetheless, crystallisation is usually employed in a fractional manner to give enough material recoveries, what translates to longer times and increasing costs [8].

The chiral separation approach responsible for leveraging the difference in the consumption rates of two enantiomers in a chemical reaction is known as kinetic resolution (Fig. 2). As a result of this kinetic difference, an excess of the less-reactive enantiomer is created, the concentration of which goes through a maximum before it disappears on full completion of the reaction. An example of this technique is the esterification of racemic mandelic acid with optically active (-)-menthol to form a pair of diastereomeric esters [6,13]. A remarkable extension of the kinetic resolution is the dynamic kinetic resolution (Fig. 2). This latter tackles the inconveniences of the former system, which are that the maximum conversion in the reaction is only 50% and the product must be separated from the reactants [6,13]. In the dynamic approach, it is possible to convert the achiral reactant with 100% completion on account of both enantiomers are connected in a chemical equilibrium. In this way, the faster-reacting enantiomer is replenished during the reaction at the expense of the slower-reacting enantiomer. An illustration of this method is a variant of the Noyori asymmetric hydrogenation [25,26].

Another method to separate enantiomers is founded on the use of membrane-based approaches (Fig. 2). Membrane separations are generally attractive options because of the clean, energy efficient, ease of performance, and continuous operation [27–31].

The preparative high-performance liquid chromatography (HPLC) was one of the first separation techniques to gain practical popularity (Fig. 2). It is used to obtain relatively small amounts of enantiopure substances due to existing stationary phases possessing enantiospecific recognition. The suitable combination of stationary and mobile phases is selected to allow the mixture of enantiomers to be eluted from a column of the stationary phase at different retention times. The separation into the pure enantiomers can be performed when performing repetitive injections of the mixture of enantiomers and collecting the effluent from the column in appropriate time segments. However, the HPLC has some drawbacks, such as the use of a substantial amount of solvent and the requirement of significant capital investment in the form of expensive stationary phase and high-pressure equipment. Furthermore, the desired product is obtained from the process in extremely dilute form, resulting in significant energy expenditure to recover the desired compound [8]. A few variants of the preparative HPLC have been invented to attempt to overcome these issues. The most important of these adaptations is the simulated moving bed (SMB) chromatography (Fig. 2). This separation method overcomes many of the limitations of the preparative HPLC described above by increasing the solvent efficiency, solvent management, adsorbate concentration, and stationary phase utilisation. The latter finds its main applications in the petrochemical industry, but it has also been used in the separation of some pharmaceutical compounds at industrial scale [6,8].

The enantioselective liquid-liquid extraction (ELLE, Fig. 2) is a specific adaptation of the well-established standard liquid-liquid extraction method which can also operate in a counter-current mode to fractionate racemates continuously into their enantiomers [15,32] but, at the same time, makes use of features of host-guest chemistry [6,33]. Thus, ELLE combines the concepts of enantiomeric recognition and solvent extraction in a single technique that results of special interest for the separation of enantiomers since it can be operated at different scales [15].

1.2. Crystallisation of chiral compounds

The documented origin of enantioseparation by means of direct crystallisation comes from Pasteur's famous experiments with sodium ammonium tartrate [14,34–36]. Since then, much research has been dedicated to study and find applications for crystallisation processes with focus on the separation of enantiomers. Remarkable progress has been achieved both in understanding the fundamentals of thermodynamics and kinetics in enantioselective crystallisation and in leveraging this knowledge for the development of new crystallisation methodologies. Generally, the advantages of crystallisation are its simplicity, wide application, and cost efficiency. This technique has been broadly embraced especially by the pharmaceutical and fine chemical industries, which helped to standardise crystallisation equipment and make it readily accessible. Crystallisation techniques are not limited to the resolution of racemates, but can also be applied for further purification of scalemic mixtures resulting from other enantioenriching techniques, such as partially selective synthesis, membrane separation, or chromatography [5,6,14].

When it comes to chirality within crystal structures, there are three main different scenarios. Enantiomers can either crystallise as a racemic compound (Fig. 3), where each crystal lattice is composed of equal amounts of both enantiomers [14]; or as a conglomerate (Fig. 3), where each crystal lattice is enantiopure per separate (contains only one of the enantiomers) [14]; or as a solid solution (Fig. 3), where both enantiomers compete for the same space within the crystal structure (random assortment of both enantiomers) [14]. Racemic compounds make up around 90-95% of all chiral compound crystal structures, conglomerates around 5-10%, and solid solutions less than 1% of the chiral compounds (Fig. 3) [5,6,13,14,37].

The form which is most stable depends on the properties of the chiral molecule itself, as well as temperature, pressure (often assumed as atmospheric pressure, so equal to 101,325 Pa), and enantiomer composition [14,37]. This can be represented in the form of a ternary phase diagram for each system, as shown below (Fig. 3). Each corner of the ternary phase diagram represents 100% of one of the three components in the system:

solvent, (*R*)-enantiomer, and (*S*)-enantiomer (Fig. 3). The determination of ternary phase diagrams is experimentally time-consuming and tedious. Similarly, the identification of the crystal lattice class of chiral compounds and measurements of some of their key properties, useful for the development of specific chiral resolution procedures, such as solubilities and eutectic point compositions also require lengthy experimentation. Thus, there is the current need to develop methods that make these determinations faster [38].

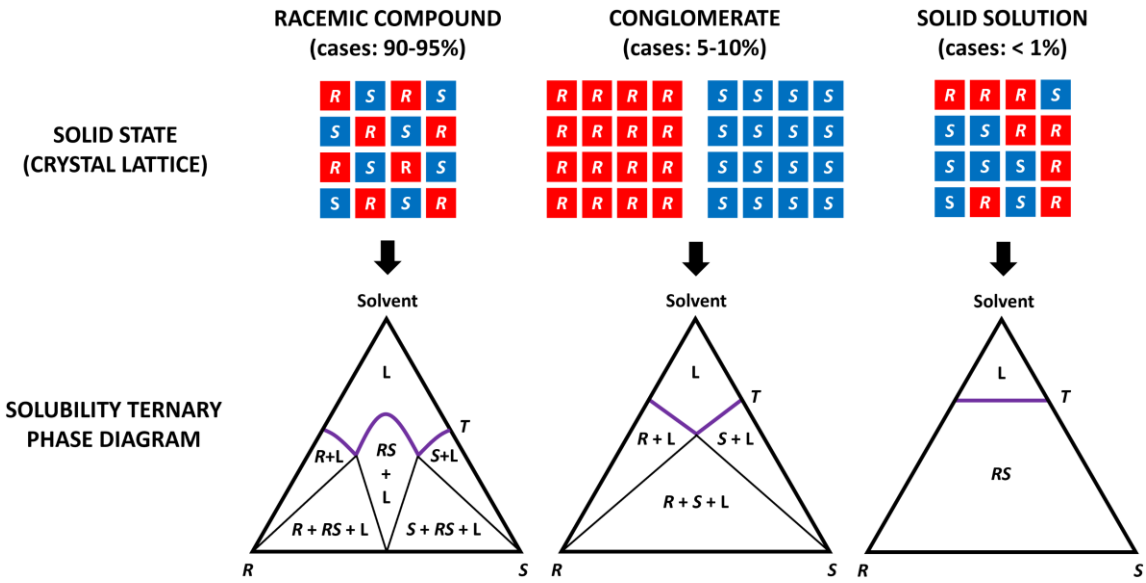

Fig. 3. Crystal structures (lattices) and solubility ternary phase diagrams, at certain temperature *T*, for the three different types of chiral compounds: racemic compound, conglomerate, and solid solution. Thick purple lines mark the saturation lines. *R*, *S*, *RS*, and L represent, respectively, the solid phase of enantiomer *R*, solid phase of enantiomer *S*, solid phase of racemic compound *RS* or solid solution *RS*, and liquid phase.

The resolution of enantiomer mixtures is mainly achieved by means of direct crystallisation of the target enantiomer or, indirectly, by means of formation and posterior separation of diastereomers (classical resolution) [5,6,14]. The latter technique requires the prior chemical transformation of the racemate into two diastereomeric salts which have different solubilities and, thus, become separable by posterior crystallisation.

Regarding the direct crystallisation of one enantiomer, mainly two techniques can be distinguished for the resolution of only conglomerates: a) the entrainment process (often called preferential crystallisation) and b) simultaneous crystallisation [14]. These techniques can be applied on both solution and melt phases. The entrainment process is a

kinetically driven separation that is based on the different crystallisation rates of the enantiomers in the presence of homochiral seeds [5,6,14]. Here, enantiomers crystallise successively from a supersaturated racemic solution and the process is not permitted to reach equilibrium. The entrainment process is usually applied on small scales in a batch mode [5,6,14,39]. Instead, simultaneous crystallisation is normally applied in larger scales. In this last case, the enantiomers crystallise simultaneously but locally separated from the solution, which is always close to the racemic composition [6,14]. Additionally, the relatively new attrition-enhanced deracemization, also known as Viedma ripening, is also a direct resolution technique founded on the ground-breaking studies developed by Viedma [40]. He found out that a racemic mixture of enantiomorphous $NaClO_3$ crystals in contact with the saturated solution deracemizes on grinding the crystals in the suspension [40]. This latter technique finds application in cases where the racemate to be resolved is a conglomerate and rapidly racemizes in the liquid [41,42]. However, it is a difficult approach to scale up to industrial production due to the large amount of grinding material required in the system, even with use of an in-situ homogenizer [43].

An additional method for the separation of racemates is the application of optically active solvents, often referred also as chiral solvents despite they might also be achiral solvents containing definite amounts of a pure enantiomer as the solute [6,14,44]. Theoretically, specific diastereomeric interactions may occur when enantiomers are dissolved in an optically active solvent. As a consequence, diastereomeric complexes are formed with distinct physicochemical properties that could potentially lead to differences in the enantiomers solubilities of the chiral compound to be resolved and, therefore, should introduce a certain degree of asymmetry in the respective solubility phase diagram. Nonetheless, albeit this concept has been considered as a relevant tool for separation of enantiomers since the beginning of the 20^{th} century, only little research has been documented [14]. Currently, a lack of methodical scientific evidence does not allow the generalisation of the results in this field.

Besides, there are few modelling and experimental works that focus on the resolution of racemic compound-forming systems by means of coupling enantioenriching techniques

in a first step followed by a final crystallisation step. This is the case of the hybrid pertraction-crystallisation [45,46] or chromatography-crystallisation [6,47,48] enantioselective separation processes where, as first steps, either pertraction using supported liquid membranes or chromatography using a simulated moving bed or HPLC column provides the initial enantiomeric enrichment, while the following selective crystallisation step delivers the enantiopure crystals as final product.

1.3. Membrane-based chiral separation

An inexpensive, continuous, high-efficient resolution technology is clearly required for the manufacturing of enantiomerically pure substances at commercial scale. Fortunately, membrane technology fulfils this need excellently on account of its low energy usage, simplicity, high efficiency, convenience for up- and/or downscaling, and continuous operability, although presenting a low number of transfer units per instrument [29,30,49–51]. The separation of enantiomers via membrane-based approaches can be accomplished using either enantioselective or non-enantioselective membranes (Fig. 4) [29–31,49,52]. The enantioselective membranes perform the chiral separation of enantiomers on their integrated chiral recognition sites, and they are usually classified as liquid or solid (Fig. 4). Instead, the non-enantioselective membranes do not present enantioselectivity themselves, but assist in the chiral resolution, for example, by acting as ultrafiltration membranes. Thus, non-enantioselective membrane-assisted processes are generally combined with other chiral recognition approaches, such as enzymatic kinetic resolution, solution systems with micelles, and systems using chiral selectors as complexing agents [31]. Currently, some applications using membrane-assisted methods are already employed at industrial production scale [31,53], and this approach has already attracted remarkable attention since the beginning of the new millennium [31].

Enantioselective membranes can separate enantiomers by means of chiral properties such as chiral recognition sites (chiral side chains, chiral backbones, or chiral selectors). They can be divided into liquid and solid membranes according to the phase of the membrane (Fig. 4). The enantioselective membranes work as selective barriers in the

separation process and they selectively transport one enantiomer as a result of the enantiospecific interaction between the enantiomer and the chiral recognition sites. This action produces a permeate solution enriched with one enantiomer. The different binding affinities of two enantiomers can be related to the different hydrogen bonding, hydrophobic, Coulombic, and van der Waals interactions and steric effects with the optically active sites [54].

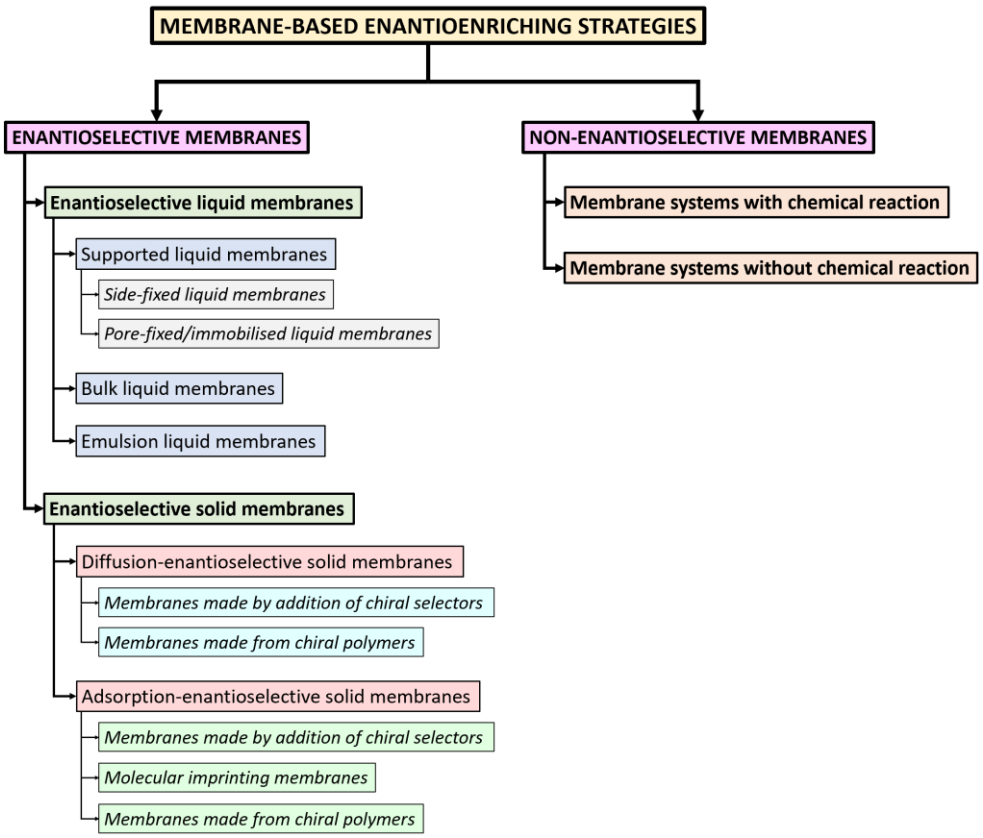

Fig. 4. Classification of membrane-based enantioenriching strategies.

In enantioselective liquid membrane systems (Fig. 4), chiral selectors are found dissolved in the liquid membrane phase. The liquid membrane must not be miscible in either the feed or the receiving phases. One of the two enantiomers is preferentially transported by means of mobile chiral carriers present in the liquid membrane phase usually facilitated by a concentration or pH gradient. A characteristic liquid membrane system consists of an organic solvent, as membrane, with aqueous feed and stripping phases (Fig. 4) [30,31,52]. Enantioselective solid membranes can be created by casting

chiral polymer solutions or mixtures that have chiral selectors (Fig. 4). As another option, chiral selectors can be immobilised by either esterification, impregnation, or grafting on the surfaces or in the pores of support membranes (Fig. 4) [31,52]. Besides, molecular imprinting can be used to form molecular recognition sites inside the membranes (Fig. 4) [31,52]. Liquid membranes normally bear high mass transfer rates and a low chiral selector consumption [55]. On the other hand, solid membranes are known by their long-term stability [30,31,50].

Non-enantioselective membranes in chiral resolution systems are typically employed as supports to capture chiral selectors or to separate particles by size rather than for distinguishing one enantiomer in a racemic mixture. That is, the enantioseparation mechanism for this type of membranes differs considerably from that for enantioselective membranes. Non-enantioselective membranes basically retain larger molecules to reach certain enrichment of smaller molecules in the stripping phase. Thus, a difference in size of the enantiomers is the key for the enantioseparation by such non-enantioselective ultrafiltration membranes [52]. Non-enantioselective membranes in combination with other chiral recognition procedures, referenced as membrane-assisted resolution techniques, are an alternative methodology to perform the separation of enantiomers. The last approach means that non-enantioselective membranes act as filtration barriers to selectively separate pure enantiomers from a solution that incorporates a racemic mixture and, at least, one type of enantioselective binding agent. Therefore, the understanding of the specific binding mechanism and the optimisation of its process conditions become crucial for the efficient chiral resolution of the racemate in procedures that use this type of membrane. The non-enantioselective membranes have also the potential to connect with enzymatic chemical reactions or act as supports for functional layers. Importantly, this technique is economical and convenient. As a result of the advantages of membranes, such as not complicated scale-up and energy-saving, this technique is appropriate for the production of enantiopure compounds at industrial scale [31]. In the same way as enantioselective membranes, two main classes of non-enantioselective membranes find application for chiral resolution processes, which can also make use of liquid or solid

versions of membranes. The combinatorial approach used with these membranes includes systems with and without chemical reaction (Fig. 4). Some application examples that can be used to achieve enantiomeric separation are the formation of a complex of one enantiomer with a large chiral molecular selector such as bovine serum albumin (BSA) or the use of enzymes to selectively hydrolyse one of the enantiomers, followed by an ultrafiltration step with a porous non-enantioselective membrane [30,31,56,57].

1.4. Enantioselective liquid-liquid extraction

Liquid-liquid extraction is an established technique which can be run in a continuous counter-current mode to separate the racemate into its enantiomers [2,15,58], which is valuable when operating at large scales. Diffusion and convection are the transport mechanisms, and high transport rates are achievable [59]. First liquid-liquid extraction experiments for chiral resolution application were reported in Russian in 1959 [15], and the first publications in English appeared in the late 1960s [60–63]. The enantioselective liquid-liquid extraction is closely related to the host-guest chemistry [33] and chiral recognition can be regarded as a mere practical application of the developments in this field. ELLE combines the notions of enantiomeric recognition [64] and solvent extraction [32,65,66] in a single technique.

The principle of enantiomeric recognition is essential for the enantioselective complexation and thus for ELLE. Enantioselective processes are not possible without enantiomeric recognition. Encounter complexes of the extractant with the enantiomers are formed as a result of intermolecular interactions [67]. These intermolecular interactions may include ion pairing, hydrogen bonding, π-π, dipole, and van der Waals interactions [16,17,64]. The complexation of a chiral host with a chiral guest which presents one stereocentre can be schematically represented as the guest binding with groups B, C, and D to the groups B’, C’, and D’ of the host (Fig. 5a, left). The opposite enantiomer will bind to two out of three sites (Fig. 5a, right) [16,17]. The three-point attachment (TPA) model states that the complex binding with the three sites (Fig. 5a, left) is the favoured one [16,17,68]. This TPA model converts into the three-point interaction (TPI) model

[2,69] when the interactions (Fig. 5a, dotted lines) represent not just attracting forces, but also repulsive forces. Besides the chiral recognition concept, the presence of two (at least partially) immiscible phases, usually an aqueous and an organic phase, is also crucial for ELLE. A representative ELLE system initially has the substrate predominantly restricted in the aqueous phase (Fig. 5b). After adding a lipophilic host or extractant, which prefers to stay in the organic phase, a host-mediated phase transfer of the substrate takes place. In the illustration below (Fig. 5b), the interaction of the host with the enantiomer *R* is favoured over the interaction with the counter enantiomer *S*. Given that, the organic phase becomes enriched with the enantiomer *R* while enantiomer *S* mainly remains and predominates in the aqueous phase (Fig. 5b).

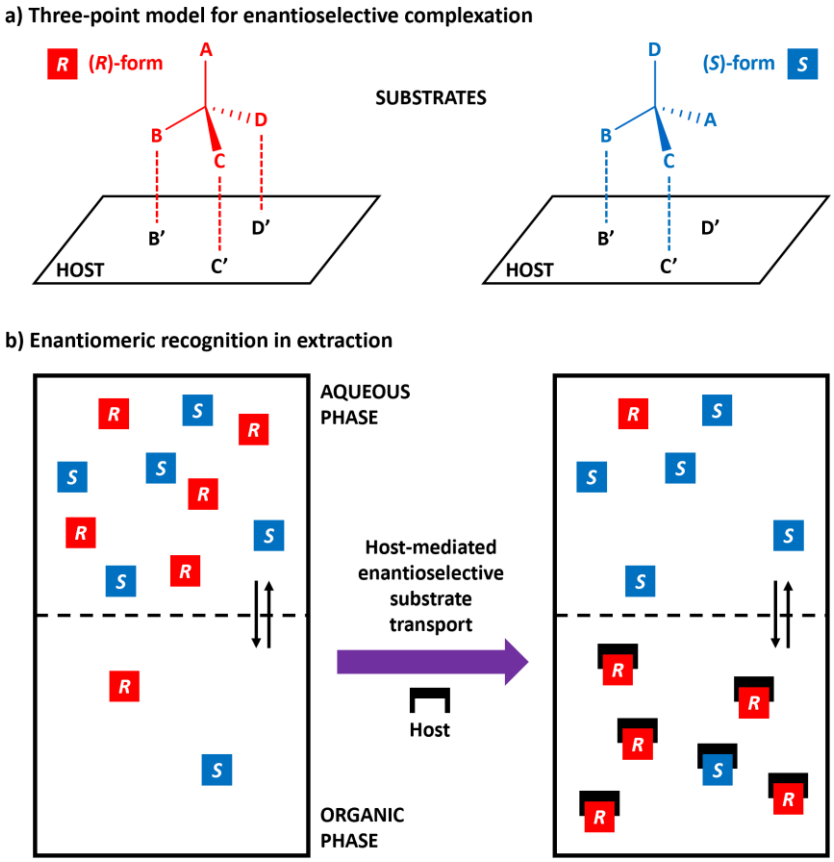

Fig. 5. a) The three-point model for the complexation of both substrate enantiomers (guests) to a chiral host and b) enantiomeric recognition and extraction in a biphasic system.

The traditional equipment for the liquid-liquid extraction employed in the chemical industry is quite varied regarding both sizes and types [70]. The selection of the most

appropriate class of apparatus depends on the process conditions and constraints and may be supported by selection charts [71]. Currently, the industrial sector makes use basically of two types of extractors: the mixer-settlers that form discrete stages and are used for the bulkiest of all separation processes, and the extraction columns that are most broadly applied in all classes of extraction processes [15].

An overview of the ELLE chemistry categorised according to the chiral extractant classes and their specific extractants (hosts) and substrates (guests) is shown below (Table 1) [2,15,58].

Table 1. Extractants classification for enantioselective liquid-liquid extraction [2,15,58].

Extractant class	Extractant	Substrate
Crown ether-based reactive extractants	Cram's dilocular host	α-Amino acids and α-amino acid ester salts
	BINOL-crown ether	α-Amino acids and ester salts
	Guanidium-crown ether	α-Amino acids
	Lipophilic crown ethers	Picrate ammonium salts
	Azophenolic crown ethers	Primary amines
Metal complexes and metalloids as reactive extractants	Proline derivative Cu(II) complexes	α-Amino acids
	Lanthanide(III)tris(β-diketonate) complexes	α-Amino acids and amino alcohols
	Metalloporphyrins	*N*-Cbz α-amino acids
	Palladium-BINAP complexes	α-Amino acids
	Salen-cobalt(III) complexes	*N*-Acyl α- and β-amino acids
Tartrate-assisted extractants	Dialkyl tartrates and boric acid	β-amino alcohols
	Di(2-ethylhexyl)phosphoric acid and a tartaric acid derivative	Amino acids
	Diphosphonium salt bearing binaphthyl hosts	Tartaric acid derivative
	Alkyl tartrate with β-cyclodextrin	Carboxylic acids, cyclopyrrolone derivate
Other chiral extractants	Carbamoylated quinine derivatives	*N*-Protected α-amino acids
	Steroidal guanidinium hosts	*N*-Acyl amino acids
	Deoxyguanosine derivatives	DNB-*N*-protected α-amino acids
	Sapphyrin-lasalocid host	α-Amino acids
	TRISPHAT salts	Tris(diimine)ruthenium(II) complexes
	Hydrogen bond-assisted BINOL-aldehyde hosts	Amino alcohols
	3,3'-Diaryl-BINOL phosphoric acids	Primary amines

Therefore, with a closer glance on the types of chemistry used so far in ELLE (Table 1), it can be noted that this technique has been mainly focused on the use of solutes as extracting agents [2,15,58]. It has not been yet considered the use of a chiral extracting solvent to act as the extractant agent itself without using or generating additional species during the extraction process. This fact gives the research possibility to discover new classes of extractant solvents that could make ELLE processes more efficient, economical, and environmentally friendly because of reducing the chemical waste due to the fact that a lower number of chemical agents would be required for the process.

1.5. Aim and objectives

The quality of a particulate chiral chemical product is mainly assessed by its enantiomeric purity as the counter enantiomer might induce unwanted biological responses inside living organisms. Thus, achieving only the desired specific biological effect requires the use of only one chiral form from the enantiomeric pair. In fact, the market demand trend for the manufacturing of enantiospecific pharmaceutical, agrochemical, fragrance, and food products is ascendant promoted especially by the recommendations of the principal health regulators during the last three decades. Therefore, the isolation of a specific enantiomer from its racemate has need of advances and developments of current and novel chiral resolution processes and methodologies. In other words, there is a drive towards new and improved chiral separation methods. At the same time, new pharmaceutical molecular entities become more complex, so separation become more challenging as well.

The main aim of this thesis is to develop novel methodologies and processes that integrate membrane filtration, crystallisation, and extraction technologies for the chiral resolution of fine chemical racemates. This aim is broken down into the different chapter objectives shown below (Fig. 6). Each experimental chapter of this thesis contributes to the overall aim through either a new procedure that facilitates the detection of the chiral compound class and the determination of its phase diagram and thus its posterior chiral

resolution; or novel chemical processes that implement membrane filtration, crystallisation, and extraction technologies for the chiral separation of racemic mixtures.

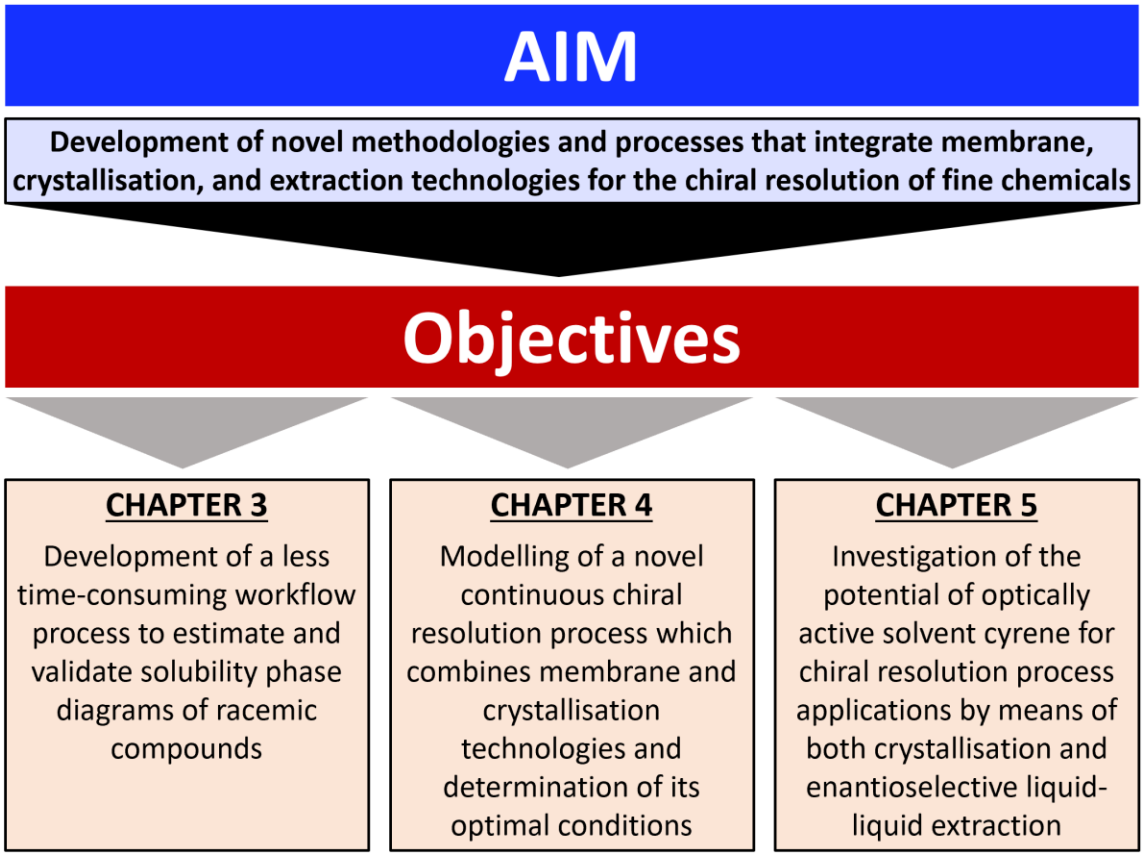

Fig. 6. The aim of this thesis is broken down into the main objectives of its experimental chapters.

Chapter 3: Temperature and pH-Dependent Solubilities of Enantiopure and Racemic Amino Acids in Complex Aqueous Solutions: a Fast and Accurate Estimation of Phase Diagrams.

The determination of solubility phase diagrams of chiral compounds is time-consuming and tedious. A necessity therefore exists to devise and develop methodologies which make these determinations, with high level of accuracy, faster. In this way, chapter 3 has the objective to develop a workflow process that allows for the fast and accurate determination of eutectic points and ternary phase diagrams of racemic compound-forming systems, which are required for several applications such as crystallisation-based chiral resolution processes. For that, this chapter also describes the effects of pH,

temperature, and enrichment on the solubility and eutectic compositions in the binary and ternary phase diagrams of three racemic compound-forming systems. In a first instance, the solubilities of the racemic and enantiopure compounds of the chiral system are determined, which leads to an estimation of its ternary phase diagram. Later, a pseudo-binary phase diagram is also measured for the same chiral system to obtain an estimation of its eutectic points. Then, a comparative accuracy study of the eutectic point values obtained from the pseudo-binary and ternary phase diagrams is carried out alongside with reported literature data in order to validate a new fast method to accurately estimate eutectic points by only determining a pseudo-binary phase diagram. These studies are performed at different pH, temperature, and concentration values to show and compare the accuracy of the new method developed under different parameter conditions. This new method is therefore proposed alongside additional solubility data obtained from the pseudo-binary phase diagrams and a few additional validation measurements to accurately determine the ternary phase diagrams of racemic compound-forming systems, which result extremely useful for the design and development of crystallisation-based chiral resolution applications.

Chapter 4: Process Modelling and Optimisation of Continuous Chiral Resolution by Integration of Membrane and Crystallisation Technologies.

The increasing market demand and complexity of new chiral active ingredients in the fine chemical industry requires for new and improved methods to separate enantiomers from their racemic solutions. This chapter suggests a novel continuous combinatorial process for the chiral resolution of racemic compound-forming systems using a complexing agent by integrating membrane ultrafiltration and selective crystallisation. First, a theoretical one-site competition model that makes use of a chiral selector to preferentially bind one of the enantiomers in the racemic mixture is developed to explore the evolution of the species concentrations in the feed. Then, optimal membrane ultrafiltration conditions for maximum enantiomeric enrichment in the permeate stream are investigated. Finally, if the permeate is sufficiently enriched, selective crystallisation of the enantiopure compound in a final step can take place. Then, the requirement of using

a single- or multi-stage membrane ultrafiltration approach is assessed depending on the chiral system, pH, chiral selector, and enantiomers concentrations; in order to optimise three key performance indicators, which are purity, recovery, and a combination of the previous two. These indicators, which are evaluated for each step of the process and for the overall process, are also used to assess the ideal chiral selector properties necessary for the process through two sensitivity studies based on both complexation and acid-base dissociation phenomena.

Chapter 5: Enantioselective Liquid-Liquid Extraction and Crystallisation of Chiral Compounds in a Green Chiral Solvent.

Cyrene is a relatively new commercial chiral solvent which has not been investigated yet for its chiral properties and related application potential. In fact, optically active solvents in general have not been extensively studied in crystallisation-based chiral resolution processes and even there is a lack of knowledge on the potential use of this kind of solvents as extractants in enantioselective liquid-liquid extraction. This chapter assesses the chiral recognition capacity of the optically active solvent cyrene and its potential for use in chiral resolution processes of racemic mixtures that make use of enantioselective liquid-liquid extraction and crystallisation techniques. For that, a chiral recognition study is performed with the chiral solvent cyrene through both undersaturated and saturated solutions analyses by means of spectroscopic techniques and solubility measurements. Afterwards, the feasibility of chiral resolution of racemates by means of enantioselective crystallisation and liquid-liquid extraction is evaluated. Further studies in the latter technique are carried out including a miscibility study and a solubility screening of the substrate for the eventual attempt of its enantioselective separation.

1.6. References

[1] S. Esteban, Liebig–Wöhler controversy and the concept of isomerism, J. Chem. Educ. 85 (2008) 1201.

[2] E.L. Eliel, S.H. Wilen, Stereochemistry of organic compounds, John Wiley & Sons, 2014.

[3] J. Singh, T.J. Hagen, D.J. Abraham, Chirality and biological activity, in: Burger's Med. Chem. Drug Discov., 2010.

[4] N. Chhabra, M. Aseri, D. Padmanabhan, A review of drug isomerism and its significance, Int. J. Appl. Basic Med. Res. 3 (2013) 16–18.

[5] H. Lorenz, A. Perlberg, D. Sapoundjiev, M.P. Elsner, A. Seidel-Morgenstern, Crystallisation of enantiomers, Chem. Eng. Process. Process Intensif. 45 (2006) 863–873.

[6] H. Lorenz, A. Seidel-Morgenstern, Processes to separate enantiomers, Angew. Chemie - Int. Ed. 53 (2014) 1218–1250.

[7] FDA's policy statement for the development of new stereoisomeric drugs, Chirality. 4 (1992) 338–340.

[8] J.E. Rekoske, Chiral separations, AIChE J. 47 (2001) 2–5.

[9] S. Mane, Racemic drug resolution: a comprehensive guide, Anal. Methods. 8 (2016) 7567–7586.

[10] M. Klussmann, A.J.P. White, A. Armstrong, D.G. Blackmond, Rationalization and prediction of solution enantiomeric excess in ternary phase systems, Angew. Chemie - Int. Ed. 45 (2006) 7985–7989.

[11] A.M. Rouhi, Chiral business, Chem. Eng. News. 81 (2003) 45–61.

[12] R.A. Sheldon, Chirotechnology, Marcel Decker, New York, 1993.

[13] E. Fogassy, M. Nógrádi, D. Kozma, G. Egri, E. Pálovics, V. Kiss, Optical resolution methods, Org. Biomol. Chem. 4 (2006) 3011–3030.

[14] J. Jacques, A. Collet, Enantiomers, racemates and resolutions, John Wiley & Sons, 1981.

[15] B. Schuur, B.J.V. Verkuijl, A.J. Minnaard, J.G. de Vries, H.J. Heeres, B.L. Feringa, Chiral separation by enantioselective liquid-liquid extraction, Org. Biomol. Chem. 9 (2011) 36–51.

[16] F.A. Carey, R.M. Giuliano, Organic chemistry, 10th ed., McGraw-Hill Education, New York, 2016.

[17] P.Y. Bruice, Organic chemistry, 5th ed., Pearson Prentice Hall, 2008.

[18] U. Klar, B. Röhr, F. Kuczynski, W. Schwede, M. Berger, W. Skuballa, B. Buchmann, Efficient chiral pool synthesis of the C1-C6 fragment of epothilones, Synthesis (Stuttg). 2005 (2005) 301–305.

[19] G. Roos, Compendium of chiral auxiliary applications, Academic Press, New York, 2002.

[20] C. Giordano, M. Villa, S. Panossian, Naproxen: industrial asymmetric synthesis, in: A.N. Collins, G.N. Sheldrake, J. Crosby (Eds.), Chirality Ind. Commer. Manuf. Appl. Opt. Act. Compd., John Wiley & Sons, Inc., Chichester, 1992: pp. 303–312.

[21] I. Ojima, Catalytic asymmetric synthesis, 3rd ed., John Wiley & Sons, Inc., Hoboken, 2010.

[22] K. Maruoka, T. Ooi, T. Kano, Design of chiral organocatalysts for practical asymmetric synthesis of amino acid derivatives, Chem. Commun. (2007) 1487–1495.

[23] H. Murakami, From racemates to single enantiomers—chiral synthetic drugs over the last 20 years, in: K. Sakai, N. Hirayama, R. Tamura (Eds.), Nov. Opt. Resolut. Technol. Top. Curr. Chem. Vol. 269, Springer, Berlin, 2006: pp. 273–299.

[24] A. Collet, Resolution of racemates: did you say “classical”?, Angew. Chemie Int. Ed. 37 (1998) 3239–3241.

[25] R. Noyori, T. Ikeda, T. Ohkuma, M. Widhalm, M. Kitamura, H. Takaya, S. Akutagawa, N. Sayo, T. Saito, T. Taketomi, H. Kumobayashi, Stereoselective hydrogenation via dynamic kinetic resolution, J. Am. Chem. Soc. 111 (1989) 9134–9135.

[26] M. Kitamura, T. Ohkuma, M. Tokunaga, R. Noyori, Dynamic kinetic resolution in BINAP—ruthenium(II) catalyzed hydrogenation of 2-substituted 3-oxo carboxylic esters, Tetrahedron: Asymmetry. 1 (1990) 1–4.

[27] D.W. Armstrong, H.L. Jin, Enrichment of enantiomers and other isomers with aqueous liquid membranes containing cyclodextrin carriers, Anal. Chem. 59 (1987) 2237–2241.

[28] J.T.F. Keurentjes, J.M. Voermans, Membrane separations in the production of optically pure compounds, in: A.N. Collins, G.N. Sheldrake, J. Crosby (Eds.), Chirality Ind. II Dev.

Commer. Manuf. Appl. Opt. Act. Compd., John Wiley & Sons, Inc., Chichester, 1997: pp. 157–180.

[29] J.T.F. Keurentjes, Chiral separation techniques, in: G. Subramanian (Ed.), Chiral Sep. Tech. a Pract. Approach, 2nd ed., WILEY-VCH Verlag, Weinheim, 2001: pp. 129–150.

[30] C.A.M. Afonso, J.G. Crespo, Recent advances in chiral resolution through membrane-based approaches, Angew. Chemie Int. Ed. 43 (2004) 5293–5295.

[31] R. Xie, L.-Y. Chu, J.-G. Deng, Membranes and membrane processes for chiral resolution, Chem. Soc. Rev. 37 (2008) 1243.

[32] J.D. Thornton, Science and practice of liquid – liquid extraction, Vol. 1-2, Clarendon, Oxford, 1992.

[33] D.J. Cram, J.M. Cram, Container molecules and their guests, Royal Society of Chemistry, Cambridge, 1994.

[34] L. Pasteur, Sur les relations qui peuvent exister entre la forme crystalline, la composition chimique et le sens de la polarization rotatoire, Ann. Chim. Phys. 24 (1848) 442–459.

[35] J. Gal, Molecular chirality in chemistry and biology: historical milestones, Helv. Chim. Acta. 96 (2013) 1617–1657.

[36] J. Gal, Pasteur and the art of chirality, Nat. Chem. 9 (2017) 604–605.

[37] S. Srisanga, J.H. Ter Horst, Racemic compound, conglomerate, or solid solution: phase diagram screening of chiral compounds, Cryst. Growth Des. 10 (2010) 1808–1812.

[38] H. Fakhraian, M. Salimi, B. Zarenezhad, E. Choobdari, Ternary phase diagram modeling of chiral medetomidine salts using NRTL-SAC Model, Phys. Chem. Res. 4 (2016) 663–671.

[39] G. Coquerel, Preferential crystallisation, Springer-Verlag, Berlin, Heidelberg, 2006.

[40] C. Viedma, Chiral symmetry breaking during crystallisation: complete chiral purity induced by nonlinear autocatalysis and recycling, Phys. Rev. Lett. 94 (2005) 065504.

[41] W.L. Noorduin, E. Vlieg, R.M. Kellogg, B. Kaptein, From Ostwald ripening to single

chirality, Angew. Chemie Int. Ed. 48 (2009) 9600–9606.

[42] L.C. Sögütoglu, R.R.E. Steendam, H. Meekes, E. Vlieg, F.P.J.T. Rutjes, Viedma ripening: a reliable crystallisation method to reach single chirality, Chem. Soc. Rev. 44 (2015) 6723–6732.

[43] R.R.E. Steendam, J.H. ter Horst, Continuous total spontaneous resolution, Cryst. Growth Des. 17 (2017) 4428–4436.

[44] S.K. Tulashie, H. Lorenz, L. Hilfert, F.T. Edelmann, A. Seidel-Morgenstern, Potential of chiral solvents for enantioselective crystallisation. 1. Evaluation of thermodynamic effects, Cryst. Growth Des. 8 (2008) 3408–3414.

[45] L. Gou, S. Robl, K. Leonhard, H. Lorenz, M. Sordo, A. Butka, S. Kesselheim, M. Wolff, A. Seidel-Morgenstern, K. Schaber, A hybrid process for chiral separation of compound-forming systems, Chirality. 23 (2011) 118–127.

[46] S. Robl, L. Gou, A. Gere, M. Sordo, H. Lorenz, A. Mayer, C. Pauls, K. Leonhard, A. Bardow, A. Seidel-Morgenstern, K. Schaber, Chiral separation by combining pertraction and preferential crystallisation, Chem. Eng. Process. Process Intensif. 67 (2013) 80–88.

[47] H. Kaemmerer, Z. Horvath, J.W. Lee, M. Kaspereit, R. Arnell, M. Hedberg, B. Herschend, M.J. Jones, K. Larson, H. Lorenz, A. Seidel-Morgensten, Separation of racemic bicalutamide by an optimized combination of continuous chromatography and selective crystallisation, Org. Process Res. Dev. 16 (2012) 331–342.

[48] J. von Langermann, M. Kaspereit, M. Shakeri, H. Lorenz, M. Hedberg, M.J. Jones, K. Larson, R. Herschend, R. Arnell, E. Temmel, J.-E. Ba, A. Kienle, A. Seidel-Morgenstern, Design of an integrated process of chromatography, crystallisation and racemization for the resolution of 2′,6′-pipecoloxylidide (PPX), Org. Process Res. Dev. 16 (2012) 343–352.

[49] N.M. Maier, P. Franco, W. Lindner, Separation of enantiomers: needs, challenges, perspectives, J. Chromatogr. A. 906 (2001) 3–33.

[50] K.B. Jirage, C.R. Martin, New developments in membrane-based separations, Trends Biotechnol. 17 (1999) 197–200.

[51] E.M. van der Ent, K. van ’t Riet, J.T.F. Keurentjes, A. van der Padt, Design criteria for

dense permeation-selective membranes for enantiomer separations, J. Memb. Sci. 185 (2001) 207–221.

[52] C. Fernandes, M.E. Tiritan, M.M.M. Pinto, Chiral separation in preparative scale: a brief overview of membranes as tools for enantiomeric separation, Symmetry (Basel). 9 (2017).

[53] J.L. Lopez, S.L. Matson, A multiphase/extractive enzyme membrane reactor for production of diltiazem chiral intermediate, J. Memb. Sci. 125 (1997) 189–211.

[54] J.T.F. Keurentjes, L.J.W.M. Nabuurs, E.A. Vegter, Liquid membrane technology for the separation of racemic mixtures, J. Memb. Sci. 113 (1996) 351–360.

[55] E. Yashima, J. Noguchi, Y. Okamoto, Enantiomer enrichment of oxprenolol through cellulose tris(3,5-dimethylphenylcarbamate) membrane, J. Appl. Polym. Sci. 54 (1994) 1087–1091.

[56] S. Poncet, J. Randon, J.L. Rocca, Enantiomeric separation of tryptophan by ultrafiltration using the BSA solution system, Sep. Sci. Technol. 32 (1997) 2029–2038.

[57] F. Garnier, J. Randon, J.L. Rocca, Enantiomeric separation by ultrafiltration: complexation mechanism of tryptophan analogs to bovine serum albumin, Sep. Purif. Technol. 16 (1999) 243–250.

[58] A.B. De Haan, B. Simandi, Extraction technology for the separation of optical isomers, in: Y. Marcus, M.M. Sharma, J.A. Marinsky (Eds.), Ion Exch. Solvent Extr., Marcel Decker, New York, 2001: pp. 255–294.

[59] R. Viegas, C. Afonso, J. Crespo, I. Coelhoso, Modelling of the enantio-selective extraction of propranolol in a biphasic system, Sep. Purif. Technol. 53 (2007) 224–234.

[60] K. Bauer, H. Falk, K. Schlogl, Racematspaltung von chiralen Ferrocenderivaten durch Gegenstromverteilung, Monatshefte Für Chemie / Chem. Mon. 99 (1968) 2186–2194.

[61] N.S. Bowman, G.T. McCloud, G.K. Schweitzer, Partial resolution of some organic racemates by solvent extraction, J. Am. Chem. Soc. 90 (1968) 3848–3852.

[62] S.J. Romanko, K.H. Wells, H.L. Rothbart, W. Rieman III, Resolution of racemic substances by liquid ion-exchange, Talanta. 16 (1969) 581–590.

[63] G.K. Schweitzer, I.R. Supernaw, N.S. Bowman, The solvent extraction resolution of some optically-active neutral chelates, J. Inorg. Nucl. Chem. 30 (1968) 1885–1890.

[64] W.H. Pirkle, T.C. Pochapsky, Considerations of chiral recognition relevant to the liquid chromatography separation of enantiomers, Chem. Rev. 89 (1989) 347–362.

[65] T.C. Lo, M.H.I. Baird, C. Hanson, Handbook of solvent extraction, Krieger Publishing Company, Malabar, USA, 1991.

[66] R.E. Treybal, Liquid extraction, 2nd ed., McGraw-Hill, New York, 1963.

[67] N.M. Maier, S. Schefzick, G.M. Lombardo, M. Feliz, K. Rissanen, W. Lindner, K.B. Lipkowitz, Elucidation of the chiral recognition mechanism of cinchona alkaloid carbamate-type receptors for 3,5-dinitrobenzoyl amino acids, J. Am. Chem. Soc. 124 (2002) 8611–8629.

[68] V.A. Davankov, The nature of chiral recognition: is it a three-point interaction?, Chirality. 9 (1997) 99–102.

[69] V. Sundaresan, R. Abrol, Biological chiral recognition: the substrate's perspective, Chirality. 17 (2005) S30–S39.

[70] J.C. Godfrey, M.J. Slater, Liquid–liquid extraction equipment, John Wiley & Sons, Inc., New York, 1994.

[71] G.S. Laddha, T.E. Degaleesan, Transport phenomena in liquid extraction, McGraw-Hill, New Delhi, 1978.

CHAPTER 2

2. Methods

2.1. Crystallisation

Crystallisation is a separation technology that exploits the first-order phase transition between liquid and solid [1,2]. By moving the system away from equilibrium in a multicomponent liquid, a driving force for crystallisation of a specific solid can be established. During crystallisation, a suspension of crystals is created which after filtration and drying gives the desired particulate product. This resulting particulate product is often seen as an advantage. Another favourable point for crystallisation compared to other separation techniques is that the product obtained normally is close to 100% purity, even in a single process step.

2.1.1. Solubility and supersaturation

The solubility of a crystalline compound forms the basis for the design of a crystallisation process. Solubility describes at which temperature a specific solution composition is in equilibrium with a specific crystalline phase. It mainly depends on the solvent composition and temperature, while also other compounds present in significant amounts may affect it. The mole fraction solubility x at certain temperature T often can be described sufficiently accurate using the van 't Hoff equation (1), as follows [3]:

$$\ln x = \frac{\Delta H}{R}\left(\frac{1}{T_m} - \frac{1}{T}\right) \tag{1}$$

The van 't Hoff equation describes an ideal solubility behaviour through the heat of fusion ΔH and the melting temperature T_m [4]. R stands for the gas constant. The non-ideality of the system causes the fitted values to deviate from the actual heat of fusion and melting temperature and poor fits may then be observed in a wide range of temperature.

The driving force for crystallisation is represented by the chemical potential difference between the prevailing out-of-equilibrium state of the system and the corresponding equilibrium state [5,6]. Therefore, this chemical potential difference is a function of both concentration c and solubility c^* at a specific temperature and pressure. Thus, the crystallisation driving force is usually represented by the supersaturation ratio S (2):

$$S = \frac{c}{c^*} \tag{2}$$

The supersaturation can be augmented by, for instance, increasing the concentration through solvent evaporation or decreasing solubility by reducing the temperature. Crystal growth reduces the solution concentration and therefore the supersaturation.

2.1.2. Crystallisation techniques

Crystallisation techniques [5–7] are defined by the way supersaturation is created. In case of evaporative crystallisation, solvent is removed by evaporation from a boiling solution [3]. After evaporating the solvent, the solute concentration increases, which raise the supersaturation. The supersaturation, in turn, is consumed by the growing crystals. Evaporative crystallisation therefore is operated close to a three-phase equilibrium point where vapor, solution and solid phase are in equilibrium. The solution volume is lowered by transferring solvent to the vapor phase and solute to the solid phase. The operating temperature can be adjusted by changing the pressure-dependent boiling point. Evaporative crystallisation is chosen if the solubility does not show a strong positive dependence on temperature [8]. Instead, cooling crystallisation can be an option if the solubility shows a strong positive dependence on temperature, and if the solubility at the lowest possible temperature is sufficiently low [3,8]. Upon decreasing the temperature of an equilibrated suspension, the solubility is decreased, and supersaturation is formed which is reduced again by the growing crystals in the suspension. Another way to create supersaturation is to add an antisolvent [3]. Despite an antisolvent dilutes the mixture and reduces the concentration, it also strongly reduces the solubility in the mixture. If the solubility reduction exceeds that of the concentration, then a supersaturation can be

originated, which induces crystallisation. Precipitation is sometimes named reactive crystallisation [3]. When mixing two streams, a reaction may occur which results in a barely soluble solute. If sufficiently high concentrations are used, the concentration is much higher than solubility and supersaturation is established. The phase diagrams from the different crystallisation techniques are depicted below (Fig. 1). They also show how supersaturation is created and the relation between concentration *c*, solubility *c**, and supersaturation ratio *S* (2).

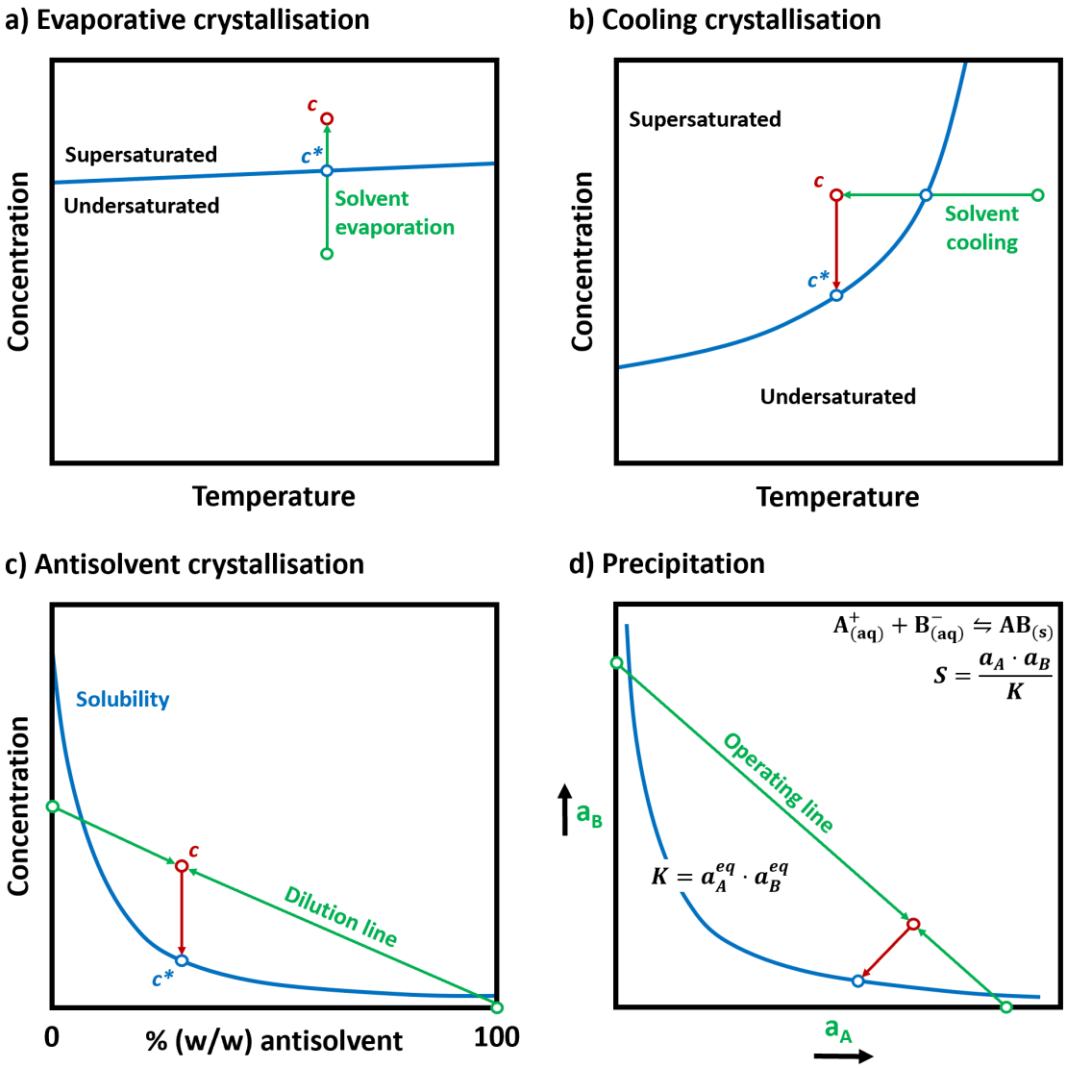

Fig. 1. The phase diagrams, solubility lines, and operating points for the different crystallisation techniques: a) evaporative crystallisation, b) cooling crystallisation, c) antisolvent crystallisation, and d) precipitation. The chemical equation in d) represents a precipitation equilibrium with thermodynamic constant *K*, there *a* accounts for activity.

2.1.3. Crystal nucleation

The beginning of a phase transition towards the crystalline solid phase is called crystal nucleation [5–7,9]. It is ergo the crystallisation subprocess with which crystals come to existence, and it takes place in a supersaturated mother phase (solution, melt, and vapor). Considering that this subprocess determines the number of crystals in which the crystalline material is divided during the crystallisation, it plays a key role in determining the crystal size distribution (CSD) [9].

During crystallisation, crystals can be created from an initial clear solution (primary nucleation) or because of the presence of parent crystals (secondary nucleation) (Fig. 2) [3,9]. In turn, primary nucleation generally is divided into homogeneous and heterogeneous nucleation (Fig. 2). In heterogeneous primary nucleation, the crystals are generated at surfaces such as dust particles, crystalliser walls, air-solution interface or by the addition of template particles. Instead, homogeneous primary nucleation takes place in the absence of a foreign substance in a clear solution. It is important to notice that in the laboratory and especially in large-scale processes on an industrial scale, the presence of many different heterogeneous particles or surfaces is impossible to prevent [3].

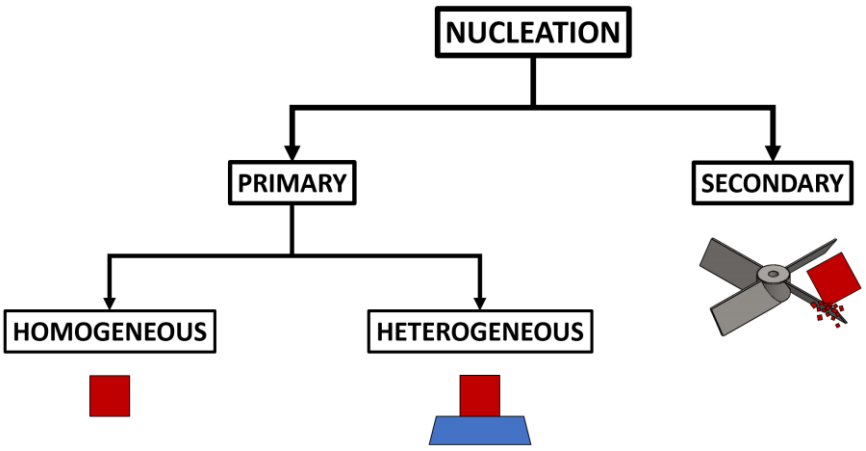

Fig. 2. Crystal nucleation pathways. Nucleation is divided into primary and secondary. Primary nucleation occurs in a clear liquid either in the absence (homogeneous) or in the presence (heterogeneous) of a foreign substance (for instance, particles or imperfections on surfaces). Secondary nucleation occurs in the presence of crystals. New crystals can be, for instance, created due to collisions of parent crystals with the stirring tip (attrition), but other secondary mechanisms are also possible.

2.1.4. Crystal growth

Crystal growth rates are important for the engineer since they mark the crystal residence time in the crystalliser to achieve a specific crystal size and, therefore, the size of the crystalliser and the investment costs [3,5–7]. The linear growth rate of a specific hkl face is often denoted as R_{hkl} [3]. Here, hkl accounts for the Miller index notation system in crystallography for planes in crystal lattices [3]. For faceted crystals, the linear growth rate between hkl faces may be quite different. The growth rate is different between faces since the surface construction differs from face to face so that also the integration process into the kink sites is distinct [5]. The growth rates of the top faces of a needle-like crystal are normally larger than the side faces. There is therefore a relation between the crystal shape and the linear growth rate: the slowest growing hkl faces determine the shape [3,6]. Diverse definitions of growth rates can be found in literature based on, for instance, the increase per unit of time of the characteristic crystal size or in terms of mass increase per surface area per unit of time [3].

In this subprocess of crystallisation, it comes into consideration the route a solute molecule travels from the bulk solution to the integrated state in a kink site of a step on the crystal surface. This takes place with several steps. The growth process is typically controlled by either volume diffusion or solute integration [7]. Then, the growth process is referred to as respectively volume diffusion-controlled growth and integration-controlled growth [3,7]. In both cases, the crystal growth rate is greater the higher the supersaturation.

The release of heat of crystallisation during nucleation and growth causes an increased temperature at the surface [10,11]. Generally, in the solution crystallisation, this heat can be taken out quite rapidly from the surface due to the large amount of solvent present that can act as a heat sink. In melt crystallisation, this heat can be substantial and greatly affect growth rates [7,12]. Other steps which may play a decisive role in the growth rate are the solvent shell removal around the solute and the volume diffusion of solvent and impurities away from the growing surface.

Therefore, growth rates depend not only on the prevailing supersaturation in the solution but may also be a function of temperature, pressure, composition of the mother liquor, fluid flow conditions, crystal growth history, and the presence of additives or impurities [3].

The crystal shape is driven by the faces with the lowest growth rates. Growth rates are a function of supersaturation and, ergo, an effect of supersaturation on the shape is inferred. Frequently, needle-like shapes are obtained at higher supersaturations. Given that growth rates are also influenced by foreign compounds such as solvents [13], impurities, and additives, the crystal shape is also impacted by their presence. Specific crystal faces may experience growth inhibition and as a result the crystal shape changes. Tailor-made additives can be used to induce a preferred crystal shape [14]. Top faces of a needle-like crystal could specifically be inhibited with such an additive to considerably reduce the needle aspect ratio and in such a way prevent filtration problems or other issues.

2.2. Chemical process configuration

There are three approaches to processing operations: batch, continuous, and semibatch or semicontinuous [15]. Batch processing is used to make most drug substances and intermediates [16]. Continuous and semicontinuous operations are most often used on large scale for the manufacture of bulk chemicals and agrochemicals [16]. Each option has its own scale-up advantages and characteristics, as discussed in the table below for the extreme cases batch and continuous modes (Table 1) [15–19]. Semibatch or semicontinuous modes features are generally found in between of the batch and continuous extreme cases.

Batch operations are employed for reactions requiring hours for completion, with relatively small product outputs [18]. Unit operations, such as crystallisation, can be finely controlled on scale for the entire batch (Table 1). The product from a batch is isolated at the end of an operations cycle and can always be readily correlated with input materials. For these reasons batch processing is used to make most drug substances and intermediates (Table 1) [15,16]. As one progresses to larger and larger vessels,

micromixing becomes a greater concern and tight temperature control becomes more difficult (Table 1) [17]. Other issues may arise, such as the optimal placement of agitators, pH probes, thermocouples, and other process analytics technologies (PAT) monitoring devices (Table 1). These parameters can be readily controlled by using a small vessel, but running many small operations is a tedious way to accumulate large amounts of material.

Continuous operations are generally used for large-volume products in which operation conditions are closely monitored to achieve maximal productivity (Table 1) [15,16]. Such operations are carried out on scale by allowing a unit process to pass through a small vessel. In case of reactive processes, the products are usually made by reactions completed in minutes, which allows for fine control of process conditions (Table 1) [18,20]. Reactions and consequent work-up operations in need of longer times may be used in continuous mode if the products are stable enough to permit recycling a stream through the vessel. The product is isolated throughout the operations cycle.

In a semicontinuous or batch flow process, one or various ingredients are charged to the vessel, and the remaining components are added step by step. None of the vessel mixture is displaced through overflow. The total volume of a vessel typically rises when the process progresses and the product is isolated at the end of the operations cycle [15,16]. This type of operation is useful for exothermic processes in vessels with limited heat transfer capacity [15,19].

There are several disadvantages to consider when using continuous processes. Resources are needed to develop the process: the appropriate residence time to reach a level of suitable process completion must be determined under the desired conditions of temperature, flow rate, and any other critical parameters [15]. The process system can have limited flexibility to run other processes. Pressure drops occur when using certain vessels. Once the conditions have been developed, time is required to reach steady-state conditions. What happens to the product material while the conditions are approaching the steady state? Such material is not produced under the desired conditions and ergo is atypical of the majority of the batch [15]. Effective control equipment is compulsory for large-scale operations; otherwise expensive material is at risk and may necessitate to be

reworked [19]. Associating batch inputs with product output may be difficult for continuous operations. The FDA and other drug regulators frown on blending batches [15,21]. One approach is to operate as semicontinuous processes. Then, the material from a continuous processing may be collected in a holding vessel for consequent isolation and drying as a discrete batch. Despite these adverse circumstances, continuous operations may be preferred over conventional ones for some processes.

Table 1. Characteristics of batch and continuous-mode chemical operations and processes [15–19].

Feature	Batch mode	Continuous mode
Typical industrial use:		
Laboratory	General approach for scale-up	Rarely used
Pilot plant	Most often used	Rarely used
Manufacturing	Often used for pharmaceutical and fine chemicals, rarely used for bulk chemicals	Often used for bulk chemicals and agricultural chemicals, rarely used for pharmaceutical and fine chemicals
Production quantity	Small	Large
Temperature and pressure response rates for content	Slower in larger vessels	Response can be very rapid
Solvent	Typically operated dilute	Neat processing possible
Localisation of physical effects	Macromixing and micromixing are always considerations	Equipment can be selected for excellent micromixing and localised effects
Time	Long or short processes times, shutdown times are typical	Shorter times than equivalent processes in batch, shutdown times are rare
Product quality	More product variability: batch to batch variation, lower product quality consistency	Less product variability: no batch to batch variation, higher and consistent product quality
Waste	Large	Small
Useful for	Most processes	Reactions where relatively stoichiometry of reactants and products is critical, reverse quenches, tight temperature controls, efficient mixing of heterogeneous streams, localisation of catalysts and physical effects
Cost	Typically, lower cost at low production rates, lower cost of equipment	Typically, lower cost at high production rates, higher cost of equipment
Equipment	Larger, typically operated in multipurpose equipment and in campaigns, often with large inventories of intermediates/finished products	Smaller, typically operated in dedicated equipment and non-stop (at steady state), often with less inventory
Controlling	Difficult to control, requires sophisticated control systems	Easier to control and maintain
Analysis (PAT)	Normally on-line/off-line/at-line.	Most adapted in-line or non-invasive (i.e. in situ). On-line/off-line/at-line with limited applicability.
Operating safety	Good	Very good, as only a small portion of batch is subjected to processing at any moment
Utility demands	Must transfer heat from entire batch and large vessel	Transfer heat from part of batch and small vessel
Additional development time	Some time may be needed to optimise processing if labile compounds are produced	Need to determine process time for suitable residence time in vessel, or recycle stream through vessel
Automation	Difficult	Easy
Troubleshooting	A fault or dealing with a batch requiring "repair" does not cause problems in the other stages, appropriate tests are conducted after each stage	The installations are interconnected, so, a fault in one causes a stoppage in all the others, material that has been damaged cannot be "repaired" under the same working conditions, it must be isolated, and the process repeated
Regulation	Accepted by legislation authorities	Relatively novel and so acceptance by companies and legislation more difficult

2.3. Process modelling

The development and testing of hypotheses about models and then revising designs or theories has its base in the experimental sciences. Similarly, computational scientists use modelling to analyse complex, real-world problems to predict what might happen with some course of action in the future term.

There are several classification categories for models [22]. A system modelled manifests probabilistic or stochastic behaviour if an element of chance exists. Alternatively, it shows deterministic behaviour [22]. A probabilistic or stochastic model exhibits random effects, while a deterministic model does not. The results of a deterministic model depend on the initial conditions; and in the case of computer implementation with specific input, the output is the same for each program execution.

Models can also be classified as static or dynamic [22]. A static model does not consider time, so that the model is comparable to a picture or a map. In contrast, dynamic models deem time changes, so that such a model is equivalent to an animated cartoon or a film.

The model is considered continuous when time changes continuously and smoothly during modelling. If time changes in incremental steps, the model is discrete [22]. A discrete model is analogous to a film. A sequence of frames moves so quickly that the viewer perceives motion. However, in a live play, the action is continuous.

In the context of crystallisation, population balances are often used to model how the number and properties of the crystals in a crystalliser are generated and eventually appear as the solid product [23]. A population balance is a mathematical description of conservation of number of particles, and accounts for how the number of particles having a specific set of properties, such as size, shape, and density; may change during the process [23]. This type of model is usually employed with stochastic, dynamic, and continuous characteristics. Nonetheless, if the aim of the crystallisation model is not particularly based on the number of particles, as it could be when focusing on properties such as overall purity, other simpler models just based on chemical thermodynamics may also be

employed such as the deterministic one-site competition model [24,25]. The latter explanation may also apply when different separation techniques are combined. Therefore, the type of model to use depends on and must be adapted to the specific application and its particular features.

The modelling process is cyclic and closely parallels the scientific method and the software life cycle for the development of a major software project [26]. The process is cyclic because at any step it might return to an earlier stage to make revisions and continue the process from that point. The steps of the modelling process are as shown in the figure below (Fig. 3).

First, the situation must be studied sufficiently to identify the problem precisely and understand its fundamental questions clearly (Fig. 3, step 1) [22,26]. At this stage, the problem's objective is determined and the modeller decide on the problem's classification, such as deterministic or stochastic. Only with a clear, precise problem identification can the modeller translate the problem into mathematical symbols and develop and solve the model.

Second, the modeller designs the model, forming an abstraction of the system that is being modelled (Fig. 3, step 2) [22,26]. Here, the modeller first collects relevant data to gain information about the system's behaviour (Fig. 3, step 2a). Then, the modeller must determine and name the variables (Fig. 3, step 2b). An independent variable is the variable on which others depend. The model will try to explain the dependent variables. There, to simplify the model, the modeller may decide to neglect some variables, treat certain variables as constants, or aggregate several variables into one. While deciding on the variables, the modeller must also establish their units. Afterwards, if possible, the modeller should draw a diagram of the model, breaking it into submodels and indicating relationships among variables (Fig. 3, step 2c). To simplify the model, it may be assumed that some of the relationships are simpler than they really are. Then, while establishing relationships between variables, the modeller determines equations and functions for these variables (Fig. 3, step 2d).

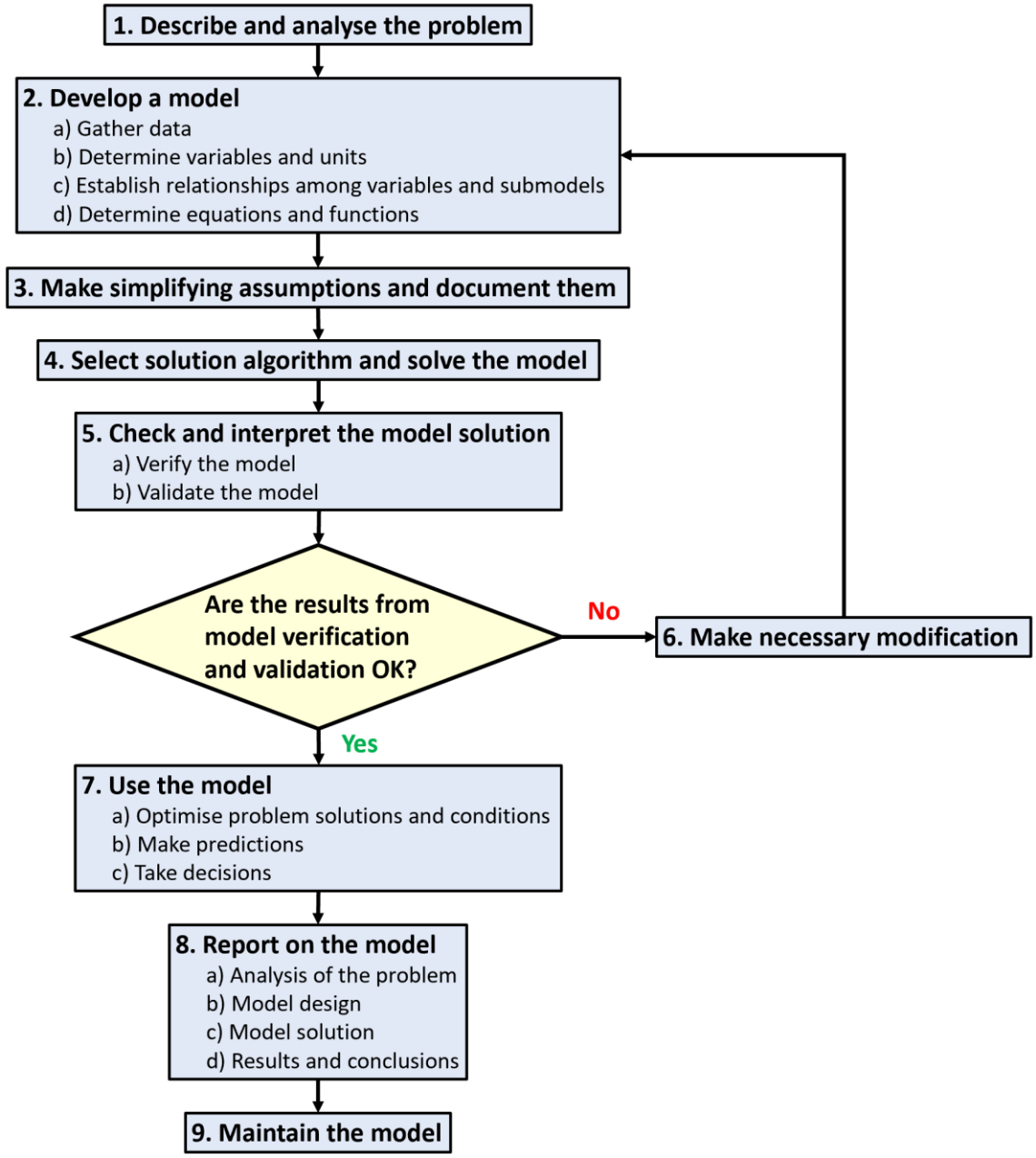

Fig. 3. The main steps of process modelling and simulation.

Third, the modeller should attempt to be as simple as reasonably possible when formulating the model. Thus, the modeller often decides to simplify some of the factors and to ignore other factors that do not seem as important (Fig. 3, step 3) [22,26]. Most problems are entirely too complex to consider every detail and doing so would only make

the model impossible to solve or to run in a reasonable amount of time on a computer. Moreover, factors often exist that do not appreciably affect outcomes. Besides simplifying factors, the modeller may decide to return to step 1 to restrict further the problem under investigation.

The fourth stage consists in selecting the solution algorithm and solve the model (Fig. 3, step 4) [22,26]. So, this stage implements the model. It is important not to jump to this step before thoroughly understanding the problem and designing the model. Otherwise, the modeller might waste much time, which can be most frustrating. Some of the techniques and tools that the solution might employ are algebra, calculus, graphs, computer programs, and computer packages. The solution might produce an exact answer or might simulate the situation. If the model is too complex to solve, the modeller must return to step 3 to make additional simplifying assumptions or to step 1 to reformulate the problem.

The fifth step accounts for checking and interpreting the model's solution (Fig. 3, step 5) [22,26]. Once a solution is obtained, the modeller should carefully examine the results to make sure that they make sense (verification) and that the solution solves the original problem (validation) and is usable. The process of verification determines if the solution works correctly (Fig. 3, step 5a), while the process of validation establishes if the system satisfies the problem's requirements (Fig. 3, step 5b). Thus, verification concerns "solving the problem right" and validation concerns "solving the right problem". Testing the solution to see if predictions agree with real data is important for verification. The modeller must be careful to apply the model only in the appropriate ranges for the independent data. Additionally, the modeller should analyse the model's solution to determine its implications. If the model solution shows weaknesses, the modeller should return to steps 1, 2 or 3 to determine if it is feasible to refine the model. If so, the modeller cycles back through the process in the sixth step (Fig. 3, step 6) [22,26]. Hence, the cyclic modelling process is a trade-off between simplification and refinement. For refinement, the modeller may need to extend the scope of the problem in step 1. In steps 2 and 3, while refining, the modeller often needs to reconsider the simplifying assumptions, include more

variables, assume more complex relationships among the variables and submodels, and use more sophisticated techniques.

The seventh step concerns the use of the model (Fig. 3, step 7) [22,26]. Once the results obtained from the model are verified and valid, the modeller can use the model further to optimise problem solutions and conditions (Fig. 3, step 7a), make predictions (Fig. 3, step 7b), and take decisions based on the model outcome and simulations (Fig. 3, step 7c).

The step eight is reporting on the model (Fig. 3, step 8) [26]. Reporting on a model is important for its utility. A report contains the following four components, which parallel the steps of the modelling process. First, an analysis of the problem (Fig. 3, step 8a), usually, assuming that the audience is intelligent but not aware of the situation, the modeller needs to describe the circumstances in which the problem arises. Then, the modeller must clearly explain the problem and the objectives of the study. Then, the model design provides the amount of detail with which we explain the model (Fig. 3, step 8b). After, the modeller describes the techniques for solving the problem and the solution (Fig. 3, step 8c). Here, detail should be given as much as necessary for the audience to understand the material without becoming mired in technical minutia. Eventually, the report should include results, interpretations, implications, recommendations, and conclusions of the model's solution (Fig. 3, step 8d). The modeller may also include suggestions for future work.

Finally, the last ninth stage is maintaining the model (Fig. 3, step 9) [26]. As the model's solution is used, it may be necessary or desirable to make corrections, improvements, or enhancements. In this case, the modeller again cycles through the modelling process to develop a revised solution.

Although the modelling process has been described as a sequence or series of steps, it may be possible developing two or more steps simultaneously.

2.3.1. GAMS: General Algebraic Modeling System

The General Algebraic Modeling System (GAMS) is a high-level modelling system for mathematical programming and optimisation [27]. It consists of a language compiler and a collection of integrated high-performance solvers. GAMS is tailored for complex, large-scale modelling applications, and allows one to build large maintainable models that can be adapted quickly to new situations. GAMS is specifically designed for modelling linear, non-linear, and mixed integer optimisation problems [28].

Various types of problems can be solved with GAMS [29]. Note that the type of the model must be known before it may be solved. The model types are briefly discussed in this section. GAMS checks that the model is in fact the type the user thinks it is, and issues explanatory error messages if it discovers a mismatch, for instance, that a supposedly linear model contains non-linear terms. Some problems may be solved in more than one way, and the user must choose which way to use. For instance, if there are binary or integer variables in the model, it can be solved either as a MIP or as a RMIP (Table 2).

The GAMS model types and their identifiers are described below (Table 2) [29].

Table 2. Classification of mathematical programming models in GAMS [29].

Model type	Description	Requirements and comments
LP	Linear Program	Model with no non-linear terms or discrete (i.e. binary, integer, etc.) variables
NLP	Non-linear Program	Model with general non-linear terms involving only smooth functions, but no discrete variables
QCP	Quadratically Constrained Program	Model with linear and quadratic terms, but no general non-linear terms or discrete variables
DNLP	Discontinuous Non-linear Program	Model with non-smooth non-linear terms with discontinuous derivatives, but no discrete variables. This is the same as NLP, except that non-smooth functions may appear as well. These models are more difficult to solve than normal NLP models and it is strongly advised not to use this model type
MIP	Mixed Integer Program	Model with binary, integer, SOS and/or semi variables, but no non-linear terms
RMIP	Relaxed Mixed Integer Program	Like MIP, except that the discrete variable requirement is relaxed
MINLP	Mixed Integer Non-linear Program	Model with both non-linear terms and discrete variables
RMINLP	Relaxed Mixed Integer Non-linear Program	Like MINLP except that the discrete variable requirement is relaxed
MIQCP	Mixed Integer Quadratically Constrained Program	Model with both quadratic terms and discrete variables, but no general non-linear term
RMIQCP	Relaxed Mixed Integer Quadratically Constrained Program	Like MIQCP except that the discrete variable requirement is relaxed
MCP	Mixed Complementarity Problem	A square, possibly non-linear, model that generalises a system of equations. Rows and columns are matched in one-to-one complementary relationships
CNS	Constrained Non-linear System	Model solving a square, possibly non-linear system of equations, with an equal number of variables and constraints.
MPEC	Mathematical Programs with Equilibrium Constraints	A difficult model type for which solvers and reformulations are currently being developed
RMPEC	Relaxed Mathematical Program with Equilibrium Constraints	A difficult model type for which solvers and reformulations are currently being developed
EMP	Extended Mathematical Program	A family of mathematical programming extensions
MPSGE	General Equilibrium	Not actually a model type but mentioned for completeness

Many solvers for mathematical programming models have been implemented in GAMS. The tables below provide a brief description of each solver and the model types each solver is capable of solving (Tables 3A-3B) [30].

Table 3A. Model solvers available in GAMS (continues in Table 3B) [30].

Solver	Description
ALPHAECP	MINLP solver based on the extended cutting plane (ECP) method
AMPL	A link to solve GAMS models using solvers within the AMPL modelling system
ANTIGONE 1.1	Deterministic global optimisation for MINLP
BARON	Branch-And-Reduce Optimisation Navigator for proven global solutions
BDMLP	LP and MIP solver that comes with any GAMS system
BENCH	A utility to facilitate benchmarking of GAMS solvers and solution verification
BONMIN 1.8	COIN-OR MINLP solver implementing various branch-and-bound and outer approximation algorithms
CBC 2.10	High-performance LP/MIP solver
CONOPT 3	Large-scale NLP solver
CONOPT 4	Large-scale NLP solver
CONVERT	Framework for translating models into scalar models of other languages
COUENNE 0.5	Deterministic global optimisation for (MI)NLP
CPLEX 12.10	High-performance LP/MIP solver
DE	Generates and solves the deterministic equivalent of a stochastic program, included in EMP/SP
DECIS	Large-scale stochastic programming solver
DICOPT	Framework for solving MINLP models
EXAMINER	A tool for examining solution points and assessing their merit
GAMSCHK	A System for Examining the Structure and Solution Properties of Linear Programming Problems Solved using GAMS
GLOMIQO 2.3	Branch-and-bound global optimisation for mixed-integer quadratic models
GUROBI 9.0	High-performance LP/MIP solver
GUSS	A framework for solving many instances of related models efficiently (Gather-Update-Solver-Scatter)
IPOPT 3.12	Interior Point Optimizer for large-scale non-linear programming
JAMS	Solver to reformulate extended mathematical programs
KESTREL	Framework for using remote NEOS solvers with a local GAMS system
KNITRO 11.1	Large-scale NLP solver
LGO	A global-local non-linear optimisation solver suite

Table 3B. Model solvers available in GAMS (Table 3A continuation) [30].

Solver	Description
LINDO 12.0	A stochastic solver from Lindo Systems, Inc. Includes an unrestricted version of LINDOGLOBAL
LINDOGLOBAL 12.0	MINLP solver for proven global solutions
LINGO	A link to solve GAMS models using solvers within the LINGO modelling system
LOCALSOLVER 9.0	Hybrid neighbourhood local search solver
LS	A Linear Regression Solver for GAMS
MILES	MCP solver
MINOS	NLP solver
MOSEK 9	Large-scale mixed-integer conic programming solver
MSNLP	Multi-start method for global optimisation
NLPEC	MPEC to NLP translator that uses other GAMS NLP solvers
ODHCPLEX 4	ODHeuristic on top of Cplex
OsiCplex	Bare-Bone link to CPLEX
OsiGurobi	Bare-Bone link to Gurobi
OsiMosek	Bare-Bone link to Mosek
OsiXpress	Bare-Bone link to Xpress
PATHNLP	Large-scale NLP solver for convex problems
PATH	Large-scale MCP solver
PYOMO	A link to solve GAMS models using solvers within the PYOMO modelling system
SBB	Branch-and-Bound algorithm for solving MINLP models
SCIP 6.0	High-performance Constraint Integer Programming solver
SELKIE	Decomposition and parallel solution for EMP
SNOPT	Large-scale SQP based NLP solver
SOLVEENGINE	Link to use solvers of the Satalia SolveEngine with a local GAMS system
SOPLEX 4.0	High-performance LP solver
XA	Large-scale LP/MIP solver
XPRESS 33.01	High-performance LP/MIP solver

Optimisation is becoming widely used in many application areas as can be evidenced by its appearance in software packages such as Excel and MATLAB. While the optimisation tools in these packages are useful for small-scale non-linear models (and to some extent for large linear models), the lack of a capability to compute automatic derivatives makes them impractical for large-scale non-linear optimisation. In sharp

contrast, modelling languages such as GAMS have had such a capability for many years and have been used in many practical large-scale non-linear applications.

On the other hand, while modelling languages have some capabilities for data manipulation and visualisation, to a large extent specialised software tools like Excel and MATLAB are much better at these tasks.

The suite of utilities GDXMRW makes possible to import and export data between GAMS and MATLAB and to call GAMS models from MATLAB and get results back in MATLAB [31,32]. The software gives MATLAB users the ability to use all the optimisation capabilities of GAMS and allows visualisation of GAMS models directly within MATLAB, in an easy and extendable manner so that optimisation results can be viewed using any of the wide variety of plots and imaging capabilities that exist in MATLAB.

2.4. Analytical techniques

2.4.1. Absorption spectroscopy

Spectroscopy is the study of the quantised interaction of energy (normally electromagnetic energy) with matter (atoms and molecules) [33,34]. Molecules exhibit electronic spectra from transitions between electronic energy levels (Fig. 4) [34]. These spectra are more complex than those of atomic spectra which involve transitions between electronic energy levels which typically produce sharp line spectra. The energies associated with molecular electronic spectra, typically in the optical/visible (Vis) or ultraviolet (UV) regions, are usually much larger than those associated with vibrational spectra, generally in the infrared (IR) region, and rotational spectra, generally in the microwave region (Fig. 4ab) [33]. This contributes to the complexity of the electronic spectra because the transitions from a multitude of vibrational and rotational levels produce many spectral lines, commonly called as a “band” of frequencies (Fig. 4c). Electronic transitions are essentially instantaneous so that there is no time for appreciable motion of the nuclei. Thus, the transitions appear as vertical lines with no change in

internuclear distance (Fig. 4ab). This is referred to as the Franck-Condon principle [35–37].

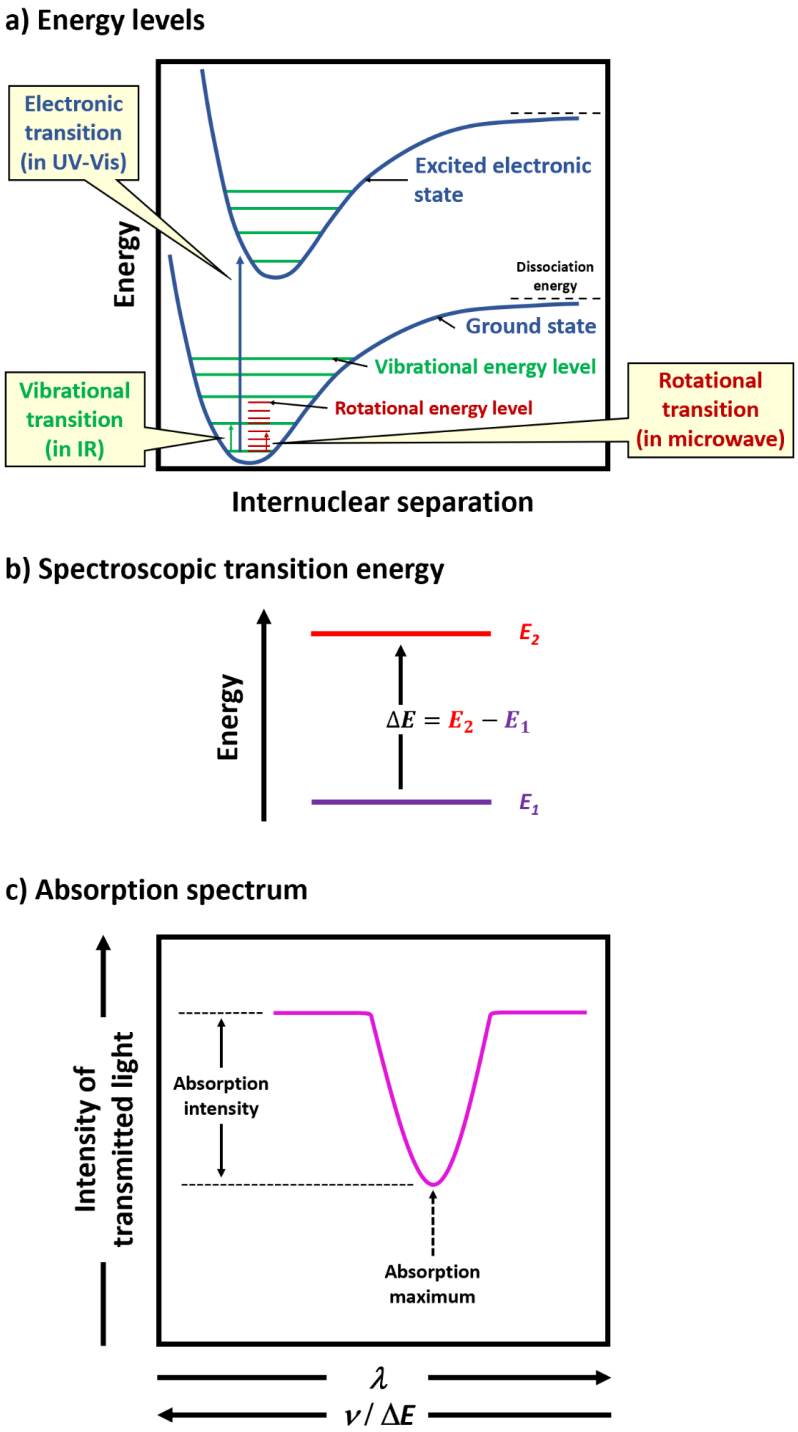

Fig. 4. a) Three types of energy levels in a diatomic molecule: electronic, vibrational, and rotational; b) description of a spectroscopic transition; and c) schematic absorption spectrum.

The absorption spectrum given above (Fig. 4c) is the representation of the energy absorption (radiation) against its wavelength λ or frequency ν. The absorption band is characterised primarily by two parameters: a) the wavelength at which maximum absorption occurs and b) the absorption intensity at this wavelength compared to the baseline (or background) absorption (Fig. 4c).

A spectroscopic transition takes a molecule from one state to another one of higher energy. For any spectroscopic transition between energy states (for instance, E_1 and E_2 in Fig. 4b), the change in energy (ΔE) is given by (3) [33]:

$$\Delta E = h\nu = h\frac{c}{\lambda} \tag{3}$$

where h and c are the Planck's constant and speed of light, respectively, and ν and λ are the frequency and wavelength of the electromagnetic energy absorbed. Therefore, ΔE is directly proportional to ν, but inversely proportional to λ.

A spectrum consists of different bands or transitions because the absorption (or emission) of energy is quantised. The energy gap of a transition is a molecular property and is characteristic of the molecular structure [33,34]. The ordinate axis (y-axis) in the spectrum (Fig. 4c) measures the intensity of the absorption band and this depends on the number of molecules observed (described by the relacted absorbance in the Beer-Lambert law [33,34,38,39]) and the probability of the transition between the energy levels. The absorption intensity is also a molecular property and both the frequency and intensity of a transition can provide structural information [33,34].

Generally, any spectral feature (band or group of bands) is due not to the whole molecule, but to an identifiable part of the molecule, which is called a chromophore [33]. The chromophore may correspond to a functional group (for instance, a hydroxyl group or the double bond in a carbonyl group). However, it may equally well correspond to a single atom within a molecule or to a group of atoms such as a methyl group which is not normally associated with chemical functionality. The detection of a chromophore permits to deduce the presence of a structural fragment or a structural element in the molecule.

The fact that it is the chromophores and not the molecules as a whole that give rise to spectral features is fortunate, if not spectroscopy would only permit us to identify known compounds by direct comparison of their spectra with authentic samples. This "fingerprint" technique is useful for establishing the identity of known compounds, but the direct determination of the molecular structure building up from the molecular fragments is far more powerful.

The basic instrumentation for the main absorption spectroscopic techniques such as UV-Vis and IR consists of an energy source, a sample cell, a dispersing device (prism or grating), and a detector; arranged as schematically shown below (Fig. 5) [33,34]. The drive of the dispersing device is synchronised with the abscissa axis (x-axis) of the recorder or fed directly to a computer, so that this indicates the wavelength of the radiation reaching the detector. The signal from the detector is transmitted to the ordinate axis of the recorder or to a computer and this indicates how much radiation is absorbed by the sample at any specific wavelength. In practice, double-beam instruments are used where the absorption of a reference cell, containing only solvent, is subtracted from the absorption of the sample cell [33,34]. Double beam instruments also cancel out absorption due to the atmosphere in the optical path as well as the solvent. The materials from which the energy source, dispersing device, and detector are constructed must be appropriate for the range of wavelength scanned and as transparent as possible to the radiation [33,34].

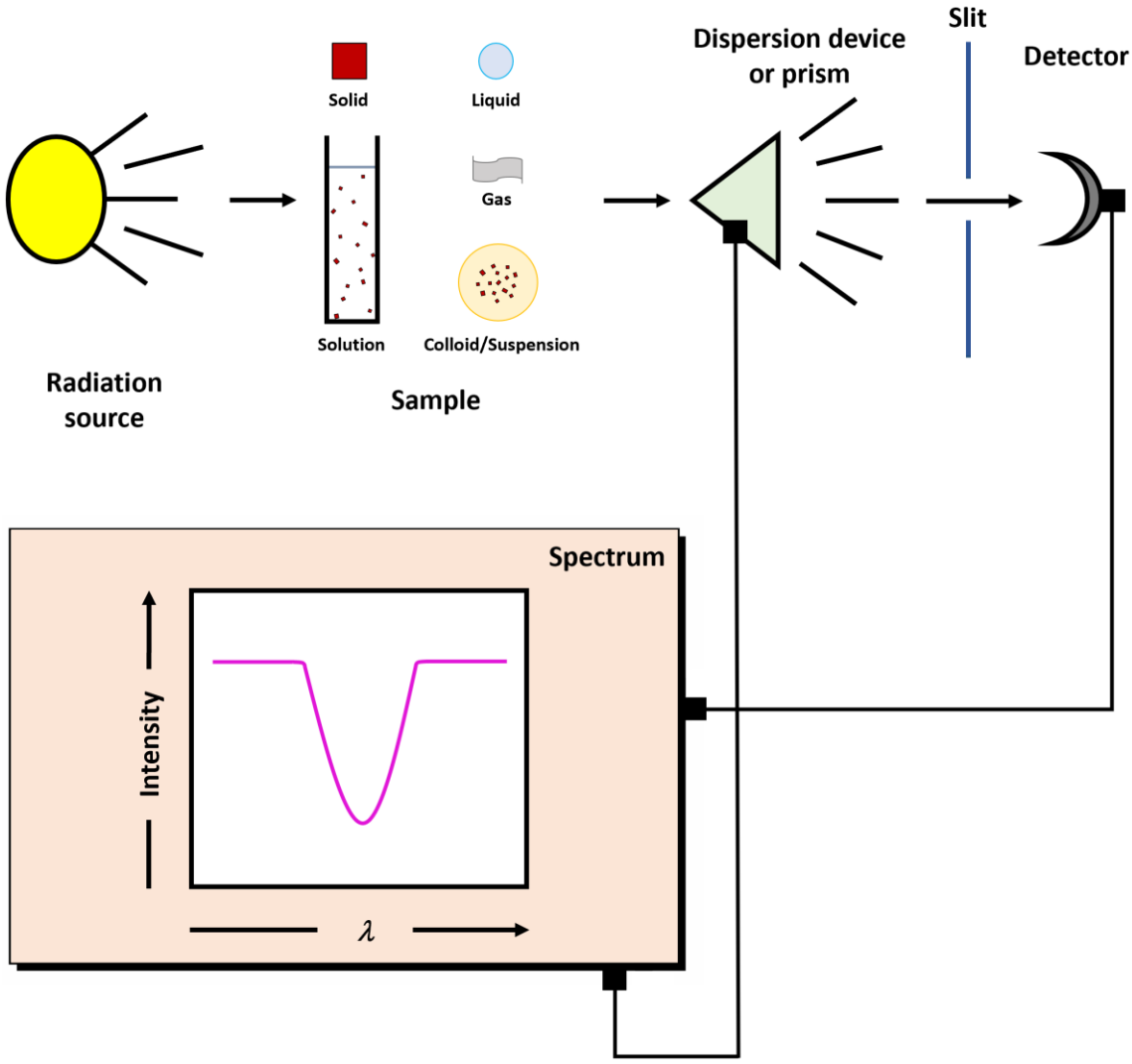

Fig. 5. General schematic representation of UV-Vis and IR spectrometers.

2.4.1.1. UV-Vis spectroscopy

The term UV-Vis spectroscopy typically refers to electronic transitions which occur in the electromagnetic spectrum region accessible to standard ultraviolet (UV) spectrometers (λ in the range of 200-380 nm) [33,40]. Electronic transitions are also responsible for absorption in the visible (Vis) region (approximately 380-800 nm) which is easily accessible instrumentally but of less importance in the solution of structural problems, because most organic compounds are colourless [34]. The vacuum ultraviolet region (λ

shorter than circa 200 nm) also corresponds to electronic transitions, but it is not readily accessible with standard instruments [40].

The y-axis of a UV-Vis spectrum may be calibrated in terms of the intensity of transmitted light (percentage of transmission or absorption), as it is shown below (Fig. 6), or it may be calibrated on a logarithmic scale in terms of absorbance *A* defined as follows (4) (Fig. 6) [33,34,40]:

$$A = \log_{10} \frac{I_0}{I} \tag{4}$$

where I_0 and I is the total intensity of transmitted light and band (chromophore) intensity of transmitted light, respectively. The absorbance *A* is proportional to concentration *C* and path length *l* according to the Beer-Lambert law [38–40]. The intensity of absorption is usually expressed in terms of molar absorbance or molar extinction coefficient ε (in $M^{-1}cm^{-1}$) given by (5) [38–40]:

$$\varepsilon = \frac{A}{Cl} \tag{5}$$

where *C* is the concentration (in M or $mol \cdot L^{-1}$) and *l* is the path length through the sample (in cm).

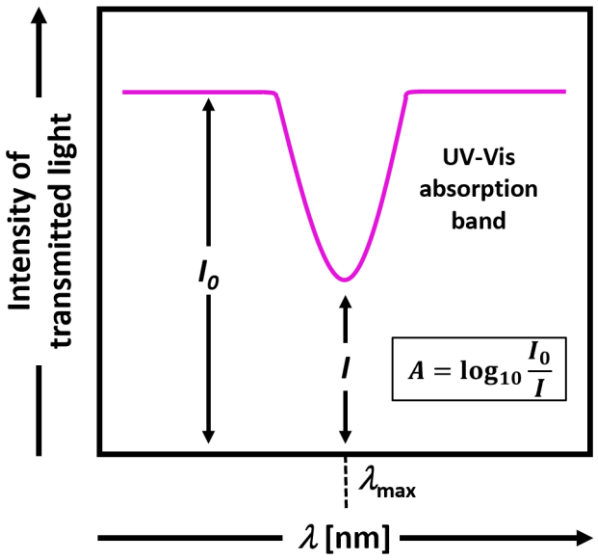

Fig. 6. Definition of absorbance *A*.

UV-Vis absorption bands (Fig. 6) are characterised by the wavelength of the absorption maximum (λ_{max}) and ε. The values of ε associated with common chromophores vary between 10 and 10^5 $M^{-1}cm^{-1}$ [34,41].

These absorption bands have a fine structure due to the presence of vibrational sub-levels, but this is rarely observed in solution on account of collisional broadening [33,40]. As the transitions are associated with changes in electronic orbitals, they are usually described in terms of the orbitals involved (Fig. 7), where n denotes a non-bonding orbital, the asterisk denotes an antibonding orbital and σ and π have the usual significance [34,40].

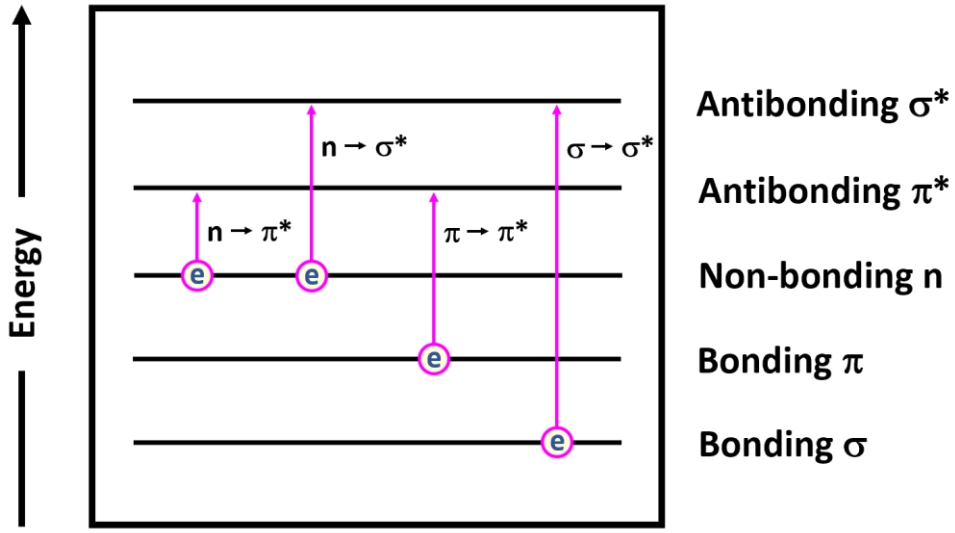

Fig. 7. Classification of UV-Vis absorption transitions and bands.

A molecule may give rise to more than one band in its UV-Vis spectrum, either because it contains more than one chromophore or since more than one transition (Fig. 7) of a single chromophore is observed [34,40].

Auxochromes (from auxiliary chromophores) are groups of atoms which have little UV-Vis absorption by themselves, but which normally have significant effects on the absorption (both λ_{max} and ε) of a chromophore to which they are attached [34,40]. In general, auxochromes involve atoms with one or more lone pairs, for instance -OH, -OR, $-NR_2$, and -halogen [34,41]. If a structural change, such as the attachment of an auxochrome, leads to the absorption maximum being shifted to a longer wavelength, the

phenomenon is termed a bathochromic shift [33,34,40]. A shift towards shorter wavelength is called a hypsochromic shift [33,34,40].

Most of the reliable and useful data is caused by relatively strongly absorbing chromophores (ε > 200 $M^{-1}cm^{-1}$) which are mainly indicative of conjugated or aromatic systems. Instances of common UV-Vis chromophores encountered are dienes and polyenes, carbonyl compounds, and benzene derivatives [34,41]. Solvent polarity may affect the absorption traits, in particular λ_{max}, since the polarity of a molecule normally changes when an electron is moved from one orbital to another [34,40,41].

2.4.1.2. IR spectroscopy

Infrared (IR) absorption spectra are measured in wavelength expressed in micrometres (1 μm = 10^{-6} m) or in frequency-related wave number $\tilde{\nu}$ (cm^{-1}) which is reciprocal of wavelength λ (6) [33]:

$$\tilde{\nu}\ (cm^{-1}) = \frac{10^4}{\lambda\ (\mu m)} \qquad (6)$$

The $\tilde{\nu}$ range accessible for standard instrumentation is usually from 4000 to 666 cm^{-1} (λ from 2.5 to 15.0 μm, respectively) [34].

Infrared absorption intensities are typically described quantitatively with the general classifications of s (strong), m (medium) or w (weak) [33,34,41,42]. The transitions responsible for IR bands are caused by molecular vibrations, that is to periodic motions involving stretching or bending of bonds (Fig. 8) [33,34,42]. Polar bonds are associated with strong IR absorption whereas symmetrical bonds may not absorb at all. The vibrational frequency position of the bands in the spectrum depends on the nature of the bond. Shorter and stronger bonds have their stretching vibrations at the higher energy end (shorter wavelength) of spectrum than the longer and weaker bonds [33,34,41]. Similarly, bonds to lighter atoms such as hydrogen, vibrate at higher energy than bonds to heavier atoms [33,34,41].

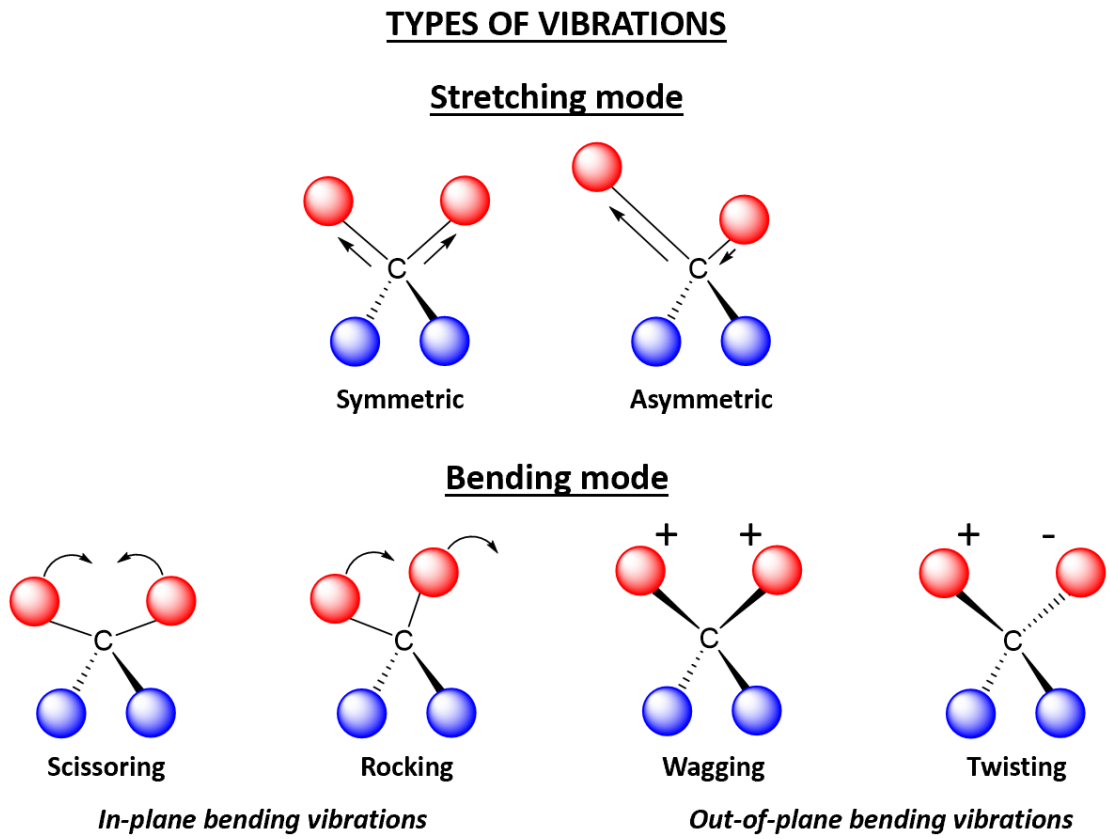

Fig. 8. Different types of vibrational modes.

The standard setup of a simple dispersive IR spectrometer is the same as for a UV-Vis spectrometer (Fig. 5), except that all components must now match the different energy range of electromagnetic radiation [33,34]. The more advanced Fourier Transform Infrared (FTIR) instruments record an infrared interference pattern generated by a moving mirror and this is transformed by a computer into an infrared spectrum [43].

Molecules typically have many bonds and each of them may have several IR-active vibrational modes. IR spectra are intricate and have many overlapping absorption bands. They are complex enough that the spectrum for each compound is unique and this fact makes IR technique very useful for identifying compounds by direct comparison with spectra from authentic samples. This method is widely known as fingerprinting [33,34,41,42]. The distinctive IR vibrations are influenced strongly by small changes in the molecular structure, therefore making it difficult to identify structural fragments by

only using IR data. Despite this, there are some groups of atoms which can be easily recognised from IR spectra.

Some important IR chromophores are functional groups containing carbonyl groups (such as ketones, aldehydes, esters, amides, carboxylic acids, acid chlorides, and acid anhydrides) and other polar functional groups (such as amines, acetylenes, imines, alkenes, alkynes, nitro groups, sulfoxides, sulfones, alcohols, ethers, nitriles, and cyanates) [34,41]. The vibrational modes of these chromophores are summarised above (Fig. 8). They may be divided into stretching or bending modes. A stretching mode may be symmetric or asymmetric whereas a bending mode may encompass in-plane vibrations (scissoring and rocking) and/or out-of-plane vibrations (wagging and twisting) (Fig. 8) [33,34,42].

2.4.2. Raman spectroscopy

Raman spectroscopy is a valuable technique to determine chemical compounds [44]. As with other spectroscopic techniques, Raman spectroscopy detects certain interactions of light with matter. In particular, this technique exploits the existence of Stokes and anti-Stokes scattering to examine the molecular structure [33,45]. When radiation in the near infrared (NIR) or visible range interacts with a molecule, several types of scattering may occur. Three of these can be seen in the energy diagram below (Fig. 9). In all three types of scattering, an incident photon of energy $h\nu$ raises the molecule from a vibrational state to one of the infinite virtual states located between the ground and first electronic states. The type of scattering observed is dependent on how the molecule relaxes after excitation [46]. In Rayleigh scattering (Fig. 9a), first the molecule is excited to any virtual state, then relaxes back to its original state, and the photon is scattered elastically leaving with its original energy $h\nu$ [44–46]. Stokes scattering (Fig. 9a) occurs when the molecule is first excited to any virtual state, relaxes back to a higher vibrational state than it was originally, and then the photon leaves with energy $h\nu$-ΔE and is scattered inelastically [44–46]. Instead, anti-Stokes scattering (Fig. 9a) may occur when the molecule begins in a vibrationally excited state, then it is excited to any virtual state, relaxes back to a lower

vibrational state than it was at the beginning, and the photon leaves with energy $h\nu+\Delta E$ and is scattered superelastically [44–46].

Rayleigh scattering is the most usual transition since no change has to occur in the vibrational state of the molecule (Fig. 9a) [44–46]. The anti-Stokes transition is the least common, as it requires the molecule to be in a vibrationally excited state before the photon is incident upon it (Fig. 9a) [44–46]. Due to the lack of intensity of the anti-Stokes signal and filtering requirements which eliminate photons with incident energy and higher, normally only Stokes scattering is used in Raman studies. The relative intensities of Rayleigh, Stokes and anti-Stokes scattering can be appreciated below (Fig. 9b) [44,45].

Raman spectroscopy examines the change in energy between the incident and scattered photons associated with the Stokes and anti-Stokes transitions [46]. This is normally measured as the change in the wave number (cm^{-1}), from the incident light source. In principle, Raman measurements can be taken using a source at any wavelength since this technique determines the change in wave number. Nevertheless, near infrared and visible radiation are the most used [45].

Raman spectroscopy has much in common with infrared spectroscopy. However, IR examines the wave number at which a functional group has a vibrational mode, while Raman identifies the shift in vibration from an incident source [33,34,43,45]. The Raman frequency shift is identical to the IR peak frequency for a given molecule or functional group (same chromophore frequencies) [33,41,44,45]. As mentioned above, this shift is independent of the excitation wavelength, giving versatility to the design and applicability of Raman instruments, which are similar to the ones described for the absorption spectroscopy but instead of registering the absorbance along the wavelength Raman spectrometers measure the scattering intensity along the Raman shift (Fig. 5). The cause of the vibration is also mechanistically different between IR and Raman [33,46]. This is because the two operate on different sets of selection rules. IR absorption requires a dipole moment or change in charge distribution to be associated with the vibrational mode [33]. Only then can photons of the same energy as the vibrational state of the molecule interact.

Raman signals, on the other hand, due to scattering, occur because of a molecule's polarizability [46]. Many molecules that are inactive or weak in the IR will have intense Raman signals [33,44,45]. This fact makes them complementary techniques.

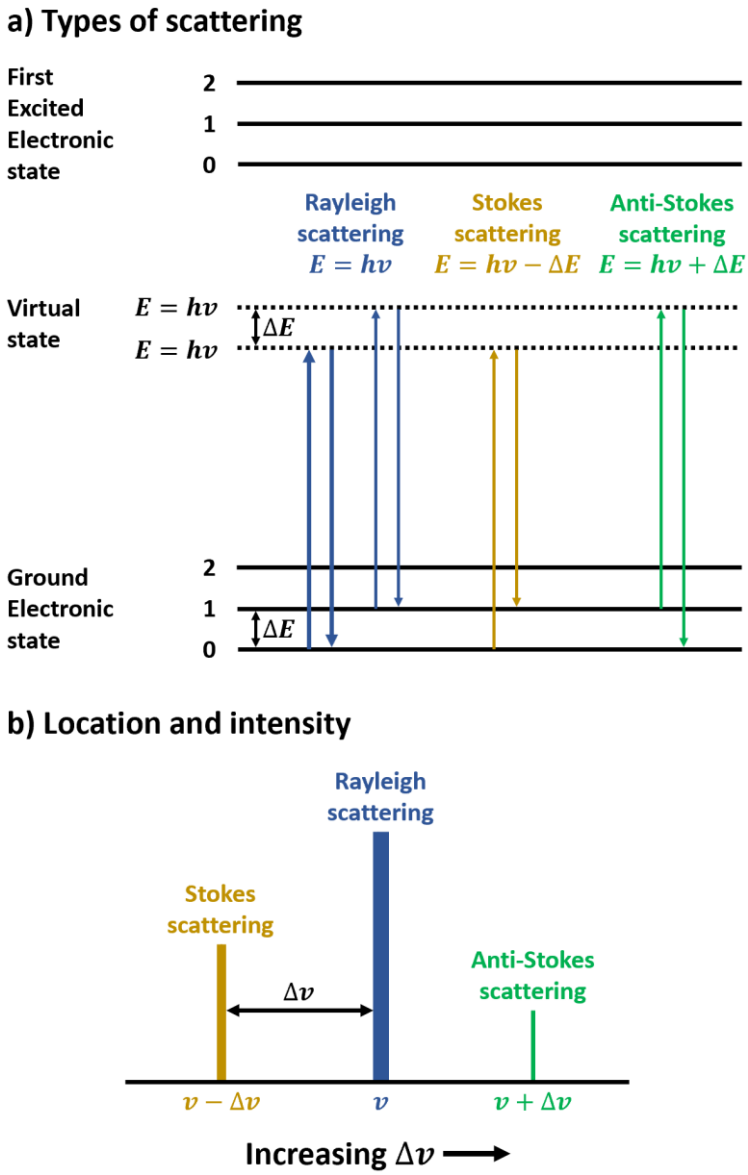

Fig. 9. a) Three types of scattering by a molecule excited by a photon with energy *E*. The most common transition is marked with bold arrows. b) Location and relative intensity (indicated by peak height and width) of the Stokes and anti-Stokes scattering relative to Rayleigh scattering.

Raman depends on the polarizability of a bond [46], which is a measure of the deformability of the bond in an electric field. This factor essentially depends on how easy

it is for the electrons in the bond to be displaced, inducing a temporary dipole. When there is a high concentration of loosely held electrons in a bond, the polarizability is also high, and the group of atoms or molecule will have an intense Raman signal [46]. For that reason, Raman is often more sensitive to the molecular structure of a molecule rather than a specific functional group as in IR [33,45]. This must not be confused with the polarity of a molecule, which is a measure of the separation of electric charge within the molecule. Polar molecules usually show very weak Raman signals because electronegative atoms hold electrons closely [46].

Raman spectroscopy is capable to provide information about both inorganic and organic chemical compounds. Many electron atoms, such as metals in coordination compounds, tend to have many loosely bound electrons, and thus tend to be Raman active. Raman can inform about the metal ligand bond, leading to knowledge of the composition, structure, and stability of these complexes [44,45]. This can be particularly useful in metal compounds that have low vibrational absorption frequencies in the IR. Raman is also useful to determine functional groups and fingerprints of organic molecules. Raman vibrations are usually highly characteristic to a specific molecule, due to vibrations of a molecule as a whole, not in localised groups [44,45]. The molecular groups that appear in Raman spectra have vibrations which are mainly localised within the group and normally have multiple bonds involved.

2.4.3. X-Ray diffraction

X-ray crystallography is a method employed to determine the arrangement of atoms of a crystalline solid in the three-dimensional space [33]. This technique leverages the interatomic spacing of most crystalline solids by using them as a diffraction gradient for X-ray light, which has wavelengths in the order of 1 Å (10^{-10} m) [47,48].

This technique therefore is also able to distinguish and classify crystals by their lattice system. There are seven different classes of crystal systems, and each class of crystal system has four different types of centrings (primitive, base-centred, body-centred, face-centred) (Fig. 10) [49]. Nevertheless, not all the combinations are unique. Some of the

combinations are equivalent whereas other combinations are not possible because of symmetry reasons. This reduces the number of unique lattices to the 14 Bravais lattices represented below (Fig. 10) [49], which are described in terms of cell parameters, that is the lengths of the principal axes of the unit cell (*a*, *b*, and *c*) and the angles between them (α, β, and γ) (Fig. 10) [49]. At the same time, these parameters give information about the unit cell, that is the smallest group of atoms which has the overall symmetry of the crystal, and from which the entire lattice can be built up by repetition in three dimensions.

Diffraction is a phenomenon that occurs when light encounters an obstacle. The waves of light can either bend around the obstacle or, in the case of slits, can travel through them [47]. The resulting diffraction pattern will show areas of constructive interference, where two waves interact in phase, and destructive interference, where two waves interact out of phase [47]. The diffraction of an X-ray beam (XRD, for X-ray diffraction), occurs when the light interacts with the electronic cloud surrounding the atoms of the crystalline solid [47,48]. Given the periodic crystalline structure of a solid, it is possible to describe it as a series of planes with an equal interplanar distance. When an X-ray's beam hits the surface of the crystal at an angle θ, some of the light will be diffracted at that same angle away from the solid (Fig. 11). The remainder of the light will travel into the crystal and some of that light will interact with the second plane of atoms. Some of the light will be diffracted at an angle θ, and the remainder will travel deeper into the solid. This process will repeat for the many planes in the crystal [47,48]. The X-ray beams travel different pathlengths before hitting the various planes of the crystal, so after diffraction, the beams will interact constructively only if the path length difference is equal to an integer number *n* of wavelengths or, which is the same, meets Bragg's law condition (7) [47,48,50] (Fig. 11):

$$2d \sin \theta = n\lambda \tag{7}$$

Bragg's law relates the distance *d* between two planes in a crystal and the angle of reflection θ to the X-ray wavelength λ (Fig. 11). The X-rays that are diffracted off the crystal must be in-phase in order to signal [47,48,50].

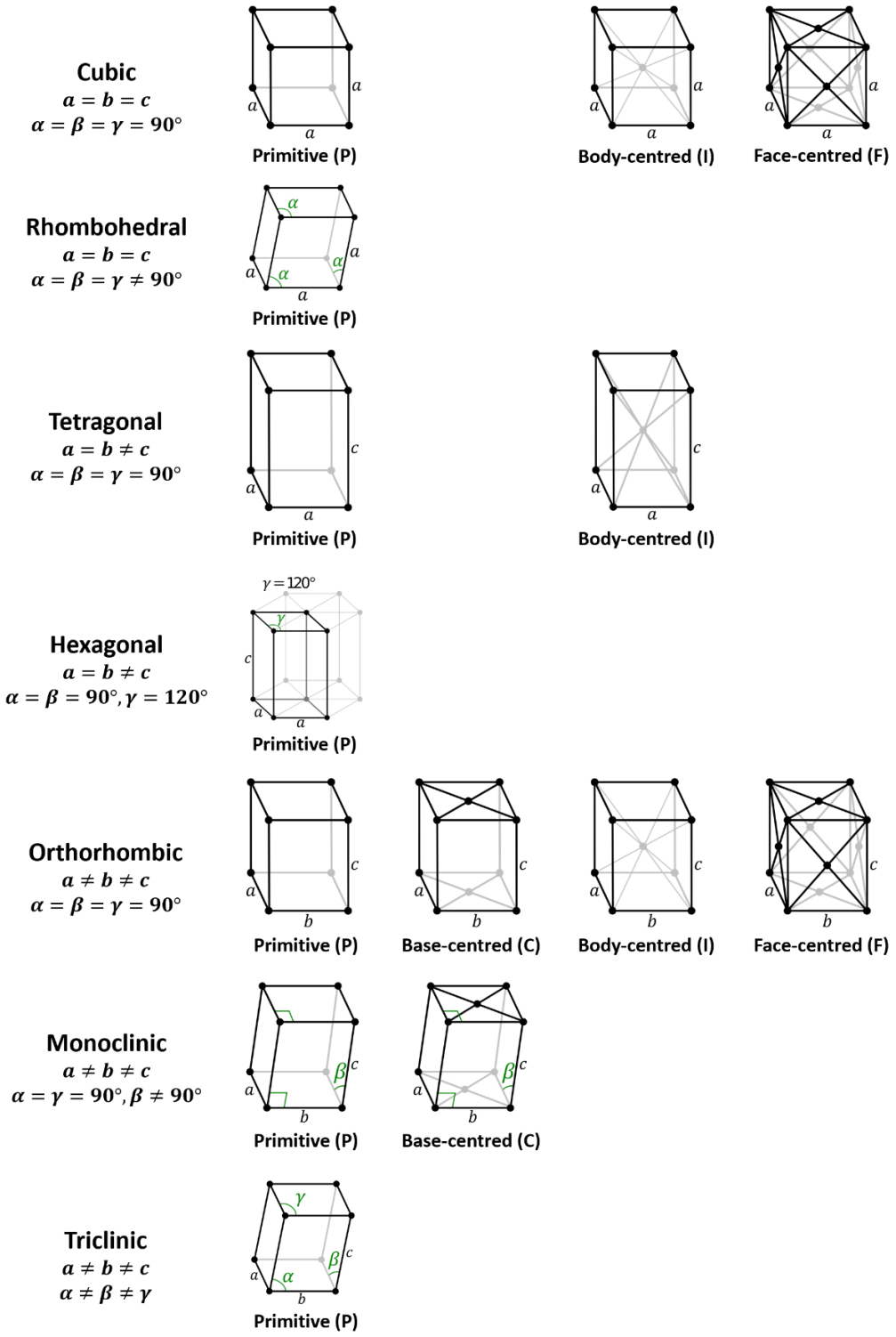

Fig. 10. Crystal lattice systems with the 14 Bravais lattices. The unit cell parameters (*a*, *b*, *c*, α, β, and γ) for each lattice system are given below the system names (left). Bravais lattices are classified in primitive (P), base-centred (C), body-centred (I), and face-centred (F) (right).

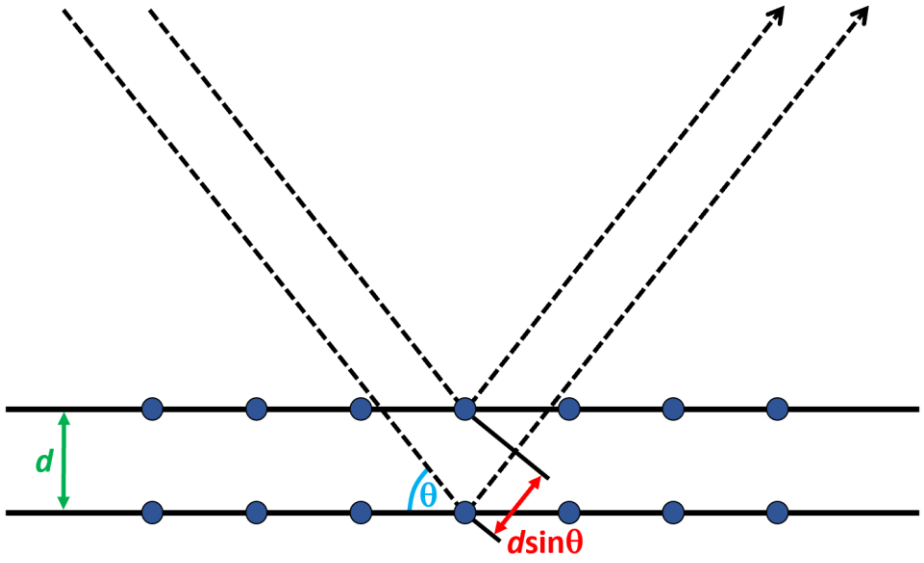

Fig. 11. Description of Bragg's law.

The main components of an X-ray instrument are like those of many optical spectroscopic instruments (Fig. 5). For X-ray diffraction, a source, primary optics (soller and divergence slits and, in some models, also monochromators), sample holder and stage, secondary optics (anti-scatter, soller, and receiving slits and single crystal monochromator), and detector are required (Fig. 12) [33,47,48].

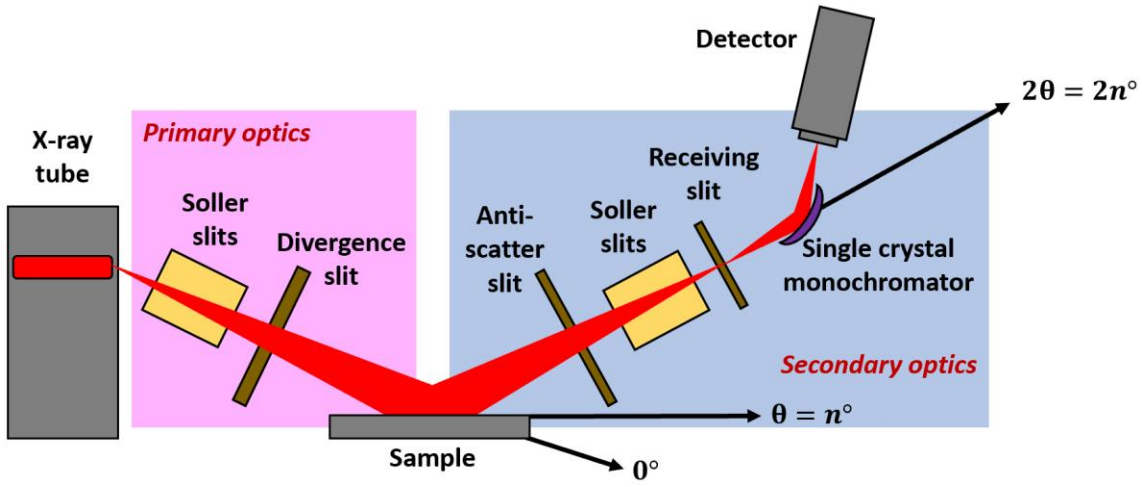

Fig. 12. Schematic representation of an X-ray diffractometer.

The two main applications of XRD are X-ray powder diffraction (XRPD) and single-crystal X-ray diffraction (SC-XRD) [47,48]. The former as its name indicates makes use

of crystalline powder to determine phase composition, quantitative phase analysis, unit cell parameters, and sometimes even the crystal structure is accessible [47,48]. Instead, the latter application just requires a large enough single crystal to run and is the preferred technique to effectively determine crystal structures [47,48].

2.4.4. High-performance liquid chromatography

High-performance liquid chromatography (HPLC) is an analytical technique employed for the separation of compounds soluble in a specific solvent [33]. All chromatographic separations, including HPLC, operate under the same basic principle: every compound interacts with other chemical species in a distinctive manner. Chromatography separates a sample into its constituent parts because of the difference in the relative affinities of different molecules for the mobile phase and the stationary phase used in the separation [33].

All chemical reactions have a characteristic equilibrium constant. For the following chemical reaction (8):

$$\mathrm{A_{(aq)} + B_{(s)} \rightleftharpoons AB_{(s)}} \tag{8}$$

There is a chemical equilibrium constant K_{eq} that dictates what percentage of compound A will be in solution and what percentage will be bound to the stationary compound B. During a chromatographic separation, there is a similar relationship between compound A and the solvent, or mobile phase. This will yield an overall equilibrium equation which dictates the quantity of A that will be associated with the stationary phase S and the quantity of A that will be associated with the mobile phase M (9):

$$\mathrm{A_M \rightleftharpoons A_S} \tag{9}$$

The equilibrium of compound A between the mobile M and stationary S phases is given by the constant K_c (10) [33,51]:

$$K_c = \frac{a_S(\mathrm{A})}{a_M(\mathrm{A})} \approx \frac{c_S(\mathrm{A})}{c_M(\mathrm{A})} \tag{10}$$

where K_c, the distribution constant, is the ratio of the activity a_S(A) of compound A in the stationary phase S and activity a_M(A) of compound A in the mobile phase M [33,51]. In most separations, which contain low concentrations of the species to be separated, the activity *a* of A in each is approximately equal to the concentration *c* of A in that state. The distribution constant indicates the amount of time that compound A spends adsorbed to the stationary phase as the opposed to the amount of time A spends solvated by the mobile phase. This relationship determines the amount of time it will take for compound A to travel the length of the column, also known as retention time in the stationary phase t_s. The more time A spends adsorbed to the stationary phase, the more time compound A will take to travel the length of the column. The amount of time between the injection of a sample and its elution from the column is known as the (total) retention time t_R (Fig. 13a). Additionally, the amount of time required for a sample that does not interact with the stationary phase, or has a K_c equal to zero, to travel the length of the column is known as the mobile phase hold-up or void time t_M (Fig. 13a) [33,51]. No compound is eluted in less than the void time.

To separate two compounds, their respective distribution constants K_c must be different, otherwise both compounds would be eluted simultaneously. This property is known as selectivity [33,51].

As a compound passes through the column it slowly diffuses away from the initial injection band, which is the area of greatest concentration. The initial narrow band which contains all the sample becomes broader the longer the analyte remains in the column. This band broadening increases the time required for the complete elution of a particular compound and is, in general, not desired [33,51]. It must be minimised so that overly broad elution bands do not overlap with one another.

The resolution R_S of the elution is a quantitative measure of how well two elution peaks can be distinguished in a chromatographic separation (Fig. 13b) [33,51]. It is defined as the difference in (total) retention times between the two peaks, divided by the combined widths of the elution peaks (11) [33,51]:

$$R_S = \frac{2[t_R(\mathrm{B}) - t_R(\mathrm{A})]}{W_A + W_B} \tag{11}$$

where A and B are the species with the shortest and longest retention times, respectively, and t_R and W are the retention time and elution peak width, respectively (Fig. 13b) [33,51]. The peaks can usually be differentiated successfully when the resolution is greater than 1, (Fig. 13b) [33,51].

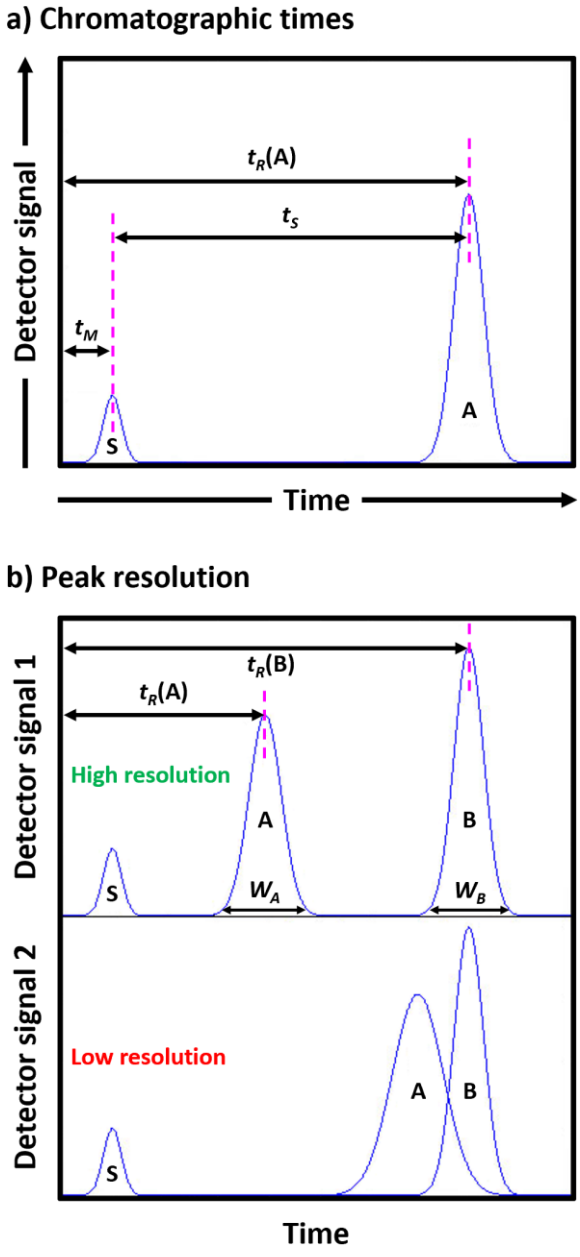

Fig. 13. Definition of a) chromatographic times and b) peak resolution. S stands for solvent or mobile phase.

While all of these basic principles hold true for all chromatographic separations, HPLC was developed as a method to solve some of the shortcomings of standard liquid chromatography [33]. Classic liquid chromatography had several severe limitations as a separation method [52]. The limiting factor in liquid chromatography was originally the size of the column packing. Once columns could be packed with particles as small as 3 μm, faster separations could be performed in smaller and narrower columns [52]. High pressure was required to force the mobile phase and sample through these new columns, and previously unneeded apparatus was required to maintain the reproducibility of results in this new instrument [52]. The use of high pressures in a narrow column allowed for a more effective separation to be achieved in much less time than was required for previous forms of liquid chromatography [52]. Specialised apparatus is required for a HPLC separation because of the high pressures and low tolerances under which the separation occurs. If the results are to be reproducible, then the conditions of the separation must also be reproducible [33,52]. Thus, HPLC equipment must be of high quality. It is therefore expensive. The main components of a HPLC apparatus system are shown below (Fig. 14) [33,52]. The mobile phase (Fig. 14), or solvent, in HPLC is usually a mixture of polar and non-polar liquid components whose respective concentrations are varied depending on the composition of the sample. In the HPLC column (Fig. 14), the components of the sample separate based on their different interactions with the column packing. If a species interacts more strongly with the stationary phase in the column, it will spend more time adsorbed to the column's adsorbent and will therefore have a greater retention time. The HPLC pump (Fig. 14) drives the solvent and sample through the column. To reduce variation in the elution, the pump must maintain a constant, pulse free, flow rate. The HPLC detector (Fig. 14), located at the end of the column, must register the presence of various components of the sample, but must not detect the solvent. For this reason, there is no universal detector that works for all separations. A common HPLC detector is a UV-Vis absorption detector since most medium to large molecules absorb UV-Vis radiation [52]. Finally, the HPLC graphic result, called chromatogram, is processed and shown at the display unit (Fig. 14).

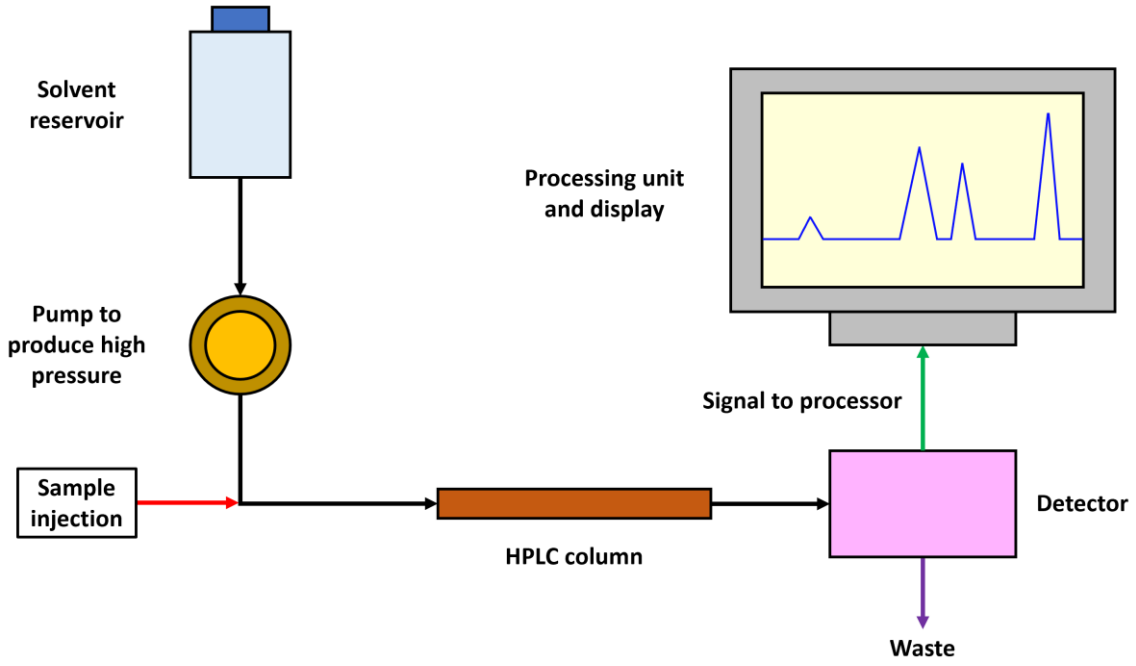

Fig. 14. Schematic representation of a HPLC apparatus system.

The separation is considered normal phase when the stationary phase is more polar than the mobile phase [33,51,52]. Instead, if the stationary phase is less polar than the mobile phase, the separation is deemed reverse phase [33,51,52]. In reverse phase HPLC, the retention time of a compound increases with decreasing polarity of the specific species. The key to an effective and efficient separation is to determine the appropriate ratio between polar and non-polar components in the mobile phase [52]. The goal is for all the compounds to elute in the shortest time possible, while still allowing for the resolution of individual peaks. Typical columns for normal phase separation are packed with alumina or silica [52]. Instead, alkyl, aliphatic or phenyl bonded phases are often used for reverse phase separation [52].

The separation is deemed an isocratic elution if the composition of the mobile phase remains constant throughout the HPLC separation [33,51,52]. Frequently, the only way to elute all of the compounds in the sample in a reasonable amount of time, while still maintaining peak resolution, is to change the ratio of polar to non-polar compounds in the

mobile phase during the sample run. Known as gradient chromatography [33,51,52], this is the technique of choice when a sample contains components of a wide range of polarities. The gradient elution offers the most complete separation of the peaks, without taking an excessive amount of time [52]. A sample containing compounds of a wide range of polarities can be separated by a gradient elution in a shorter time period without a loss of resolution in the earlier peaks or excessive broadening of later peaks [52].

HPLC can be used in both qualitative and quantitative applications, that is for both compound identification and quantification [52]. Normal phase HPLC is only seldom used now. Practically all HPLC separation can be performed in reverse phase. Reverse phase HPLC (RPLC) is ineffective only for a few separation types. It cannot separate inorganic ions (they can be separated by ion exchange chromatography) [52], nor polysaccharides (they are too hydrophilic for any solid phase adsorption to occur), nor polynucleotides (they adsorb irreversibly to the reverse phase packing) [52]. Additionally, incredibly hydrophobic compounds cannot be separated effectively by RPLC (there is little selectivity) [52]. Aside from these few exceptions, RPLC is employed for the separation of almost all other compound varieties. RPLC can be used to effectively separate similar simple and aromatic hydrocarbons, even those that differ only by a single methylene group [52]. RPLC effectively separates simple amines, sugars, lipids, and even pharmaceutically active compounds [52]. RPLC can be also employed in the separation of amino acids, peptides, and proteins [52]. RPLC is used to separate molecules of biological origin. Finally, enantiomers of chiral compounds can be also separated from its racemic mixture by means of chiral HPLC by using compound-specific chiral columns [52]. Therefore, HPLC is a useful addition to an analytical arsenal, especially for the separation of a sample before further analysis.

2.5. References

[1] J.D. Seader, E.J. Henley, Separation process principles, 2nd ed., John Wiley & Sons, Inc., New Jersey, 2006.

[2] A.B. de Haan, H. Bosch, Industrial separation processes: fundamentals, Walter de

Gruyter GmbH, Berlin, 2013.

[3] J.H. ter Horst, C. Schmidt, J. Ulrich, Fundamentals of industrial crystallization, in: Handb. Cryst. Growth Bulk Cryst. Growth Second Ed., 2014: pp. 1317–1349.

[4] F.L. Nordström, Å.C. Rasmuson, Prediction of solubility curves and melting properties of organic and pharmaceutical compounds, Eur. J. Pharm. Sci. 36 (2009) 330–344.

[5] J.W. Mullin, Crystallization, 4th ed., Butterworth-Heinemann, Oxford, 2001.

[6] A.S. Myerson, Handbook of industrial crystallization, 2nd ed., Butterworth-Heinemann, Boston, 2002.

[7] A. Mersmann, Crystallization technology handbook, 2nd ed., Marcel Decker, Inc., New York, 2001.

[8] H.J.. Kramer, S.K. Bermingham, G.M. van Rosmalen, Design of industrial crystallisers for a given product quality, J. Cryst. Growth. 198–199 (1999) 729–737.

[9] D. Kashchiev, Nucleation: basic theory with applications, Butterworth-Heinemann, Oxford, 2000.

[10] M. Matsuoka, J. Garside, Non-isothermal effectiveness factors and the role of heat transfer in crystal growth from solutions and melts, Chem. Eng. Sci. 46 (1991) 183–192.

[11] J.H. ter Horst, D. Bedeaux, S. Kjelstrup, The role of temperature in nucleation processes, J. Chem. Phys. 134 (2011) 054703.

[12] J. Ulrich, H. Glade, Melt crystallization: fundamentals, equipment and applications., Shaker Verlag GmbH, Aachen, 2003.

[13] J.H. ter Horst, R.M. van Rosmalen, R.M. Geertman, CRYSTALLIZATION | Additives: molecular design, in: Encycl. Sep. Sci., Academic Press, 2000: pp. 931–

940.

[14] L. Addadi, Z. Berkovitch-Yellin, N. Domb, E. Gati, M. Lahav, L. Leiserowitz, Resolution of conglomerates by stereoselective habit modifications, Nature. 296 (1982) 21–26.

[15] N.G. Anderson, Practical process research & development: a guide for organic chemists, 2nd ed., Academic Press, Oxford, 2012.

[16] O. Levenspiel, Chemical reaction engineering, 3rd ed., WILEY-VCH Verlag, New York, 1999.

[17] J.Y. Oldshue, Fluid mixing technology, McGraw-Hill, New York, 1983.

[18] S.M. Walas, Chemical reactors, in: R.H. Perry, D.W. Green, J.O. Maloney (Eds.), Perry's Chem. Eng. Handb., 7th ed., McGraw-Hill, New York, 1997: pp. 23-1-23–61.

[19] A. Bisio, R.L. Kabel, eds., Scaleup of chemical processes. Conversion from laboratory scale tests to successful commericial size design, WILEY-VCH Verlag, New York, 1985.

[20] K.G. Denbigh, J.C.R. Turner, Chemical reactor theory, 3rd ed., Cambridge University Press, Cambridge, 1984.

[21] FDA's policy statement for the development of new stereoisomeric drugs, Chirality. 4 (1992) 338–340.

[22] F.R. Giordano, M.D. Weir, W.P. Fox, A first course in mathematical modeling, 3rd ed., Brooks/Cole Thomson Learning, London, 2003.

[23] Å.C. Rasmuson, Crystallization process analysis by population balance modeling, in: Handb. Ind. Cryst., Cambridge University Press, 2019: pp. 172–196.

[24] F. Garnier, J. Randon, J.L. Rocca, Enantiomeric separation by ultrafiltration: complexation mechanism of tryptophan analogs to bovine serum albumin, Sep.

Purif. Technol. 16 (1999) 243–250.

[25] J. Randon, F. Garnier, J.L. Rocca, B. Maïsterrena, Optimization of the enantiomeric separation of tryptophan analogs by membrane processes, J. Memb. Sci. 175 (2000) 111–117.

[26] A.B. Shiflet, G.W. Shiflet, Introduction to computational science: modeling and simulation for the sciences, 2nd ed., Princeton University Press, Princeton, 2014.

[27] GAMS Software GmbH, GAMS, (2019). https://www.gams.com/ (accessed August 5, 2019).

[28] GAMS Software GmbH, An introduction to GAMS, (2020). https://www.gams.com/products/introduction/ (accessed May 21, 2020).

[29] GAMS Software GmbH, Classification of models in GAMS, (2020). https://www.gams.com/latest/docs/UG_ModelSolve.html#UG_ModelSolve_ModelClassificationOfModels (accessed May 21, 2020).

[30] GAMS Software GmbH, GAMS solver manual, (2020). https://www.gams.com/latest/docs/S_MAIN.html (accessed May 21, 2020).

[31] S. Dirkse, M.C. Ferris, J. Ramakrishnan, GDXMRW: interfacing GAMS and MATLAB, (2014). https://www.gams.com/latest/docs/T_GDXMRW.html (accessed August 5, 2019).

[32] M.C. Ferris, R. Jain, S. Dirkse, GDXMRW: interfacing GAMS and MATLAB, Wisconsin, 2010.

[33] D.A. Skoog, F.J. Holler, S.R. Crouch, Principles of instrumental analysis, 6th ed., Thomson Brooks/Cole, Belmont, 2007.

[34] L.D. Field, S. Sternhell, J.R. Kalman, Organic structures from spectra, 5th ed., John Wiley & Sons, 2013.

[35] J. Franck, E.G. Dymond, Elementary processes of photochemical reactions, Trans.

Faraday Soc. 21 (1926) 536–542.

[36] E. Condon, A theory of intensity distribution in band systems, Phys. Rev. 28 (1926) 1182–1201.

[37] E.U. Condon, Nuclear motions associated with electron transitions in diatomic molecules, Phys. Rev. 32 (1928) 858–872.

[38] J.H. Lambert, Photometria sive de mensura et gradibus luminis, colorum et umbrae, Augustae Vindelicorum, Torino, 1760.

[39] Beer, Bestimmung der Absorption des rothen Lichts in farbigen Flüssigkeiten, Ann. Der Phys. Und Chemie. 162 (1852) 78–88.

[40] H.-H. Perkampus, UV-Vis spectroscopy and its applications. Springer lab manuals., Springer, Berlin, Heidelberg, 1992.

[41] E. Pretsch, P. Bühlmann, M. Badertscher, Structure determination of organic compounds. Tables of spectral data, 4th ed., Springer, 2009.

[42] P.Y. Bruice, Organic chemistry, 5th ed., Pearson Prentice Hall, 2008.

[43] P.R. Griffiths, J.A. de Haseth, Fourier transform infrared spectrometry, 2nd ed., John Wiley & Sons, Inc., Hoboken, 2007.

[44] R.L. McCreery, Raman spectroscopy for chemical analysis, John Wiley & Sons, Inc., New York, 2000.

[45] D.J. Gardiner, P.R. Graves, Practical Raman spectroscopy, Springer-Verlag, Berlin, Heidelberg, 1989.

[46] D.A. Long, The Raman effect: a unified treatment of the theory of Raman scattering by molecules, John Wiley & Sons, Ltd, Chichester, 2002.

[47] C. Hammond, The basics of crystallography and diffraction, 4th ed., Oxford University Press, Oxford, 2015.

[48] Y. Waseda, E. Matsubara, K. Shinoda, X-ray diffraction crystallography, Springer-Verlag, Berlin, Heidelberg, 2011.

[49] T. Hahn, Space-group symmetry, in: Int. Tables Crystallogr., 5th ed., Springer-Verlag, Berlin, New York, 2002.

[50] W.H. Bragg, W.L. Bragg, The reflection of X-rays by crystals, Proc. R. Soc. London. Ser. A, Contain. Pap. a Math. Phys. Character. 88 (1913) 428–438.

[51] S. Lindsay, D. Kealey, High performance liquid chromatography, John Wiley & Sons, Ltd, Chichester, 1987.

[52] J.K. Swadesh, HPLC: practical and industrial applications, 2nd ed., CRC Press, Boca Raton, 2000.

CHAPTER 3

3. Temperature and pH-Dependent Solubilities of Enantiopure and Racemic Amino Acids in Complex Aqueous Solutions: a Fast and Accurate Estimation of Phase Diagrams

Jose Capdevila-Echeverria, Joop H. ter Horst

Racemic solutions usually crystallise to form a racemic compound, conglomerate or solid solution. Chiral resolution of a chiral compound depends on the type of solid state it forms. A phase diagram screening of these solutions is then crucial to identify what chiral separation method can be applied. We explore an efficient and simple phase diagram screening method for chiral compounds in solution in order to validate the methodology for a wide range of applications. We focus on racemic compounds, which accounts for the 90-95% of the cases, by estimating the eutectic point compositions of three amino acid systems, comparing the accuracy between different screening methods and literature determinations, and proposing a workflow process for the estimation and validation of a multicomponent phase diagram of a racemic compound-forming system. In addition, we study how temperature, pH, and concentration affect the solubility and eutectic compositions for these amino acid systems and solubility binary, pseudo-binary, and ternary phase diagrams explored. We observed that alanine can be analysed via a faster temperature variation method which uses light for crystallisation detection. Instead, phenylalanine and valine, which present fouling-related phenomena, need a gravimetric approach through an equivalent method. The results show that pseudo-binary phase diagrams can estimate the eutectic point compositions in a wide range of pH, from acidic to basic conditions, with very high accuracy (>95.0%) in a less time-consuming manner than existing methods. For instance, this methodology estimates that the eutectic point

compositions, given in enantiomeric ratio for enantiomer L, of alanine, phenylalanine, and valine in water are 0.784 (pH 6.1, 44.4ºC), 0.906 (pH 6.7, 25.0ºC), and 0.719 (pH 6.2, 25.0ºC), respectively. Additionally, it opens the possibility to use this type of diagrams in a new workflow process proposed for the determination of ternary phase diagrams of racemic compound-forming systems.

3.1. Introduction

Enantiomers are the stereoisomers of a chiral compound which are mirror images of each other that are non-superposable [1,2]. The enantiomers of a chiral drug may differ significantly in their therapeutic effects and toxicity inside the living organisms [3]. As an example, (*R*)-ketamine is responsible for agitation, hallucination, restlessness, in contrast to (*S*)-ketamine that is an antidepressant [4]. The chiral separation of racemic mixtures or impure enantiomers would prevent such undesired effects in the absence of in vivo racemization. Thus, chiral resolution processes are of major importance in industries such as pharmaceuticals, agrochemicals, food, and cosmetics [5,6].

The solid phase obtained from a racemic solution can be a racemic compound, a conglomerate, or a solid solution (Fig. 1) [5]. Each of these classes of chiral compounds has different physical features in terms of natural abundance, crystal lattice, melt, solubility, and more [2,5–10]. Racemic compounds, which accounts for the 90-95% of existing chiral compounds, form a single crystalline phase in which the two enantiomers are present in an ordered 1:1 ratio in the elementary cell. Adding a small amount of one enantiomer to the racemic compound decreases the melting point, but the pure enantiomer can have a higher or lower melting point than the racemate [5]. Conglomerates, which include 5-10% of the cases, are formed when molecules of the substance have more affinity for the same enantiomer than for the opposite one. Then, a mechanical mixture of enantiomerically pure crystals results. The melting point of the conglomerate is always lower than that of the pure enantiomer. The addition of a small amount of one enantiomer to the conglomerate increases the melting point [5]. Solid solutions, which account for

less than 1% of the cases, form when there is no large difference in affinity between the same and opposite enantiomers, then in contrast to the racemic compound and conglomerate, the two enantiomers will coexist in an unordered manner in the crystal lattice. There, the addition of a small amount of one enantiomer may change the melting point slightly or not at all [5]. Figure 1 shows the classification of chiral compounds in the solid state and compares their crystal lattice, melt binary, and solubility ternary phase diagrams.

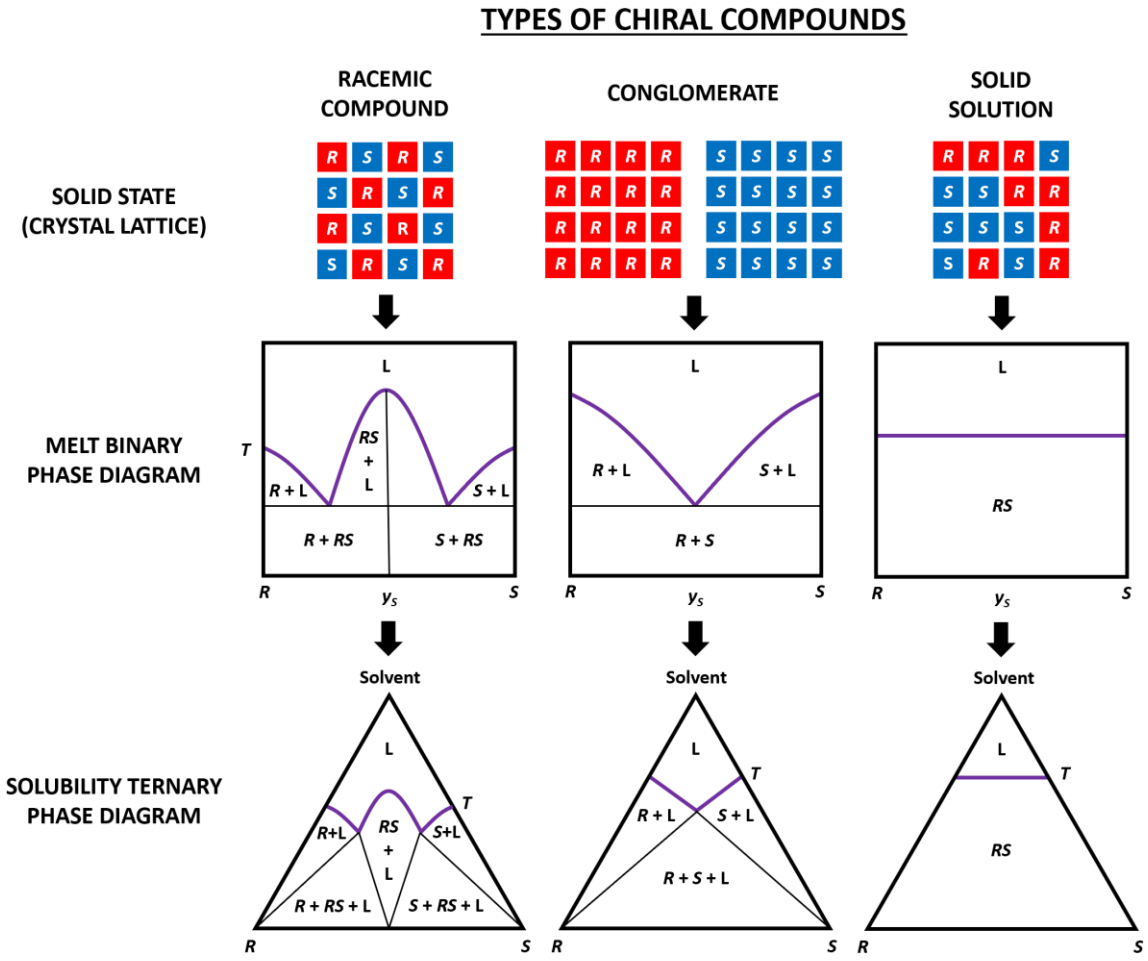

Fig. 1. Solid state (crystal lattice), melt binary, and solubility ternary phase diagrams, at certain temperature *T*, for the three different types of chiral compounds: racemic compound, conglomerate, and solid solution. *R*, *S*, *RS*, and L represent, respectively, solid phase of enantiomer *R*, solid phase of enantiomer *S*, solid phase of racemic compound *RS* or solid solution *RS*, and liquid phase.

The class of solid state of a chiral compound has important implications on the ability for resolution through a crystallisation process. This explains the importance of developing methodologies to fast screen the phase diagrams and therefore be able to identify the type of chiral compound which we are dealing with [2,6,8]. Furthermore, the phase diagram gives quantitative data that may enable chiral separation methods to be identified and designed [5,6,11].

It is important therefore to determine the class of chiral compound and phase diagram in the least time- and money-consuming way, but at the same time analyse the accuracy of the measurements and propose a methodology on how to proceed. This paper builds on a fast clear point temperature screening method [2] and proposes an equivalent method using pseudo-binary phase diagrams for determining the chiral compound class, the solubilities of the different solid forms in ternary solutions, and the eutectic point compositions of racemic compound-forming systems. The proposed method is compared to other screening methods and its results are compared to literature determinations. Finally, a workflow process is proposed to fast estimate accurately and validate the ternary phase diagram of a racemic compound. We describe the study of three amino acids which are known to behave as racemic compound-forming systems [12,13]. We study the effect of temperature, pH, and enrichment on the solubility and eutectic compositions of the three amino acid systems.

3.2. Experimental section

3.2.1. Materials

The amino acids DL-alanine (DL-ala; Sigma-Aldrich, ≥99%), L-alanine (L-ala; Sigma-Aldrich, ≥99%), DL-phenylalanine (DL-phe; Sigma-Aldrich, 99%), L-phenylalanine (L-phe; Sigma-Aldrich, ≥99%), DL-valine (DL-val; Sigma-Aldrich, ≥99%), and L-valine (L-val; Sigma-Aldrich, ≥98%) were used as purchased.

The solvents and media used were aqueous 1.0 M HCl and 1.0 M NaOH solutions, aqueous pH 1.68 buffer solution (pH 1.68 at 20-25ºC, HI 5016, Hanna Instruments Ltd.), aqueous pH 7.00 buffer solution (di-sodium hydrogen phosphate/potassium dihydrogen phosphate, pH 7.00 at 20-25ºC, Sigma-Aldrich), aqueous pH 7.01 buffer solution (pH 7.01 at 20-25ºC, HI 5007, Hanna Instruments Ltd.), aqueous pH 12.45 buffer solution (pH 12.45 at 20-25ºC, HI 5124, Hanna Instruments Ltd.), formic acid (LC-MS grade, LiChropur, 98-100%), methanol (LC-MS grade, LiChrosolv, ≥99.9%), Milli-Q water, water (LC-MS grade, LiChrosolv, ≥99.9%). The Milli-Q water was taken from a Merck Millipore purification system and had a resistivity of 18.2 MΩ·cm at 25°C (Milli-Q water is referred to as water unless otherwise indicated). A 100 mL aqueous 1.0 M HCl solution was prepared by slowly adding 8.2 mL of HCl stock solution (Sigma-Aldrich, 37.0% w/w) to 25 mL of water, then adjusting the final volume of the solution to 100 mL with water. A 100 mL aqueous 1.0 M NaOH solution was prepared by first dissolving 4.1 g of NaOH (anhydrous, Sigma-Aldrich, ≥98%) in 70 mL of water and then adjusting the final volume of the solution to 100 mL by adding water. Magnetic stirring was necessary to dissolve suspensions made with the 1.0 M NaOH and HCl solutions. All aqueous buffer solutions and LC-MS (HPLC) grade solvents were used as purchased.

3.2.2. Methods

3.2.2.1. Determination of solubility

Two methods were used to determine the solubility binary phase diagrams. The two methods used are called temperature variation (TV) and equilibrium concentration (EqC) methods [14].

3.2.2.1.1. Temperature variation (TV) method

The temperature variation protocol was adapted from literature [14] using the Crystal16 multiple reactor setup (Technobis Crystallisation Systems). Samples were prepared by adding a specific amount of the solid and subsequently 1 mL of aqueous medium (water,

pH 7.00 buffer solution, 1.0 M HCl solution or 1.0 M NaOH solution) to each 1.5-mL sample vial (screw neck clear glass vial). The samples were agitated using magnetic stirrer bars with a stirring rate of 700 rpm. Three temperature cycles were applied starting at 20.0ºC, with maximum and minimum temperatures of 80.0ºC and 1.0ºC, respectively, and with heating and cooling rates of 0.3ºC/min. Hold times of 1 h were applied when maximum (80.0ºC) and minimum (1.0ºC) temperatures were reached in each cycle. Clear and cloud points were registered based on the transmission of a light through each vial. Then, the saturation temperature of the composition in the vial was determined by the average of three clear points measurements (*RSD* within ±3%). This method was used for the solubility determination of DL- and L-alanine. Solubilities are expressed in mg of chiral compound per gram of water. Mass corrections, as described in EqC method (see section 3.2.2.1.2.), were applied to adjust the solubility values, discounting the mass contributions of solid residues from buffer solutions.

3.2.2.1.2. Equilibrium concentration (EqC) method

A similar gravimetric protocol was used similar to one reported in literature [14]. Samples were prepared by adding an excess of compound in 1 mL of aqueous medium (water, pH 7.00 buffer solution, 1.0 M HCl solution or 1.0 M NaOH solution) in each 1.5-mL sample vial. Then, the suspensions in the vials were equilibrated at different constant temperatures in the Crystal16 multiple reactor setup (Technobis Crystallisation Systems) for at least 2-3 days. During that period, the samples were agitated using magnetic stirrer bars with a stirring rate of 700 rpm. Afterwards, at various temperatures, solution samples of less than 1 mL were taken with a syringe, filtered, weighed, and left to evaporate in the oven (65ºC) for at least 7 days. After this, the crystals appeared dry and they were weighed. Two days later, they were weighed again to check for any additional mass loss until the mass was constant. Experiments with pH 7.00 buffer and 1.0 M NaOH solutions required final mass corrections since gravimetric determinations (12 for each medium) of these media alone measured 9.9±0.1 mg of solid residue per gram of pH 7.00 buffer solution and 47.4±0.1 mg of solid residue per gram of 1.0 M NaOH

solution. Instead, experiments with water and 1.0 M HCl solution did not need any final mass adjustment since no solid residue was gravimetrically detected, meaning everything evaporated. The solubility of the compound at certain temperature was determined by the average of three gravimetric measurements (*RSD* within ±3%). Solubilities are expressed in mg of chiral compound per gram of water. This method was used for the solubility determination of DL- and L-phenylalanine and DL- and L-valine.

3.2.2.2. Determination of (solubility) ternary phase diagrams

An estimation of the solubility ternary phase diagram of the amino acid systems was carried out by first determining the liquidus by means of van 't Hoff-type equations for enantiopure and racemic compounds. Once the solubility line was found, the phase diagram estimation was obtained for alanine, phenylalanine, and valine (for detailed description, see section 3.3.2.).

For alanine system, an estimation of enantiopure and racemic regions of the complete ternary phase diagram was made based on an ideal non-complex racemic compound-forming system behaviour (Fig. 1) [5]. The ternary phase diagram of alanine was then validated with extra TV measurements, single crystal x-ray diffraction (SC-XRD), and eutectic points from literature (Fig. 2).

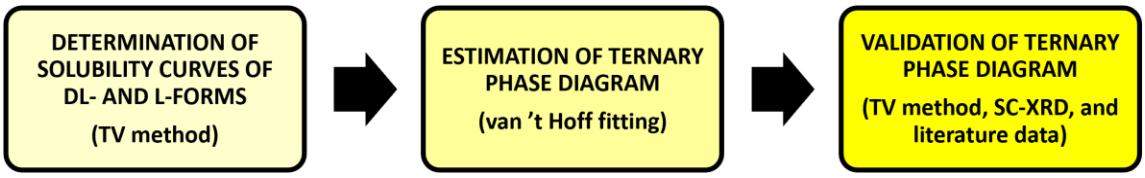

Fig. 2. Workflow process for the validated estimation of the ternary phase diagram of alanine.

The additional TV measurements, using also Crystal16, consisted in the registration of four saturation temperatures T_s with three different enantiomeric ratios y_L of 0.714, 0.815, and 0.889 (that is x_L/x_D equal to 2.5, 4.4, and 8.0, respectively). The four fixed total masses for each enantiomeric ratios y_L were of 220, 230, 240, and 250 mg of alanine. Each of these amounts was dissolved in 1 mL of water in a magnetically stirred vial. Then, the

same protocol described above (see section 3.2.2.1.1.) was applied to assess real liquidus points at 25.0ºC.

SC-XRD data was collected from 2-10 mm length alanine crystals, obtained from vials when using Crystal16 in crystallisation experiments, on a Bruker D8 Venture single crystal diffractometer (GC001015). The emission setup consisted in a IμS microfocus source (point focused), Cu Kα1 (1.540596 Å) as radiation source, and operating voltage and current of 50 kV and 1 mA, respectively. Regarding sample setup, a three-circle fixed chi goniometer (stage) and low diffraction loop (mount) were required. Regarding detection, a photon II CCD detector was used with a 1024x1024 frame size. Operations were performed using Bruker APEX3 software (v2016.5-0) [15]. Crystal structure was elucidated using WinGX software with SHELX package [16–19].

3.2.2.3. Determination of pseudo-binary phase diagrams

3.2.2.3.1. Temperature variation (TV) method

A similar protocol was used as reported above for binary phase diagrams to determine saturation temperatures T_s (see section 3.2.2.1.1.). Samples were prepared, in vials, by dissolving constant total amounts (250 mg for neutral aqueous media or 300 mg for acid and basic aqueous media) of chiral mixtures of DL- and L-alanine with enantiomeric ratios y_L from 0.50 (racemic mixture) to 1.00 (enantiopure L-form) with 1 mL of one of the following aqueous media: water, pH 7.00 buffer solution, 1.0 M HCl solution or 1.0 M NaOH solution. This method was used for alanine systems.

3.2.2.3.2. Equilibrium concentration-HPLC (EqC-HPLC) method

A similar gravimetric protocol was used as described above for binary phase diagrams to determine saturation concentrations C_s (see section 3.2.2.1.2.). Here, constant total excess amounts were employed (phenylalanine: 40 mg for neutral media, 170 mg for acid medium, and 205 mg for basic medium; valine: 100 mg for neutral media, 300 mg for acid

medium, and 195 mg for basic medium) of chiral mixtures of DL- and L-forms with enantiomeric ratios y_L from 0.50 (racemic mixture) to 1.00 (enantiopure L-form) with 1 mL of one of the following aqueous media: water, pH 7.00 buffer solution, 1.0 M HCl solution or 1.0 M NaOH solution.

High-performance liquid chromatography (HPLC) was required for the determination of the exact enantiomeric ratio y_L of the dried solid product obtained from each vial. The HPLC equipment used was an Agilent Technologies 1100 with the following features: Astec CHIROBIOTIC T column (25 cm x 4.6 mm I.D., 5 μm particles (12024AST) at 25.0ºC, mobile phase of water:methanol:formic acid (30:70:0.02, HPLC grade), flow rate of 1 mL/min, filtered sample of 1 mg/mL in water:methanol (30:70, HPLC grade), injection volume of 10 μL, UV detection at 205 nm, stop time of 10 min, and retention times of amino acid enantiomer assessed were of 4.994 (L-phe), 6.170 (D-phe), 4.472 (L-val), and 5.385 min (D-val) [20,21]. This combined methodology has the advantage to avoid the registration of HPLC calibration curves to determine total concentrations and therefore it is more robust to apply over time. This method was employed for phenylalanine and valine systems.

3.2.2.4. Determination of pH

The pH of each vial solution was measured with a wireless pH electrode with a micro bulb spherical tip of 3 mm (HI-10832 HALO, Hanna Instruments Ltd.) [22], which was possible to introduce inside the 1.5-mL vials used for the crystallisation experiments described above (see sections 3.2.2.1. and 3.2.2.3.). The pH values were registered through the Hanna Lab App (iOS) [22].

The device calibration was carried out just before the determination of the pH of the samples of interest with three buffer solutions, supplied by Hanna Instruments Ltd., with pH values of 1.68, 7.01, and 12.45. For TV method (see sections 3.2.2.1.1. and 3.2.2.3.1.), once the electrode was calibrated, the pH of the samples was measured always at 25ºC at the beginning and end of each experiment (SD = ±0.1), so in the suspension. For EqC

method (see sections 3.2.2.1.2. and 3.2.2.3.2.), the pH of each sample was measured twice after filtration, in the saturated solutions at the equilibration temperature before starting the evaporation ($SD = \pm 0.1$).

3.3. Results

3.3.1. Determination of solubility in aqueous systems

While the compound alanine in aqueous media results in reliable saturation temperature measurements using the temperature variation (TV) method [14], the phenylalanine and valine systems present fouling-related phenomena: phenylalanine and valine crystals are observed to accumulate at the solution interface with air and walls and bottom of the vial during the crystallisation step in the TV measurement. This behaviour then makes saturation temperature detection unreliable using light-enabled techniques such as the TV method. Thus, the gravimetric-type equilibrium concentration (EqC) data is used in Fig. 3 for the latter two systems [14].

Solubility binary phase diagrams of alanine, phenylalanine, and valine determined with different aqueous media by the TV and EqC methods are shown below (Fig. 3). The solubilities C_s of the racemic (DL) and enantiopure (L) chiral compounds are measured in a temperature range of 20-80ºC. For instance, the solubilities in water at 50ºC for the racemic compounds of alanine, phenylalanine, and valine are 219, 21, and 106 mg/g, respectively; and for their enantiopure compounds are 208, 40, and 69 mg/g (Fig. 3). All systems show their solubilities C_s increasing with temperature T. We observe the strongest temperature dependence of solubility in the alanine systems (Fig. 3a), then phenylalanine (Fig. 3b), and valine systems bear the lowest one (Fig. 3c). At the same temperature, alanine (Fig. 3a) shows the highest solubility in the aqueous systems studied and phenylalanine the lowest (Fig. 3b), in accordance to their chemical structure, from the most to the least polar (Table 1), if we assume a similar solubility effect regarding their crystal phases.

Racemates of alanine and valine show higher solubilities than the enantiopure compound (L-form) in all aqueous media tested. Instead, racemic phenylalanine shows lower solubility than its enantiopure form (Fig. 3). For instance, in water at 50ºC, racemic and enantiopure alanine have solubilities of 219 and 208 mg/g, respectively; and the same chiral forms for valine show values of 106 and 69 mg/g. Instead, under the same conditions, the solubilities of racemic and enantiopure phenylalanine are 21 and 40 mg/g, respectively. As the racemate compositions are equal amounts of both enantiomers, we observe that in all cases the single enantiomer concentration in a solvent equilibrating with a racemic compound is lower than the single enantiomer concentration in solutions equilibrating with the enantiopure compound: 208, 69, and 40 mg/g are higher than 109.5, 53, and 10.5 mg/g for alanine, valine, and phenylalanine, respectively. Thus, the racemic solids alanine, valine, and phenylalanine are 1.9, 1.3, and 3.8 times more stable in the racemic solution than the enantiopure solids. These differences in stability have strong implications for the eutectic point composition of a system, whose determination simplifies the chiral resolution of such system by crystallisation.

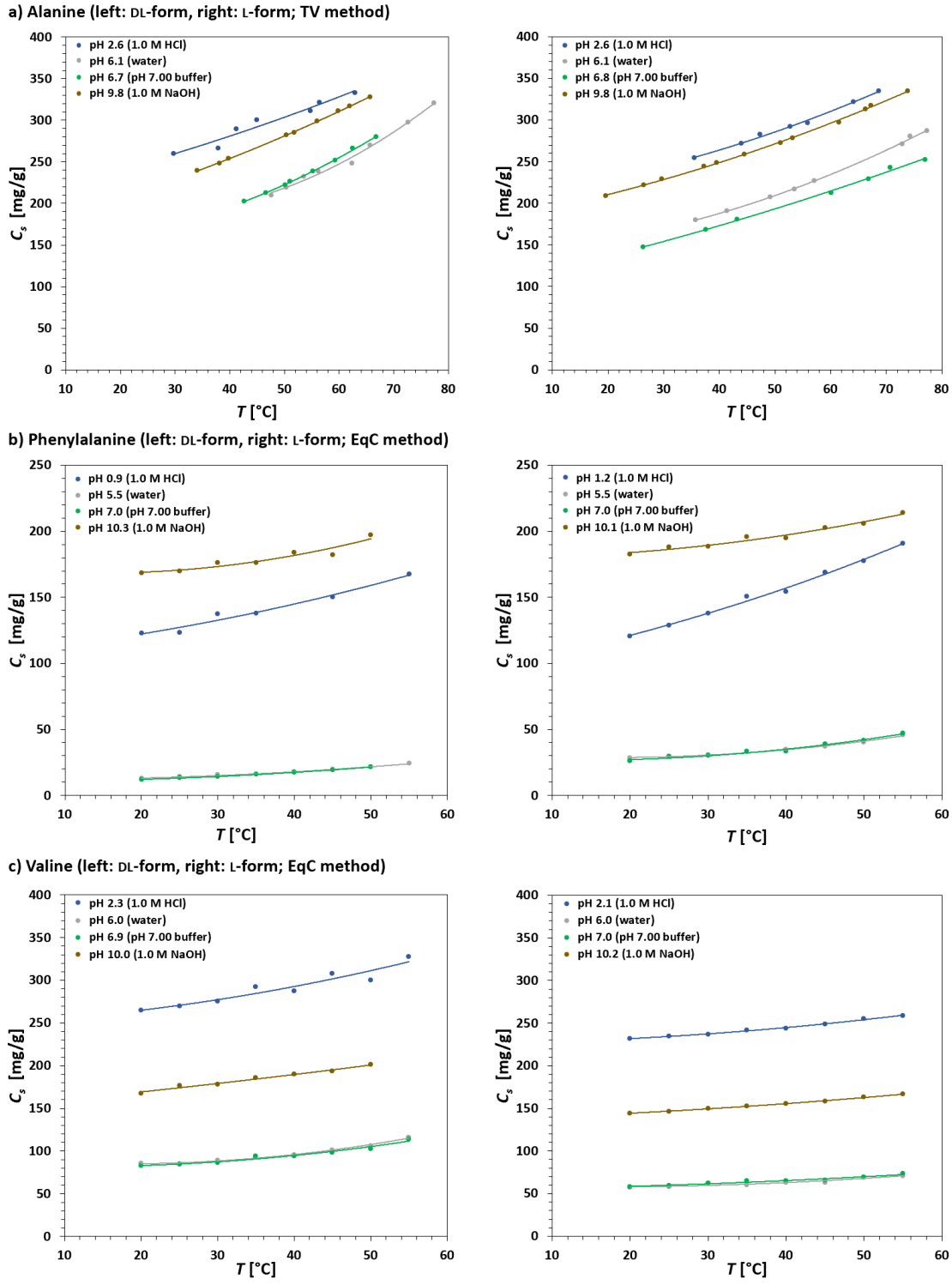

Fig. 3. Solubility for: a) alanine, b) phenylalanine, and c) valine in complex aqueous media. Both DL- (left) and L-form (right) solubilities at different pH are represented for each amino acid system. Lines represent the van 't Hoff fitting for each series of experimental solubility dots (see Table 2).

All the amino acids systems tested present higher solubilities in acidic (pH ≤ 2.6) and basic (pH ≥ 9.8) media than in neutral media (Fig. 3) due to their common chemical structure with two proton-dissociable functional groups, the acidic carboxyl and basic amino groups (Table 1).

Table 1. Acid-base dissociation equilibria for amino acids with non-dissociable side chain R. Literature pK_a and pI (isoelectric point) values for the amino acid systems studied, at 25.0ºC [23,24]. Formulas: $pK_a = -\log_{10} K_a$ and $pI = \frac{pK_{a1}+pK_{a2}}{2}$.

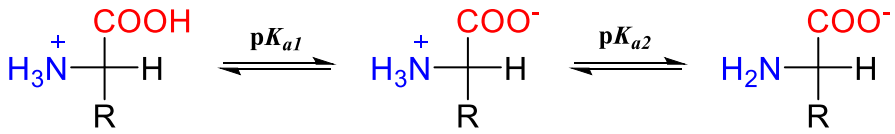

Cation form Acidic media Low pH | **Zwitterion form** Neutral media Medium pH | **Anion form** Basic media High pH

Amino acid	Side chain, R (chemical formula)	pK_{a1}	pK_{a2}	pI
Alanine	-Me (-CH_3)	2.34	9.69	6.02
Phenylalanine	-Bn (-$CH_2C_6H_5$)	1.83	9.13	5.48
Valine	-*i*Pr (-$CH_2(CH_3)_2$)	2.32	9.62	5.97

At pK_{a1} < pH < pK_{a2} (neutral media), the zwitterion form of the amino acids predominates (Table 1), which is the least hydrophilic form because its net molecular charge is zero, and therefore under these conditions the lowest solubilities are detected for a particular solid form (Fig. 3). More exactly, the lowest solubility value for each system is found at the isoelectric point pI (Table 1) since it is the pH value of each system at which the zwitterion form reaches the highest concentration [23,24]. For the chiral compounds dissolved in water, the pH measured (Fig. 3) agree with the pI values found in literature [23,24]. We observe, both in water and in pH 7.00 buffer solution, similar solubility profiles in all the amino acids examined (Fig. 3).

At pH < pK_{a1} (acidic media) and pH > pK_{a2} (basic media), the cation and anion forms of the amino acids, respectively, are predominant (Table 1) which due to their ionic nature have a higher affinity with water which results in higher solubilities (Fig. 3). At lower pH, a large fraction of the solutes is present in the cationic form instead of the zwitterion.

However, the zwitterion concentration determines the solubility. Thus, at low pH, a large reservoir of cations must be filled before equilibrium between the solid and solution can be reached. As the reservoir is smaller around the pI and increases size away from it, the solubility increases with the distance of the pH from pI [25–27]. The same explanation for increasing solubilities applies at higher pH but for the anion form instead of the cation form.

Alanine and valine solubility in acidic media at pH = 2.1-2.6 present higher values than in basic media at pH = 9.8-10.2 (Fig. 3ac). Instead, phenylalanine shows the opposite behaviour: solubilities in the basic medium at pH = 10.1-10.3 are higher than in the acidic medium at pH = 0.9-1.2 (Fig. 3b), even when the pH in the acidic medium is lower for phenylalanine (0.9-1.2) than for alanine and valine (2.1-2.6). The reason for this experimental observation is directly linked to their chemical structure, especially in the different side chain R, which influences their thermodynamic acid-base dissociation constants and therefore their isoelectric point pI (Table 1). Alanine and valine present higher pK_a values, and thus pI, than phenylalanine. A lower pI means that the neutral species zwitterion, the least hydrophilic and then soluble, has a major presence at lower pH in the acid-base amino acid equilibria than in systems with higher pI (Table 1). The latter fact explains the difference observed in acidic and basic solubility curves, independently of the chiral form studied, racemic or enantiopure compound (Fig. 3). This behaviour agrees with previous works reported in literature [25–27], where different authors modelled pH-dependent solubilities and obtained U-type curves when representing amino acid solubilities versus pH at certain temperatures. Then, the pH values at which solubilities make the largest changes are around the amino acid pK_a values [25–27].

3.3.2. Estimation of ternary phase diagrams

Solubility ternary phase diagrams of alanine, phenylalanine, and valine aqueous systems at 25.0ºC are estimated with the protocol described above (see section 3.2.2.2.). We then collect the solubility data from the racemic and enantiopure forms of the amino

acids binary phase diagrams obtained through the TV and EqC methods, reported in the previous section (Fig. 3), and apply a solubility model fitting with van 't Hoff-type equations. The van 't Hoff-type equations of Schröder–Van Laar (1) and Prigogine–Defay (2) [5,28] have been used to describe the solid–liquid equilibria in binary systems at temperature T^f.

$$\ln x^* = \frac{\Delta H_A^f}{R}\left(\frac{1}{T_A^f} - \frac{1}{T^f}\right) \tag{1}$$

$$\ln 4x(1-x) = \frac{2\Delta H_R^f}{R}\left(\frac{1}{T_R^f} - \frac{1}{T^f}\right) \tag{2}$$

where x is the mole fraction of the more abundant enantiomer in a solvent-free mixture, R the gas constant [29], T_A^f and T_R^f are, respectively, the melting temperatures of the enantiomer and racemic compound, and ΔH_A^f and ΔH_R^f are the enthalpies of fusion of the enantiomer and racemic compound, respectively. The equation (1) describes the ideal behaviour in a binary solute-solution system, where x^* indicates the solute mole fraction in an enantiopure system; and the equation (2) describes the ideal behaviour in a binary D-L system. These equations can be adapted to describe the equilibrium of the solids with a solution, in which a third component, the solvent, is present [5,28,30–34]. Then, the adapted van 't Hoff-type equations are expressed as follows for the enantiopure (D- and L-forms) and racemic (DL-form) compounds (3)-(4) [5,28,30–34]:

$$\ln {x_L}^* = -\frac{\Delta H_{s,L}}{RT} + \frac{\Delta S_{s,L}}{R} \tag{3}$$

$$\ln 4(x_D x_L)^* = -\frac{2\Delta H_{s,DL}}{RT} + \frac{2\Delta S_{s,DL}}{R} \tag{4}$$

where ΔH_s and ΔS_s are, respectively, the enthalpy and entropy of the solution formation process [5,30,31]. The solubility of pure enantiomer D ${x_D}^*$ and L ${x_L}^*$ are the same [5], for simplicity Eq. (3) is just described for enantiomer L. These equations assume that enantiomer activity coefficients γ_D and γ_L are equal to 1 and thus the equations can be

simplified just using molar fraction solubilities x_D and x_L instead of the respective activities, since then $a_D = \gamma_D x_D = x_D$ and $a_L = \gamma_L x_L = x_L$. This ideality behaviour considers then the same intermolecular forces between solvent-solvent, solute-solute, and solvent-solute molecules. For non-ideal systems, as we use ΔH_s and ΔS_s in Eqs. (3)-(4) as fitting parameters, the activity coefficients (which in reality may be different from 1) can be considered as included in these terms [5,30,31]. Note that the effect of the amino acid dissociation in the solvent (amino acid speciation, see Table 1) would also be incorporated in ΔH_s and ΔS_s upon fitting.

Using the enantiopure and racemic compound solubilities we can estimate the full ternary phase diagrams of the amino acids in the aqueous system. First, we assume that the enantiomers do not influence each other's pure solubilities x_D^* and x_L^* in the pure component regions. This means that straight lines, perpendicular to each *x*-axis represent the pure component solubilities of D- and L-enantiomers (Figs. 4-6). We further assume that the solubility product $(x_D x_L)^*$ of the racemic compound is not a function of the relative amounts of enantiomer present: the solubility product is not a function of the D-L stoichiometry in the solution. Then, we can estimate the two eutectic points by the points of intersection of the solubility line of the racemate with that of the enantiopure compound D and L. This is the solution composition where it is valid that $x_L = x_L^*$ and $x_D x_L^* = (x_D x_L)^*$ for both enantiomers of each amino acid system. The same pure enantiomer solubility ($x_D^* = x_L^*$) accounts for the appearance of symmetry in the ternary (and other) phase diagrams of unsolvated chiral systems (Figs. 4-6) [5]. A difference between the two enantiomers and their properties only may show up when we put them in a chiral environment, not our case here [5].

The van 't Hoff model fitting data is presented below with the variation in solution enthalpy ΔH_s and entropy ΔS_s for each amino acid aqueous system studied here (Table 2).

Table 2. Thermodynamic data of the solution processes of alanine, phenylalanine, and valine in aqueous media at different pH obtained from the linear regression of a $\ln x$ vs. $1/T$ representation, with Eqs. (3)-(5). Variation of ΔH_s and ΔS_s is given as standard deviation due to the fitting in each parameter.

System (method)	Solvent (aqueous medium)	pH	ΔH_s [kJ/mol]	ΔS_s [J/(mol·K)]	σ
DL-alanine (TV)	1.0 M HCl	2.6	6.2±0.7	-4.4±0.9	0.041
	Water	6.1	12.2±0.6	11±4	0.035
	pH 7.00 buffer	6.7	11.6±0.2	10±2	0.011
	1.0 M NaOH	9.8	8.2±0.1	1.2±0.1	0.006
L-alanine (TV)	1.0 M HCl	2.6	5.5±0.6	-7±2	0.023
	Water	6.1	9.9±0.2	3.9±0.7	0.010
	pH 7.00 buffer	6.8	8.2±0.8	-1.4±0.4	0.045
	1.0 M NaOH	9.8	6.9±0.1	-3.1±0.4	0.008
DL-phenylalanine (EqC)	1.0 M HCl	0.9	8.0±0.2	-9.2±0.4	0.012
	Water	5.5	13.9±0.6	-7±1	0.048
	pH 7.00 buffer	7.0	15.1±0.5	-3.8±0.7	0.034
	1.0 M NaOH	10.3	4.0±0.4	-20±1	0.020
L-phenylalanine (EqC)	1.0 M HCl	1.2	9.4±0.7	-4±2	0.026
	Water	5.5	10.4±0.9	-13±3	0.035
	pH 7.00 buffer	7.0	13±1	-6±3	0.040
	1.0 M NaOH	10.1	3.3±0.3	-22±1	0.011
DL-valine (EqC)	1.0 M HCl	2.3	3.1±0.1	-16.2±0.2	0.004
	Water	6.0	7.2±0.2	-12.1±0.5	0.010
	pH 7.00 buffer	6.9	6.7±0.7	-14±2	0.049
	1.0 M NaOH	10.0	4.4±0.3	-15.7±0.6	0.017
L-valine (EqC)	1.0 M HCl	2.1	2.4±0.3	-19.8±0.9	0.010
	Water	6.0	4.7±0.2	-23.3±0.6	0.006
	pH 7.00 buffer	7.0	4.5±0.3	-24±1	0.008
	1.0 M NaOH	10.2	3.2±0.1	-20.9±0.4	0.005

The significance of the data in this fitting procedure is provided by the standard deviation σ for each system (Table 2), which we define in (5) by using the difference x_i-x_i^m between the measured and modelled solubility relative to the experimental solubility x_i:

$$\sigma = \sqrt{\frac{1}{(N-1)}\sum_{i=1}^{N}\left(\frac{x_i - x_i^m}{x_i}\right)^2} \quad (5)$$

where *N* represents the number of observations per system. The standard deviation σ in (5) expresses the average deviation as a fraction of the experimental solubility. A standard deviation of 1% thus shows that, on average 66% (one standard deviation) of the fitted solubilities lie within 1% of the experimental solubility. Here we consider a standard deviation σ below 5% for 9 solubility measurements to be reasonable (Table 2).

At this point, we have enough data to estimate the ternary phase diagrams. For instance, the ternary phase diagram of alanine in water at 25.0ºC is estimated below (Fig. 4). We now can validate this by means of extra TV measurements in order to assess the liquidus line. We do this by measuring solubility points at different enantiomeric ratio y_L at 25.0ºC (see section 3.2.2.2.). We then find that the further TV refinement provides liquidus values very similar to our previous estimation from van 't Hoff-type model equations (3)-(4) (Fig. 4, black diamond dots). These little differences explain the small deviation from the ideal behaviour found in the thermodynamic data for the amino acids presented above (Table 2), with $\Delta S_s < 0$, in accordance with literature [25,26,30,35–37].

In one of the TV measurements, we obtained a single crystal of alanine in the region of enantiopure L-form of the size of 2-10 mm which allowed to perform SC-XRD. The crystal structures obtained via SC-XRD (formula: $C_3H_7NO_2$, formula weight: 89.10 g·mol^{-1}, wavelength: 1.54178 Å, T = 293 K, crystal system: orthorhombic, space group: $P2_12_12_1$, number of molecules in the unit cell: 4, a = 5.7861(2) Å, b = 6.0413(2) Å, c = 12.3544(2) Å, $\alpha = \beta = \gamma$ = 90º, volume: 431.85(2) Å^3, density: 1.370 g·cm^{-3}, number of observed and independent reflections: 836 and 842, number of parameters: 83, F000 = 192, R_1 = 0.0224, wR_2 = 0.0593, *GoF* = 1.088, largest difference peak and hole: 0.153 and -0.143 e Å^{-3}) are consistent with reported L-alanine structure (Fig. 4) [38–40]. The stereochemistry is confirmed via reliable Flack parameter determination using anomalous dispersion statistics.

In addition, we observe that the estimated position of the eutectic point (y_L = 0.815, Fig. 4) is very similar to the one reported in the literature (y_L = 0.802) from a validated but more time-consuming gravimetric method, at 25.0ºC [12,13].

With all these data, we then validate the initial estimation of the ternary phase diagram of alanine (Fig. 4), ergo the whole workflow process itself, and confirm a racemic compound-forming system crystallisation behaviour. However, the time required to carry out all these measurements and verifications is still long, and similar information can be obtained faster by applying a different strategy (see sections 3.3.3. and 3.4.).

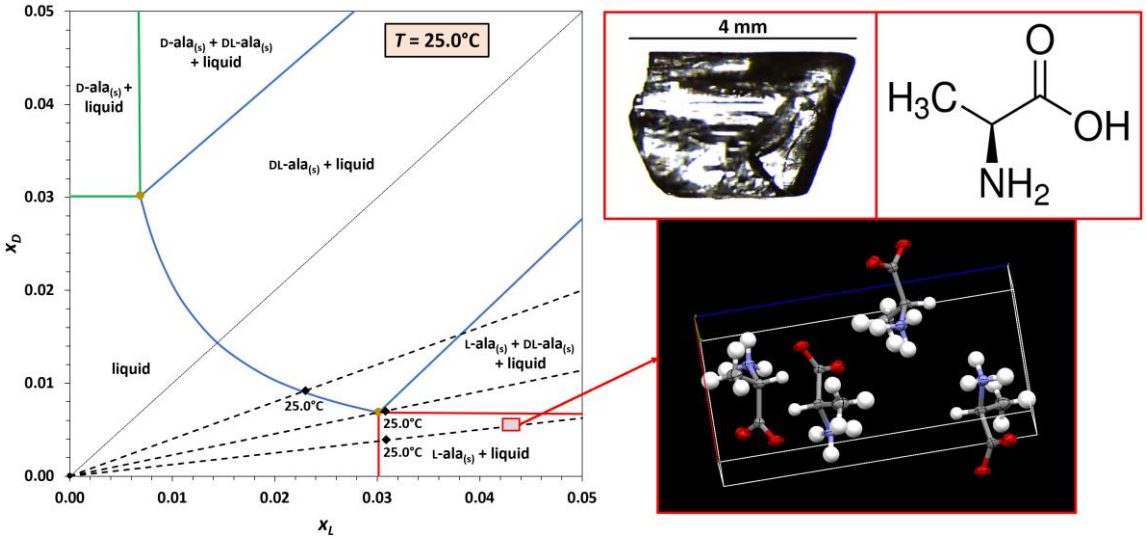

Fig. 4. Left: ternary phase diagram of alanine in water, at 25.0ºC. Filled lines delimit the ternary phase diagram chiral species regions: D-alanine (green), DL-alanine (blue), L-alanine (red). There are two regions where racemate and enantiopure alanine are present (green-blue and blue-red). Black dotted line represents $x_D = x_L$. Black dashed lines at enantiomeric ratios y_L of 0.714, 0.815, and 0.889 that show the extra TV measurements. Black diamond dots on these lines are the liquidus points with a saturation temperature of 25.0ºC found by the extra TV measurements. Brown dots on intersections represent the eutectic points. Right: L-alanine crystal with its molecular structure and SC-XRD lattice, obtained from conditions in the red-grey squared area (left).

3.3.2.1. Effect of temperature in solubility ternary phase diagrams

The procedure described above permits the estimation of the solubility ternary phase diagrams for alanine, phenylalanine, and valine and study the effect of temperature on them (Fig. 5).

We observe the common pattern of increasing solubilities (liquidus) when increasing temperature for the three amino acids in water. Solubilities increase from 1.0 to 80.0ºC (Fig. 5). This phenomenon can be understood by looking back to the solubility curves (Fig. 3) and van ’t Hoff-type model equations (3)-(4), which clearly explains the positive temperature dependence observed in solubility.

When looking to the liquidus (Fig. 5), we also observe that alanine presents the highest solubility, then valine, and phenylalanine has the lowest one. This agrees with the trend observed in the solubility curves (Fig. 3). We can also observe that the temperature dependence of the amino acid solubilities is stronger for alanine, then phenylalanine, and finally valine since the mole fraction steps (x_D or x_L) are larger for alanine when temperature increases and lower for phenylalanine and valine systems (Fig. 5).

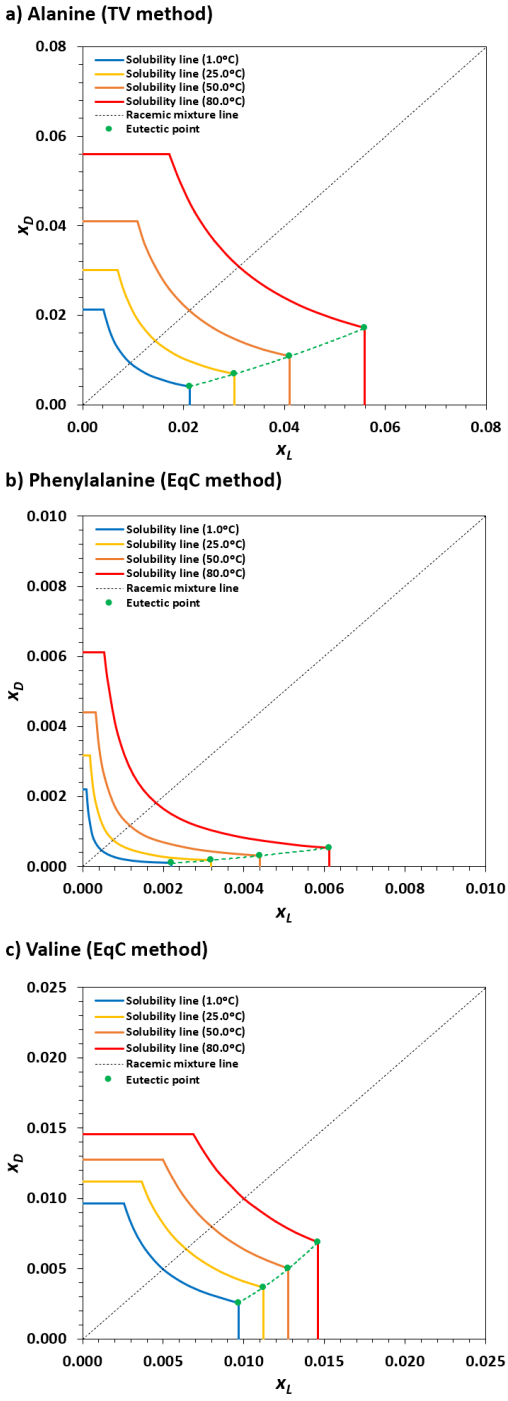

Fig. 5. Effect of temperature on solubility lines (or liquidus) of ternary phase diagrams of amino acid systems: a) alanine, b) phenylalanine, and c) valine in water. The temperatures represented are: 1.0ºC (blue), 25.0ºC (yellow), 50.0ºC (orange), and 80.0ºC (red). Eutectic points on the L-form side of the diagram are indicated with green dots (green dashed trendline obtained from Eq. (9)). Black dashed line indicates racemic mixture composition. For simplicity the phase domains are not indicated.

The eutectic points estimated from solubility ternary phase diagrams of alanine, phenylalanine, and valine in water at different temperatures are shown below (Table 3). Eutectic points enantiomeric ratios $y_{L,eu}$ are given in terms of solvent-excluded L-enantiomer ratio y_L, which can be defined as follows (6):

$$y_L = \frac{n_L}{n_D + n_L} = \frac{x_L}{x_D + x_L} = \frac{x_L}{x_t} \tag{6}$$

where n_D and n_L accounts for mole of D- and L-enantiomers, respectively, x_D and x_L for mole fraction of D- and L-enantiomers, respectively, and x_t for total amount of enantiomer [2]. Both D- and L-forms eutectic compositions can be given with y_L. The sum of both y_L for D-form and y_L for L-form is 1 due to the same solubility behaviour assumption for both enantiomers in the presence of an achiral environment (water). For simplicity, only y_L for L-form is showed below (Table 3). Then, we can confirm the racemic compound-forming system behaviour for alanine, phenylalanine, and valine in aqueous media for the fact of detecting two eutectic points in their (solubility) ternary phase diagrams, as described in literature [12,13].

Table 3. Solvent-excluded enantiomeric ratios of eutectic points $y_{L,eu}$ for L-form estimated from solubility ternary phase diagrams of alanine, phenylalanine, and valine in water at different temperatures (Fig. 5). $y_{L,eu}$ error ≤ ±0.009.

System	Method	pH	T_s [ºC]	$y_{L,eu}$ (L-form)
Alanine	TV	6.1	1.0	0.838
			25.0	0.815
			50.0	0.791
			80.0	0.766
Phenylalanine	EqC	5.5	1.0	0.957
			25.0	0.946
			50.0	0.934
			80.0	0.919
Valine	EqC	6.0	1.0	0.790
			25.0	0.754
			50.0	0.719
			80.0	0.680

From Table 3, we observe that both methods, TV and EqC methods, give good estimations of eutectic compositions $y_{L,eu}$ for the amino acids in water systems at 25.0ºC when comparing with values found in the literature (lit.) under the same conditions: alanine (TV method: 0.815 *vs.* lit.: 0.802), phenylalanine (EqC method: 0.946 *vs.* lit.: 0.916), and valine (EqC method: 0.754 *vs.* lit.: 0.734) [12,13]. We also detect that eutectic point compositions $y_{L,eu}$ (L-form) decrease when temperature increases for the three amino acids studied (Fig. 5, Table 3). This change in the eutectic point composition with temperature can be explained when we observe the dependence of mole fraction solubilities of racemic and enantiopure compounds with temperature in Eqs. (3)-(4). The composition, in terms of enantiomeric ratio y_L, at the eutectic point (L-form) is the same for the racemic and enantiopure compounds (DL- and L-forms, respectively) at certain temperature *T*. Then, assuming this condition to solve the equations system composed by Eqs. (3)-(4), we obtain $x_{L,eu}$ (7) and $x_{D,eu}$ (8):

$$x_{L,eu} = \mathrm{e}^{-\frac{\Delta H_{S,L}}{RT}+\frac{\Delta S_{S,L}}{R}} \tag{7}$$

$$x_{D,eu} = \frac{\mathrm{e}^{-\frac{2\Delta H_{S,DL}}{RT}+\frac{2\Delta S_{S,DL}}{R}}}{4x_{L,eu}} = \mathrm{e}^{-\frac{2\Delta H_{S,DL}-\Delta H_{S,L}}{RT}+\frac{2\Delta S_{S,DL}-\Delta S_{S,L}}{R}-\ln 4} \tag{8}$$

Therefore, we find the following temperature-dependent expression for the eutectic composition enantiomeric ratio $y_{L,eu}$ (9):

$$y_{L,eu} = \frac{x_{L,eu}}{x_{D,eu}+x_{L,eu}} = \frac{\mathrm{e}^{-\frac{\Delta H_{S,L}}{RT}+\frac{\Delta S_{S,L}}{R}}}{\mathrm{e}^{-\frac{2\Delta H_{S,DL}-\Delta H_{S,L}}{RT}+\frac{2\Delta S_{S,DL}-\Delta S_{S,L}}{R}-\ln 4}+\mathrm{e}^{-\frac{\Delta H_{S,L}}{RT}+\frac{\Delta S_{S,L}}{R}}} \tag{9}$$

The relationship derived in (9) for $y_{L,eu}$ with *T* is better appreciated when represented graphically (Fig. 5, green dashed lines; Fig. 6, lines). Then, we observe clearly how $y_{L,eu}$ decreases when temperature increases, as observed in Table 3 (Fig. 5, green dots; Fig. 6, dots).

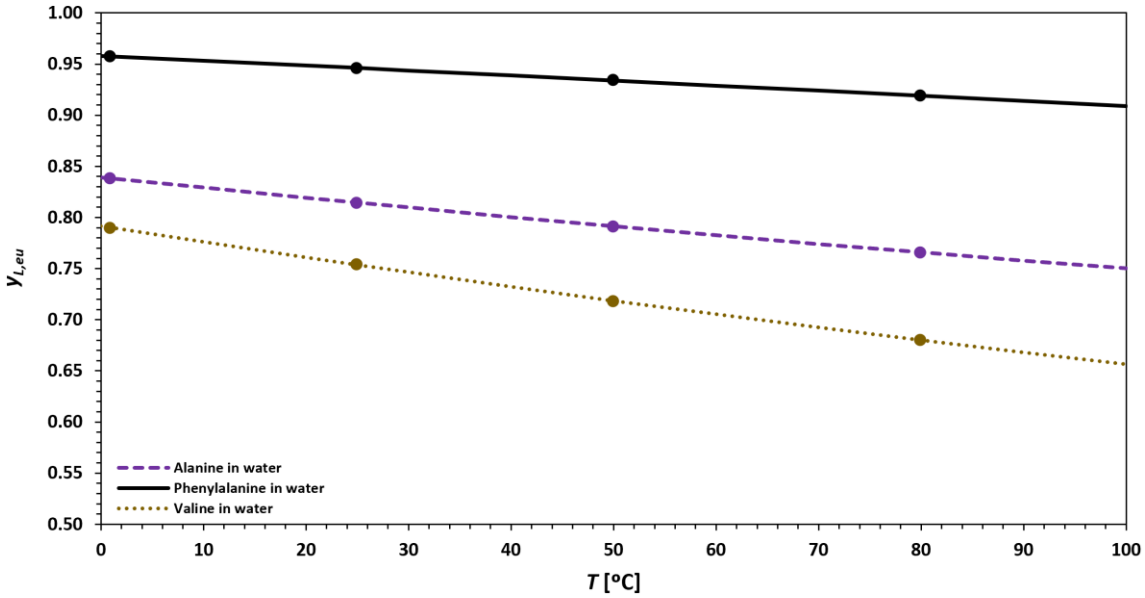

Fig. 6. Temperature dependence of the solvent-excluded enantiomeric ratios of eutectic points $y_{L,eu}$ on the L-form side of the ternary phase diagrams for alanine, phenylalanine, and valine systems in water. Lines obtained from Eq. (9). Filled dots are the $y_{L,eu}$ values obtained at 1, 25, 50, and 80ºC; which are the same as the ones obtained above (Fig. 5, green dots; Table 3).

3.3.2.2. Effect of pH in solubility ternary phase diagrams

The pH has the same effect on liquidus lines of solubility ternary phase diagrams as that observed already in the solubility curves above (Fig. 3, see section 3.3.1.). Low and high pH values related to acidic and basic media, respectively, give higher solubility and therefore also higher mole fraction solubilities x_D and x_L (Fig. 7). Instead, medium pH values, related to neutral media, give the lowest mole fraction solubilities x_D and x_L (Fig. 7). This is due to the ionizable behaviour of the amino acid systems explained above (Table 1, see section 3.3.1.). The pH effect is observed to have major impact on phenylalanine, then valine, and alanine presents the lowest pH dependence (Fig. 7). This behaviour agrees with what we observed in the solubility curves (Fig. 3).

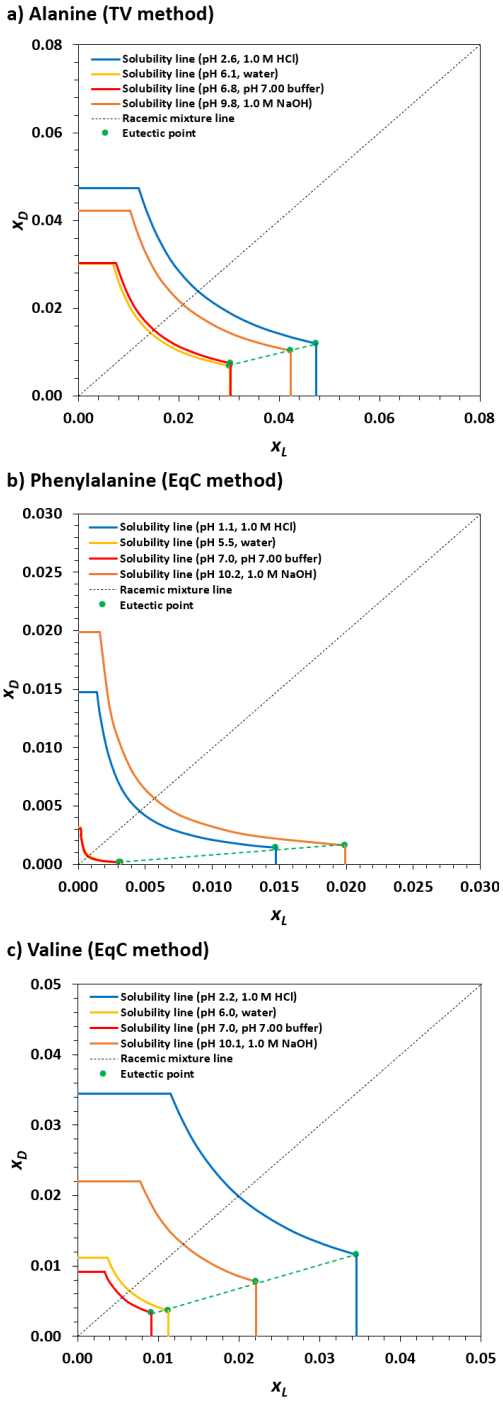

Fig. 7. Effect of pH on solubility lines (or liquidus) of ternary phase diagrams of amino acid systems: a) alanine, b) phenylalanine, and c) valine in aqueous media, at 25.0ºC. The pH media are: 1.0 M HCl (blue), water (yellow), pH 7.00 buffer (red), and 1.0 M NaOH (orange). Eutectic points on the L-form side of the diagram are indicated with green dots (green dashed trendline is only a guide to the eyes). Black dashed line indicates racemic mixture composition. For simplicity the phase domains are not indicated.

The eutectic points compositions $y_{L,eu}$ estimated from solubility ternary phase diagrams of alanine, phenylalanine, and valine in aqueous media at different pH are shown below (Table 4). We observe again a racemic compound-forming behaviour in all amino acid systems at different pH since we detect two eutectic points (Fig. 7, Table 4). Here, we do not observe an appreciable effect of pH on the eutectic point compositions y_L of the amino acids aqueous systems (Fig. 7, Table 4). Eutectic point compositions $y_{L,eu}$ are expected constant since there is no direct dependence of mole fraction solubilities of racemates and enantiopure compounds with proton concentration, as observed in Eqs. (3)-(4) and (9) and in the literature [41]. However, we relate the little trendless differences observed in $y_{L,eu}$ (Table 4) to experimental error (Table 4) and/or neglection of the chemical components in the buffer solutions used.

Table 4. Solvent-excluded enantiomeric ratios of eutectic points $y_{L,eu}$ for L-form estimated from solubility ternary phase diagrams of alanine, phenylalanine, and valine at different pH values and 25.0ºC (Fig. 7). $y_{L,eu}$ error $\leq \pm 0.009$.

System	Method	Solvent (aqueous medium)	pH	$y_{L,eu}$ (L-form)
Alanine	TV	1.0 M HCl	2.6	0.798
		Water	6.1	0.815
		pH 7.00 buffer	6.8	0.803
		1.0 M NaOH	9.8	0.804
Phenylalanine	EqC	1.0 M HCl	1.1	0.912
		Water	5.5	0.946
		pH 7.00 buffer	7.0	0.948
		1.0 M NaOH	10.2	0.925
Valine	EqC	1.0 M HCl	2.2	0.750
		Water	6.0	0.754
		pH 7.00 buffer	7.0	0.733
		1.0 M NaOH	10.1	0.741

3.3.3. Determination of pseudo-binary phase diagrams as a fast tool to accurately estimate eutectic points

The accurate determination of eutectic points of racemic compound-forming systems is key to develop chiral resolution techniques based on crystallisation, as described in the introduction (see section 3.1.). So, here we present two similar methods based on the determination of pseudo-binary phase diagrams of this type of chiral compounds: TV and EqC-HPLC methods. The former one results faster than the latter one mainly due to the avoidance of long waiting times for equilibration, gravimetric measurements, and enantiomeric ratios y_L post-analyses. The TV method was already used for a fast phase diagram screening of chiral compounds [2]. Here, we assess the equivalence between both TV and EqC-HPLC methods, the pH dependence of pseudo-binary phase diagrams obtained from them, and the level of accuracy that these methods provide to estimate the eutectic point compositions $y_{L,eu}$ compared to results obtained from conventional determination of ternary phase diagrams and data reported in the literature.

3.3.3.1. Equivalence of saturation temperature and concentration measurements in pseudo-binary phase diagrams: a pH-dependent study

Pseudo-binary phase diagrams are presented in two different types, depending on which method is used (Fig. 8, Table 5). Saturation temperatures T_s are measured versus enantiomeric ratios y_L when light detection of crystallisation processes is feasible (see section 3.2.2.3.1.). This is the case of TV method used for alanine aqueous systems (Fig. 8a). Instead, when light detection is not suitable, we use a gravimetric approach by means of EqC-HPLC method to register the saturation concentrations C_s at different enantiomeric ratios y_L (see section 3.2.2.3.2.). This second case is required for phenylalanine and valine aqueous systems (Fig. 8bc).

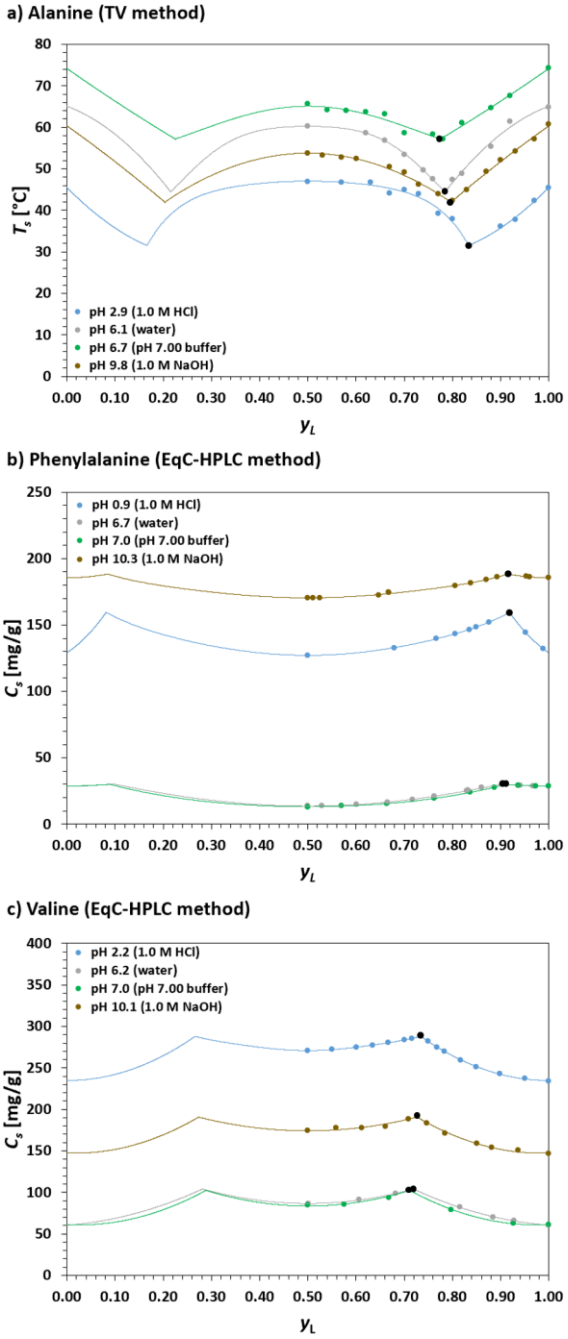

Fig. 8. Pseudo-binary phase diagrams with saturation curves of a) alanine (TV method), b) phenylalanine (EqC-HPLC method), and c) valine (EqC-HPLC method) at different pH. In alanine (a), different concentrations are represented due to experimental requirement, saturation lines with pH 6.1 (grey) and 6.7 (green) are of 250 mg/g, whereas saturation lines with pH 2.9 (blue) and 9.8 (brown) are of 300 mg/g. Data represented in phenylalanine (b) and valine (c) were registered at 25.0ºC. Black dots are the estimations of the eutectic points (see Table 5). Lines are a guide to the eyes.

We can observe the relationship of equivalence between saturation temperature T_s and concentration C_s measurements since an inverse proportionality exists between both saturation variables (Fig. 8), in accordance with previous results (Fig. 3). So, a saturation temperature T_s decrease is directly related to an increase in its saturation concentration C_s (Fig. 8). This relationship makes the measurement of one or other saturation variable equivalent for the detection and estimation of the eutectic point compositions, in terms of the enantiomeric ratio y_L. Then, the saturation temperature T_s curve adopts a W-form (TV method, Fig. 8a), whereas saturation concentration C_s curves adopt a M-form or inverted W-form (EqC-HPLC method, Fig. 8bc). The estimation of the eutectic points is carried out by extrapolating the curves from racemic and enantiopure compositions until a scalemic composition where T_s (for alanine) or C_s (for phenylalanine and valine) meet for both curves (intersection) (Fig. 8, black dots). Experimental points on the left of each eutectic point estimated in each curve in Fig. 8 are considered to belong to the racemic compound region. Instead, those points on the right of each eutectic point are assumed to belong to the enantiopure region (Fig. 8).

Pseudo-binary phase diagrams show that alanine and valine racemic forms are more soluble than their enantiopure forms, instead, phenylalanine chiral forms show the opposite behaviour (Fig. 8). This agrees with the solubility curves presented above (Fig. 3).

We observe that acidic and basic aqueous media account for the lowest saturation temperatures T_s and therefore for the highest saturation concentrations C_s, whereas neutral pH curves show the contrary effect (Fig. 8). This is related to the acid-base dissociation equilibria of the amino acids (Table 1) explained above (see section 3.3.1.) and the effect of pH over solubility curves (see section 3.3.2.2.). We observe that the pH effect even dominates a concentration effect on the saturation temperature T_s of alanine aqueous systems. There, the acidic and basic curves required a higher concentration of amino acid (300 mg/g) to be determined compared to neutral curves (250 mg/g), however the acidic and basic curves give lower saturation temperatures T_s than the neutral curves (Fig. 8a).

The higher solubility observed for phenylalanine system in the basic medium, compared to the acidic medium, which is different than the behaviour observed for alanine and valine can be related to the chemical structure of phenylalanine and its lower pI (Table 1).

Table 5. Solvent-excluded enantiomeric ratios of eutectic points $y_{L,eu}$ estimated from pseudo-binary phase diagrams of alanine, phenylalanine, and valine at different pH (Fig. 8). Due to the different methods used, C_s is constant for each pH in Ala and T_s is constant for each pH in Phe and Val. $y_{L,eu}$ error $\leq \pm 0.009$.

System (method)	Solvent (aqueous medium)	pH	C_s at eutectic [mg/g]	T_s at eutectic [°C]	$y_{L,eu}$ (L-form)
Alanine (TV)	1.0 M HCl	2.9	300.0	31.4	0.833
	Water	6.1	250.0	44.4	0.784
	pH 7.00 buffer	6.7	250.0	57.1	0.774
	1.0 M NaOH	9.8	300.0	41.8	0.795
Phenylalanine (EqC-HPLC)	1.0 M HCl	0.9	159.4	25.0	0.919
	Water	6.7	30.3	25.0	0.906
	pH 7.00 buffer	7.0	30.1	25.0	0.911
	1.0 M NaOH	10.3	188.3	25.0	0.915
Valine (EqC-HPLC)	1.0 M HCl	2.2	288.3	25.0	0.734
	Water	6.2	103.9	25.0	0.719
	pH 7.00 buffer	7.0	103.1	25.0	0.711
	1.0 M NaOH	10.1	192.2	25.0	0.727

The eutectic point compositions $y_{L,eu}$ of the amino acid systems are not affected by a change in pH (Table 5), in agreement with the observations in the ternary phase diagrams (see section 3.3.2.2.). So, their values are kept almost constant in the different media tested, especially for phenylalanine and valine systems. We also observe that both methods, TV and EqC-HPLC methods, give good estimations of eutectic compositions $y_{L,eu}$ for the amino acids in water systems when comparing with values found in the literature under the same conditions: alanine (TV method: 0.784 *vs.* lit.: 0.802), phenylalanine (EqC-HPLC method: 0.906 *vs.* lit.: 0.916), and valine (EqC-HPLC method: 0.719 *vs.* lit.: 0.734) [12,13]. For alanine at the eutectic, we appreciate a temperature effect on $y_{L,eu}$, it decreases when saturation temperatures T_s increases (Table 5). This behaviour agrees with observations in the ternary phase diagrams (see section 3.3.2.1.).

3.3.3.2. Comparative accuracy study of eutectic point values obtained via pseudo-binary and ternary phase diagrams

At this point, we have obtained eutectic point compositions, in terms of y_L, for alanine, phenylalanine, and valine in different aqueous media by means of three different ways. These ways include the estimated values from ternary phase diagrams (TPD, Tables 3-4) and pseudo-binary phase diagrams (PBPD, Table 5) and literature values [12,13].

We now can examine how good these estimations of the eutectic compositions $y_{L,eu}$ are by means of an accuracy study. The accuracy *A* of a measurement system is the degree of closeness of measurements of a quantity to that quantity's true value, so indicating the proximity of measurement of the true value [42]. For the calculation of the accuracy of the eutectic compositions in terms of enantiomeric ratios y_L, we then define accuracy *A* in a general formulation as follows (10):

$$A = \left(1 - \frac{|z_m - z_r|}{z_r}\right) \cdot 100 \tag{10}$$

where measurement z_m and reference z_r account for the eutectic composition enantiomeric ratio $y_{L,eu}$ measured or estimated and true values, respectively.

Then, we can adapt the general formula of accuracy *A* (10) to the three cases we want to examine here, which are the comparison of the eutectic enantiomeric ratios $y_{L,eu}$ values of PBPD *vs.* TPD (11), TPD *vs.* lit. (12), and PBPD *vs.* lit. (13), as defined below:

$$A_{PBPD-TPD} = \left(1 - \frac{\left|y_{L,eu}(\text{TPD}) - y_{L,eu}(\text{PBPD})\right|}{y_{L,eu}(\text{PBPD})}\right) \cdot 100 \tag{11}$$

$$A_{TPD-lit.} = \left(1 - \frac{\left|y_{L,eu}(\text{TPD}) - y_{L,eu}(\text{lit.})\right|}{y_{L,eu}(\text{lit.})}\right) \cdot 100 \tag{12}$$

$$A_{PBPD-lit.} = \left(1 - \frac{\left|y_{L,eu}(\text{PBPD}) - y_{L,eu}(\text{lit.})\right|}{y_{L,eu}(\text{lit.})}\right) \cdot 100 \tag{13}$$

The choice of $y_{L,eu}$(PBPD) value as reference in (11) accounts for the assumption that our PBPD estimated data is more directly reliable than our TPD estimated data. For Eqs. (12)-(13), the reference value is the one found in the literature for a particular system, then it is reported as an accepted determination, not an estimation [12,13]. Thus, it is the best reference value possible.

We observe a good agreement between the eutectic enantiomeric ratios yl,eu (l-form) values estimated via ternary (Figs. 5-7, Tables 3-4) and pseudo-binary phase diagrams (Fig. 8, Table 5), with an accuracy ≥95.1% for the three amino acid aqueous systems tested at different pH levels (Table 6). Those values which can be compared to the ones reported in the literature also show a high level of accuracy, here between 96.7-98.9%, independently of the type of phase diagram used (Table 6). We can also confirm that our initial assumption to take the PBPD data as more accurate than the TPD data is valid since we found that the $A_{PBPD\text{-}lit.}$ is higher than the $A_{TPD\text{-}lit.}$ for phenylalanine and valine, and for alanine these two *A* are approximately equal (Table 6). Thus, here we confirm the validity of our predictions on the eutectic points compositions that we estimated in the previous sections 3.3.2. and 3.3.3.1., which are valid with a high accuracy level (Table 6). Besides, we observe that $y_{L,eu}$(TPD) values are always slightly above the reference literature value, whereas $y_{L,eu}$(PBPD) values are always slightly below of it (Table 6). We note that the eutectic enantiomeric ratios $y_{L,eu}$ from the PBPD were easier and faster to obtain than those from the TPD (see section 3.2.2.).

We do not see a significant difference in variation in the quality of the result when using TV or EqC methods (Table 6). However, results from TV method are faster to obtain than those from EqC method, which is the most convenient and has application to a major diversity of systems (see section 3.2.2.).

Therefore, we validate the capacity of pseudo-binary phase diagrams to provide reliable eutectic compositions for racemic compound-forming systems, in terms of enantiomeric ratios y_L, in a fast and accurate manner (Table 6).

Table 6. Comparative accuracy *A* study of eutectic points compositions values $y_{L,eu}$ obtained via pseudo-binary and ternary phase diagrams (Figs. 5-8, Tables 3-5) *vs.* values reported in the literature [12,13]. All data at 25.0ºC, except $y_{L,eu}$(PBPD) for alanine (see Table 5). Phe and Val systems employed simple EqC method for TPD and EqC-HPLC method for PBPD.

System (method)	Solvent (aq. medium)	$y_{L,eu}$ (TPD)	$y_{L,eu}$ (PBPD)	$y_{L,eu}$ (lit.)	$A_{TPD\text{-}PBPD}$ [%]	$A_{TPD\text{-}lit.}$ [%]	$A_{PBPD\text{-}lit.}$ [%]
Alanine (TV)	1.0 M HCl	0.798	0.833	-	95.8	-	-
	Water	0.815	0.784	0.802	96.0	98.4	97.8
	pH 7.00 buffer	0.803	0.774	-	96.3	-	-
	1.0 M NaOH	0.804	0.795	-	98.9	-	-
Phenylalanine (EqC)	1.0 M HCl	0.912	0.919	-	99.2	-	-
	Water	0.946	0.906	0.916	95.6	96.7	98.9
	pH 7.00 buffer	0.948	0.911	-	95.9	-	-
	1.0 M NaOH	0.925	0.915	-	98.9	-	-
Valine (EqC)	1.0 M HCl	0.750	0.734	-	97.8	-	-
	Water	0.754	0.719	0.734	95.1	97.3	98.0
	pH 7.00 buffer	0.733	0.711	-	96.9	-	-
	1.0 M NaOH	0.741	0.727	-	98.1	-	-

3.3.4. Determination of accurate ternary phase diagrams

The solubility data obtained for the phenylalanine and valine systems by means of the pseudo-binary phase diagrams (Fig. 9, diamonds and solid lines) enable a more accurate determination of the ternary phase diagrams than our initial estimations by the van 't Hoff data obtained from Eqs. (3)-(4) (Fig. 9, dashed solubility lines). The most accurate PBPD data show a small difference when compared with the estimated TPD solubility lines (Fig. 9). The latter indicates that, at least for phenylalanine and valine at different pH aqueous media (Fig. 9), the enantiomers do have certain influence to each other's pure solubilities in the pure component regions and that the solubility product of the racemic compound depends in certain measure on the relative amounts of enantiomer present (see section 3.3.2.). The latter shows the effect of the D-L stoichiometry in the solution, which we assumed absent in our estimated ternary phase diagrams with the van 't Hoff data (Fig. 9). However, this small discrepancy observed between the actual and estimated phase diagrams (Fig. 9, PBPD data *vs.* TPD van 't Hoff data, respectively) does not affect the

conclusions derived earlier in section 3.3.2. Additionally, this same small deviation was observed when assessing and validating, with the extra TV measurements, the ternary phase diagram of alanine in water at 25.0ºC, initially estimated from the van 't Hoff data (Fig. 4). These similarities found among the three amino acids alanine, phenylalanine, and valine confirms their similar crystallisation behaviour in aqueous media.

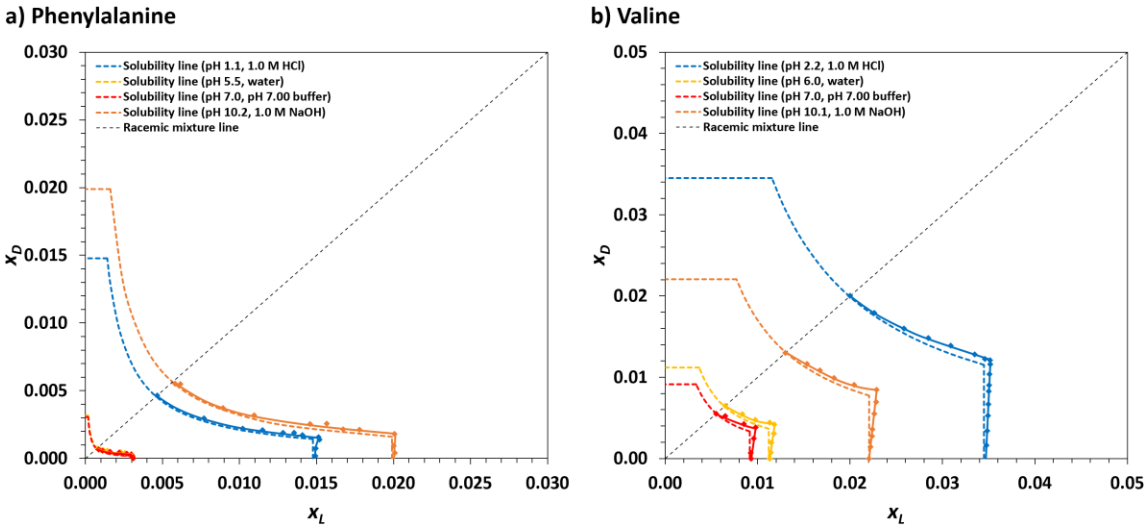

Fig. 9. Solubility lines (or liquidus) of ternary phase diagrams of amino acid systems: a) phenylalanine and b) valine in aqueous media, at 25.0ºC. The pH media are: 1.0 M HCl (blue), water (yellow), pH 7.00 buffer (red), and 1.0 M NaOH (orange). Blue, yellow, red, and orange dashed lines represent the estimations of the solubility lines obtained from the van 't Hoff TPD data (see Fig. 7bc). Coloured diamonds correspond to the most accurate solubilities determined with the PBPD on the L-form side (see Fig. 8bc). Blue, yellow, red, and orange solid lines represent the most accurate solubility lines obtained from the PBPD data on the L-form side as a guide to the eye. Black dashed line indicates racemic mixture composition. For simplicity the phase domains are not indicated.

3.4. Discussion

The determination of solubility C_s of the three amino acids alanine, phenylalanine, and valine in aqueous media required the use of both TV and EqC methods. Alanine was suitable to be analysed through the faster TV method. Instead, phenylalanine and valine needed the slower EqC method since their crystallisation processes present fouling-related

phenomena, making not proper then the assessment of their solubilities by means of a light beam.

All three amino acids aqueous systems show a temperature dependence in solubility C_s with the strongest behaviour in alanine (Fig. 3). For the same aqueous medium at certain temperature, alanine presents the highest solubility, then valine, and the lowest for phenylalanine (Fig. 3). This has sense from the point of view of the chemical structure since the same order is followed in terms of chemical structure polarity, from highest to lowest (Table 1) [23,24], assuming similar crystal phase effects in solubility among the three amino acids. Despite amino acids bear the same characteristic functional groups around the alpha carbon, what makes them different is the side chain. In this case, these species have hydrophobic side chains so that the amino acid which has the smallest hydrophobic side chain is the most polar (alanine) and the one with the largest side chain has the lowest polarity (phenylalanine) (Table 1) [23,24]. However, there is a distinction in solubility C_s depending if the amino acid is in their racemate or enantiopure form. The racemic compound of alanine and valine show higher solubilities than the enantiopure compound (L-form), under the same conditions tested. Instead, racemic phenylalanine shows lower solubility than its enantiopure form (Fig. 3). This difference in solubilities that depends on the chiral form of the specie is related to the differences inside their internal crystal lattice [5].

The pH affects the solubility of the amino acids due to their chemical structure with two proton-dissociable functional groups, independently of the chiral form considered. They show higher solubilities in acidic and basic media than neutral media (Fig. 3). This is related to the different proportion of distinct ionic forms at different pH (Table 1). Zwitterion form (medium pH) is the least soluble and cation (low pH) and anion (high pH) forms are the most soluble. This is also in accordance with the polarity rule explained above, but here charged ionic forms are more polar than the electroneutral species so that ionic forms present higher affinity for the polar solvent water (Table 1) [23,24].

The van 't Hoff-type model fitting permit us to estimate reliable ternary phase diagrams, as proved with the validation of alanine in water system (Fig. 4). This estimation procedure for ternary phase diagrams enables to study the effect of temperature and pH on solubility (liquidus) and eutectic point compositions $y_{L,eu}$ (Figs. 5-7, Tables 3-4). Regarding the temperature effect, we observe solubilities increasing when temperature goes up (Fig. 5). The temperature solubility dependence can be explained by means of the van 't Hoff-type model equations (3)-(4) [5,30,31]. Looking at the liquidus lines, we observe that alanine presents the highest solubility, then valine, and phenylalanine has the lowest; in agreement with previous observations (Fig. 3, Table 2). The finding of two eutectic points in the solubility ternary phase diagrams for each system validates their racemic compound-forming system behaviour [12,13]. Eutectic point enantiomeric ratios $y_{L,eu}$ are found to decrease with temperature (Fig. 5, Table 3). The temperature-dependent expression for the eutectic composition enantiomeric ratio $y_{L,eu}$ (9) explains this change (Fig. 6). Regarding the pH effect, we observe the same trend in liquidus lines (Fig. 7) than that observed with solubility curves (Fig. 3). That is to say, acidic and basic amino acid aqueous systems present higher solubilities than neutral systems, which is associated to the acid-base dissociation nature of amino acids (Table 1) [23,24]. The eutectic point compositions $y_{L,eu}$ are not affected by changing the pH of the media (Fig. 7) in accordance with the lack of proton concentration dependence in equations (3)-(4) and (9). The little differences are associated to experimental error and/or neglection of the chemical components in the buffer solutions used.

We propose the use of pseudo-binary phase diagrams as a fast methodology to accurately estimate the eutectic points of racemic compound-forming systems. For that, we take a previous reported work based on TV method to fast screen pseudo-binary phase diagrams to identify the class of chiral compound (racemic compound, conglomerate or solid solution) [2]. We further investigate the potential of this methodology introducing the equivalence in pseudo-binary phase diagrams obtained via TV and EqC-HPLC methods based on the inverse relationship between saturation temperature T_s and concentration C_s. Then, the saturation temperature T_s curve adopts a W-form (TV method,

Fig. 8a), whereas saturation concentration C_s curves adopt a M-form or inverted W-form (EqC-HPLC method, Fig. 8bc). Although the curves look different, they provide equivalent data and enable us to estimate the eutectic point compositions $y_{L,eu}$ of any racemic compound-forming system. We can use the faster TV method when light detection is possible (alanine) or EqC-HPLC method when it is not (phenylalanine and valine) (Fig. 8). The solubility results obtained with both types of pseudo-binary phase diagrams (Fig. 8, Table 5) agree with previous ternary phase diagrams observations (Figs. 5-7, Tables 3-4). The accuracy study proves the agreement between the eutectic enantiomeric ratios $y_{L,eu}$ (L-form) values estimated via pseudo-binary and ternary phase diagrams, with an accuracy higher or equal than 95.1% for the three amino acid aqueous systems tested at different pH levels (Table 6). Those values which can be compared to ones reported in the literature [12,13] show also a high level of accuracy, here between 96.7-98.9%, independently of the type of phase diagram used (Table 6). We do not appreciate a significant variation in the quality of the results when using TV or EqC methods (Table 6).

Thus, we confirm the capacity of pseudo-binary phase diagrams to provide reliable estimations of eutectic point compositions $y_{L,eu}$ for racemic compound-forming systems in a fast and accurate manner. We also show that the ternary phase diagrams can be estimated faster and more accurately by measuring the solubility data via the pseudo-binary phase diagrams than using the van 't Hoff-type modelling (Fig. 9). The most accurate ternary phase diagrams show that the enantiomers do have certain influence on each other's pure solubilities in the pure component regions and that the solubility product of the racemic compound depends on the relative amounts of enantiomer present, for alanine, phenylalanine, and valine aqueous systems (Figs. 4 and 9).

At this point, we can propose the following workflow process for the accurate estimation of eutectic points and ternary phase diagrams of racemic compound-forming systems (Fig. 10). For an accurate determination of the ternary phase diagrams, the penultimate step requires an analysis of the physical phases (for example, by XRD)

present around the estimated eutectic point found (Fig. 10), especially when the literature does not provide knowledge about these phases and eutectic points. For a fast and accurate estimation of the ternary phase diagrams, only the last two steps involving the PBPD determination can be sufficient (Fig. 10). The final ternary phase diagrams obtained are helpful and necessary for several applications such as processes to separate enantiomers via crystallisation (Fig. 10) [5,6,48–51,7,8,11,43–47].

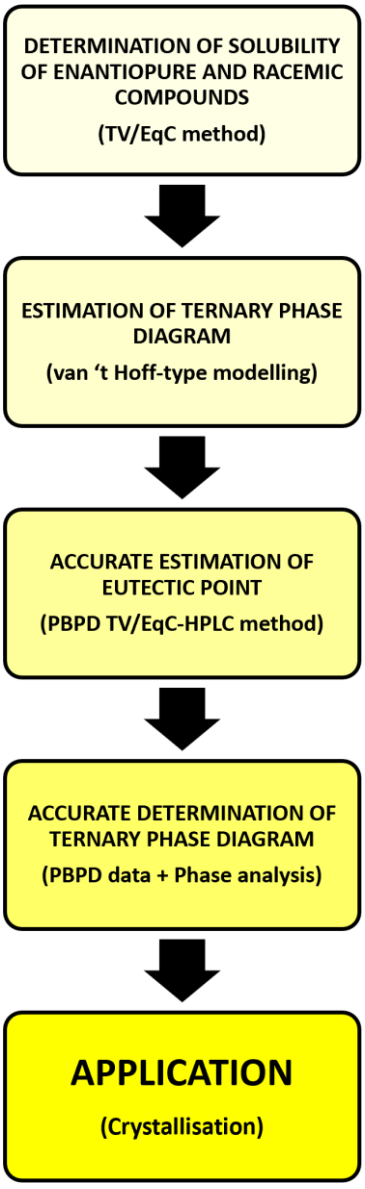

Fig. 10. Workflow process for the accurate determination of ternary phase diagrams of racemic compound-forming systems.

3.5. Conclusions

We determined the solubility of the amino acids alanine, phenylalanine, and valine in aqueous media by means of both the TV and EqC method. The faster TV method is suitable for those cases, such as alanine, which do not present fouling-related phenomena during crystallisation. For all other cases, such as phenylalanine and valine, the less time efficient EqC method can be applied. All three amino acids systems show solubility dependence with temperature and pH in water. Solubility curves grow with temperature and saturation concentrations are higher at lower (acidic media) or higher (base media) pH compared with medium pH values (neutral media). For instance, alanine solubility in water increases from 210.1 mg/g at 47.6ºC to 320.7 mg/g at 77.3ºC and its solubilities at 56.0ºC are 238.6 mg/g at pH 6.1, 321.5 mg/g at pH 2.6, and 298.7 mg/g at pH 9.8. The temperature effect on solubility is well described by the van ’t Hoff equation. The pH effect is due to the acid-base dissociation equilibria that exist because of the two proton-dissociable functional groups present in the amino acid structure. If we consider similar solid characteristics for the three hydrophobic amino acids, the molecular structure of the amino acids suggests the differences observed in solubility among them, focusing on their particular side chains. As water is a polar solvent, the larger and more hydrophobic the side chain of the chiral compound, the lower the polarity of the entire molecule and therefore the lower the solubility. The solubility differences observed depending on the chiral form of the compound studied can be explained because of the different crystal lattice between the racemate and enantiopure compound. Pseudo-binary phase diagrams are a fast methodology to accurately estimate the eutectic points of racemic compound-forming systems. Additionally, the latter phase diagrams also give an impression of the solubility of racemic and enantiopure compounds over the entire range of solvent-excluded enantiomeric ratios and can be used to estimate accurately ternary phase diagrams. We introduce the equivalence in pseudo-binary phase diagrams obtained via TV and EqC-HPLC methods based on the inverse relationship between saturation temperature and concentration. Both methods enable the estimation of the eutectic point compositions of any racemic compound-forming system. For example, the eutectic point

compositions given in enantiomeric ratios for the L-form of alanine, phenylalanine, and valine in water are estimated at 0.784 (44.4ºC), 0.906 (25.0ºC), and 0.719 (25.0ºC), respectively. Finally, the proposed workflow process for the efficient determination of the phase diagrams of racemic compound-forming systems, allows access to the eutectic point which is required in applications such as crystallisation-enhanced resolution processes.

3.6. Notation

A	Accuracy [%]
a_D	Activity of enantiomer D [-]
a_L	Activity of enantiomer L [-]
$A_{PBPD\text{-}lit.}$	Accuracy of *PBPD vs. lit.* [%]
$A_{TPD\text{-}lit.}$	Accuracy of *TPD vs. lit.* [%]
$A_{TPD\text{-}PBPD}$	Accuracy of *TPD vs. PBPD* [%]
Ala	Alanine
aq.	Aqueous
AU	Arbitrary units
C_s	Saturation concentration or solubility [mg/g]
D	Enantiomer D, D-form
ΔH^f_A	Enthalpy (variation) of fusion of the enantiomer [kJ/mol]
ΔH^f_R	Enthalpy (variation) of fusion of the racemic compound [kJ/mol]
ΔH_s	Enthalpy (variation) of the solution formation process [kJ/mol]
ΔS_s	Entropy (variation) of the solution formation process [J/(mol·K)]
DL	Racemate, DL-form
EqC	Equilibrium concentration method
EqC-HPLC	Equilibrium concentration-High-performance liquid chromatography method
F	Structure factor in SC-XRD

γ_D	Activity coefficient of enantiomer D [-]
γ_L	Activity coefficient of enantiomer L [-]
GoF	Goodness of fit [-]
HPLC	High-performance liquid chromatography
N	Number of observations per system [-]
n_D	Mole of enantiomer D [mol]
n_L	Mole of enantiomer L [mol]
L, l	Liquid phase (undersaturated)
L	Enantiomer L, L-form
LC-MS	Liquid chromatography-mass spectrometry
lit.	Literature
PBPD	Pseudo-binay phase diagram
pI	Isoelectric point
pK_a	Negative natural logarithm of an acid-base dissociation constant
Phe	Phenylalanine
R	Enantiomer *R* or gas constant [J/(mol·K)]
R_1	R-factor based on *F* [-]
RS	Racemate
RSD	Relative standard deviation [%]
S	Enantiomer *S*
s	Solid state (s)
σ	Standard deviation relative to x_i in the van ’t Hoff fitting [-]
SC-XRD	Single crystal X-ray diffraction
SD	Standard deviation [-]
T	Temperature [ºC] ([K], when indicated)
T^f	Melting point of the mixture [K]

T^f_A	Melting point of the enantiomer [K]
T^f_R	Melting point of the racemic compound [K]
TPD	Ternary phase diagram
T_s	Saturation temperature [ºC]
TV	Temperature variation method
Val	Valine
wR_2	R-factor based on F^2 [-]
x	Mole fraction of the more abundant enantiomer in the mixture [-]
x^*	Solute mole fraction in an enantiopure system [-]
x_D	Mole fraction solubility for enantiomer D [-]
x_D^*	Pure mole fraction solubility for enantiomer D [-]
$x_{D,eu}$	Eutectic enantiomeric ratio in the eutectic point (also referred as eutectic point composition) for enantiomer D [-]
x_i	Experimental/measured mole fraction solubility [-]
x_i^m	Modelled mole fraction solubility [-]
x_L	Mole fraction solubility for enantiomer L [-]
x_L^*	Pure mole fraction solubility for enantiomer L [-]
$x_{L,eu}$	Eutectic enantiomeric ratio in the eutectic point (also referred as eutectic point composition) for enantiomer L [-]
x_t	Total amount of enantiomer [-]
XRD	X-ray diffraction
y_L	Solvent-excluded enantiomeric ratio (for enantiomer L) [-]
$y_{L,eu}$	Eutectic solvent-excluded enantiomeric ratio (for enantiomer L) [-]
z_m	Measurement value [AU]
z_r	Reference value [AU]

3.7. References

[1] E.L. Eliel, S.H. Wilen, Stereochemistry of organic compounds, John Wiley & Sons, 2014.

[2] S. Srisanga, J.H. Ter Horst, Racemic compound, conglomerate, or solid solution: phase diagram screening of chiral compounds, Cryst. Growth Des. 10 (2010) 1808–1812.

[3] K. Williams, E. Lee, Importance of drug enantiomers in clinical pharmacology, Drugs. 30 (1985) 333–354.

[4] L.A. Nguyen, H. He, C. Pham-Huy, Chiral drugs: an overview, Int. J. Biomed. Sci. 2 (2006) 85–100.

[5] J. Jacques, A. Collet, Enantiomers, racemates and resolutions, John Wiley & Sons, 1981.

[6] H. Lorenz, A. Seidel-Morgenstern, Processes to separate enantiomers, Angew. Chemie - Int. Ed. 53 (2014) 1218–1250.

[7] H. Lorenz, D. Sapoundjiev, A. Seidel-Morgenstern, Solubility equilibria in chiral systems and their importance for enantioseparation, Eng. Life Sci. 3 (2003) 132–136.

[8] H. Lorenz, A. Perlberg, D. Sapoundjiev, M.P. Elsner, A. Seidel-Morgenstern, Crystallization of enantiomers, Chem. Eng. Process. Process Intensif. 45 (2006) 863–873.

[9] J.H. ter Horst, C. Schmidt, J. Ulrich, Fundamentals of industrial crystallization, in: Handb. Cryst. Growth Bulk Cryst. Growth Second Ed., 2014: pp. 1317–1349.

[10] L.C. Sögütoglu, R.R.E. Steendam, H. Meekes, E. Vlieg, F.P.J.T. Rutjes, Viedma ripening: a reliable crystallisation method to reach single chirality, Chem. Soc. Rev. 44 (2015) 6723–6732.

[11] E. Fogassy, M. Nógrádi, D. Kozma, G. Egri, E. Pálovics, V. Kiss, Optical resolution methods, Org. Biomol. Chem. 4 (2006) 3011–3030.

[12] M. Klussmann, A.J.P. White, A. Armstrong, D.G. Blackmond, Rationalization and prediction of solution enantiomeric excess in ternary phase systems, Angew. Chemie - Int. Ed. 45 (2006) 7985–7989.

[13] M. Klussmann, H. Iwamura, S.P. Mathew, D.H. Wells, U. Pandya, A. Armstrong, D.G. Blackmond, Thermodynamic control of asymmetric amplification in amino acid catalysis, Nature. 441 (2006) 621–623.

[14] M.A. Reus, A.E.D.M. van der Heijden, J.H. ter Horst, Solubility determination from clear points upon solvent addition, Org. Process Res. Dev. 19 (2015) 1004–1011.

[15] Bruker, Bruker APEX3 software, (2016). www.bruker.com/products/x-ray-diffraction-and-elemental-analysis/single-crystal-x-ray-diffraction/sc-xrd-software/apex3.html (accessed March 6, 2020).

[16] L.J. Farrugia, WinGX Program System, (2012). www.chem.gla.ac.uk/~louis/software/wingx/ (accessed March 6, 2020).

[17] L.J. Farrugia, WinGX and ORTEP for Windows: an Update, J. Appl. Crystallogr. 45 (2012) 849–854.

[18] G.M. Sheldrick, The SHELX homepage, (2008). shelx.uni-goettingen.de/index.php (accessed March 6, 2020).

[19] G.M. Sheldrick, A short history of SHELX, Acta Crystallogr. Sect. A Found. Adv. 64 (2008) 112–122.

[20] Merck, HPLC analysis of phenylalanine enantiomers on Astec CHIROBIOTIC T (formic acid mobile phase additive), (2020). www.sigmaaldrich.com/technical-documents/articles/analytical-applications/hplc/hplc-analysis-of-phenylalanine-

enantiomers-g005342.html (accessed March 5, 2020).

[21] J.E. Claus, Chiral HPLC analysis of underivatized amino acid enantiomers, 2020.

[22] Hanna Instruments Ltd., HI-10832 HALO wireless pH electrode with microbulb, (2018). www.hannainstruments.co.uk/hi-10832-halor-wireless-ph-electrode-with-microbulb.html#specifications (accessed March 5, 2020).

[23] P.Y. Bruice, Organic chemistry, 5th ed., Pearson Prentice Hall, 2008.

[24] F.A. Carey, R.M. Giuliano, Organic chemistry, 10th ed., McGraw-Hill Education, New York, 2016.

[25] R.B. Gupta, R.A. Heidemann, Solubility models for amino acids and antibiotics, AIChE J. 36 (1990) 333–341.

[26] S.P. Pinho, C.M. Silva, E.A. Macedo, Solubility of amino acids: a group-contribution model involving phase and chemical equilibria, Ind. Eng. Chem. Res. 33 (1994) 1341–1347.

[27] H.-C. Tseng, C.-Y. Lee, W.-L. Weng, I.-M. Shiah, Solubilities of amino acids in water at various pH values under 298.15K, Fluid Phase Equilib. 285 (2009) 90–95.

[28] T. Le Minh, J. Von Langermann, H. Lorenz, A. Seidel-Morgenstern, Enantiomeric 3-chloromandelic acid system: binary melting point phase diagram, ternary solubility phase diagrams and polymorphism, J. Pharm. Sci. 99 (2010) 4084–4095.

[29] National Institute of Standards and Technology, Molar gas constant. Fundamental physical constants, (n.d.). physics.nist.gov/cgi-bin/cuu/Value?eqr (accessed March 10, 2020).

[30] M. Tao, Z. Wang, J. Gong, H. Hao, J. Wang, Determination of the solubility, dissolution enthalpy, and entropy of pioglitazone hydrochloride (form II) in different pure solvents, Ind. Eng. Chem. Res. 52 (2013) 3036–3041.

[31] B. Long, J. Li, Y. Song, J. Du, Temperature dependent solubility of α-form L-

glutamic acid in selected organic solvents: measurements and thermodynamic modeling, Ind. Eng. Chem. Res. 50 (2011) 8354–8360.

[32] S. Jin, X. Cui, Y. Qi, Y. Shen, H. Li, Measurement and correlation of the solubility of β-cyclodextrin in different solutions at different temperatures and thermodynamic study of the dissolution process, Processes. 7 (2019) 135.

[33] G. Chen, J. Liang, J. Han, H. Zhao, Solubility modeling, solute-solvent interactions, and thermodynamic dissolution properties of p-nitrophenylacetonitrile in sixteen monosolvents at temperatures ranging from 278.15 to 333.15 K, J. Chem. Eng. Data. 64 (2019) 315–323.

[34] F.L. Nordström, Å.C. Rasmuson, Prediction of solubility curves and melting properties of organic and pharmaceutical compounds, Eur. J. Pharm. Sci. 36 (2009) 330–344.

[35] G.R. Pazuki, M. Nikookar, A new local composition model for predicting of activity coefficient and solubility of amino acids and peptides in water, Biochem. Eng. J. 28 (2006) 44–49.

[36] G.R. Pazuki, V. Taghikhani, M. Vossoughi, Correlation and prediction the activity coefficients and solubility of amino acids and simple peptide in aqueous solution using the modified local composition model, Fluid Phase Equilib. 255 (2007) 160–166.

[37] C. Held, L.F. Cameretti, G. Sadowski, Measuring and modeling activity coefficients in aqueous amino-acid solutions, Ind. Eng. Chem. Res. 50 (2011) 131–141.

[38] H.J. Simpson, R.E. Marsh, The crystal structure of L-alanine, Acta Crystallogr. 20 (1966) 550–555.

[39] M. Barthes, F. Dénoyer, J.-E. Lorenzo, J. Zaccaro, A. Robert, F. Zontone, H.N. Bordallo, Micro-transitions or breathers in L-alanine?, Eur. Phys. J. B - Condens.

Matter. 37 (2003) 375–382.

[40] N.A. Tumanov, E. V. Boldyreva, B.A. Kolesov, A. V. Kurnosov, R. Quesada Cabrera, Pressure-induced phase transitions in L-alanine, revisited, Acta Crystallogr. Sect. B Struct. Sci. 66 (2010) 458–471.

[41] L. Brunet, J. Caillard, P. André, Thermodynamic calculation of n-component eutectic mixtures, Int. J. Mod. Phys. C. 15 (2004) 675–687.

[42] Joint Committee for Guides in Metrology, JCGM 200:2008 International vocabulary of metrology — Basic and general concepts and associated terms (VIM), 3rd ed., 2008.

[43] K. Galan, M.J. Eicke, M.P. Elsner, H. Lorenz, A. Seidel-Morgenstern, Continuous preferential crystallization of chiral molecules in single and coupled mixed-suspension mixed-product-removal crystallizers, Cryst. Growth Des. 15 (2015) 1808–1818.

[44] A. Mersmann, Crystallization technology handbook, 2nd ed., Marcel Decker, Inc., New York, 2001.

[45] S. Robl, L. Gou, A. Gere, M. Sordo, H. Lorenz, A. Mayer, C. Pauls, K. Leonhard, A. Bardow, A. Seidel-Morgenstern, K. Schaber, Chiral separation by combining pertraction and preferential crystallization, Chem. Eng. Process. Process Intensif. 67 (2013) 80–88.

[46] J. Wang, R. Lakerveld, Continuous membrane-assisted crystallization to increase the attainable product quality of pharmaceuticals and design space for operation, Ind. Eng. Chem. Res. 56 (2017) 5705–5714.

[47] L. Gou, S. Robl, K. Leonhard, H. Lorenz, M. Sordo, A. Butka, S. Kesselheim, M. Wolff, A. Seidel-Morgenstern, K. Schaber, A hybrid process for chiral separation of compound-forming systems, Chirality. 23 (2011) 118–127.

[48] G. Coquerel, Preferential crystallization, Springer-Verlag, Berlin, Heidelberg, 2006.

[49] J. von Langermann, M. Kaspereit, M. Shakeri, H. Lorenz, M. Hedberg, M.J. Jones, K. Larson, R. Herschend, R. Arnell, E. Temmel, J.-E. Ba, A. Kienle, A. Seidel-Morgenstern, Design of an integrated process of chromatography, crystallization and racemization for the resolution of 2′,6′-pipecoloxylidide (PPX), Org. Process Res. Dev. 16 (2012) 343–352.

[50] D. Polenske, H. Lorenz, A. Seidel-Morgenstern, Separation of propranolol hydrochloride enantiomers by preferential crystallization: thermodynamic basis and experimental verification, Cryst. Growth Des. 7 (2007) 1628–1634.

[51] H. Kaemmerer, Z. Horvath, J.W. Lee, M. Kaspereit, R. Arnell, M. Hedberg, B. Herschend, M.J. Jones, K. Larson, H. Lorenz, A. Seidel-Morgensten, Separation of racemic bicalutamide by an optimized combination of continuous chromatography and selective crystallization, Org. Process Res. Dev. 16 (2012) 331–342.

CHAPTER 4

4. Process Modelling and Optimisation of Continuous Chiral Resolution by Integration of Membrane and Crystallisation Technologies

Jose Capdevila-Echeverria[*], *Jiayuan Wang*[*], *Richard Lakerveld*[*], *Joop H. ter Horst*

Chiral resolution will increase its importance in the pharmaceutical, pesticide, and food industries since future chiral products will be structurally more complex while their quality will need to meet stringent demands to accomplish with health, crop, and environmental purposes. Currently, obtaining enantiopure crystals from racemic compound-forming systems (90-95% of chiral compounds) remains a challenge. The combination of membrane ultrafiltration and crystallisation in a continuous process is a potential solution to this problem. This work aims to optimise this continuous chiral resolution process using process modelling. First, a model for the membrane ultrafiltration step assumes a one-site competition in which the chiral selector binds preferentially to one of the enantiomers. The amino acids phenylalanine, alanine, and valine in aqueous media along with the chiral selector BSA are the model systems studied. Then, three process performance parameters (purity, recovery, and a combination of the previous two) are assessed to optimise the conditions for the continuous membrane-based step. Recoveries up to 70% are achieved while fulfilling purity levels beyond eutectic point compositions, a requirement for the enantiopure crystallisation. Additionally, the properties of an ideal process chiral selector are explored. Finally, the crystallisation step (with recoveries up to 65%) is coupled to evaluate the maximum recovery of the overall process. Simulations show that the membrane-crystallisation process performance is governed by a trade-off

[*] Department of Chemical and Biological Engineering, The Hong Kong University of Science and Technology, Clear Water Bay, Hong Kong

between purity and recovery. We predict that an ideal BSA-similar chiral selector should bear an unprotonated binding site for a wide pH range and a difference between enantiomer complexation constants of at least 2-3 *pK* units to improve the process performance.

4.1. Introduction

Chiral molecules occur in left- and right-handed configurations that can be considered as mirror images (enantiomers), and that, like hands, cannot be superimposed onto each other [1]. Enantiomers of chiral drugs may present different pharmacological and toxicological effects [1,2]. For instance, the (*S*)-enantiomer of naproxen when administered in the human body has an anti-inflammatory effect whereas the (*R*)-enantiomer is poisonous to the liver [3,4]. In the absence of in vivo racemization, chiral resolution (the process to obtain enantiopure molecules by means of the physical separation of enantiomers) of racemic mixtures or impure enantiomers would prevent the undesired effects. Chiral resolution processes are therefore of great importance in the pharmaceutical industry as well as in the agrochemical and food manufacturing sectors [5–7]. The chiral separation of racemic environmental pollutants has also attracted attention due to the different impact of each enantiomer to the environment [8,9]. The chiral pollution is a serious issue for health and environment due to the enantioselective biodegradation of the chiral pollutants. More than 1500 chiral pollutants are present in the environment [10]. Chiral resolution will increase its already sizeable importance in these fields where future chemical products will be larger and contain more stereocentres while their quality and purity will require to meet increasingly stringent demands and specifications. However, the separation of enantiomers into highly enantiopure crystalline products from a complex multicomponent mixture remains a challenge.

Although continuous membrane technologies could potentially be used to achieve enantiomer enrichment, they cannot reach enantiomer purity levels close to 100% in a feasible manner. The consecution of high purity would require several membranes, a fact

that would compromise the recovery of the process, and therefore making the process unfeasible [11]. Some efforts have been done in obtaining high purity levels in solution, but none of them led to the full separation and neither to the recovery of a pure solid product [12–14]. While crystallisation-enabled resolution such as preferential crystallisation can be highly effective and efficient due to the near-perfect selectivity of the solid phase, it relies on the formation of a conglomerate [5,6]. Nonetheless, in racemic solutions, only 5-10% of the chiral compounds form such conglomerates while the majority of the chiral compounds (90-95%) form a racemic compound [5,6,15–19]. Therefore, obtaining enantiopure crystalline products from racemic solutions of racemic compounds is currently a challenge.

Integrated processes can combine the high productivity of a not too selective separation technology with a narrow process window but highly selective separation technology. The first technology is used to create the conditions with the right process window for the second technology. Here, the selectivity is understood in terms of the required enantiomeric enrichment that the first technology will be able to provide to the second technology, which will produce the enantiopure products. Examples of these integrated processes are pertraction-crystallisation [20,21] and chromatography-crystallisation [22,23]. A third novel approach is to couple membrane ultrafiltration and crystallisation processes, so forming a membrane ultrafiltration-crystallisation integrated process. In this latter, a chiral selector is used to preferentially complex one of the enantiomers. A membrane ultrafiltration process renders enantiomeric enrichment by means of a size-exclusion non-enantioselective solid membrane. This type of membranes is promising due to its convenience, affordability, energy efficiency, and ease of scale-up [11]. From the enriched solution, the enriched enantiomer can be selectively crystallised in the permeate as an enantiopure solid.

Here we report the process modelling and optimisation of a continuous chiral resolution process that combines membrane ultrafiltration and cooling crystallisation to produce enantiopure crystal products starting from racemic solutions of racemic compound-

forming systems. The chiral systems chosen to demonstrate the feasibility of the membrane-assisted crystallisation resolution are the hydrophobic amino acids phenylalanine (Phe), alanine (Ala), and valine (Val) in aqueous media. Bovine serum albumin (BSA) is a chiral selector, which is known to have enantiomeric selectivity with this class of amino acids [12–14]. A one-site competition model is presented to describe the complexation interaction of these amino acids systems with the chiral selector BSA. The model is validated and its predictions determine the optimal conditions for the membrane process. In addition, sensitivity studies of thermodynamic constants permit the prediction of the ideal chiral selector properties. Finally, the feasibility of coupling the membrane ultrafiltration and crystallisation is investigated.

4.2. Experimental section

4.2.1. Materials

D-phenylalanine (D-Phe, Sigma-Aldrich, ≥98%), D-alanine (D-Ala, Sigma-Aldrich, ≥98%), and D-valine (D-Val, Sigma-Aldrich, ≥98%). Milli-Q water was taken from a Merck Millipore purification system and had a resistivity of 18.2 MΩ·cm at 25ºC.

4.2.2. Solubility determination methodologies

Two different methods were used to determine the solubilities at temperatures T = 80ºC and T’ = 1ºC because some systems present fouling phenomena when they crystallise, which prevented using light to detect the presence of crystals for some of the amino acid systems studied. A second gravimetric method based on equilibrium concentration was required to assess their solubilities. The two methods used were the temperature variation (TV) and equilibrium concentration (EqC) methods [24].

4.2.2.1. Temperature variation (TV) method

For the TV method, a similar protocol was used as reported in the literature [24] using the Crystal16 multiple reactor setup (Technobis Crystallization Systems). Samples were prepared by dissolving increasing amounts of the solid with 1 mL of Milli-Q water in each vial. The samples were agitated using a magnetic stirrer bar with a stirring rate of 700 rpm. Three temperature cycles were applied starting at 20ºC, with maximum and minimum temperatures of 90ºC and 1ºC, respectively, and with heating and cooling rates of 0.3 ºC/min. Hold times of 1 h were applied when maximum (90ºC) and minimum (1ºC) temperatures were reached in each cycle. Clear and cloud points were registered based on the transmission of the light. Then, the solubility at a certain temperature was determined by taking the average of three clear points measurements (*RSD* within ±1%). This method was used for the solubility determination of D-alanine.

4.2.2.2. Equilibrium concentration (EqC) method

For the EqC method, a similar gravimetric protocol was used as reported in the literature [24]. Samples were prepared by adding an excess of compound to 1 mL of Milli-Q water in each vial. Then, the saturated solutions in the vials were equilibrated at different constant temperatures in the Crystal16 multiple reactor setup (Technobis Crystallization Systems) for at least 2-3 days. During that period, the samples were agitated using a magnetic stirrer bar with a stirring rate of 700 rpm. Afterwards, at various temperatures, solution samples of approximately 1 mL were taken with a syringe, filtered, weighed and left in the oven (65ºC) for at least 7 days for the solvent to evaporate. When the crystals appeared dry, they were weighed. Two days later, they were weighed again to check for any additional mass loss until the mass was constant. The solubility at a certain temperature was determined by taking the average of three gravimetric measurements (*RSD* within ±2%). This method was used for the solubility determination of D-phenylalanine and D-valine.

4.2.3. Computational software

The process model presented in this document was implemented in GAMS 24.7.4 [25] and all the optimisation problems were solved using the GAMS/CONOPT solver, which is based on the generalised reduced gradient method and generally used for large-scale non-linear programming (NLP) optimisation problems [26]. To avoid local optima, multiple initial guesses were provided by a random number generator in MATLAB R2018A [27] to GAMS using the GDXMRW interface [28].

4.3. Results

4.3.1. Model development

The novel chiral resolution process consists in an initial feed of a racemic amino acid aqueous solution which first undergoes an enantiomeric enrichment by means of a chiral selector-assisted membrane ultrafiltration step followed by selective crystallisation of an enantiopure crystalline product (Fig. 1).

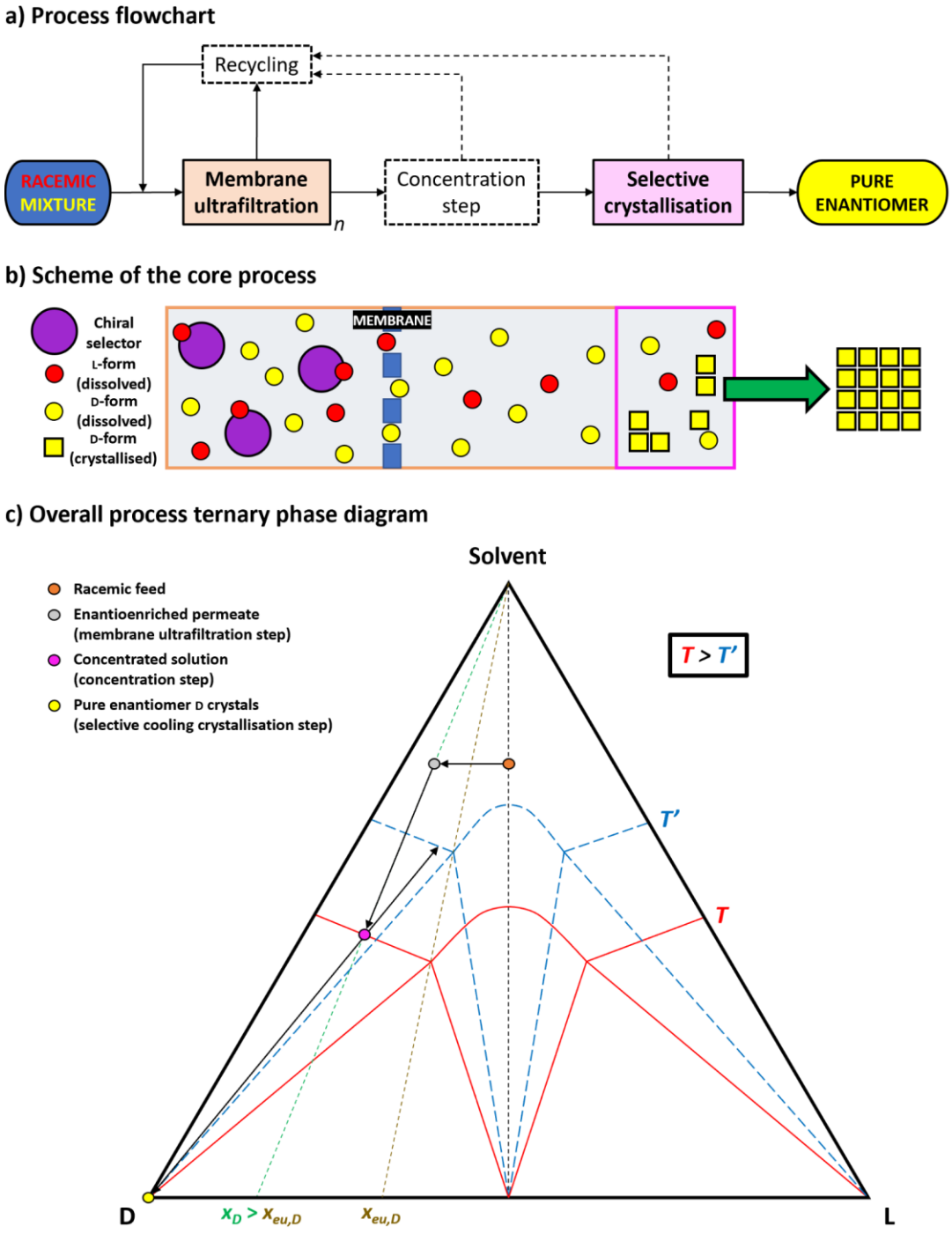

Fig. 1. a) Process flowchart for the membrane-crystallisation chiral resolution. b) Scheme of the core process (colours relate to the core steps in bold in a). c) Overall process ternary phase diagram for the resolution of a racemic compound-forming system. *T* and *T'* account for both initial and final temperatures in the cooling crystallisation step, respectively; and x_D and $x_{eu,D}$ are the solvent-free enantiomer fraction and eutectic point composition for enantiomer D, respectively.

4.3.1.1. Membrane ultrafiltration step

We assumed that the one-site competition model [12–14] explains the complexation between the chiral selector BSA and the enantiomers of hydrophobic amino acids phenylalanine (Phe), alanine (Ala), and valine (Val) in the membrane ultrafiltration step (Fig. 1). This one-site competition model was applied to systems with the similar amino acids tryptophan (Trp) and kynurenine, as reported by Garnier [13] and Randon [14]. The mechanism considers that only the zwitterionic forms of both enantiomers of the amino acid will compete to bind to a single unprotonated site of the chiral selector BSA (Fig. 1b).

In this way, this model accounts for the speciation found in the membrane ultrafiltration step (Fig. 1b) taking into consideration the combination of three thermodynamic equilibria:

1) Complexation equilibria of chiral selector BSA with the zwitterionic form of the amino acid enantiomers

$$\mathrm{D}^{\pm} + \mathrm{BSA} \rightleftharpoons \mathrm{D}^{\pm}\mathrm{BSA}, \quad K_D = \frac{C_{D\pm BSA}}{C_{D\pm} C_{BSA}} \tag{1a}$$

$$\mathrm{L}^{\pm} + \mathrm{BSA} \rightleftharpoons \mathrm{L}^{\pm}\mathrm{BSA}, \quad K_L = \frac{C_{L\pm BSA}}{C_{L\pm} C_{BSA}} \tag{1b}$$

K and *C* represent the thermodynamic constants and species concentrations involved in the complexation equilibria, respectively (see Notation section 4.6.). K_D and K_L should differ from each other as much as possible for the pair of enantiomers, indicating then a much higher selectivity of the chiral selector for one of the two enantiomers. This difference is essential to obtain an enantiopure crystalline product at the end of the overall process (Fig. 1).

2) Acid-base dissociation equilibria of each amino acid enantiomer with solvent

$$\mathrm{D^+ + H_2O \rightleftharpoons D^{\pm} + H_3O^+},\ K_{a1,D} = \frac{C_{D\pm}C_{w+}}{C_{D+}C_w} \tag{2a}$$

$$\mathrm{D^{\pm} + H_2O \rightleftharpoons D^- + H_3O^+},\ K_{a2,D} = \frac{C_{D-}C_{w+}}{C_{D\pm}C_w} \tag{2b}$$

$$\mathrm{L^+ + H_2O \rightleftharpoons L^{\pm} + H_3O^+},\ K_{a1,L} = \frac{C_{L\pm}C_{w+}}{C_{L+}C_w} \tag{2c}$$

$$\mathrm{L^{\pm} + H_2O \rightleftharpoons L^- + H_3O^+},\ K_{a2,L} = \frac{C_{L-}C_{w+}}{C_{L\pm}C_w} \tag{2d}$$

K_a and C represent the thermodynamic constants and species concentrations involved in the acid-base dissociation equilibria, respectively (see Notation section 4.6.). Here, $K_{a1,D} = K_{a1,L}$ and $K_{a2,D} = K_{a2,L}$ because the acid-base dissociation thermodynamic equilibria are not affected by stereoisomerism.

3) Acid-base dissociation equilibrium of the chiral selector BSA with solvent

$$\mathrm{BSA^+ + H_2O \rightleftharpoons BSA + H_3O^+},\ K_{BSA} = \frac{C_{BSA}C_{w+}}{C_{BSA+}C_w} \tag{3}$$

K_{BSA} and C represent the thermodynamic constant and species concentrations involved in the acid-base dissociation equilibrium of BSA, respectively (see Notation section 4.6.). The values for the above thermodynamic constants are given in Table 1, indicated as pK (which means -$\log_{10}K$). The values of pK_D and pK_L for alanine and valine systems are assumed equal to those for phenylalanine [29] because of the similar hydrophobic amino acid behaviour (Table 1). As mentioned above, acid-base dissociation constants, and then also pK_{a1} and pK_{a2}, have the same values for both enantiomers [30]. The acid-base dissociation equilibrium of BSA with water is reported in the literature [13,14].

Table 1. pK values for thermodynamic equilibria constants in Eqs. (1)-(3) for the amino acid systems studied at 25ºC. pK_D and pK_L, pK_{a1} and pK_{a2}, and pK_{BSA} account for the complexation constants of both amino acid enantiomers with BSA and acid-base dissociation constants of the amino acid enantiomers and BSA with water, respectively.

Amino acid	pK_D	pK_L	pK_{a1}	pK_{a2}	pK_{BSA}
Phenylalanine			1.83	9.13	
Alanine	-5.27	-6.25	2.34	9.69	9.40
Valine			2.32	9.62	

The thermodynamic constants described above (Table 1) along with the material balances for each enantiomer of the amino acid and chiral selector permit the study of the speciation in the membrane ultrafiltration step (Fig. 1ab). The material balances considered for the different species x involved in this step can be expressed as follows (4):

$$C_{x,0} = \sum_{i \in species\ x\ forms} C_i \tag{4}$$

Species x are enantiomer D or L or chiral selector BSA. $C_{x,0}$ and C_i represent the total concentration of species x and concentration for each form of species x present in the membrane ultrafiltration step, respectively.

The membrane ultrafiltration step consists of a filtration system which makes use of a size-exclusion non-stereoselective solid membrane. This membrane is assumed to have total rejection for the chiral selector and chiral selector-amino acid complexes. In that way, only the free enantiomers of the amino acids (D and L-forms) can permeate the membrane. The model membrane is also assumed to not influence the permeate concentration compared to the retentate solution which means that the free enantiomers concentrations in the retentate and permeate solutions are equal ($C_{D,r} = C_{D,p}$ and $C_{L,r} = C_{L,p}$). Only the retentate volume V_r and permeate volume V_p vary over time. As the chiral selector, present at the retentate side of the membrane, preferentially binds one of the enantiomers, the permeate solution gets enantioenriched with the other (Fig. 1ab) [31,32]. In the amino acid systems treated here, the enantiomer L preferentially binds to the chiral selector and therefore the enantiomer D is enriched in the permeate (Fig. 1b), which can be seen from

the higher complexation value of K_L (more negative pK) compared to K_D (less negative pK) (see Table 1). Several recirculation cycles of the retentate solution occur in the membrane ultrafiltration step to produce enough permeate volume V_p to go further in the next steps of the overall process at the end of the membrane step. That is, a certain volume V_p from the initial feed volume V_0 is collected at the permeate side. The enantiomeric enrichment level reached in the permeate solution can be increased if the number of membrane ultrafiltration stages n is also increased (Fig. 1a). This option can be used to optimise the process, meaning that the membrane ultrafiltration step can be adapted with more stages for chemical systems that require a higher enantiomeric enrichment. The model description in this section mainly refers to the single-stage membrane ultrafiltration (n = 1) case. Then, the two outgoing streams in the membrane ultrafiltration step (Fig. 1a) are taken as the retentate and permeate. The multi-stage membrane ultrafiltration (n > 1) case is treated with further detail in section 4.3.3. as an extended approach for those systems that require high enantioenrichment.

We define three key performance indicators (KPIs) to assess the performance of the membrane ultrafiltration step (Fig. 1ab) as defined below (5)-(7):

1) Purity of the membrane ultrafiltration step (for permeate stream, Table 2)

$$Pu_m = x_D = \frac{C_{D,p}}{C_{D,p} + C_{L,p}} \tag{5}$$

Purity Pu_m is defined by the solvent-free enantiomer D fraction x_D. $C_{D,p}$ and $C_{L,p}$ represent the total concentrations of enantiomers D and L in the permeate p, respectively.

2) Recovery of the membrane ultrafiltration step (Table 2)

$$Re_m = \frac{V_p C_{D,p}}{V_0 C_{D,0}} \tag{6}$$

$C_{D,0}$ represents the total initial concentration of enantiomer D in the feed solution.

3) *PuRe* of the membrane ultrafiltration step (Table 2)

$$PuRe = E_{D,p}Re_m = (2Pu_m - 1)Re_m \quad (7)$$

This *PuRe* definition can be inferred from Pu_m and Re_m alongside their relationship with the enantiomeric excess $E_{D,p}$ defined as:

$$E_{D,p} = \frac{C_{D,p} - C_{L,p}}{C_{D,p} + C_{L,p}} = x_D - x_L = 2Pu_m - 1 \quad (8)$$

Note that we use the fact that the total sum of both solvent-free enantiomer fractions for enantiomers D and L (x_D and x_L, respectively) is equal to 1. Equation (7) assumes equal weighting between Pu_m and Re_m.

The three KPIs defined for the membrane ultrafiltration step, indicated by the subscript *m*, are considered sufficient to study this step with a thermodynamic approach considering the equilibria and concentrations that involve the one-site competition model. Purity Pu_m accounts for the enantiomeric enrichment of the membrane ultrafiltration step and indicates whether the process liquid can continue to the following steps or, instead, needs further enrichment. Recovery Re_m accounts for the performance of the membrane ultrafiltration step regarding the amount of enantiomer D obtained in the permeate in comparison with its initial amount in the feed. *PuRe* accounts for both the purity and recovery of enantiomer D, which allows for the use of one parameter for optimisation. The objective is to find the highest *PuRe* value for the membrane ultrafiltration step, which will strike a balance between obtaining a high purity and recovery.

4.3.1.2. Concentration and selective crystallisation steps

Once sufficient enantioenrichment is obtained in the permeate for the enantiomer D, it is possible to selectively crystallise this enantiomer (Fig. 1). The three model amino acid systems are racemic compounds. Their ternary phase diagram represents the phase behaviour of the mixture containing the solvent, enantiomer D, and enantiomer L; at a fixed temperature and pressure (Fig. 1c) [5,6]. Standard atmospheric pressure (101,325

Pa) is typically assumed for crystallisation-based chiral resolution methods [5,6]. For racemic compounds, the ternary phase diagrams are characterised for having two symmetric eutectic points (Fig. 1c). A more detailed description about ternary phase diagrams of racemic compound-forming systems can be found in the literature [5,6,16]. In each eutectic point, a saturated liquid phase solution of the racemate is in equilibrium with the solid phases of the racemic compound and one of the pure enantiomers (D or L). Therefore, these points also distinguish the limits of the phase regions where we can find only one solid phase crystallising (racemic compound or one enantiomer) (Fig. 1c). Our process focuses on the left side of the ternary phase diagram (Fig. 1c) because it is where the enantiomer D region lies down (Fig. 1c). The solvent-free enantiomer D fraction at the eutectic $x_{eu,D}$ indicates the enantiomeric ratio required to reach the eutectic equilibrium where both chiral solids coexist. Thus, the selective crystallisation of the enantiopure product is only attainable as long as the enantiomeric enrichment level x_D reached surpasses the eutectic point composition $x_{eu,D}$ in the ternary phase diagram (Fig. 1c). So,

$$x_D > x_{eu,D} \tag{9}$$

Then, if the concentration in the permeate fulfils this boundary condition (9) so that x_D can be kept stable and above $x_{eu,D}$ under supersaturated conditions, the pure enantiomer can be crystallised (Fig. 1c).

We consider a cooling crystallisation method for the last step of the process. However, the requirement of a concentration step (Fig. 1ac) between the membrane ultrafiltration and cooling crystallisation steps is also studied.

For that, we define the concentration factor *F*:

$$F = \frac{C^*_{D,T}}{C_{D,p}} \tag{10}$$

which indicates how much the permeate concentration of enantiomer D $C_{D,p}$ needs to be concentrated to reach the solubility concentration $C^*_{D,T}$ of enantiomer D at temperature T in order to start the selective cooling crystallisation step (Fig. 1c).

The crystallisation step is assumed selective for only one of the two enantiomers (enantiomer D), meaning that the crystallisation of the counter enantiomer L is prevented if the overall composition remains inside the two-phase region (where only the solid phase of enantiomer D can crystallise from the supersaturated liquid phase solution) of the ternary phase diagram during crystallisation (Fig. 1c). The model considers that crystallisation starts when the system is in this two-phase region of the ternary phase diagram (Fig. 1c) and that this point in the phase diagram will be maintained constant while the whole crystallisation step takes place. This becomes feasible if we assume a steady-state condition that is given when operating in continuous mode.

The selective cooling crystallisation starts at the saturation concentration $C^*_{D,T}$ of enantiomer D at temperature T and ends at the saturation concentration $C^*_{D,T'}$ of enantiomer D at temperature T' (Fig. 1c). Then, only enantiomer D crystallises out of the solution at T' (Fig. 1c), obtaining thus the enantiopure crystalline product (Fig. 1).

At this point, the model requires the definition of a fourth KPI, Re_c, the recovery in the selective cooling crystallisation step:

4) Recovery of the selective crystallisation step (Table 2)

$$Re_c = \frac{C^*_{D,T} - C^*_{D,T'}}{C^*_{D,T}} \tag{11}$$

The subscript c refers to the crystallisation step. Here, crystallisation volume V_c is assumed equal for both saturation concentrations $C^*_{D,T}$ and $C^*_{D,T'}$. Thus, Re_c assesses the amount of pure enantiomer crystals which can be collected from the crystallisation step.

4.3.1.3. Overall process

The racemic feed for the membrane ultrafiltration step renders an enantioenriched solution in the permeate (Fig. 1). Then, a concentration step between the membrane ultrafiltration and crystallisation steps (Fig. 1ac) is required as the concentration in the permeate is low compared to the solubility of the enantiomer. Finally. if the

enantioenriched permeate fulfils condition (9), the enantiomer can be selectively crystallised (Fig. 1).

We require a last KPI, Re_p, in order to account for the recovery of the overall process, which can be defined as follows:

5) Recovery of the overall process (Table 2)

$$Re_p = Re_m Re_c = \frac{V_c C^*_{D,T} - V_c C^*_{D,T'}}{V_0 C_{D,0}} \quad (12)$$

The subscript *p* refers to the overall process. The recovery Re_p compares the amount of pure enantiomer crystals obtained at the end of the process with the amount of the same enantiomer in the feed. Note that the overall process recovery Re_p is the product of the recoveries of the membrane ultrafiltration and selective crystallisation (Fig. 1).

Table 2. Model key performance indicators (KPIs) of the membrane-crystallisation chiral resolution process.

KPI	Symbol	Mathematical definition	Equation
Membrane ultrafiltration purity	Pu_m	$Pu_m = \frac{C_{D,p}}{C_{D,p} + C_{L,p}}$	(5)
Membrane ultrafiltration recovery	Re_m	$Re_m = \frac{V_p C_{D,p}}{V_0 C_{D,0}}$	(6)
Membrane ultrafiltration *PuRe*	*PuRe*	$PuRe = (2Pu_m - 1)Re_m$	(7)
Selective crystallisation recovery	Re_c	$Re_c = \frac{C^*_{D,T} - C^*_{D,T'}}{C^*_{D,T}}$	(11)
Overall process recovery	Re_p	$Re_p = \frac{V_c C^*_{D,T} - V_c C^*_{D,T'}}{V_0 C_{D,0}}$	(12)

4.3.2. Exploration of complexation conditions for the membrane ultrafiltration step

4.3.2.1. Speciation

The amino acid species concentrations evolve differently depending on the pH of the medium and the presence of the chiral selector BSA (Fig. 2). The concentrations of the different BSA species also depend on the pH because of the acid-base dissociation equilibrium with water (3) (Fig. 2a).

In the absence of chiral selector (Fig. 2bc left), the concentration profiles for enantiomers D and L species are the same when comparing each ionic species of the two enantiomers. This is found for the three amino acid systems phenylalanine, alanine, and valine (Fig. 2bc right). This means that both enantiomers have the same acid-base dissociation behaviour when BSA is not present. Instead, when BSA is available (Fig. 2a and 2bc right), enantiomer D and L species concentration profiles are not the same anymore and differ from those with no chiral selector (Fig. 2bc). A maximum of complexation between the zwitterionic form of both enantiomers and chiral selector BSA is observed at pH = 9.3-9.5, where species $L^{\pm}$ binds more than $D^{\pm}$ to the BSA (Fig. 2a), which is consistent with the larger value of the thermodynamic complexation constant K_L compared to K_D (Table 1). This different complexation behaviour between both amino acid enantiomers can be exploited in the membrane ultrafiltration step and explains the enantiomeric enrichment that is obtained in the permeate, where the total concentration of the free enantiomer D species $C_{D,p}$ is higher than the total concentration of the free enantiomer L species $C_{L,p}$ (Fig. 2bc right).

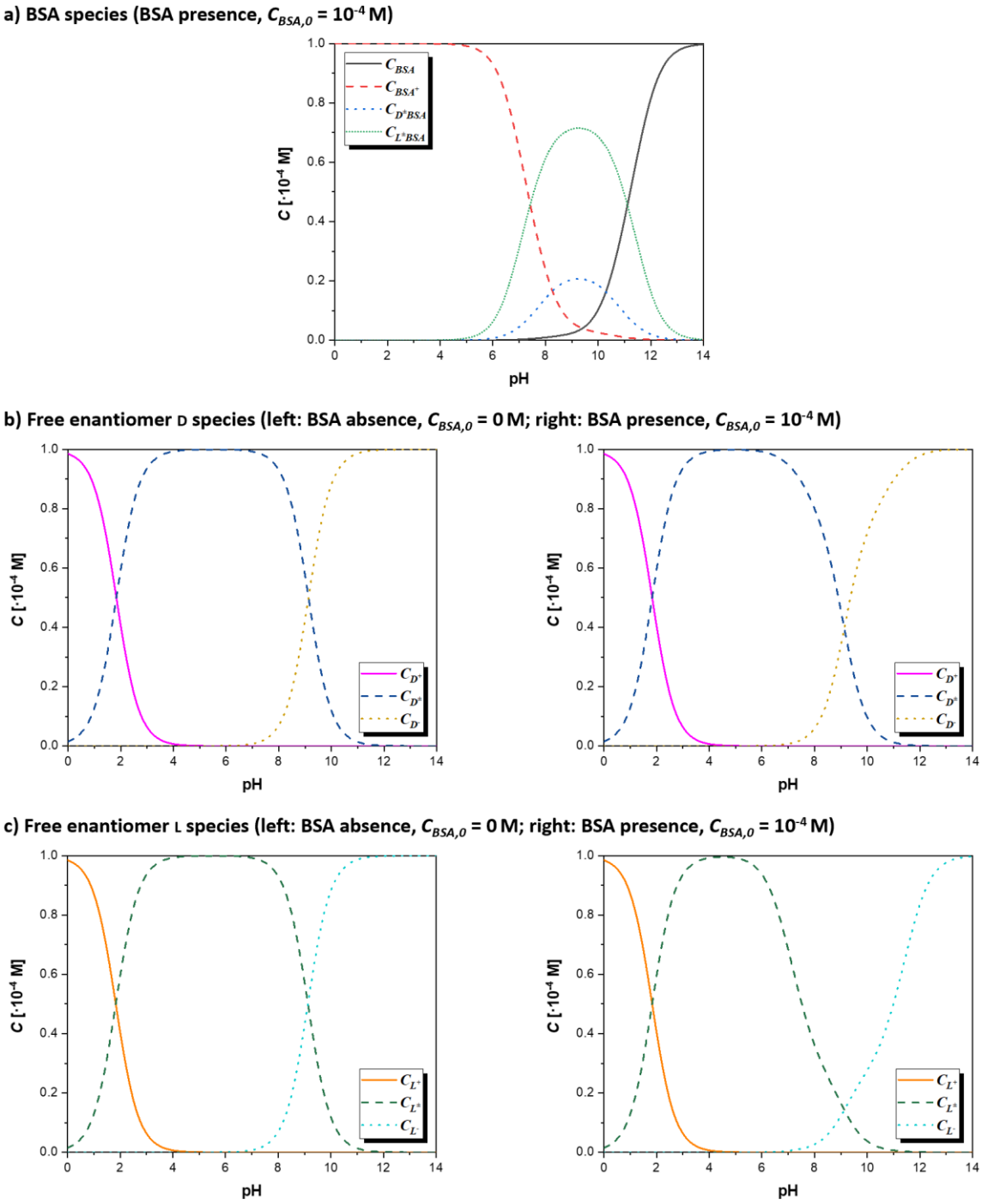

Fig. 2. Evolution of concentrations *C* of all the species involved in the complexation process, described by Eqs. (1)-(4), between the amino acids and chiral selector BSA: a) BSA species, b) free enantiomer D species, and c) free enantiomer L species. The simulations are for the phenylalanine system in absence of BSA with $C_{D,0} = C_{L,0} = 10^{-4}$ M and $C_{BSA,0} = 0$ M (b and c, left) and presence of BSA with $C_{D,0} = C_{L,0} = C_{BSA,0} = 10^{-4}$ M (a; b and c, right). Alanine and valine systems present similar concentration profiles.

4.3.2.2. Optimal complexation conditions

The model describing the complexation of the enantiomers of hydrophobic amino acids to the chiral selector BSA enables the exploration of process conditions to maximise purity Pu_m and recovery Re_m in the membrane ultrafiltration step. For that, Pu_m and Re_m equations are taken independently in a way that first the purity Pu_m equation is the objective function to be maximised for the one-site competition model, using Eqs. (1)-(6), and then after recovery Re_m is calculated for the optimal values obtained for purity Pu_m. The parameters for this optimisation take the values of the thermodynamic constants provided in Table 1 and the fixed total amino acid enantiomer concentrations $C_{D,0} = C_{L,0} = 10^{-4}$ M. Then, the simulations reveal the maxima of purity Pu_m and their corresponding recovery Re_m in the BSA concentration range of $C_{BSA,0} = 10^{-8}$-10^{-1} M and pH range of pH = 0-14 (Fig. 3ab), based on the speciation dictated by the chemical equilibria (1)-(3). In practice, BSA concentrations $C_{BSA,0}$ would be fixed by dissolving the required amount of chiral selector BSA in the aqueous buffer solutions with the pH values required in each case. For these simulations' series, we assumed that the full initial volume V_0 fully converts into the permeate volume V_p, so the volume split ratio V_p/V_0 is equal to 1. This approach gives the same results when taking first recovery Re_m equation as the objective function to be maximised and after calculating purity Pu_m based on recovery Re_m optimal values. Thus, this means that the outcome of these simulations on purity Pu_m and recovery Re_m gives their maxima surfaces as a function of BSA concentration $C_{BSA,0}$ and pH ranges, as represented below (Fig. 3ab).

For the three amino acids under study (Phe, Ala, and Val), the same maxima are predicted due to the similar thermodynamic constants associated to their equilibria (Table 1). For the same initial concentrations of each enantiomer $C_{D,0} = C_{L,0} = 10^{-4}$ M, Pu_m maximum of 0.91 (Fig. 3a, in red) and Re_m maximum of 1.00 (Fig. 3b, in red) are obtained at different $C_{BSA,0}$ and pH values. Thus, it is observed that when the maximum of Pu_m is reached (Fig. 3a, in red) then, at the same $C_{BSA,0}$ and pH conditions, the minimum is obtained for Re_m (Fig. 3b, in blue). This is observed when $C_{BSA,0} \geq C_{D,0} = C_{L,0} = 10^{-4}$ M and

pH = 9.3-9.5. This result agrees with the binding ratio of 1:1 between the zwitterionic form of one amino acid enantiomer and the unprotonated site in the chiral selector BSA, as the model proposes in Eq. (1). Therefore, the membrane process outcome is determined by the trade-off between the purity Pu_m and recovery Re_m in the membrane ultrafiltration step. Amino acid enantiomers concentrations $C_{D,0}$ and $C_{L,0}$ are chosen equal to 10^{-4} M based on the literature [32], indicating that the initial racemic solution concentration needs to be not very high to assume that the membrane ultrafiltration system does not present fouling phenomenon.

The trade-off observed makes desirable the optimisation of the third KPI *PuRe*, which includes both purity Pu_m and recovery Re_m (Table 2), to determine the process conditions for the membrane ultrafiltration step at which the purity Pu_m is most balanced with the recovery Re_m. A U-type optimal *PuRe* surface is obtained in the pH-BSA concentration $C_{BSA,0}$ window at which *PuRe* has a value of around 0.40 for a wide range of combinations of pH and BSA concentration $C_{BSA,0}$. This optimal range corresponds to a value of purity Pu_m = 0.78 and recovery Re_m = 0.70 (Fig. 3c, light blue). Nevertheless, when considering the economics of the process, meaning using the least amount of chiral selector possible, since the use of it is costly, only one maximum appears, which is the one at $C_{BSA,0} = C_{D,0} = C_{L,0} = 10^{-4}$ M and pH = 9.3-9.5 (Fig. 3c, yellow circle). This maximum represents the optimal conditions to reach the enantioenriched permeate point for the membrane ultrafiltration step (Fig. 1c, grey point), starting from the initial racemic feed (Fig. 1c, orange point). A *PuRe* value of 0.40 also indicates that there is still room for improvement until reaching the ideal *PuRe* = 1.00 (so, $Pu_m = Re_m$ = 1.00). For that, two possibilities for improvement arise: trying to improve the current chemical system by a membrane cascade (see section 4.3.3.) or by improving the chemical system itself (see section 4.3.5.).

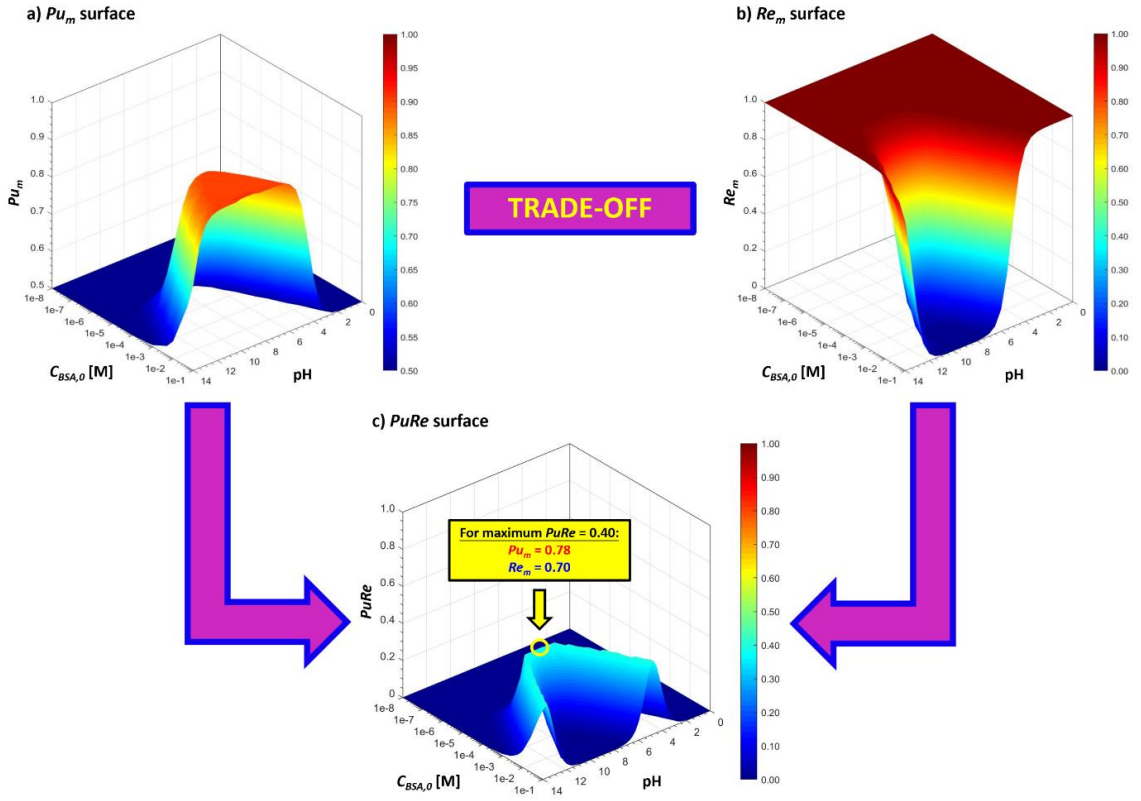

Fig. 3. a) Pu_m, b) Re_m, and c) *PuRe* surfaces as a function of BSA concentration $C_{BSA,0}$ and pH. There is a trade-off between Pu_m (a) and Re_m (b). The optimisation of *PuRe* (c) indicates the best membrane ultrafiltration conditions (light blue region in the U-type surface in c) for the enantioenriched amino acid concentration, especially when considering the minimum use of BSA (yellow circle in c).

4.3.3. The need for a multi-stage membrane approach

Enantiopurity x_D data can be compared with the eutectic point composition $x_{eu,D}$, which is the limit that must be surpassed for the crystallisation of the pure enantiomer (Table 3). The phenylalanine and alanine systems do not meet the condition $x_D > x_{eu,D}$ (9), whereas the valine system does (Table 3). This means that D-valine could be separated with a single-stage membrane ultrafiltration crystallisation process because the enantiomeric enriched point in the ternary phase diagram of valine (Fig. 1c, grey point) would already be inside the two-phase region (Fig. 1c, fuchsia point) where D-valine is the only solid that can crystallise after concentrating the permeate stream. On the contrary,

phenylalanine and alanine would require a multi-stage membrane step to make the enantiomeric fraction x_D surpass their eutectic point compositions $x_{eu,D}$ (Table 3).

Table 3. Comparison of literature eutectic point composition $x_{eu.D}$ [33,34] with predicted enantiomeric purity x_D (here, equal to Pu_m) for the aqueous systems of amino acids Phe, Ala, and Val with chiral selector BSA, at 25ºC. Re_m and *PuRe* parameter values are also shown. *PuRe* value is obtained from its maximisation in the one-site competition model, then Pu_m and Re_m values are related to this *PuRe* maximum.

System	Eutectic point composition, $x_{eu,D}$	x_D (Pu_m, model)	Re_m (model)	*PuRe* (model)
Phenylalanine	0.92			
Alanine	0.80	0.78	0.70	0.40
Valine	0.73			

A multi-stage membrane cascade approach (Fig. 4) is proposed in order to find the number of membrane stages *n* required to increase the solvent-free enantiomer fraction x_D.

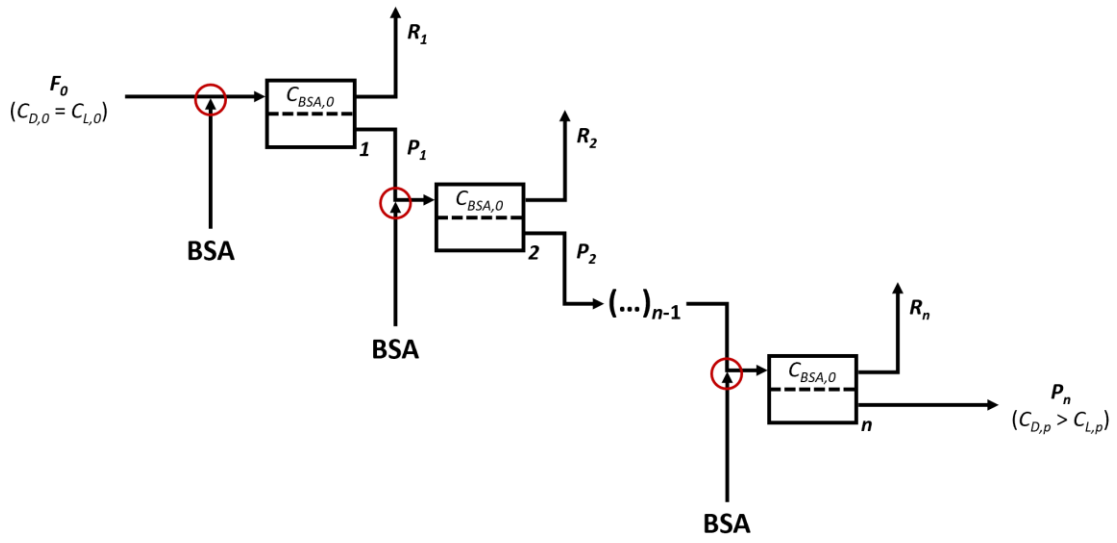

Fig. 4. A multi-stage membrane cascade for the membrane ultrafiltration step in order to enhance the enantiomeric enrichment. The feed F_0 consists of a racemic solution of amino acid to which is added a certain amount of BSA until reaching $C_{BSA,0}$. The equilibrated solution is filtered through the ultrafiltration membrane in stage 1, giving a permeate P_1 enriched with enantiomer D. The enriched permeate stream is fed into the next stage after fresh BSA is added. This process is repeated with *n* membrane stages until fulfilling $x_D > x_{eu,D}$ (9) in the permeate P_n. Retentates streams (R_1 to R_n) have the potential to be recycled in a further approach of the membrane cascade. So far, recycling is not considered in the simulations.

The retentate-permeate splitting effect studied relates the retentate volume V_r with the permeate volume V_p, which informs about how the feed volume V_0 is distributed to the retentate and permeate streams. Then, the retentate-permeate splitting can be seen as a parameter capable to inform about the membrane permeability (which is not explicitly included in our model) with a direct proportional relationship, and so with the effective membrane surface area. A splitting with higher fraction of permeate volume V_p indicates higher membrane permeability and/or effective membrane surface area. Contrarily, a splitting with lower permeate volume V_p proportion indicates lower membrane permeability and/or effective membrane surface area. Both number of membrane stages and splitting effects are studied in the outcome of the membrane ultrafiltration step (Pu_m and Re_m) for the three systems under study (Fig. 5). Phenylalanine, alanine, and valine systems show similar predicted purities when the number of membrane stages n and the retentate-permeate splitting effects are varied (Fig. 5). The main difference among these systems is the eutectic point composition $x_{eu,D}$ that phenylalanine, alanine, and valine require to surpass for the crystallisation of the pure D-form (Table 3, Fig. 5 blue dotted line). Note that only the valine system meets the condition $x_D > x_{eu,D}$ (9) with a single membrane stage, as concluded earlier. The other two systems (Phe and Ala) require one more membrane stage to achieve such condition (9) (Fig. 5). Therefore, a 2-stage membrane ultrafiltration step for phenylalanine and alanine systems is needed for the feasible crystallisation of their pure enantiomers. Note that the different retentate-permeate splitting, that are related with the membrane permeability and/or effective membrane surface area, is predicted to have no effect on the purity obtained for the same membrane stage (Fig. 5). The recoveries of the three systems are different (Fig. 5). The predicted Re_m for valine will be higher than the ones for phenylalanine and alanine since the incorporation of an extra membrane stage translates to a decrease in Re_m (Fig. 5). Moreover, this change in the recovery will not only be affected by the number of membrane stages n but also by the retentate-permeate splitting. In addition, we observe that when the permeate volume V_p decreases to the detriment of the retentate volume V_r, then Re_m also decreases, even in the same membrane stage (Fig. 5).

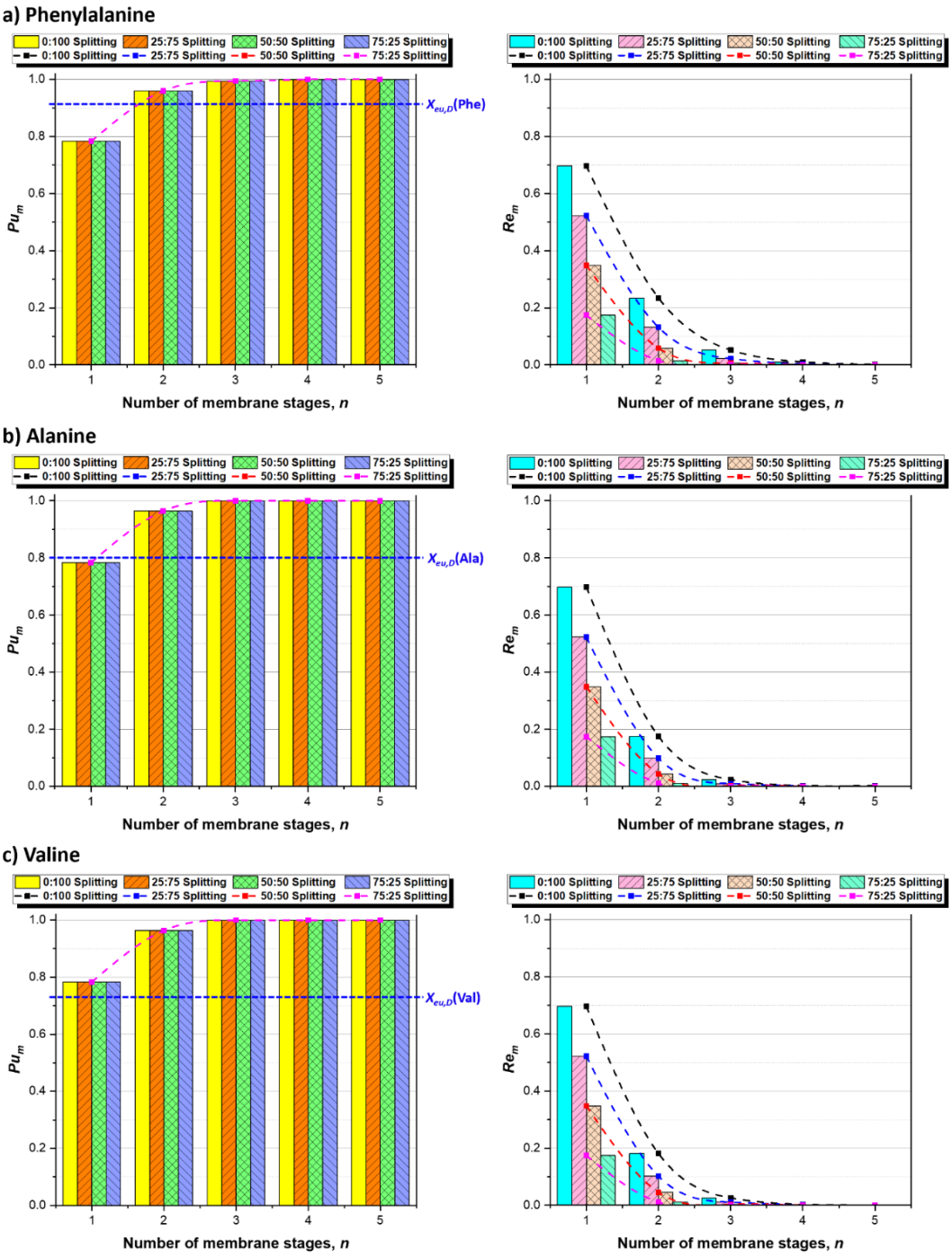

Fig. 5. Predicted Pu_m and Re_m obtained depending on the retentate-permeate splitting and number of membrane stages n applied in the membrane ultrafiltration step, for the three systems under study: a) phenylalanine, b) alanine, and c) valine. The blue dotted line in purity graphs represents the eutectic point composition $x_{eu,D}$ at 25ºC that each amino acid system requires to surpass to make feasible, in terms of purity, the crystallisation of their pure D-form: a) $x_{eu,D}$(Phe) = 0.92, b) $x_{eu,D}$(Ala) = 0.80, and c) $x_{eu,D}$(Val) = 0.73.

4.3.4. Model validation

The results predicted from the one-site competition model for the membrane ultrafiltration step are validated for a single membrane stage. Several predicted amino acid enantiomers concentrations C_{pre} ($C_{D,p}$ and $C_{L,p}$) of phenylalanine are calculated using Eqs. (1)-(6) of the model and compared to the experimental C_{exp} values found in the literature (Fig. 6) [32].

The model predicts the experimental results better when the amino acid concentrations are low. A major discrepancy between prediction and experiments is observed when the concentrations are increasing (Fig. 6). At higher concentrations, only the D-form concentration is well predicted. The L-form shows higher calculated concentrations C_{pre} than the ones obtained in the experiments, C_{exp}. This last scenario seems to reflect a stronger interaction between the L-form and the chiral selector BSA at higher concentrations than the one predicted by their complexation constant in the model.

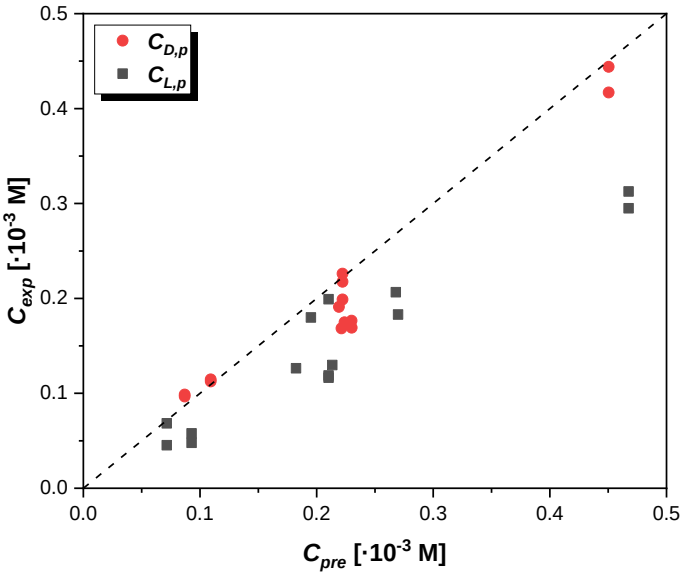

Fig. 6. Experimental permeate amino acid enantiomers concentrations C_{exp} (for Phe: $C_{D,p} = C_{L,p} = 0.3\text{-}5.0 \cdot 10^{-4}$ M) at a chiral selector concentration $C_{BSA,0} = 10^{-4}$ M in the pH range from 3 to 11 [32], versus their predicted concentration C_{pre} values calculated from the one-site competition model equations frame (see Eqs. (1)-(6)). The dashed line is just for comparison between experimental C_{exp} and predicted C_{pre} values.

4.3.5. Description of the ideal BSA-similar chiral selector

We now investigate the sensitivities of the complexation and chiral selector acid-base dissociation constants with respect to the KPIs Pu_m, Re_m, and *PuRe* (Figs. 7-9).

The complexation constant sensitivity study is first conducted for the purity Pu_m that can be achieved by a single-membrane ultrafiltration step. The Pu_m maxima surfaces are different when varying pK_D and pK_L values and keeping all the other parameters in the model constant (Fig. 7).

The enantioenrichment obtained increases when increasing the absolute difference between pK_D and pK_L. The highest Pu_m can be obtained when pK_D = -4.0 and pK_L = -7.0 for the studied conditions (Fig. 7, green box). No enantiomeric enrichment (x_D = 0.5) is obtained when pK_D = pK_L = -5.5 (Fig. 7, red box).

Similar conclusions are obtained when analysing the other two KPIs Re_m and *PuRe* under the same conditions as the Pu_m case (Figs. 8-9).

In the case of recovery Re_m, the width of the well of the maxima surfaces indicating no recovery (Re_m = 0) changes when varying the pK_D and pK_L parameters (Fig. 8). A desirable situation with a larger part of the tested conditions leading to a high Re_m is obtained when the values of pK_D and pK_L have the largest absolute difference (-4.0 and -7.0, respectively) (Fig. 8, green box). The least desirable situation is reached when, again, pK_D and pK_L values are equal (Fig. 8, red box).

The *PuRe* maxima surfaces are qualitatively different when varying pK_D and pK_L values (Fig. 9). It is also observed that *PuRe* can be positive only when pK_D is different than pK_L. Similarly, *PuRe* increases when increasing the absolute difference between pK_D and pK_L. The highest *PuRe* is reached for the surface with pK_D = -4.0 and pK_L = -7.0 (Fig. 9, green box).

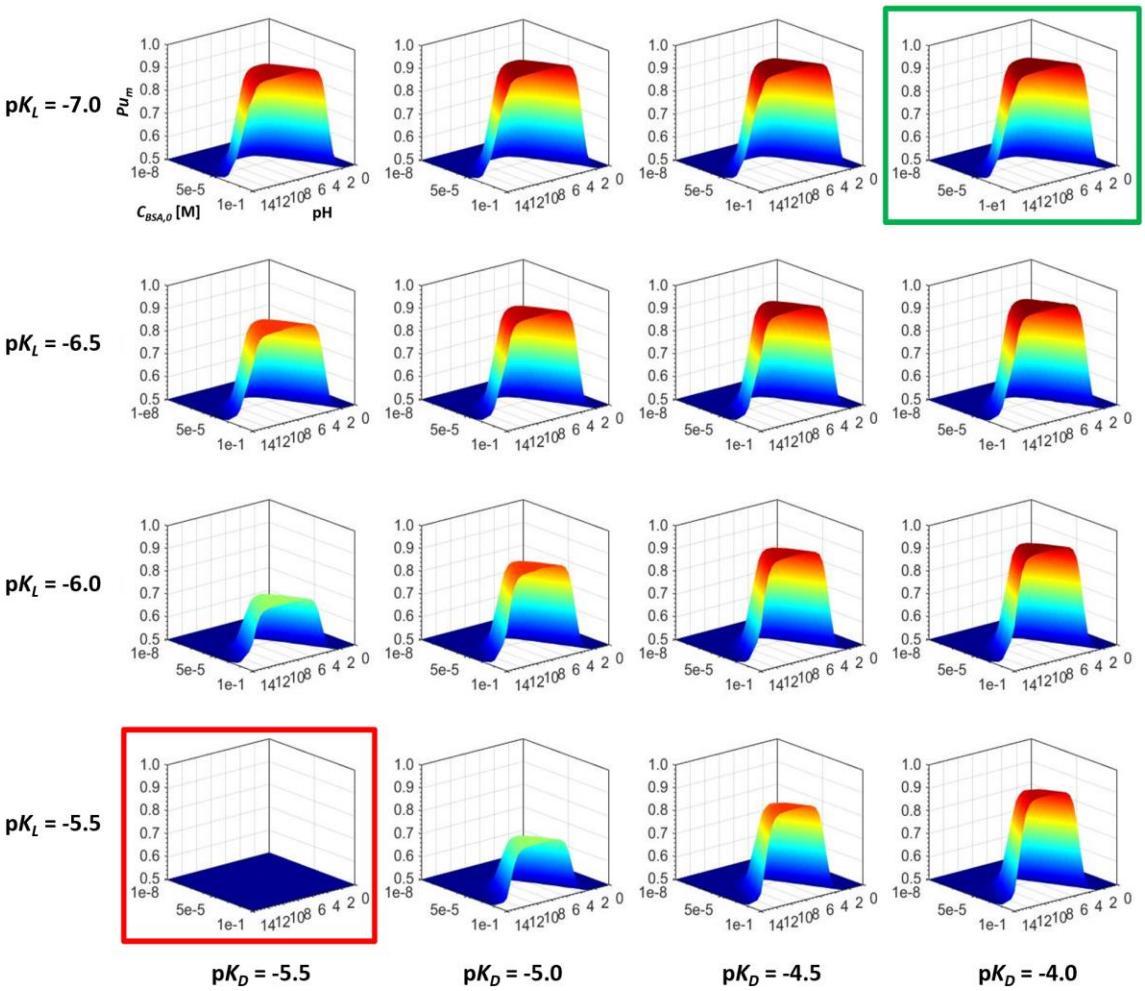

Fig. 7. Complexation constant sensitivity study on purity Pu_m (z-axis). Each Pu_m maxima surface is assessed along BSA concentrations $C_{BSA,0}$ = 10^{-8}-10^{-1} M (y-axis) and pH = 0-14 (x-axis) ranges. Axis titles in all the graphs are as in the top-left graph (pK_D = -5.5 and pK_L = -7.0). The highest Pu_m is reached for differentiated complexation constants pK_D = -4.0 and pK_L = -7.0 (green box), whereas the lowest Pu_m is observed for equal complexation constants pK_D = pK_L = -5.5 (red box). These data are for the phenylalanine system (pK_{a1} = 1.83 and pK_{a2} = 9.13). The alanine and valine systems show similar results.

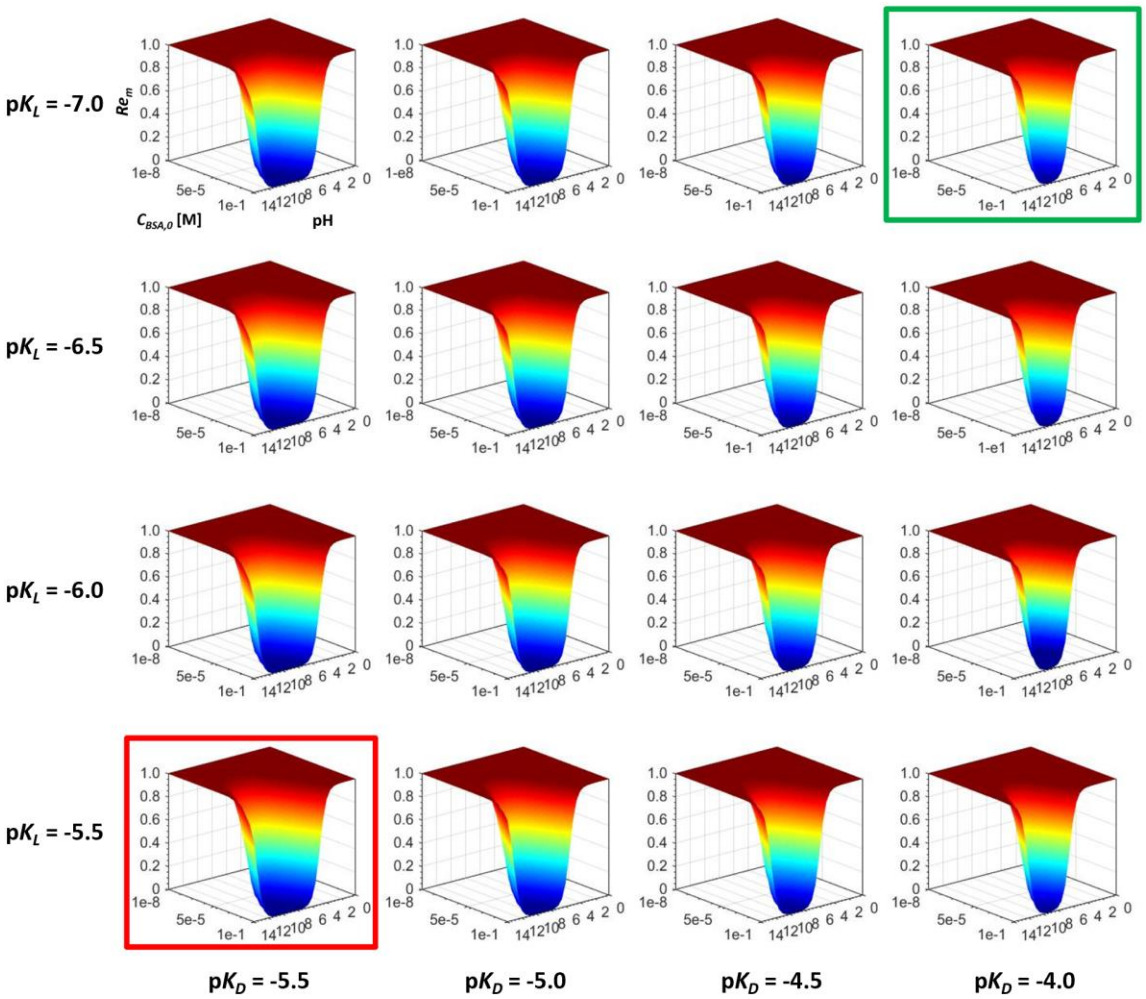

Fig. 8. Complexation constant sensitivity study on Re_m (z-axis). Each Re_m maxima surface is assessed along BSA concentrations $C_{BSA,0}$ = 10^{-8}-10^{-1} M (y-axis) and pH = 0-14 (x-axis) ranges. Axis titles in all the graphs are as in the top-left graph (pK_D = -5.5 and pK_L = -7.0). The highest Re_m is reached for differentiated complexation constants pK_D = -4.0 and pK_L = -7.0 (green box), whereas the lowest Re_m is observed for equal complexation constants pK_D = pK_L = -5.5 (red box). These data are for the phenylalanine system (pK_{a1} = 1.83 and pK_{a2} = 9.13). The alanine and valine systems show similar results.

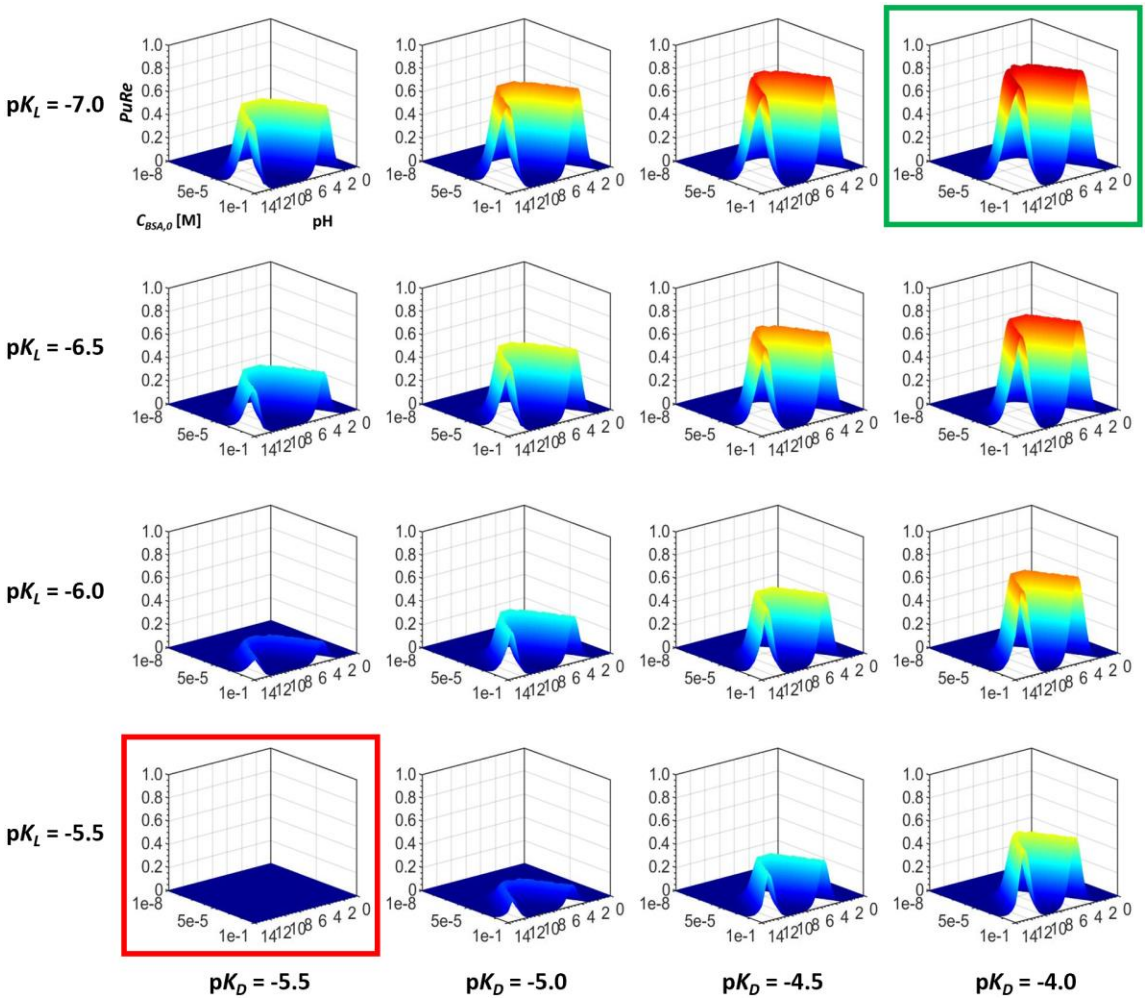

Fig. 9. Complexation constant sensitivity study on *PuRe* (z-axis). Each *PuRe* maxima surface is assessed along BSA concentrations $C_{BSA,0}$ = 10^{-8}-10^{-1} M (y-axis) and pH = 0-14 (x-axis) ranges. Axis titles in all the graphs are as in the top-left graph (pK_D = -5.5 and pK_L = -7.0). The highest *PuRe* value is reached for differentiated complexation constants pK_D = -4.0 and pK_L = -7.0 (green box), whereas the lowest *PuRe* value is observed for equal complexation constants pK_D = pK_L = -5.5 (red box). These data are for the phenylalanine system (pK_{a1} = 1.83 and pK_{a2} = 9.13). The alanine and valine systems show similar results.

The degree of protonation of the specific binding site of the chiral selector also affects the mechanism of complexation between the chiral selector and the enantiomers. For BSA with hydrophobic amino acids, it is described that the specific interaction only occurs with a single unprotonated site of the protein [12–14]. The acid-base dissociation equilibrium constant describes this acid-base behaviour. It is studied how the KPIs related to the membrane step (Table 2) change when the pK_{BSA} changes (Fig. 10). All the other

parameters in the model are kept constant (see Table 1). Pu_m and *PuRe* increase when pK_{BSA} is decreasing. The maximum values for both parameters are obtained when pK_{BSA} = 0, and the minimum values are obtained for the highest pK_{BSA} tested (pK_{BSA} = 14.0) (Fig. 10). Re_m shows the opposite behaviour. It increases when increasing pK_{BSA}. Maximum values for Re_m are obtained at pK_{BSA} = 14.0 and minimum values at pK_{BSA} = 0 (Fig. 10). It is also predicted that the pH operation window at which the highest *PuRe* values are obtained expands when decreasing the pK_{BSA} (Fig. 10, purple arrow). The best operation conditions, meaning that the highest values for *PuRe* with the largest pH operation window at the lowest and thus most economical BSA concentrations $C_{BSA,0}$, are achieved for the three KPIs (Pu_m, Re_m, and *PuRe)* at pK_{BSA} = 0 (Fig. 10, green box) and the worst ones at pK_{BSA} = 14.0 (Fig. 10, red box).

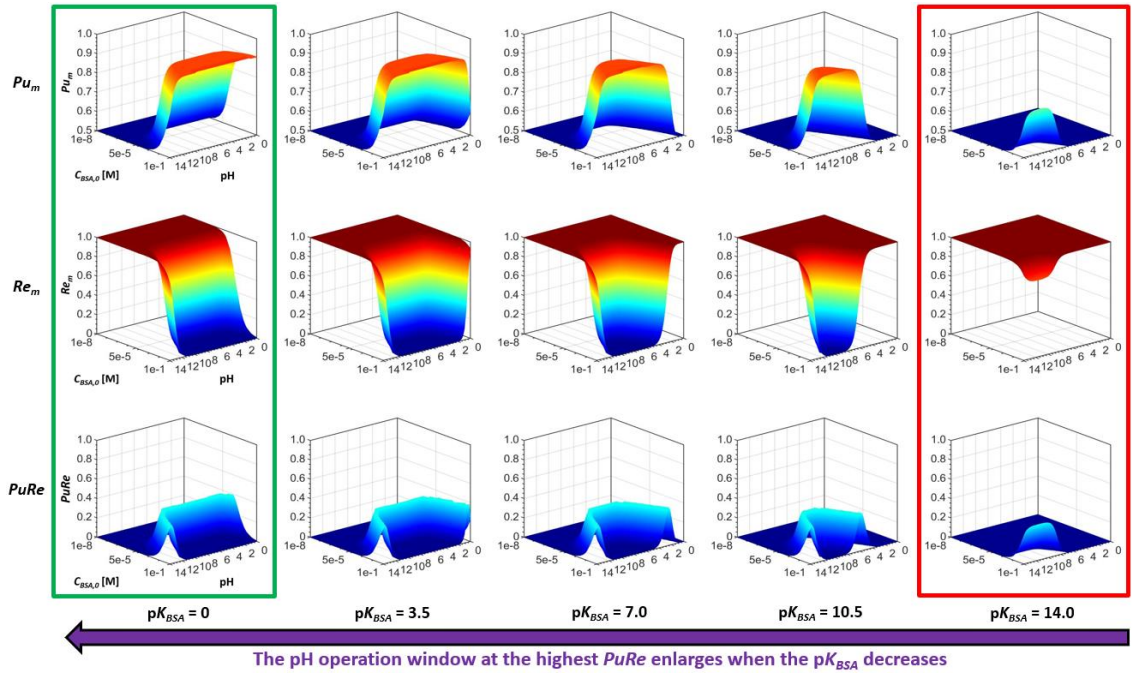

Fig. 10. Chiral selector acid-base dissociation constant sensitivity study on Pu_m, Re_m, and *PuRe* (z-axis). Each parameter maxima surface is assessed along BSA concentrations $C_{BSA,0}$ = 10^{-8}-10^{-1} M (y-axis) and pH 0-14 (x-axis) ranges. Axis titles in all the graphs columns are as in the first left column of graphs (pK_{BSA} = 0, green box). The pH operation window with the highest PuRe values grows from pK_{BSA} = 14.0 to pK_{BSA} = 0 (purple arrow). The best operation conditions are reached at the lowest pK_{BSA} (pK_{BSA} = 0, green box) and the worst ones are predicted for the highest pK_{BSA} (pK_{BSA} = 14.0, red box). These data are for phenylalanine system (pK_{a1} = 1.83 and pK_{a2} = 9.13). The alanine and valine systems show similar results.

We think that the results showed in the previous sensitivity studies for both types of thermodynamic constants that involve BSA as chiral selector, pK_D/pK_L and pK_{BSA}, might be translated for any BSA-similar chiral selector. That is, other chiral selectors which share the type of interaction, complexation mechanism, and similar binding site with BSA are expected to behave in the same way with hydrophobic amino acids. The ideal BSA-similar chiral selector should bear an unprotonated binding site for a large pH range (low pK_{BSA}) (Fig. 10) and very different complexation constants for each enantiomer, meaning a $\left| pK_D - pK_L \right| \geq$ 2-3 (Figs. 7-9). These are the main chiral selector properties that will enable sufficient enantiomeric enrichment, according to Eq. (9), with also enough recovery for the crystallisation of the pure enantiomer in the next steps of the chiral resolution process.

4.3.6. Feasibility of the coupled crystallisation step

Once the enantiomeric purity requirement is fulfilled, cooling crystallisation can be applied just after the membrane ultrafiltration step or a concentration step may be needed first. Furthermore, the recovery for the overall process Re_p can be determined when the crystallisation step is considered in the model.

The concentration and crystallisation steps are assumed to be coupled to the membrane ultrafiltration step as represented in the phase diagram (Fig. 1c, fuchsia and yellow points). First, the permeate solution is concentrated from $C_{D,p}$ to $C^*_{D,T}$ and, then, this concentrate is cooled until reaching $C^*_{D,T'}$ to permit the crystallisation of the D-form of the different amino acids considered (Phe, Ala, and Val). For this thermodynamic process, the following solubilities of the D-form of the amino acids studied were considered: $C^*_{D,T}$ = 56.4 (Phe), 292.9 (Ala), 78.3 mg·g^{-1} (Val) and $C^*_{D,T'}$ = 20.3 (Phe), 107.4 (Ala), and 49.5 mg·g^{-1} (Val). These solubilities were determined experimentally with the TV and EqC methods. Also, it is implied that only the D-form can crystallise because of meeting condition $x_D > x_{eu,D}$ (9) at the steady-state of the continuous process, as explained in section 4.3.1.2.

A concentration step is required between the membrane ultrafiltration and selective cooling crystallisation steps. The concentration gap between the membrane ultrafiltration and crystallisation steps is about 10^4-$2 \cdot 10^5$ times, when using the concentration levels reported in the literature for the membrane ultrafiltration step [32]. Specifically, the concentration factors F calculated with Eq. (10) are, from the highest to the lowest: $1.9 \cdot 10^5$ (Ala) > $1.5 \cdot 10^5$ (Phe) > $9.6 \cdot 10^4$ (Val), indicating a demanding process in terms of concentration process efficiency. The recoveries for each step Re_m and Re_c and for the overall process Re_p are illustrated below (Fig. 11) for different retentate-permeate splitting factors.

The membrane ultrafiltration recovery Re_m followed the same decreasing pattern with the retentate-permeate splitting ratio observed before (Fig. 5). The valine system has the highest Re_m value, then phenylalanine, and the lowest value is for alanine. The crystallisation recovery Re_c does not depend on the retentate-permeate splitting and is higher for phenylalanine and alanine (both similar, ca. 65%) than valine system (ca. 40%). The overall process recovery Re_p decreases with the retentate-permeate splitting ratio and the highest value is predicted for valine, then phenylalanine, and the lowest value is predicted for the alanine system. Therefore, the splitting causes a decrease in Re_m, and then also in Re_p.

The highest overall process recoveries Re_p are expected for those systems that only require one membrane stage in the ultrafiltration step and have solubilities with strong temperature dependence. The number of membrane stages n seems more impactful than solubility, for temperature-dependent solubilities.

A coupled chiral resolution process consisting of a membrane ultrafiltration step followed by a concentration and selective cooling crystallisation steps may be envisaged despite the concentration gap found for the systems investigated here.

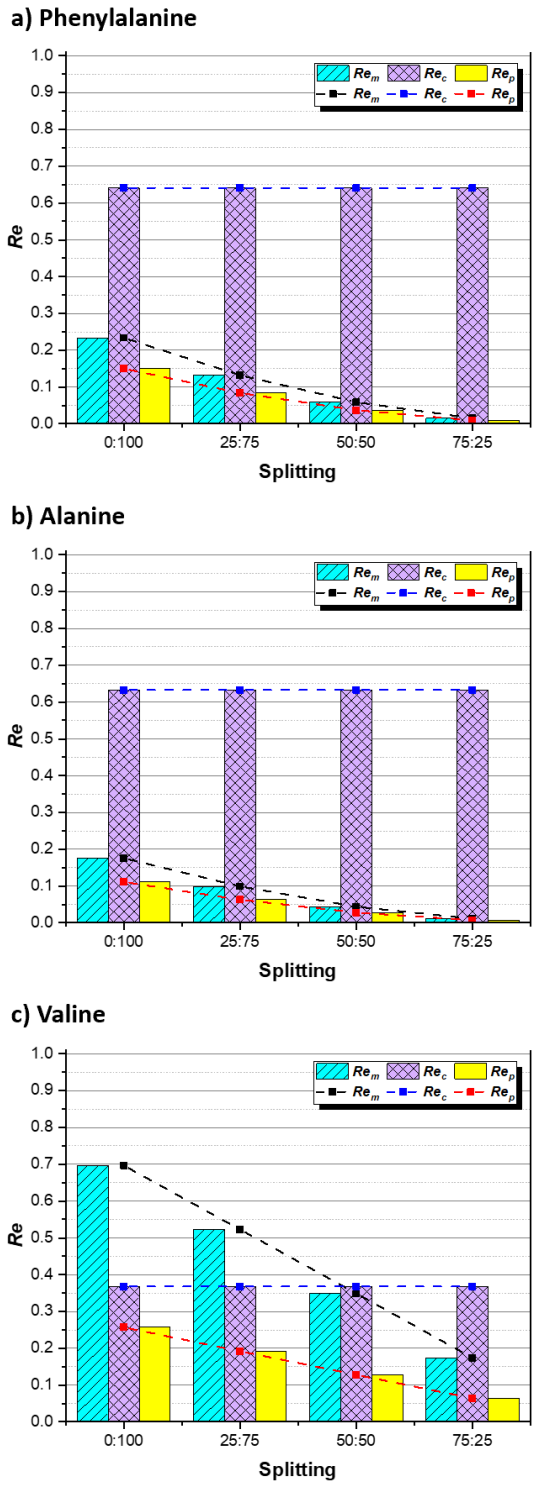

Fig. 11. Effect of retentate-permeate splitting on the predicted recoveries for the membrane ultrafiltration and crystallisation steps (Re_m and Re_c, respectively) and overall process (Re_p) for the three amino acid systems under study: a) Phe, b) Ala, and c) Val.

4.4. Discussion

The process optimisation of the membrane ultrafiltration step determines the best conditions to separate one enantiomer from the other as much as possible and, at the same time, obtaining the highest recovery Re_m possible for the desired enantiomer in the permeate. The optimisation permits to find and treat the trade-off behaviour between both purity Pu_m and recovery Re_m for the amino acids aqueous systems studied: phenylalanine, alanine, and valine. The one-site competition model predicts a maximum Pu_m and minimum Re_m for $C_{BSA,0} \geq C_{D,0} = C_{L,0} = 10^{-4}$ M and pH = 9.3-9.5, in agreement with the binding ratio of 1:1 between the zwitterionic form of one amino acid enantiomer and the unprotonated site in the chiral selector BSA, previously reported in the literature for tryptophan in water [13,14]. The optimisation of *PuRe* and a process economics consideration predicts the optimal process conditions for the membrane ultrafiltration step at $C_{BSA,0} = C_{D,0} = C_{L,0} = 10^{-4}$ M and pH = 9.3-9.5 (Fig. 3c, yellow circle).

The model predicts a single-stage membrane ultrafiltration for valine in terms of enantiopurity x_D. However, it predicts at least one stage more for the other two systems phenylalanine and alanine in order to meet condition $x_D > x_{eu,D}$ (9) for the crystallisation of a pure enantiomer (Fig. 5). For all the systems, the Pu_m obtained is very similar showing no differences with retentate-permeate splitting ratio and following the same pattern with the number of membrane stages n. The last fact occurs because of taking the same complexation constants (pK_D and pK_L) for phenylalanine as for alanine and valine calculations, assuming that hydrophobic amino acids with similar structure should have similar interactions with the same chiral selector. In that way, Pu_m is expected to change more when systems are more different between them, that is, having different interaction affinities with the chiral selector. The model predicts higher Re_m in valine than in phenylalanine and alanine due to the incorporation of an extra membrane stage, fact seen as the trigger for the decrease in Re_m.

The membrane ultrafiltration model, validated with experimental data obtained from the literature for phenylalanine system [32], predicts better results at low concentrations.

At higher concentrations, D-form concentration is adjusted to its prediction, whereas L-form shows higher predicted concentrations values than the ones obtained in the experiments (Fig. 6). This fact seems to reflect a stronger interaction between L-form and BSA at higher concentrations. This observation can be of utility for the refinement of equilibria complexation constants, a procedure that might help to predict or give a more accurate estimation of these thermodynamic constants in accordance to experiments.

The complexation and chiral selector acid-base dissociation constants sensitivity studies (Figs. 7-10) not only confirmed the modelled behaviour reported [13,14], but also affirmed that an ideal BSA-similar chiral selector should bear an unprotonated binding site for a large pH range and very different complexation constants for each enantiomer, meaning that a $\left| pK_D - pK_L \right| \geq$ 2-3. These are the main chiral selector properties that will make possible the obtaining of sufficient enantiomeric enrichment with also enough recovery in the membrane ultrafiltration step. Furthermore, we believe that the type of sensitivity studies shown can be useful even when considering BSA-different chiral selectors. For them, new parameters and values might be required, but the importance of assessing the KPIs (Table 2) in the way we describe here will permit researchers to optimise the chiral selectivity conditions in the process, which are tightly linked to the overall process outcome. We also think that molecular docking and molecular dynamics simulations would be helpful tools for the major understanding of the fit between the enantiomers and chiral selector systems which require molecular interaction specificity.

The feasibility study for the coupling of the cooling crystallisation step confirms that a concentration step (e.g. distillation or simple evaporation) is required between the membrane ultrafiltration and the crystallisation steps. The concentration factors *F* for the three amino acid systems investigated (Phe, Ala, and Val) are found high, indicating a demanding process in terms of concentration process efficiency. However, when analysing the recoveries for the membrane ultrafiltration Re_m and crystallisation Re_c steps as well as for the overall process Re_p, we can infer that, when saving the concentration step is possible or this is small, this process in a whole could become feasible and be able

to produce good recoveries for those systems that only require one membrane stage in the ultrafiltration step and have solubilities with a strong temperature dependence.

Finally, we envisage that the overall process recovery Re_p can be increased when applying the recycling step in the process (Fig. 12a). This new step can be easily understood as the introduction of a recycled enantioenriched solution which includes: the retentate (or retentates, if several membrane stages apply) in the membrane ultrafiltration step, the pure solvent from the concentration step, and the enantioenriched remaining solution from the selective crystallisation step. This is shown in the overall process represented in the ternary phase diagram (Fig. 12b, green and white points).

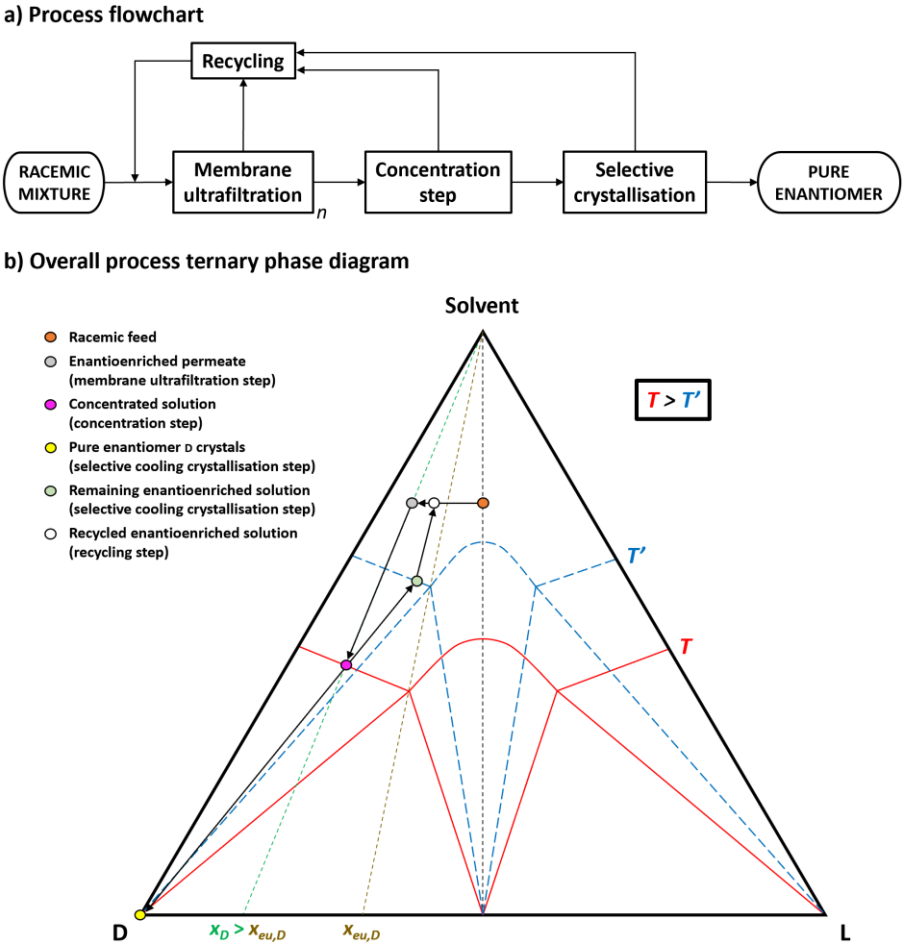

Fig. 12. a) Process flowchart starting from an equilibrated racemic mixture (feed) until the obtaining of a pure enantiomer and b) overall process ternary phase diagram for the resolution of a racemic compound-forming system, now completed with the recycling step.

4.5. Conclusions

The one-site competition model is well applicable to describe the complexation interaction between the chiral selector BSA and the hydrophobic amino acids phenylalanine, alanine, and valine in aqueous media. In the membrane ultrafiltration step, a trade-off exists between the purity and recovery in the permeate because the same complexation conditions that favoured purity also favoured the binding of both competing enantiomers to BSA. Although with different binding proportion of both enantiomers to BSA, the recovery decreases. The conditions to obtain the optimal purity and recovery correspond to $C_{BSA,0} = C_{D,0} = C_{L,0}$, based on the minimum use of BSA in view of its high cost, and pH = 9.3-9.5. The model predicts that, starting from a racemic solution, a single-stage membrane ultrafiltration can lead to a purity that is enriched sufficiently beyond the eutectic point composition for the valine system to enable, after a concentration step, the continuous crystallisation of the pure enantiomer solid product. However, for those systems with a more demanding eutectic point composition, such as phenylalanine and alanine, more membrane stages are needed. The sensitivity studies for the complexation and chiral selector acid-base dissociation constants predict that an optimal chiral selector similar to BSA should bear an unprotonated binding site for a large pH range, so a low pK_{BSA}, and highly distinct complexation constants for the two enantiomers with $|pK_D - pK_L|$ equal or larger than 2. The overall process obtains the optimal recovery when the concentration gap between the membrane ultrafiltration and crystallisation steps is saved or small and for those systems which only require one membrane stage in the ultrafiltration step and have solubilities with a strong temperature dependence. We envisage that the sensitivity study of other chiral selectors and its optimisation in a similar way as described here along with the introduction of a recycling step, which will recirculate a partial enantioenriched solution into the process, will increase the overall process recovery not only for the systems investigated here, but also for other chiral systems. Therefore, this novel membrane ultrafiltration-crystallisation resolution process has application potential for the enantioseparation of racemic solutions of racemic compound-forming systems.

4.6. Notation

Ala	Alanine
BSA	Bovine serum albumin
C	Concentration [M]
C_{BSA}	Concentration of chiral selector BSA with unprotonated complexation site [M]
C_{BSA+}	Concentration of chiral selector BSA^+ with protonated complexation site [M]
$C_{BSA,0}$	Total (feed/initial) concentration of chiral selector BSA [M]
C_{D+}	Concentration of cation D^+ (amino group protonated) [M]
$C_{D\pm}$	Concentration of zwitterion $D^\pm$ (amino group protonated and carboxyl group deprotonated) [M]
C_{D-}	Concentration of anion D^- (carboxyl group deprotonated) [M]
$C_{D\pm BSA}$	Concentration of complex $D^\pm$BSA [M]
$C_{D,p}$	Total concentration of enantiomer D (all free species) in permeate [M]
$C_{D,r}$	Total concentration of enantiomer D (just free species) in retentate [M]
$C_{D,0}$	Total (feed/initial) concentration of enantiomer D [M]
$C^*_{D,T}$	Solubility concentration for enantiomer D at temperature T [$mg \cdot g^{-1}$]
$C^*_{D,T'}$	Solubility concentration for enantiomer D at temperature T' [$mg \cdot g^{-1}$]
C_{exp}	Experimental concentration [M]
C_{L+}	Concentration of cation L^+ (amino group protonated) [M]
$C_{L\pm}$	Concentration of zwitterion $L^\pm$ (amino group protonated and carboxyl group deprotonated) [M]
C_{L-}	Concentration of anion L^- (carboxyl group deprotonated) [M]
$C_{L\pm BSA}$	Concentration of complex $L^\pm$BSA [M]
$C_{L,p}$	Total concentration of enantiomer L (all free species) in permeate [M]
$C_{L,r}$	Total concentration of enantiomer L (just free species) in retentate [M]
$C_{L,0}$	Total (feed/initial) concentration of enantiomer L [M]
C_{pre}	Predicted concentration [M]

C_w	Concentration of H_2O [M]
C_{w+}	Concentration of H_3O^+ [M]
$C_{x,0}$	Total (feed/initial) concentration of species *x* [M]
$E_{D,p}$	Enantiomeric excess of enantiomer D in the permeate [-]
EqC	Equilibrium concentration method
F_0	Feed stream
F	Concentration factor [-]
$K_{a1,D}$	Dissociation constant of the first proton of enantiomer D [-]
$K_{a2,D}$	Dissociation constant of the second proton of enantiomer D [-]
$K_{a1,L}$	Dissociation constant of the first proton of enantiomer L [-]
$K_{a2,L}$	Dissociation constant of the second proton of enantiomer L [-]
K_{BSA}	Dissociation constant of proton of chiral selector BSA complexation site [-]
K_D	Complexation constant of enantiomer D and chiral selector BSA [-]
K_L	Complexation constant of enantiomer L and chiral selector BSA [-]
KPI	Key performance indicator
n	Number of membrane ultrafiltration stages [stage or stages]
Phe	Phenylalanine
P_n	Permeate stream of stage *n* of the membrane ultrafiltration step
Pu_m	Purity of the membrane ultrafiltration step [-]
PuRe	PuRe of the membrane ultrafiltration step [-]
R_n	Retentate stream of stage *n* of the membrane ultrafiltration step
Re_c	Recovery of the crystallisation step [-]
Re_m	Recovery of the membrane ultrafiltration step [-]
Re_p	Recovery of the overall process [-]
RSD	Relative standard deviation [%]
T	Initial temperature for the cooling crystallisation step [ºC]

T'	Ending temperature for the cooling crystallisation step [ºC]
Trp	Tryptophan
TV	Temperature variation method
V_0	Feed (initial) volume [L]
Val	Valine
V_c	Crystallisation volume [L]
V_p	Permeate volume [L]
V_r	Retentate volume [L]
x_D	Solvent-free enantiomer fraction for enantiomer D [-]
$x_{eu,D}$	Enantiomeric ratio in the eutectic point (also referred as eutectic point composition) for enantiomer D [-]
x_L	Solvent-free enantiomer fraction for enantiomer L [-]

4.7. References

[1] J.E. Rekoske, Chiral separations, AIChE J. 47 (2001) 2–5.

[2] N. Chhabra, M. Aseri, D. Padmanabhan, A review of drug isomerism and its significance, Int. J. Appl. Basic Med. Res. 3 (2013) 16–18.

[3] W.H. Pirkle, C.J. Welch, An improved chiral stationary phase for the chromatographic separation of underivatized naproxen enantiomers, J. Liq. Chromatogr. 15 (1992) 1947–1955.

[4] Y. Yang, B. Su, Q. Yan, Q. Ren, Separation of naproxen enantiomers by supercritical/subcritical fluid chromatography, J. Pharm. Biomed. Anal. 39 (2005) 815–818.

[5] J. Jacques, A. Collet, Enantiomers, racemates and resolutions, John Wiley & Sons, 1981.

[6] H. Lorenz, A. Seidel-Morgenstern, Processes to separate enantiomers, Angew.

Chemie - Int. Ed. 53 (2014) 1218–1250.

[7] S. Mane, Racemic drug resolution: a comprehensive guide, Anal. Methods. 8 (2016) 7567–7586.

[8] I. Ali, V.K. Gupta, H.Y. Aboul-Enein, Chiral resolution of racemic environmental pollutants by capillary electrophoresis, Crit. Rev. Anal. Chem. 38 (2008) 132–146.

[9] R. Kallenborn, H. Hühnerfuss, Chiral environmental pollutants: trace analysis and ecotoxicology, Springer, 2010.

[10] A.A. Basheer, Chemical chiral pollution: impact on the society and science and need of the regulations in the 21st century, Chirality. 30 (2018) 402–406.

[11] R. Xie, L.-Y. Chu, J.-G. Deng, Membranes and membrane processes for chiral resolution, Chem. Soc. Rev. 37 (2008) 1243–1263.

[12] S. Poncet, J. Randon, J.L. Rocca, Enantiomeric separation of tryptophan by ultrafiltration using the BSA solution system, Sep. Sci. Technol. 32 (1997) 2029–2038.

[13] F. Garnier, J. Randon, J.L. Rocca, Enantiomeric separation by ultrafiltration: complexation mechanism of tryptophan analogs to bovine serum albumin, Sep. Purif. Technol. 16 (1999) 243–250.

[14] J. Randon, F. Garnier, J.L. Rocca, B. Maïsterrena, Optimization of the enantiomeric separation of tryptophan analogs by membrane processes, J. Memb. Sci. 175 (2000) 111–117.

[15] H. Lorenz, A. Perlberg, D. Sapoundjiev, M.P. Elsner, A. Seidel-Morgenstern, Crystallization of enantiomers, Chem. Eng. Process. Process Intensif. 45 (2006) 863–873.

[16] H. Lorenz, D. Sapoundjiev, A. Seidel-Morgenstern, Solubility equilibria in chiral systems and their importance for enantioseparation, Eng. Life Sci. 3 (2003) 132–

136.

[17] J.H. ter Horst, C. Schmidt, J. Ulrich, Fundamentals of industrial crystallization, in: Handb. Cryst. Growth Bulk Cryst. Growth Second Ed., 2014: pp. 1317–1349.

[18] S. Srisanga, J.H. Ter Horst, Racemic compound, conglomerate, or solid solution: phase diagram screening of chiral compounds, Cryst. Growth Des. 10 (2010) 1808–1812.

[19] L.C. Sögütoglu, R.R.E. Steendam, H. Meekes, E. Vlieg, F.P.J.T. Rutjes, Viedma ripening: a reliable crystallisation method to reach single chirality, Chem. Soc. Rev. 44 (2015) 6723–6732.

[20] L. Gou, S. Robl, K. Leonhard, H. Lorenz, M. Sordo, A. Butka, S. Kesselheim, M. Wolff, A. Seidel-Morgenstern, K. Schaber, A hybrid process for chiral separation of compound-forming systems, Chirality. 23 (2011) 118–127.

[21] S. Robl, L. Gou, A. Gere, M. Sordo, H. Lorenz, A. Mayer, C. Pauls, K. Leonhard, A. Bardow, A. Seidel-Morgenstern, K. Schaber, Chiral separation by combining pertraction and preferential crystallization, Chem. Eng. Process. Process Intensif. 67 (2013) 80–88.

[22] H. Kaemmerer, Z. Horvath, J.W. Lee, M. Kaspereit, R. Arnell, M. Hedberg, B. Herschend, M.J. Jones, K. Larson, H. Lorenz, A. Seidel-Morgensten, Separation of racemic bicalutamide by an optimized combination of continuous chromatography and selective crystallization, Org. Process Res. Dev. 16 (2012) 331–342.

[23] J. von Langermann, M. Kaspereit, M. Shakeri, H. Lorenz, M. Hedberg, M.J. Jones, K. Larson, R. Herschend, R. Arnell, E. Temmel, J.-E. Ba, A. Kienle, A. Seidel-Morgenstern, Design of an integrated process of chromatography, crystallization and racemization for the resolution of 2′,6′-pipecoloxylidide (PPX), Org. Process Res. Dev. 16 (2012) 343–352.

[24] M.A. Reus, A.E.D.M. van der Heijden, J.H. ter Horst, Solubility determination

from clear points upon solvent addition, Org. Process Res. Dev. 19 (2015) 1004–1011.

[25] GAMS Software GmbH, GAMS, (2019). https://www.gams.com/ (accessed August 5, 2019).

[26] GAMS Software GmbH, GAMS solver manual, (2020). https://www.gams.com/latest/docs/S_MAIN.html (accessed May 21, 2020).

[27] TheMathWorks, MATLAB, (2019). https://uk.mathworks.com/?s_tid=gn_logo (accessed August 5, 2019).

[28] S. Dirkse, M.C. Ferris, J. Ramakrishnan, GDXMRW: interfacing GAMS and MATLAB, (2014). https://www.gams.com/latest/docs/T_GDXMRW.html (accessed August 5, 2019).

[29] A. Higuchi, T. Hashimoto, M. Yonehara, N. Kubota, K. Watanabe, S. Uemiya, T. Kojima, M. Hara, Effect of surfactant agents and lipids on optical resolution of amino acid by ultrafiltration membranes containing bovine serum albumin, J. Memb. Sci. 130 (1997) 31–39.

[30] F.A. Carey, R.M. Giuliano, Organic chemistry, 10th ed., McGraw-Hill Education, New York, 2016.

[31] J. Romero, A.L. Zydney, Staging of affinity ultrafiltration processes for chiral separations, J. Memb. Sci. 209 (2002) 107–119.

[32] J. Tian, M. Pan, Y. Ma, J.W. Chew, Effect of membrane fouling on chiral separation, J. Memb. Sci. 593 (2019) 117352.

[33] M. Klussmann, H. Iwamura, S.P. Mathew, D.H. Wells, U. Pandya, A. Armstrong, D.G. Blackmond, Thermodynamic control of asymmetric amplification in amino acid catalysis, Nature. 441 (2006) 621–623.

[34] M. Klussmann, A.J.P. White, A. Armstrong, D.G. Blackmond, Rationalization and

prediction of solution enantiomeric excess in ternary phase systems, Angew. Chemie - Int. Ed. 45 (2006) 7985–7989.

CHAPTER 5

5. Enantioselective Liquid-Liquid Extraction and Crystallisation of Chiral Compounds in a Green Chiral Solvent

Jose Capdevila-Echeverria, Raghunath Venkatramanan, Joop H. ter Horst

Chiral separation will increase its importance in the pharmaceutical, pesticide, cosmetic, and food industries in the next years. This is because future product molecules will be larger and contain more stereocentres while their purity will need to meet increasingly demanding requirements to fulfil health, crop, and environmental purposes and regulations. Newly developed chiral solvents open the door to novel chiral resolution processes based on the physicochemical differences of enantiomers in optically active solvents. The dipolar aprotic chiral solvent cyrene shows potential of application at industrial scale due to its biorenewable nature. The combination of interests to study the enantiomeric recognition of chiral solvents and the lack of literature on the green and sustainable cyrene lead us to investigate its potential use in enantioselective liquid-liquid extraction and crystallisation as chiral resolution techniques. Here, we aim to establish the extent of cyrene's chiral recognition power using the chiral compounds mandelic acid and naproxen by means of spectroscopic techniques and thermodynamic measurements. We found that FTIR and Raman spectra suggest certain enantiomeric recognition of cyrene. Unfortunately, the use of cyrene as a solvent in enantioselective liquid-liquid extraction is hampered by the miscibility of cyrene with many organic solvents as well as water. However, the solubility of the two mandelic acid enantiomers in cyrene is significantly different (10-20 mg/g) in the range of temperatures between 36-46ºC, with the solubility of L-mandelic acid being the highest. This solubility difference could be large enough to enable the chiral resolution of mandelic acid using cyrene as solvent by crystallising D-

mandelic acid under conditions where L-mandelic acid is supersaturated but still in the metastable zone.

5.1. Introduction

A chiral compound exists in two enantiomers which are stereoisomeric molecules that are images of each other and non-superposable [1]. The enantiomers of a chiral drug may differ significantly in their bioavailability, metabolism, elimination, potency, and selectivity for receptors, transporters, and/or enzymes, and toxicity inside the living organisms [2]. For instance, L-DOPA (levodopa) is used for the treatment of Parkinson disease whereas its counter enantiomer D-DOPA provokes agranulocytosis [3]. The chiral separation of racemic mixtures or impure enantiomers would prevent such undesired effects in the absence of in vivo racemization. Therefore, chiral resolution processes are of major significance in industries such as pharmaceuticals, agrochemicals, food, and cosmetics [4,5]. The importance of these kind of separation processes will increase in the future when larger molecules with higher chiral complexity will be manufactured and will need to meet high standard specifications and regulations.

A wide variety of techniques for chiral separations have been developed in the past. Some techniques mimic the way biological systems distinguish chirality. Others exploit minor differences in physical properties or interactions with other chemical entities. The main chiral separation methodologies are: crystallisation, kinetic resolution, reaction/resolution combinations, membrane-based separations, and liquid chromatography [6,7]. Another chiral resolution methodology is based on the traditional liquid-liquid extraction technique. Works on enantioselective liquid-liquid extraction (ELLE) have been explored from more than half a century ago [8]. However, this methodology has only been reported by using host-guest chemistry with the presence of additional species other than the racemate and liquid solvents [8–10]. Chiral selectivity in ELLE could be achieved using a chiral solvent as one of the liquid phases of the extraction which, ideally, would selectively capture one of the enantiomers of the racemate. Then, a

basic extraction process involving the two enantiomers and the chiral and achiral liquid phases would result in the complete or partial separation of the enantiomers.

The potential of chiral solvents to discriminate between both enantiomers in a racemic mixture through specific enantioselective interactions has been investigated from the point of view of an enantioselective crystallisation, focusing on both thermodynamics and kinetics aspects [7,11–13]. A thermodynamic asymmetry in the solubility phase diagrams might be observed when using chiral solvents because of the formation of specific diastereomeric complexes which have different physical properties that could be employed for resolution processes [11,12]. Differences in the metastable zone width (MSZW) with regard to primary nucleation between the enantiomers of mandelic acid in different chiral solvents have been found [13], which led to the successful racemate resolution by means of both preferential nucleation and preferential crystallisation [13].

Here we report the potential of the chiral solvent cyrene for its application in chiral resolution processes based on enantioselective liquid-liquid extraction and crystallisation. Cyrene ((-)-dihydrolevoglucosenone, CAS Number: 53716-82-8, Fig. 1) is a bio-based organic chiral molecule derived from cellulose which demonstrates significant promise as a dipolar aprotic solvent [14,15]. It is one of the first true greener solvents since it is produced from renewable resources and it is safe for end of life disposal, decomposing into CO_2 and H_2O [15–17]. It has been found to be a safer alternative to common solvents, such as *N*-methyl-2-pyrrolidone (NMP) and *N*,*N*-dimethylformamide (DMF), which are of health concern due to its acute inhalation, dermal, and reproductive toxicity and because they irritate the eyes and skin [18,19]. It is therefore a potential green and sustainable solvent candidate for industrial physicochemical applications [15–17,20]. We analyse how the optically active solvent may affect differently one specific enantiomeric form of the chiral compounds mandelic acid and naproxen by means of spectroscopic techniques. We also carry out a miscibility study of cyrene with several achiral solvents alongside a solubility study of racemic mandelic acid in different solvent candidates. This is to assess the capability of cyrene to be used as a chiral extracting solvent in the enantioselective

liquid-liquid extraction of mandelic acid enantiomers. In addition, solubility measurements of mandelic acid are done to explore the existence of solubility differences between its enantiomers.

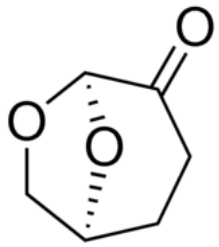

Fig. 1. Chemical structure of the chiral dipolar aprotic solvent cyrene.

5.2. Experimental section

5.2.1. Materials

(*RS*)-(±)-mandelic acid (DL-mandelic acid; Tokyo Chemical Industry UK Ltd., >99%; and Sigma-Aldrich from Merck, ≥99%), (*R*)-(-)-mandelic acid (D-mandelic acid; Tokyo Chemical Industry UK Ltd., >99%; and Sigma-Aldrich from Merck, ≥99%), (*S*)-(+)-mandelic acid (L-mandelic acid; Tokyo Chemical Industry UK Ltd., >99%; and Sigma-Aldrich from Merck, ≥99%), (*RS*)-(±)-naproxen (Tokyo Chemical Industry UK Ltd., >98%), (*S*)-(+)-naproxen (Tokyo Chemical Industry UK Ltd., >99%), 1,2-dichloroethane (anhydrous, Sigma-Aldrich, 99.8%), 1,4-dioxane (anhydrous, Sigma-Aldrich, 99.8%), 1-bromobutane (Sigma-Aldrich, 99%), 1-butanol (Sigma-Aldrich, ≥99%), 1-nonanol (Sigma-Aldrich, ≥98.0%), 1-octanol (anhydrous, Sigma-Aldrich, ≥99%), 1-pentanol (Sigma-Aldrich, ≥99%), 3-methyl-1-butanol (anhydrous, Sigma-Aldrich, ≥99%), 3-pentanone (Sigma-Aldrich, ≥99%), 4-methyl-2-pentanone (Sigma-Aldrich, ≥99.5%), acetone (Sigma-Aldrich, ≥99.9%), acetonitrile (anhydrous, Sigma-Aldrich, 99.8%), anisole (anhydrous, Sigma-Aldrich, 99.7%), chloroform (Sigma-Aldrich, ≥99.5%), cyclohexane (anhydrous, Sigma-Aldrich, 99.5%), cyrene ((1*S*,5*R*)-6,8-dioxabicyclo[3.2.1]octan-4-one or (-)-dihydrolevoglucosenone, Circa Group Pty Ltd., 99.78%), diethyl ether (Sigma-Aldrich, ≥99.8%), dimethyl sulfoxide (anhydrous, Sigma-

Aldrich, ≥99.9%), ethanol (anhydrous, Sigma-Aldrich, ≥99.0%), ethyl acetate (anhydrous, Sigma-Aldrich, 99.8%), isopropanol (Sigma-Aldrich, ≥99.7%), methyl *tert*-butyl ether (anhydrous, Sigma-Aldrich, 99.8%), *N*,*N*-dimethylformamide (anhydrous, Sigma-Aldrich, 99.8%), *n*-heptane (Sigma-Aldrich, ≥99%), *n*-hexane (anhydrous, Sigma-Aldrich, ≥97.0%), nitromethane (Sigma-Aldrich, ≥98.5%), pyridine (Sigma-Aldrich, ≥99.9%), tetrahydrofuran (anhydrous, Sigma-Aldrich, ≥99.9%), toluene (anhydrous, Sigma-Aldrich, 99.8%), and xylenes (Sigma-Aldrich, ≥98.5%). Milli-Q water was taken from a Merck Millipore purification system and had a resistivity of 18.2 MΩ·cm at 25°C.

5.2.2. Methods

5.2.2.1. Spectral analysis of undersaturated solutions

The undersaturated cyrene solutions were prepared by dissolving separately 1000 mg of DL-, L-, and D-mandelic acid in 6.25 g of cyrene, in three different vials at 25ºC. For naproxen, 200 mg of (*RS*)- and (*S*)-naproxen were dissolved separately in 6.25 g of cyrene, in two different vials at 25ºC. Undersaturated solutions of enantiopure and racemic mandelic acid and naproxen were prepared with concentrations of 160 mg/g and 32 mg/g, respectively. A blank solution that only contained cyrene was also prepared as a reference for spectrophotometric measurements. Samples were magnetically agitated at 1000 rpm for 3 days. Complete dissolution of all the samples was reached after 3 days, obtaining for all clear solutions (transparent). Cyrene is light yellow per se (Figs. 1-2). Undersaturated solutions of DL- and L-mandelic acid with cyrene as the solvent were dark yellow whereas the unsaturated solution of D-mandelic acid in cyrene was light yellow (Fig. 2). The undersaturated solution of (*RS*)-naproxen in cyrene was a darker yellow colour than the respective undersaturated solution of (*S*)-naproxen (Fig. 2). Afterwards, FTIR spectra were registered off-line at 25ºC for all solution systems using a single reflection diamond ATR crystal in TENSOR II FT-IR spectrometer (Bruker Optics Inc.) in absorbance mode, with a spectral range from 4000 to 400 cm^{-1} (standard KBr beam splitter), resolution of 1 cm^{-1}, 64 scans, Globar as the IR light source, DLATGS detector system, and OPUS

spectroscopy software. Raman spectra were also registered at 25ºC for each solution system using a RamanRxn2 Hybrid Raman analyser with a *P*^{h}*AT* probe (Kaiser Optical Systems, Inc.) and 785 nm laser, with a spectral range from 1890 to 100 cm^{-1}, resolution of 1 cm^{-1}, 64 scans, and iC Raman 4.1 spectroscopy software. Both spectroscopic techniques were used in order to assess the existence of differentiation between enantiomers because of the effect of the chiral solvent cyrene. This protocol was repeated twice to assess the reproducibility of the results obtained. The solvent-corrected FTIR and Raman spectra for the different solute species dissolved in cyrene were obtained by first normalising both solute species solutions and solvent spectra with respect to the maximum response collected in these spectra and then subtracting the normalised solvent spectrum from each normalised solute species solutions spectra. For the case of subtraction of one solute solution spectrum from another, a similar approach was carried out by subtracting the normalised spectrum of one solute solution from the other solute solution spectrum. The software employed for the treatment of the spectroscopic raw spectra is OriginPro 2018.

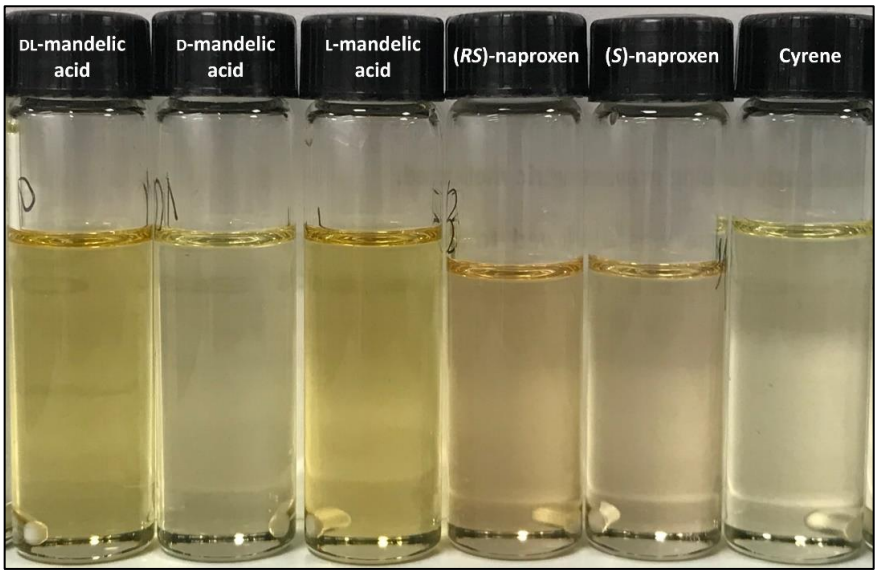

Fig. 2. Undersaturated solutions with cyrene and reference (cyrene) at 25°C. From left to right: DL-mandelic acid, D-mandelic acid, L-mandelic acid, (*RS*)-naproxen, (*S*)-naproxen, and cyrene (blank).

5.2.2.2. Feasibility of chiral resolution of DL-mandelic acid via extraction

5.2.2.2.1. Cyrene miscibility study

Mixtures of 1:1 (v/v) of cyrene and each solvent candidate (see section 5.2.1. for solvent candidates) were added in 1 mL vials, then magnetically agitated at 1000 rpm for 30 min at 25ºC. After, each vial was examined by eye to determine the existence of one or more liquid phases in the mixtures. Then, each combination was classified as completely miscible (existence of only one liquid phase), partially miscible (existence of two phases with different original 1:1 (v/v) ratio) or immiscible (existence of two phases with the same original 1:1 (v/v) ratio).

5.2.2.2.2. Screening of DL -mandelic acid solubility in achiral solvents

The temperature variation method (TV method) for solubility determination was applied similarly as described in the literature [21], using the Crystal16 multiple reactor setup (Technobis Crystallisation Systems). The samples were agitated using magnetic stirrer bars with a stirring rate of 700 rpm. Three temperature cycles were applied starting at 20ºC, with maximum and minimum temperatures of 50ºC and 1ºC, respectively, and with heating and cooling rates of 0.3 ºC/min. Then, clear and cloud points were registered based on the transmission of the light. Then, the solubility at certain temperature was determined by the average of three clear points measured. This method was used for the solubility screening of DL-mandelic acid in 1-nonanol, 1-octanol, cyclohexane, Milli-Q water, *n*-heptane, and *n*-hexane.

5.2.2.2.3. Preparation of the liquid mixtures for liquid-liquid extraction

175 mg of DL-mandelic acid were dissolved separately with 2.5 mL of 1-nonanol and 2.5 mL of 1-octanol in two different 5 mL vials. The complete dissolution of DL-mandelic acid in both 1-nonanol and 1-octanol occurred after magnetically agitating the initial

mixtures for 30 min at 25ºC. Then, 2.5 mL of cyrene was added in each vial to obtain a 1:1 (v/v) ratio with the achiral solvents. The mixture was agitated for 30 min at 25ºC.

5.2.2.3. Solubility analysis

The saturated cyrene solutions were prepared mixing separately 3000 mg of D-, L-, and DL-mandelic acid in 3.75 g of cyrene, in three different vials at 25ºC. The saturated aqueous solutions were prepared mixing separately 3000 mg of D-, L-, and DL-mandelic acid in 3.00 g of water, in three different vials at 25ºC. Two blank solutions that only contained cyrene and water, per separate in two vials, were also prepared as reference for spectrophotometric measurements. Samples were magnetically agitated at 1000 rpm for 3 days. After, the suspensions were filtered and the clear filtrates were collected separately in new vials. The temperature was adjusted at 25ºC and controlled during the whole solution preparation procedure. DL- and L-mandelic acid saturated solutions containing cyrene as solvent were dark yellow whereas the D-mandelic acid saturated solution in cyrene was light yellow; but all cyrene samples were transparent (Fig. 2, same colour as only cyrene and undersaturated solutions of mandelic acid in cyrene). Water and all saturated aqueous solutions were observed colourless and transparent (Fig. 3). Afterwards, UV-Vis spectra were registered at 25ºC for all solution systems using a UV-Vis MCS 600 spectrometer (Carl Zeiss Spectroscopy Gmbh) with a 6 mm diameter 3-bounce sapphire ATR crystal probe (Hellma) in absorbance mode, with a spectral range from 200 to 500 nm, resolution of 1 nm, 16 scans (3 replicate measurements), deuterium light source CLD 600 as UV-Vis light source, and Aspect Plus spectroscopy software. This protocol was repeated twice to assess the reproducibility of the results obtained.

Fig. 3. Filtered saturated aqueous solutions and reference (water) at 25°C. From left to right: DL-mandelic acid, D-mandelic acid, L-mandelic acid, and water (blank).

Quantification of solubility was carried out by means of the temperature variation method (TV method). This method was applied similarly as described in the literature [21], using the Crystal16 multiple reactor setup (Technobis Crystallisation Systems). The samples were agitated using a magnetic stirrer bar with a stirring rate of 700 rpm. Three temperature cycles were applied starting at 20ºC, with maximum and minimum temperatures of 50ºC and -5ºC, respectively, and with heating and cooling rates of 0.3 and 2.0ºC/min, respectively. Hold times of 1 h were applied when maximum (50ºC) and minimum (-5ºC) temperatures were reached in each cycle. Clear points were registered based on the transmission of the light through each sample. The solubility at certain temperature was determined by the average of three clear points measurements (relative standard deviation within ±1%). This method was used for the solubility quantification of DL-, D-, and L-mandelic acid in cyrene.

5.3. Results

5.3.1. Spectral analysis of unsaturated solutions

The chiral recognition capacity of cyrene is assessed in undersaturated solutions of different chiral species of mandelic acid and naproxen in cyrene focusing on the exploration of their molecular vibrational responses under FTIR and Raman spectroscopies. These spectroscopies were registered for the undersaturated solutions, at the same concentration, in order to observe potential peak shifts between enantiomers which could be correlated to a different interaction between the chiral solvent and each chiral form of the solute due to differences in intermolecular forces, which may affect the bonds vibrations in the molecules.

5.3.1.1. FTIR spectroscopy

The direct FTIR spectra measurements of DL-, D-, and L-mandelic acid and (*RS*)- and (*S*)-naproxen in cyrene find that the cyrene signal dominates the spectra. Only a few peaks can be related to the solutes when comparing with the reference cyrene spectrum (Fig. 4). Those peaks which can be assigned to the chiral forms seem the same among DL-, D-, and L-mandelic acid. The same happens with the peaks related to (*RS*)- and (*S*)-naproxen (Fig. 4).

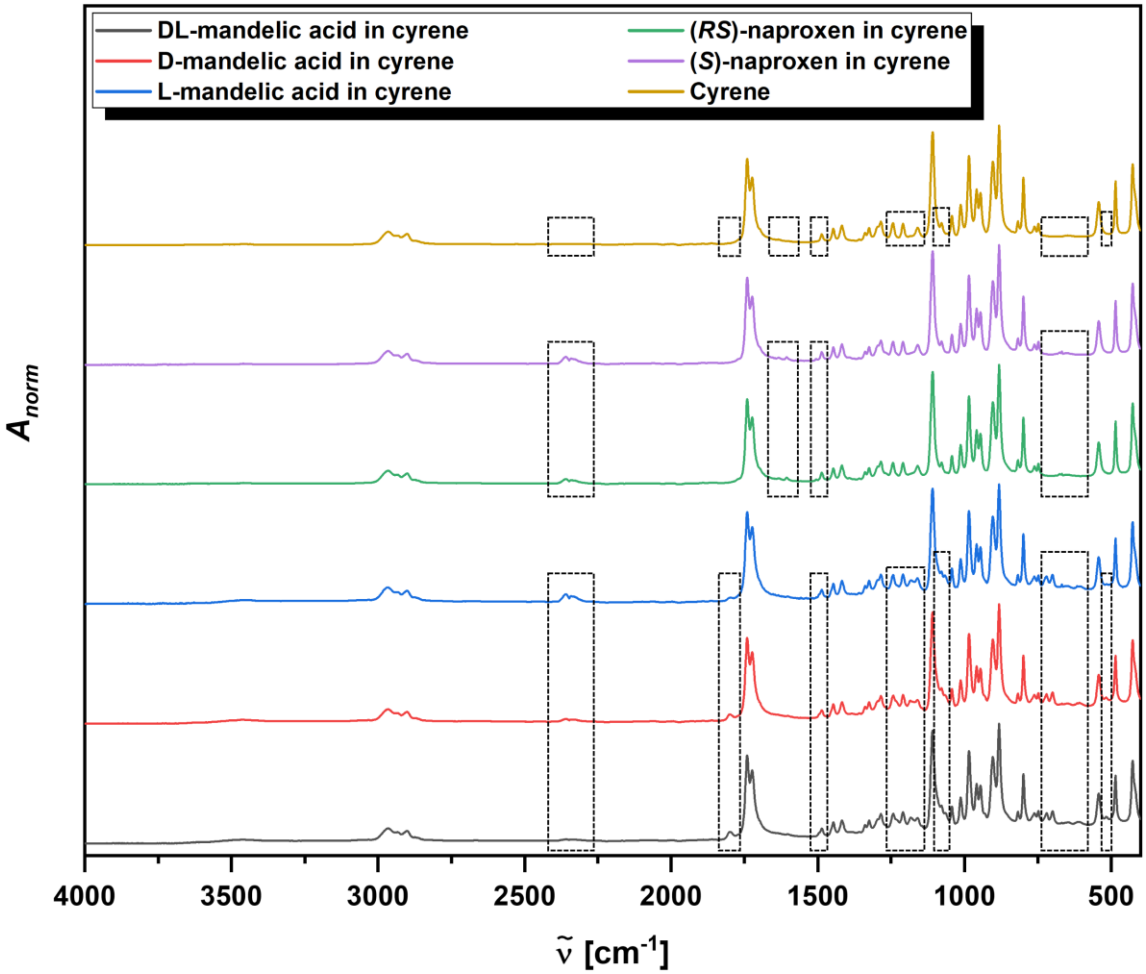

Fig. 4. FTIR spectra of undersaturated solutions of DL-, D-, and L-mandelic acid (160 mg/g) and (*RS*)-, (*S*)-naproxen (32 mg/g) in cyrene and reference (cyrene) at 25°C. A_{norm} and $\tilde{\nu}$ refer to normalised absorbance and wave number, respectively. The dashed black squares identify the signals caused by the mandelic acid and naproxen species, which are not present in the cyrene spectrum.

Due to the inconvenience of the predominant cyrene signal in all the spectra, the subtraction of cyrene signal is required. For that, we subtracted the normalised pure cyrene solvent reference spectrum from the solution spectra (Figs. 5-6), which then reflect only the infrared responses caused by the presence of the solute species in the solvent. The latter also includes the possible interactions between the solutes and solvent. From the solvent-corrected spectra, we can just observe subtle shifts in both wave number $\tilde{\nu}$ and absorbance which are difficult to attribute to any specific chiral-discriminative interaction between mandelic acid and naproxen enantiomers and chiral solvent cyrene (Figs. 5-6).

A further detailed look is possible for the mandelic acid case by subtracting the spectrum of enantiomer D from the spectrum of enantiomer L (Fig. 5, green line). Here, we do observe better that there are indeed differences in absorbance and wave number between the two mandelic acid enantiomers spectra in the presence of the chiral solvent cyrene, which suggests certain enantiomeric discrimination power from the optically active solvent cyrene. It is important to note here that if both enantiomers have the same interaction behaviour with the chiral solvent, we should expect to obtain a perfect straight line, which is not the case (Fig. 5, green line).

The FTIR responses observed for the chiral species of both mandelic acid and naproxen can be examined in the table below (Table 1). There, we assign the peaks observed in the spectra to the related bond vibrations. The signals arise from the solute species and chiral solvent molecular structures. However, the subtle differences observed in the spectra (Figs. 5-6) can be now assigned to the vibrational signals (Table 1). Regarding mandelic acid in cyrene, when subtracting enantiomer L spectrum from enantiomer D spectrum (Fig. 5, green line), we observed three different main regions with peak differences. The first region counted with two peak shifts at 3000-2880 and 2400-2300 cm^{-1} (Table 1) which can be related to a different intensity of intermolecular hydrogen bonding interaction (O-H stretching, Table 1) between the hydroxyls from alcohol (3000-2880 cm^{-1}) and carboxyl (2400-2300 cm^{-1}) functional groups in mandelic acid and the oxygen atoms in the ketone and ether groups in cyrene. The second region at 1800-1650 cm^{-1} (Fig. 5, green line; Table 1) also suggests a different influence between enantiomers with cyrene in the C=O stretching vibrations in the carboxyl and ketone groups. The third part is the fingerprint region (≤1500 cm^{-1}) which normally is characteristic of each given compound. In this case, when comparing two enantiomers of the same compound, we should expect these two regions to be equal since enantiomers cannot be distinguished with infrared light. However, the many subtle peak shifts observed in this region (Fig. 5, green line) may suggest a distinct effect exerted by cyrene in some intramolecular stretching and bending vibrations (Table 1) in both mandelic acid enantiomers.

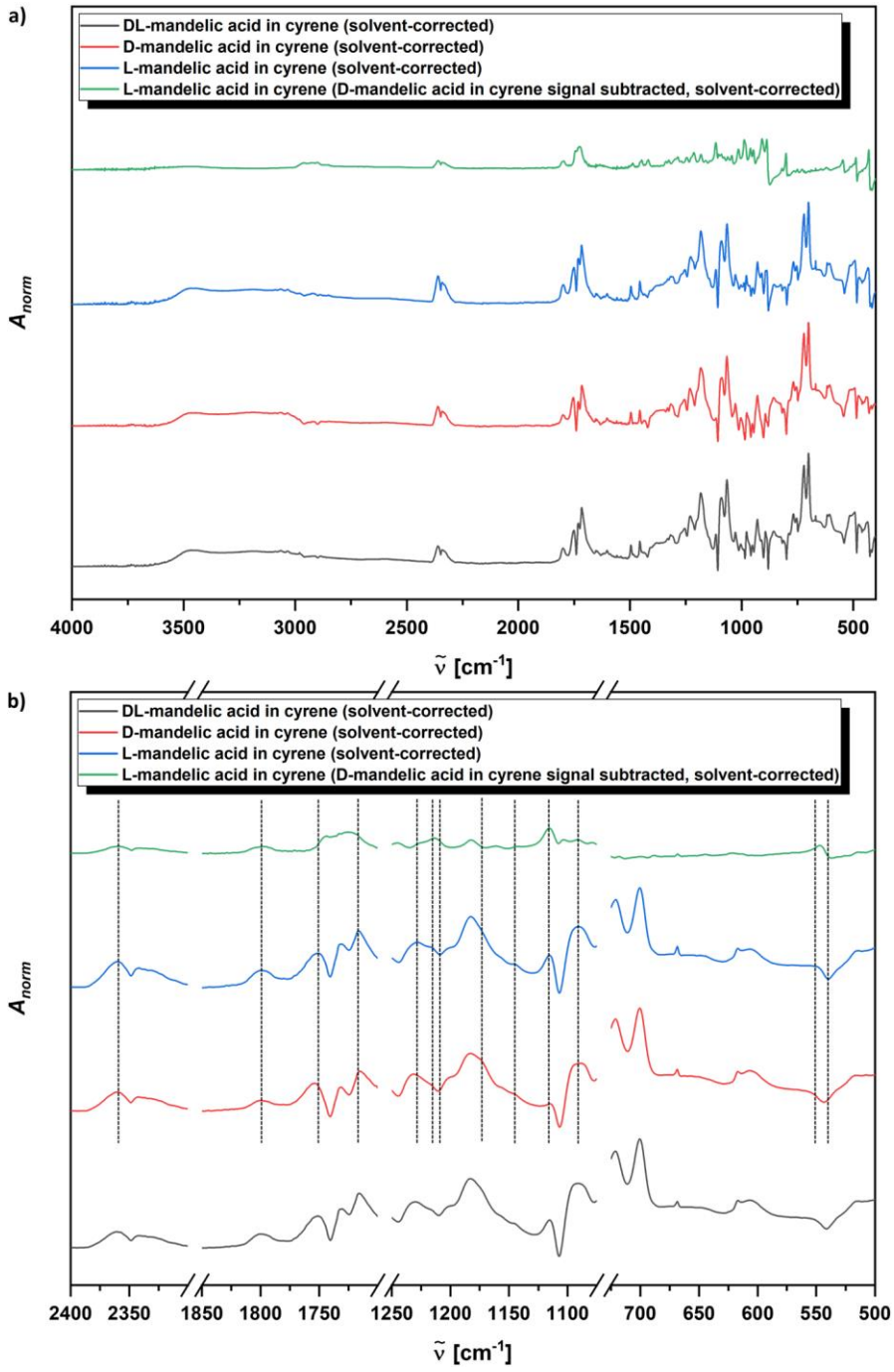

Fig. 5. Solvent-corrected FTIR spectra of undersaturated solutions of DL-, D-, and L-mandelic acid in cyrene (160 mg/g) and also L-mandelic acid spectrum with D-mandelic acid spectrum subtracted, at 25°C. A_{norm} and $\tilde{\nu}$ refer to normalised absorbance and wave number, respectively. The spectra in a) are for the whole range of $\tilde{\nu}$ collected and the spectra in b) are enlargements of selected regions dominated by the solute response (see Fig. 4). The dashed black lines in b) mark shifts in $\tilde{\nu}$ between D- and L-mandelic acid spectra.

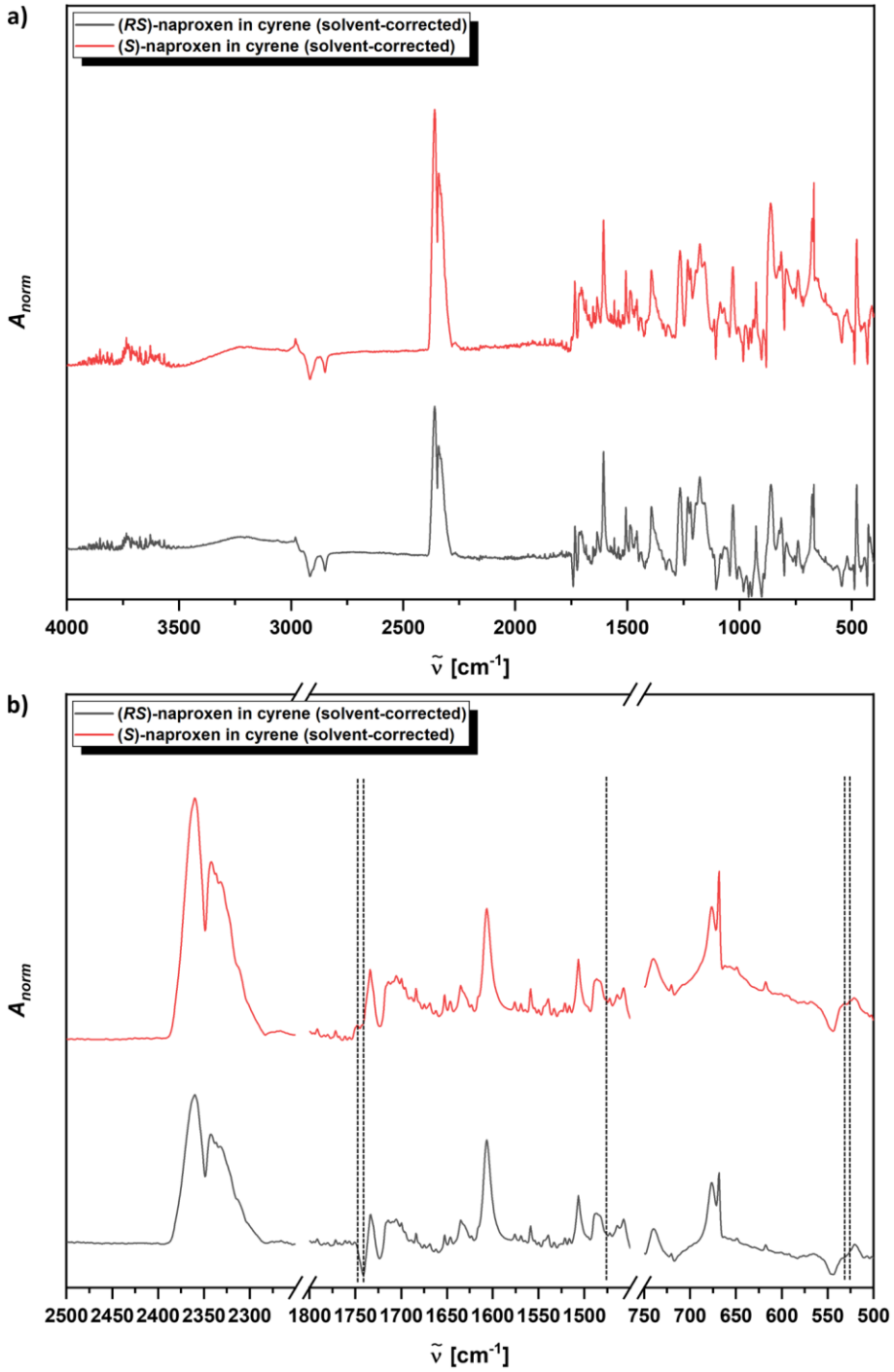

Fig. 6. Solvent-corrected FTIR spectra of undersaturated solutions of (*RS*)- and (*S*)-naproxen in cyrene (32 mg/g) at 25°C. A_{norm} and $\tilde{\nu}$ refer to normalised absorbance and wave number, respectively. The spectra in a) are for the whole range of $\tilde{\nu}$ collected and the spectra in b) are enlargements of selected regions dominated by the solute response (see Fig. 4). The dashed black lines in b) mark shifts in $\tilde{\nu}$ between (*RS*)- and (*S*)-naproxen spectra.

Regarding naproxen, we can also observe some subtle differences that are mainly located in the fingerprint region (Fig. 6). However, these differences are more difficult to appreciate than in the mandelic acid case. For naproxen, we suggest the possible formation of hydrogen bonding intermolecular interactions between the carboxyl group from naproxen and, again, the oxygen atoms in the ketone and ether groups in cyrene. So, a similar type of intermolecular forces, but with different extension due to the distinct stereochemistry of enantiomers, in both naproxen and mandelic acid would be the origin for these subtle infrared spectral differences observed (Figs. 4-6, Table 1).

The enlargement of some of the peaks found in the regions where we detected the dominance of the solute response in Fig. 4 (Figs. 5b-6b) enables the identification of the wave number shifts and differences in absorbances related to changes in the enantiomers molecular vibrations caused by the presence of cyrene. In mandelic acid, these shifts in wave number between enantiomers D and L, which are identified with the dashed black lines (Fig. 5b), are found at 2365 cm^{-1} (O-H st, intermolecular); 1800, 1750, and 1720 cm^{-1} (C=O st); 1230-1200 cm^{-1} (O-H δ ip, OC-OH st, and C-OH δ); 1170, 1140, 1120, and 1085 cm^{-1} (ar C-H δ ip); and 550 and 540 cm^{-1} (O-H δ oop) (Table 1). In naproxen, a lower number of wave number shifts are observed between (*RS*)- and (*S*)-naproxen signals (Fig. 6b), which are found at 1750-1740 (C=O st), 1475 (ar C-C), and 535-525 cm^{-1} (O-H δ oop) (Table 1). These differences observed between (*RS*)- and (*S*)-naproxen solutions indicate that the (*R*)-naproxen contained in the (*RS*)-naproxen solution is the main reason for such distinctions because of its different interaction with cyrene compared to (*S*)-naproxen. The previous assignments of the signals dominated by the solutes are in accordance with the analysis above suggesting certain distinct hydrogen bonding interaction between the two enantiomers of mandelic acid and cyrene and also between the two enantiomers of naproxen and cyrene.

Table 1. FTIR and Raman spectral data and vibrational assignment for mandelic acid and naproxen species in cyrene and for pure cyrene (reference) (Figs. 4-6) [22–24].

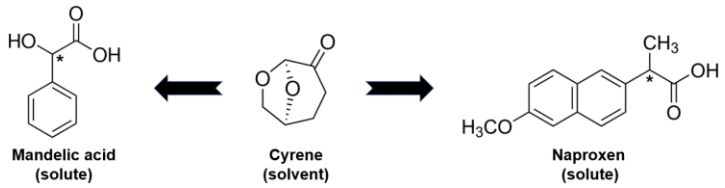

Solute	Solvent	Signal $\tilde{\nu}$ [cm^{-1}]	Vibrational assignment[a]
DL-, D-, and L-mandelic acid	Cyrene	3650-3200	O-H st
DL-, D-, and L-mandelic acid	Cyrene	3550-2880	O-H st, intermolecular
DL-, D-, and L-mandelic acid	Cyrene	3550-2500	COO-H st
DL-, D-, and L-mandelic acid	Cyrene	3080-3030	ar C-H st
DL-, D-, and L-mandelic acid	Cyrene	3000-2840	C-H st
DL-, D-, and L-mandelic acid	Cyrene	2400-2300	O-H st, intermolecular
DL-, D-, and L-mandelic acid	Cyrene	2000-1650	Comb, ar overtones (mono-substituted aromatic group)
DL-, D-, and L-mandelic acid	Cyrene	1800-1675	C=O st
DL-, D-, and L-mandelic acid	Cyrene	1625-1560, 1525-1450	ar C-C
DL-, D-, and L-mandelic acid	Cyrene	1450-1200	O-H δ ip
DL-, D-, and L-mandelic acid	Cyrene	1440-1210	OC-OH st, C-OH δ
DL-, D-, and L-mandelic acid	Cyrene	1250-950	ar C-H δ ip
DL-, D-, and L-mandelic acid	Cyrene	1075-1000	C-O st
DL-, D-, and L-mandelic acid	Cyrene	960-880	OC-OH δ oop, ar CH δ
DL-, D-, and L-mandelic acid	Cyrene	900-650	ar C-H δ oop
DL-, D-, and L-mandelic acid	Cyrene	<720	O-H δ oop
(*RS*)- and (*S*)-naproxen	Cyrene	3550-2500	COO-H st
(*RS*)- and (*S*)-naproxen	Cyrene	3080-3030	ar C-H st
(*RS*)- and (*S*)-naproxen	Cyrene	3000-2840	C-H st
(*RS*)- and (*S*)-naproxen	Cyrene	2850-2815	C-H st (methyl ether)
(*RS*)- and (*S*)-naproxen	Cyrene	2400-2300	O-H st, intermolecular
(*RS*)- and (*S*)-naproxen	Cyrene	2000-1650	Comb, ar overtones
(*RS*)- and (*S*)-naproxen	Cyrene	1800-1650	C=O st
(*RS*)- and (*S*)-naproxen	Cyrene	1625-1560, 1525-1450	ar C-C
(*RS*)- and (*S*)-naproxen	Cyrene	1470-1430	CH_3 δ as
(*RS*)- and (*S*)-naproxen	Cyrene	1440-1210	OC-OH st, C-OH δ
(*RS*)- and (*S*)-naproxen	Cyrene	1395-1310	CH_3 δ sy
(*RS*)- and (*S*)-naproxen	Cyrene	1275-1200	ar C-O-al C st as
(*RS*)- and (*S*)-naproxen	Cyrene	1250-800	CH_3 γ
(*RS*)- and (*S*)-naproxen	Cyrene	1075-1020	ar C-O-al C st sy, C-O st
(*RS*)- and (*S*)-naproxen	Cyrene	960-880	OC-OH δ oop, ar CH δ
(*RS*)- and (*S*)-naproxen	Cyrene	900-650	ar C-H δ oop
(*RS*)- and (*S*)-naproxen	Cyrene	<720	O-H δ oop
-	Cyrene	3000-2850	C-H st (acetal)
-	Cyrene	1750-1675	C=O st
-	Cyrene	1500-1430	H-C-H δ
-	Cyrene	1310-800	C-O-C st as
		1250-950	ar C-H δ ip
-	Cyrene	1055-870	C-O-C st sy C-O st
-	Cyrene	770-740	H-C-H γ

[a]Description of abbreviations in vibrational assignment: al (aliphatic), ar (aromatic), as (asymmetric), comb (combination vibration), δ (deformation vibration), γ (skeletal vibration), ip (in plane vibration), oop (out of plane vibration), st (stretching vibration), and sy (symmetric) [23,24].

5.3.1.2. Raman spectroscopy

Similar to previous FTIR measurements, the direct Raman measurements of DL-, D-, and L-mandelic acid and naproxen in cyrene find that the cyrene signal dominates the spectra. Only a small number of peaks can be related to the solutes when comparing with the reference cyrene spectrum (Fig. 7). Those peaks which can be assigned to the chiral forms seem to have the same Raman shifts among DL-, D-, and L-mandelic acid. The same behaviour is observed for the chiral forms of racemic and enantiopure naproxen (Fig. 7). Higher intensity fluorescence backgrounds are observed in DL- and L-mandelic acid solutions compared to D-mandelic acid solution and reference (cyrene), but this effect, which is related to the technique, does not impede the comparison of the peaks among all the spectra registered. Instead, this fluorescence effect is almost non-existent in the naproxen spectra (Fig. 7).

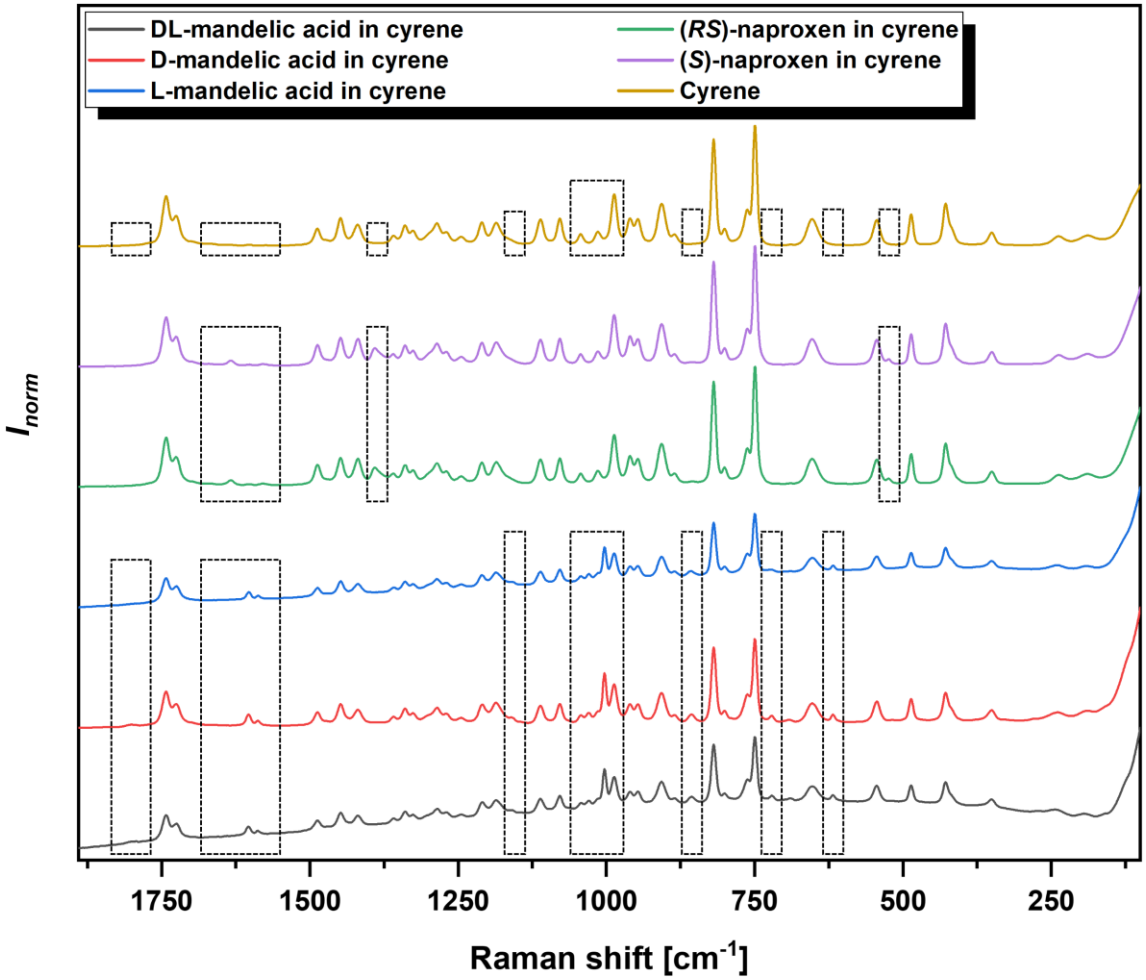

Fig. 7. Raman spectra of undersaturated solutions of DL-, D-, and L-mandelic acid (160 mg/g) and (*RS*)-, (*S*)-naproxen (32 mg/g) in cyrene and reference (cyrene) at 25°C. I_{norm} refers to normalised intensity. The dashed black squares identify the signals caused by the mandelic acid and naproxen species, which are not present in the cyrene spectrum.

As for the FTIR measurements, we subtracted the normalised cyrene reference spectrum from the spectrum of each chiral species of mandelic acid and naproxen dissolved in cyrene to obtain solvent-corrected Raman spectra (Figs. 8-9). Like this, we can observe the Raman responses caused by the solute species when they are dissolved in cyrene. This also permits examination of the effect of the specific interaction between each chiral solute with the chiral solvent cyrene. The fluorescence effect associated with this technique and the compound analysed can be appreciated in the solvent-corrected DL- and L-mandelic acid spectra (Fig. 8). From that, we can infer that enantiomer L is the main

chiral form contributing most to this Raman phenomenon. The spectra show almost no distinction in the Raman shift and intensity of the peaks of DL-, D-, and L-mandelic acid (Fig. 8). Furthermore, when we subtract the D-mandelic acid spectrum from the spectrum of L-mandelic acid, we obtain almost a perfect straight line (Fig. 8, green line). The residual negative peaks and increasing intensity in the low Raman shift range observed in this green line are caused because of the presence of the fluorescence effect in the enantiomer L spectrum whereas the spectrum of the enantiomer D does not present it (Fig. 8, green line). Then, this indicates that, at least with Raman spectroscopy, the possible enantiomeric discrimination effect exerted by cyrene is difficult to determine. If we now examine the naproxen spectra (Fig. 9), they appear to be apparently identical in terms of Raman shifts and intensity of the peaks, making even difficult to suggest certain chiral discrimination. However, despite the Raman shifts of the peaks do not change in both chiral compound systems and the intensity variation observed in mandelic acid spectra seem mainly attributable to fluorescence effect, we do clearly observe negative peaks when applying the solvent correction and this could be linked to certain solvent-solute interactions (Figs. 8-9). Nonetheless, these negative peaks still keep the same observations in terms of Raman shift and intensity, so it is not clear that those suggested solvent-solute interactions could distinguish the two enantiomers of a chiral compound.

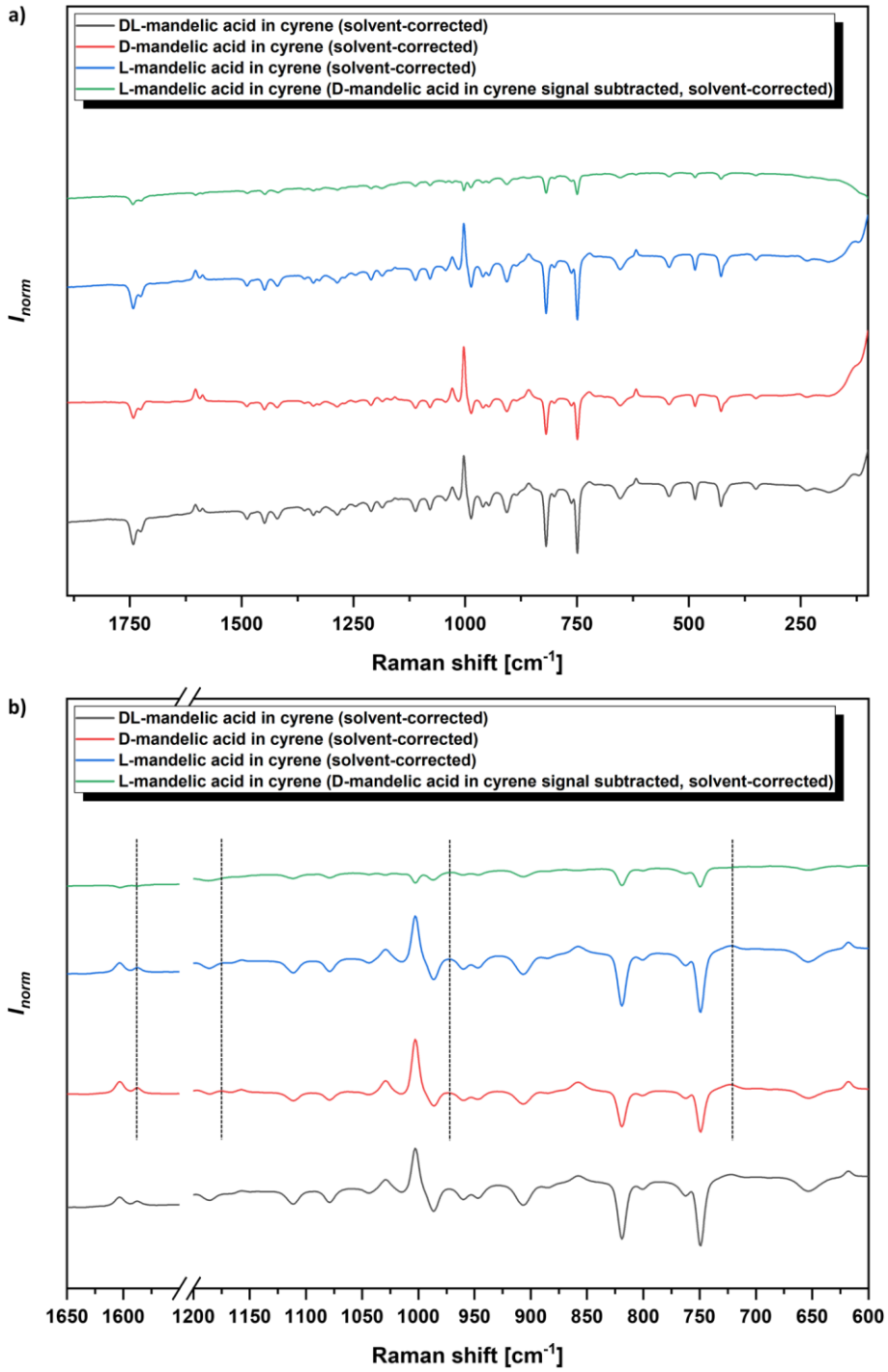

Fig. 8. Solvent-corrected Raman spectra of undersaturated solutions of DL-, D-, and L-mandelic acid in cyrene (160 mg/g) at 25°C. I_{norm} refers to normalised intensity. The spectra in a) are for the whole range of Raman shift collected and the spectra in b) are enlargements of selected regions dominated by the solute response (see Fig. 7). The dashed black lines in b) mark subtle differences in Raman shift between D- and L-mandelic acid spectra.

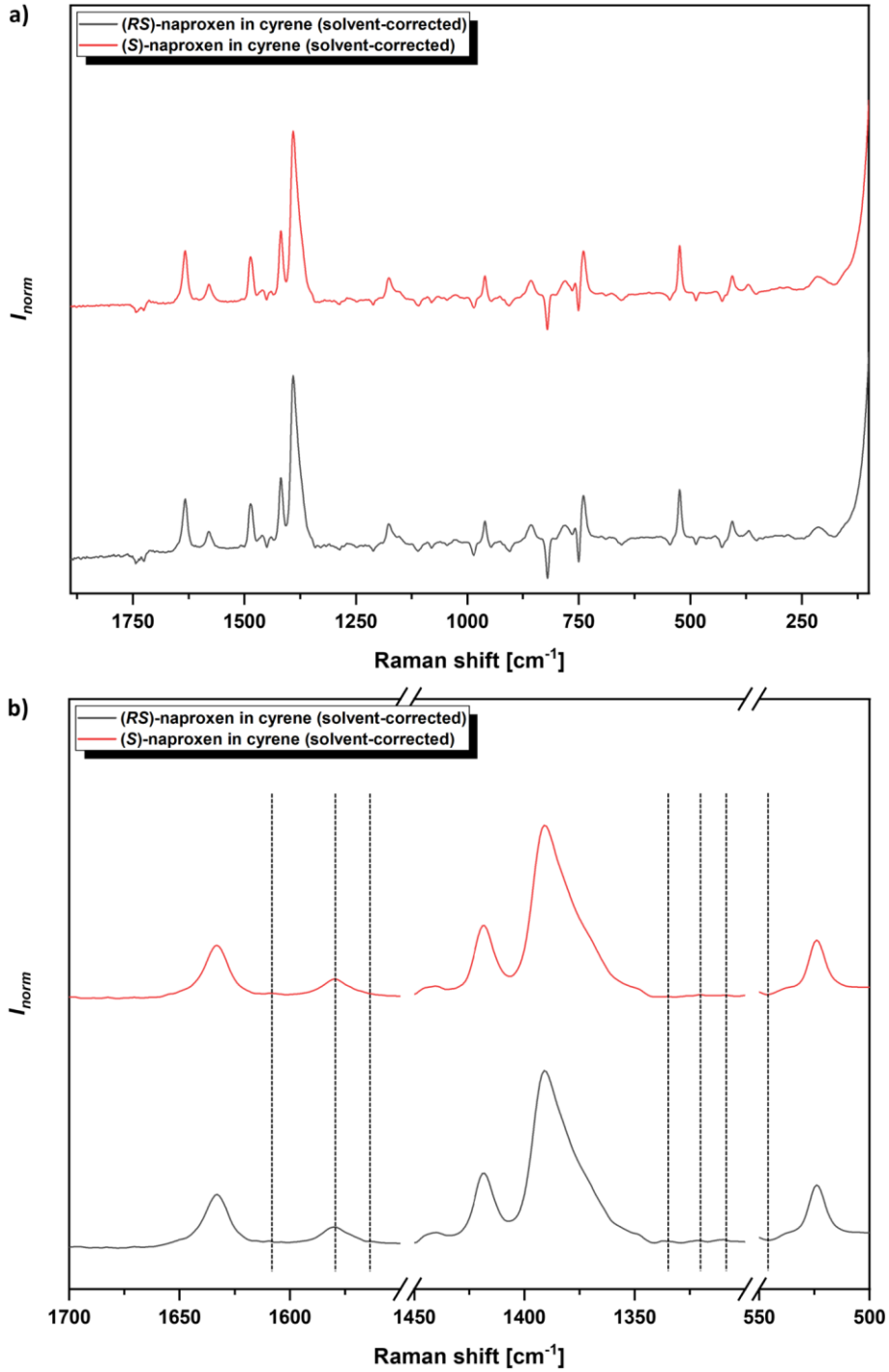

Fig. 9. Solvent-corrected Raman spectra of undersaturated solutions of (*RS*)- and (*S*)-naproxen in cyrene (32 mg/g) at 25°C. I_{norm} refers to normalised intensity. The spectra in a) are for the whole range of Raman shift collected and the spectra in b) are enlargements of selected regions dominated by the solute response (see Fig. 7). The dashed black lines in b) mark subtle differences in Raman shift between (*RS*)- and (*S*)-naproxen spectra.

The Raman responses observed for the chiral species of both mandelic acid and naproxen can be examined in Table 1. FTIR and Raman signals are complementary. However, Raman spectroscopy could only register peaks in the range of 1890-100 cm^{-1} (Figs. 7-9). We assigned the peaks observed in the spectra to the related bond vibrations, which coincide to the ones assigned in FTIR with the only difference of the intensity of the peaks. We find remarkable to assign the bond vibrations of the negative peaks observed (Figs. 8-9) because they could inform us about what structural parts of the solute and solvent molecules may be interacting. Regarding mandelic acid, three main negative peaks are detected (Fig. 8). The peak around 1740 cm^{-1} relates to the C=O stretching of the carboxyl group (Fig. 8, Table 1), whereas the peaks at 820 and 750 cm^{-1} relate to the C-H bending in the aromatic ring in mandelic acid (Fig. 8, Table 1). This suggests the same intermolecular hydrogen bonding interaction detected with FTIR between the carboxyl group from mandelic acid and the functional groups containing the oxygen atoms in cyrene. Besides, the effect of this intermolecular interaction seems that could be extended until the electronic cloud disposition in the aromatic ring, showing an effect in its C-H bending bond vibrations. Although it may appear that this interaction is stronger for L-mandelic acid when comparing its spectrum with its counter enantiomer one due to differences in the intensity of the signals, we need to recall the fluorescence effect that may be the reason for such distinctions. The enlargement of certain peaks found in the regions where we detected the dominance of the solute response in Fig. 7 (Fig. 8b) makes also difficult the distinction in Raman shift between the two mandelic acid enantiomers. The dashed black lines drawn to indicate such discrimination between D- and L-mandelic acid (Fig. 8b) only spot slight differences in the Raman shift. The distinctive peaks at 1590, 1170, 960, and 720 cm^{-1} are assigned to the following vibrations, respectively: ar C-C, ar C-H δ ip, OC-OH δ oop/ar CH δ, and O-H δ oop (Table 1); which support the idea of the hydrogen bonding interaction extended until the aromatic electronic cloud suggested above. Regarding naproxen, we identify three similar main negative peaks at the same Raman shift as in the mandelic acid case (Figs. 8-9). The peak at 1745 cm^{-1} relates to the C=O stretching of the carboxyl group (Fig. 9, Table 1), whereas the peaks at

820 and 750 cm^{-1} relate to the C-H bending in the aromatic systems in naproxen (Fig. 9, Table 1). Additionally, the enlargement of the peaks found in the regions where we detected the dominance of the naproxen response in Fig. 7 (Fig. 9b) show again slight differences in Raman shift between its two enantiomers. The dashed black lines are drawn to indicate the discrimination between (*RS*)- and (*S*)-naproxen spectra (Fig. 9b), which show the contribution of (*R*)-naproxen that is contained in the racemic solution. Signal distinctions are observed at 1610-1565, 1335-1310, and 545 cm^{-1} which are assigned, respectively, to the ar C-C, CH_3 δ sy, and O-H δ oop vibrations (Table 1). The latter results suggest that the chiral solvent cyrene interacts in a similar way with the carboxyl group of naproxen, as observed before for mandelic acid. However, as suggested before, these intermolecular interactions detected in Raman spectroscopy between solute and solvent molecules are difficult to link with the specific chiral-discriminative power of cyrene that we did observe in FTIR spectroscopy (Figs. 5-6). Therefore, other clearer evidences are required before confirming the enantioselective effect of cyrene.

5.3.2. Feasibility of chiral resolution of DL-mandelic acid via extraction

The previous spectroscopic analyses suggested the existence of a certain chiral discrimination of the mandelic acid enantiomers by cyrene (see section 5.3.1.). With this in mind, we envisage the possibility to develop a liquid-liquid extracting chiral resolution of DL-mandelic acid by using the chiral solvent cyrene as one of the phases and an achiral solvent for the other immiscible phase. For that, we need to study the miscibility behaviour of cyrene with other achiral solvents for the selection of extraction solvent candidates. Then, we do a screening of the DL-mandelic acid solubility in these achiral solvent candidates selected and, eventually, attempt the separation of enantiomers via the liquid-liquid extraction process.

5.3.2.1. Cyrene miscibility study

The miscibility study, at 25ºC, shows that cyrene is completely miscible with most organic solvents, except those most non-polar ones. Partial miscibility is observed with

1-nonanol and 1-octanol, and immiscibility is observed with cyclohexane, *n*-heptane, and *n*-hexane. Cyrene is also completely miscible with the inorganic solvent water (Table 2). Thus, at this point, only the achiral solvents that present a certain degree of immiscibility with cyrene, those assigned as partially miscible and immiscible, are selected as candidates for testing the liquid-liquid extraction along with cyrene. These candidates are: 1-nonanol, 1-octanol, cyclohexane, *n*-heptane, and *n*-hexane.

Table 2. Miscibility table of chiral solvent cyrene with several organic and inorganic solvents at 25ºC.

COMPLETELY MISCIBLE
PARTIALLY MISCIBLE
IMMISCIBLE

Achiral solvent	Miscibility with cyrene
1,2-dichloroethane	
1,4-dioxane	
1-bromobutane	
1-butanol	
1-nonanol	
1-octanol	
1-pentanol	
3-methyl-1-butanol	
3-pentanone	
4-methyl-2-pentanone	
Acetone	
Acetonitrile	
Anisole	
Chloroform	
Cyclohexane	

Achiral solvent	Miscibility with cyrene
Diethyl ether	
Dimethyl sulfoxide	
Ethanol	
Ethyl acetate	
Isopropanol	
Methyl *tert*-butyl ether	
N,N-dimethylformamide	
n-heptane	
n-hexane	
Nitromethane	
Pyridine	
Tetrahydrofuran	
Toluene	
Xylenes	
Water	

5.3.2.2. Screening of DL-mandelic acid solubility in achiral solvents

We used the TV method to assess the solubility concentration of DL-mandelic acid in the range of 10-70 mg/g for the achiral solvent candidates selected: 1-nonanol, 1-octanol, cyclohexane, *n*-heptane, and *n*-hexane. The solubility screening finds that DL-mandelic acid is completely insoluble in the most non-polar candidates: cyclohexane, *n*-heptane, and *n*-hexane; but completely soluble in the least non-polar: 1-nonanol and 1-octanol. Ergo, 1-nonanol and 1-octanol are the two achiral solvent candidates with the ability to dissolve the solute of interest (DL-mandelic acid) and, at the same time, capable of being

partially immiscible with the chiral solvent cyrene tested here for the chiral resolution potential via liquid-liquid extraction.

5.3.2.3. Liquid mixtures for enantioselective liquid-liquid extraction

Finally, we attempt the liquid-liquid extraction chiral resolution by first dissolving the DL-mandelic acid into the achiral solvents selected (1-nonanol and 1-octanol, per separate) and after adding the chiral solvent cyrene, with potential of enantiomer discrimination, to the first DL-mandelic acid solutions. At this point, we observe two homogeneous solutions (Fig. 10) instead of two heterogenous solutions with two separated liquid phases, as we might expect from the previous observations in the miscibility study of cyrene with the achiral solvents (Table 2). We infer that the solute DL-mandelic acid exercises a miscibility driving force for these two mixtures, giving then just one yellowish transparent liquid phase on each vial (Fig. 10).

Fig. 10. Homogeneous solutions (only one liquid phase for each) obtained when assessing the feasibility of the chiral resolution of DL-mandelic acid via extraction with chiral solvent cyrene and achiral solvents 1-octanol (left) and 1-nonanol (right).

Therefore, the chiral resolution of DL-mandelic acid using cyrene as an extracting chiral solvent alongside the achiral solvents 1-nonanol and 1-octanol has to be discarded.

5.3.3. Solubility analysis

In an achiral solvent, the solubilities of enantiopure solids of both enantiomers are equal [1,4,22]. However, the introduction of a chiral environment by means of a chiral solvent such as cyrene could affect the solubilities of the enantiopure compounds differently. Here, we therefore measure solubilities of the enantiopure compounds in the chiral solvent and compare it to that of the racemic compound as well.

5.3.3.1. UV-Vis spectroscopy

The UV-Vis spectroscopy measurements of the saturated solutions of DL-, D-, and L-mandelic acid in the achiral solvent water and the chiral solvent cyrene permit the assessment of their concentrations at saturation. This technique that registers the energy exchanged due to electronic transitions in a molecule relates the absorbance A measured with the solution concentration C by means of the Beer-Lambert law [22,25–27]:

$$A = \varepsilon C l \tag{1}$$

where ε is the molar absorbance or molar extinction coefficient, l is the path length through the sample. Therefore, for saturated solutions, this technique can determine the solubility concentration C_s.

UV-Vis spectroscopy can also account for the observation of potential distinct band shifts between enantiomers due to different interactions between the chiral solvent and each enantiomer caused by differences in the intermolecular forces, which therefore would affect differently the energy gaps between electronic levels in both chiral forms of a molecule. This phenomenon is similar to the solvatochromic effect, which is the variation in the spectrum of a solution of a substance (solute) with the used solvent due to changes in polarity (dielectric constant) and intermolecular forces such as hydrogen bonding [22–24].

5.3.3.1.1. UV-Vis spectroscopy of mandelic acid in water

The UV-Vis spectra of the saturated solutions of D- and L-mandelic acid are the same (Fig. 11a), which means that both enantiomers have the same solubility in water. The solubilities of both enantiomers are the same because of the presence of a symmetric environment given by the achiral solvent water, which cannot differentiate them. Enantiomers are reported to present the same chemical and physical properties in such type of solvents, except for their ability to rotate plane-polarised light which is not the case here [1,4,22].

The saturated racemate solution differs in the UV absorbance compared to the saturated pure enantiomer solutions (Fig. 11a). Although DL-mandelic acid shows the same maximum wavelengths λ_{max} (207, 258, and 263 nm) than D- and L-mandelic acid, the absorbance of the band, which here is directly proportionally related to the solubility concentration by means of the Beer-Lambert law (1) [22,25–27], is much higher for the racemate (Fig. 11a). Therefore, this indicates that DL-mandelic acid presents a higher solubility than D- and L-mandelic acid in the achiral solvent water. This detected concentration difference is related to the different crystal structure of the racemic compound compared to the enantiopure one [1,4]. The much higher solubility of the stable racemic compound in the racemic solution indicates that the system is non-ideal and that the presence of one enantiomer as a solute strongly influences the other one. It might also be a pH effect, as the higher the concentration of mandelic acid, the lower the pH, which in turn influences the solubility.

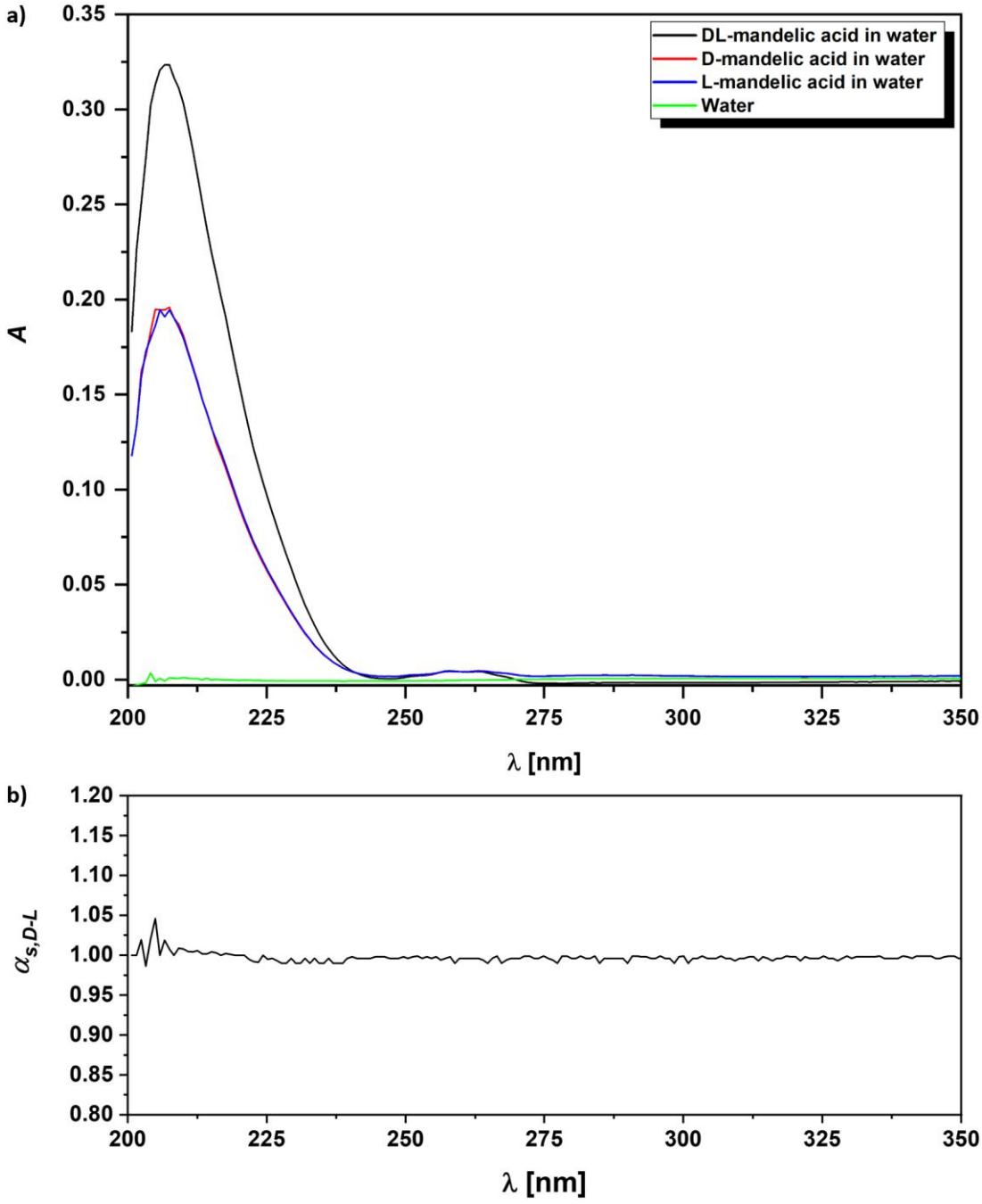

Fig. 11. a) UV-Vis spectra of saturated solutions of DL-, D-, and L-mandelic acid in the achiral solvent water and for pure water at 25°C. Three identical spectra were acquired for each saturated solution, only one spectrum is represented here per species for clarity. *A* and λ refer to absorbance and wavelength, respectively. While at 25°C the solubility of D- and L-mandelic acid are identical, the solubility of the racemic compound DL-mandelic acid is much higher. b) The ratio of solubilities of D- and L-mandelic acid $\alpha_{s,D-L}$ in water as a function of the wavelength.

The UV-Vis bands observed in Fig. 11 are assigned to their corresponding electronic transitions in Table 3.

Table 3. UV-Vis spectral data from saturated solutions of DL-, D-, and L-mandelic acid in water and pure water (Fig. 11) [22–24].

Solute	Solvent	λ_{max} [nm]	Electronic transitions assignment
DL-mandelic acid	Water	207, 258, and 263	$n \rightarrow \sigma^*$, $n \rightarrow \pi^*$, $\pi \rightarrow \pi^*$
D-mandelic acid		207, 258, and 263	$n \rightarrow \sigma^*$, $n \rightarrow \pi^*$, $\pi \rightarrow \pi^*$
L-mandelic acid		207, 258, and 263	$n \rightarrow \sigma^*$, $n \rightarrow \pi^*$, $\pi \rightarrow \pi^*$
-		negligible	$n \rightarrow \sigma^*$

An estimation of the ratio of solubilities of D- and L-mandelic acid $\alpha_{s,D\text{-}L}$ is calculated with the following expression (2) (Fig. 11b), deduced from the Beer-Lambert law (1) and assuming the same molar extinction coefficient ε for both enantiopure compounds:

$$\alpha_{s,D-L} = \frac{C_{s,D}}{C_{s,L}} = \frac{A_D(\lambda)}{A_L(\lambda)} \quad (2)$$

where $C_{s,D}$ and $C_{s,L}$ are the solubility concentrations of the enantiomers D and L, respectively. $A_D(\lambda)$ and $A_L(\lambda)$ refers, respectively, to the absorbances of the enantiomers D and L at λ. If the solvent does absorb in the UV-Vis, a solvent correction is needed in $A_D(\lambda)$ and $A_L(\lambda)$. In the last case, the absorbance caused by only the solvent must be subtracted from the absorbances of the enantiomers since they will also have the solvent response included.

The solubility ratio $\alpha_{s,D\text{-}L}$ (2) for the mandelic acid system in water is equal to ~1.00 from 200-350 nm (Fig. 11b) and matches well with the concentration ratio of 1.00 obtained from the solubility data reported in the literature at 25ºC [28,29] (Table 4). This agreement in solubility ratios values validates the UV-Vis method employed. The same values of $\alpha_{s,D\text{-}L}$ equal to 1.00 determined and reported for mandelic acid (Table 4) indicate, as expected, the absence of enantiomeric discrimination power in the achiral solvent water. In Table 4, the large difference in absorbance between the racemic compound (A =

0.32) of mandelic acid and its two enantiomers (A = 0.20) at 207 nm also relates well with the large difference in solubilities found in the literature for the racemic compound (C_s = 204.00 mg/g) and both enantiomers (C_s = 126.80 mg/g) at 25ºC [28,29].

Table 4. Absorbances A, solubilities C_s, and calculated solubility ratios $\alpha_{s,D\text{-}L}$ (2) for mandelic acid in water from own UV-Vis spectroscopy (Fig. 11) and literature (lit.) [28,29] data, at 25ºC. Literature assumes C_s value determined for enantiomer L to be the same for enantiomer D. A and $\alpha_{s,D\text{-}L}$ obtained at λ_{max} (main band).

Solute	Solvent	λ_{max} [nm]	A	$\alpha_{s,D\text{-}L}$ (UV-Vis)	C_s (lit.) [mg/g]	$\alpha_{s,D\text{-}L}$ (lit.)
DL-mandelic acid	Water	207	0.32	-	204.00	-
D-mandelic acid		207	0.20	1.00	126.80	1.00
L-mandelic acid		207	0.20		126.80	

5.3.3.1.2. UV-Vis spectroscopy of mandelic acid in cyrene

The UV-Vis spectrum of cyrene shows that the chiral solvent absorbs in the UV range from 200 to 350 nm (Fig. 12a), with two absorption bands at λ_{max} = 207 and 272 nm (Table 5). The UV-Vis spectra of saturated solutions of DL-, D-, and L-mandelic acid in cyrene show that each chiral species presents a different spectral response. First, we observe a difference in the absorbance of the three saturated solutions of mandelic acid (Fig. 12a). This means that not only the solubilities of the enantiopure and racemic compound are different, but also that of both enantiopure compounds. The solubilities of mandelic acid present the following trend: DL-mandelic acid > L-mandelic acid > D-mandelic acid. This may indicate the discriminant interaction between the chiral solvent cyrene and both chiral forms (D and L) of mandelic acid that we suggested before, especially with FTIR spectroscopy (Fig. 5). In particular, cyrene seems to have more affinity for L-mandelic acid than for D-mandelic acid since its solubility is higher (Fig. 12a).

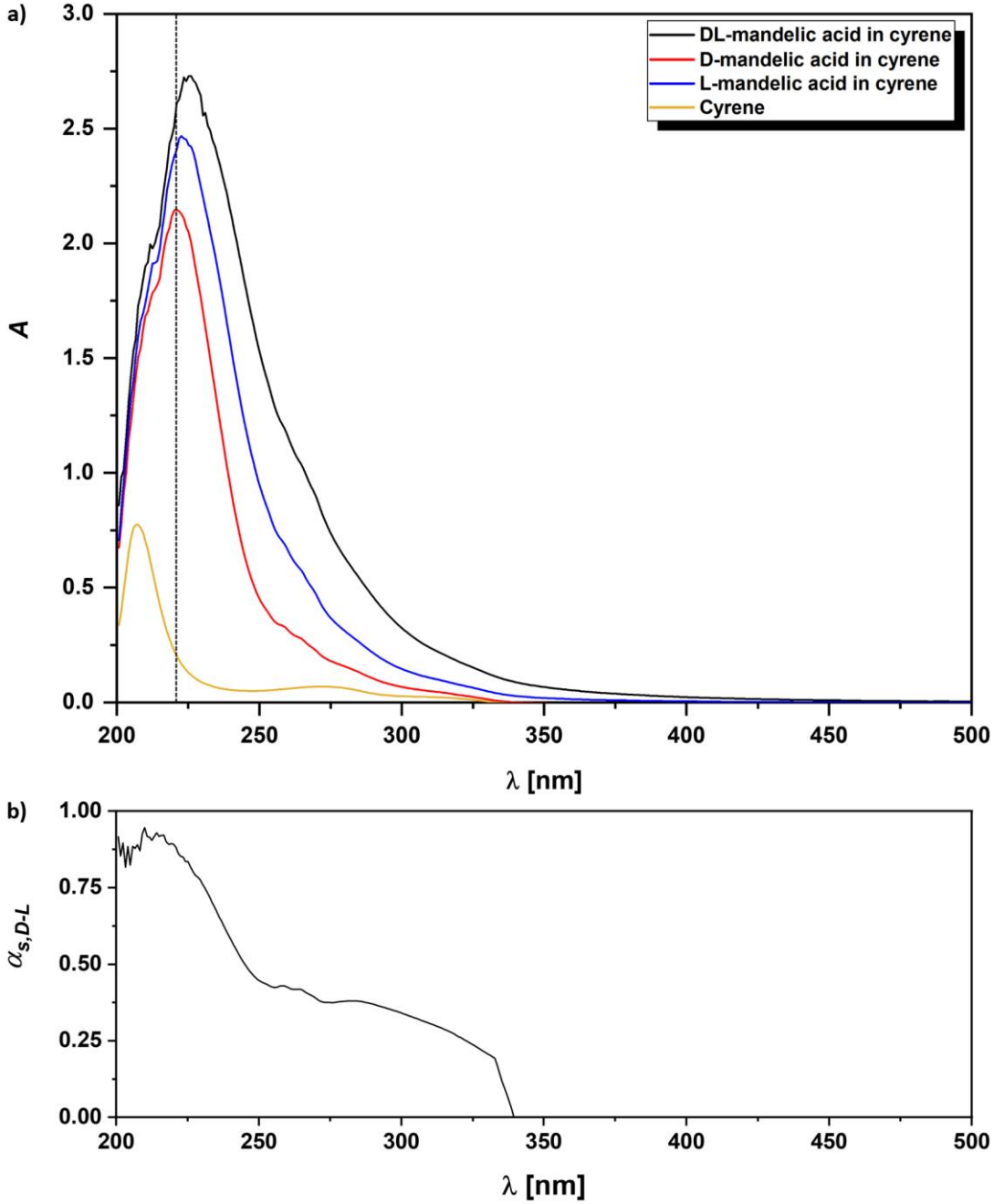

Fig. 12. a) UV-Vis spectra of saturated solutions of DL-, D-, and L-mandelic acid in the chiral solvent cyrene and for pure cyrene at 25°C. Three identical spectra were acquired for each saturated solution, only one spectrum is represented here per species for clarity. *A* and λ refer to absorbance and wavelength, respectively. The dashed black line indicates the shift in wavelength for the band with the highest absorbance in the mandelic acid spectra. At 25°C, the solubilities of DL-, D- and L-mandelic acid are different and with the following order, from the highest to the lowest: DL- > L- > D-mandelic acid. b) The ratio of solubilities of D- and L-mandelic acid $\alpha_{s,D-L}$ in cyrene as a function of the wavelength.

In addition, we also observe different λ_{max} for the same band on each UV-Vis spectrum (Fig. 12a, Table 5). A hypsochromic shift occurs for λ_{max}: DL-mandelic acid (226 nm) > L-mandelic acid (223 nm) > D-mandelic acid (221 nm) > cyrene (207 nm), which may be attributed to the same enantiomeric discrimination effect exercised by the chiral solvent. Therefore, both observations, in band absorbances and λ_{max}, support each other (Fig. 12a, Table 5).

Table 5. UV-Vis spectral data from saturated solutions of DL-, D-, and L-mandelic acid in cyrene and pure cyrene (Fig. 12) [22–24].

Solute	Solvent	λ_{max} [nm]	Electronic transitions assignment
DL-mandelic acid	Cyrene	226 (overlapped)	$n \rightarrow \sigma^*$, $n \rightarrow \pi^*$, $\pi \rightarrow \pi^*$
D-mandelic acid		221 (overlapped)	$n \rightarrow \sigma^*$, $n \rightarrow \pi^*$, $\pi \rightarrow \pi^*$
L-mandelic acid		223 (overlapped)	$n \rightarrow \sigma^*$, $n \rightarrow \pi^*$, $\pi \rightarrow \pi^*$
-		207 and 272 (overlapped)	$n \rightarrow \sigma^*$, $n \rightarrow \pi^*$, $\pi \rightarrow \pi^*$

The reason why DL- and L-mandelic acid solutions in cyrene present a darker yellow colour than D-mandelic acid solution can also be explained here when observing again the UV-Vis spectra in more detail (Figs. 2 and 12a). DL- and L-mandelic acid solutions absorb more than D-mandelic acid solution in the region of 380-450 nm (violet-blue region of the visible light spectrum), which gives the darker yellow as the perceived complementary colour for DL- and L-mandelic acid solutions (Fig. 2) [22]. In the same way, all aqueous solutions of mandelic acid species are colourless because they do not absorb (and neither emit) in the visible light range (380-750 nm) (Fig. 3) [22].

The ratio of solubilities of D- and L-mandelic acid $\alpha_{s,D\text{-}L}$ in cyrene from the UV-Vis spectroscopy is represented as a function of the wavelength from 200 to 500 nm (Fig. 12b). As cyrene is a solvent that absorbs in the UV range, a solvent correction in the absorbances of the saturated solutions of the enantiomers D and L, as explained in the definition of $\alpha_{s,D\text{-}L}$ (2) earlier, has been applied. In the case of $\alpha_{s,D\text{-}L}$ with cyrene, we observe that it is not constant and decreases from 0.88 at 200 nm to 0 at 339 nm, with a maximum of 0.95 at 210 nm. So, an $\alpha_{s,D\text{-}L}$ of 1.00 is not reached for any of the wavelengths registered.

This suggests the presence of enantiomeric discrimination power in the chiral solvent cyrene.

In summary, we observe how the chiral environment created by the optically active solvent cyrene around the enantiomeric forms of mandelic acid presents a chiral recognition (Fig. 12, Table 5). This phenomenon is not observed in the achiral solvent water (Fig. 11, Tables 3-4).

5.3.3.2. Solubility determination of mandelic acid in cyrene

The chiral differentiation exerted by the chiral solvent cyrene over mandelic acid chiral species observed in UV-Vis spectroscopy is also apparent in their solubilities C_s measured by the TV method. The L-mandelic acid presents a higher solubility in cyrene than the D-mandelic acid (Fig. 13). This solubility difference between both enantiomers is about 10-20 mg/g (2ºC) in the range of temperatures T between 36-46ºC (Fig. 13). Note that the relative standard deviation of ±1% (see section 5.2.2.3.) makes this difference significant. The association of this solubility difference to a possible contamination with small amounts of one enantiomer on the other can be discarded since the same results were obtained in separated experiments with commercial chemicals with very high purity (>99%) and from two different suppliers. Additionally, reported solubilities of the chiral mandelic species in water using the same levels of purity and suppliers were equal for the two enantiopure solids [30,31]. This also rejects then the possible contamination effect. Thus, the cyrene potential for the chiral discrimination of enantiomers can be confirmed for the mandelic acid system.

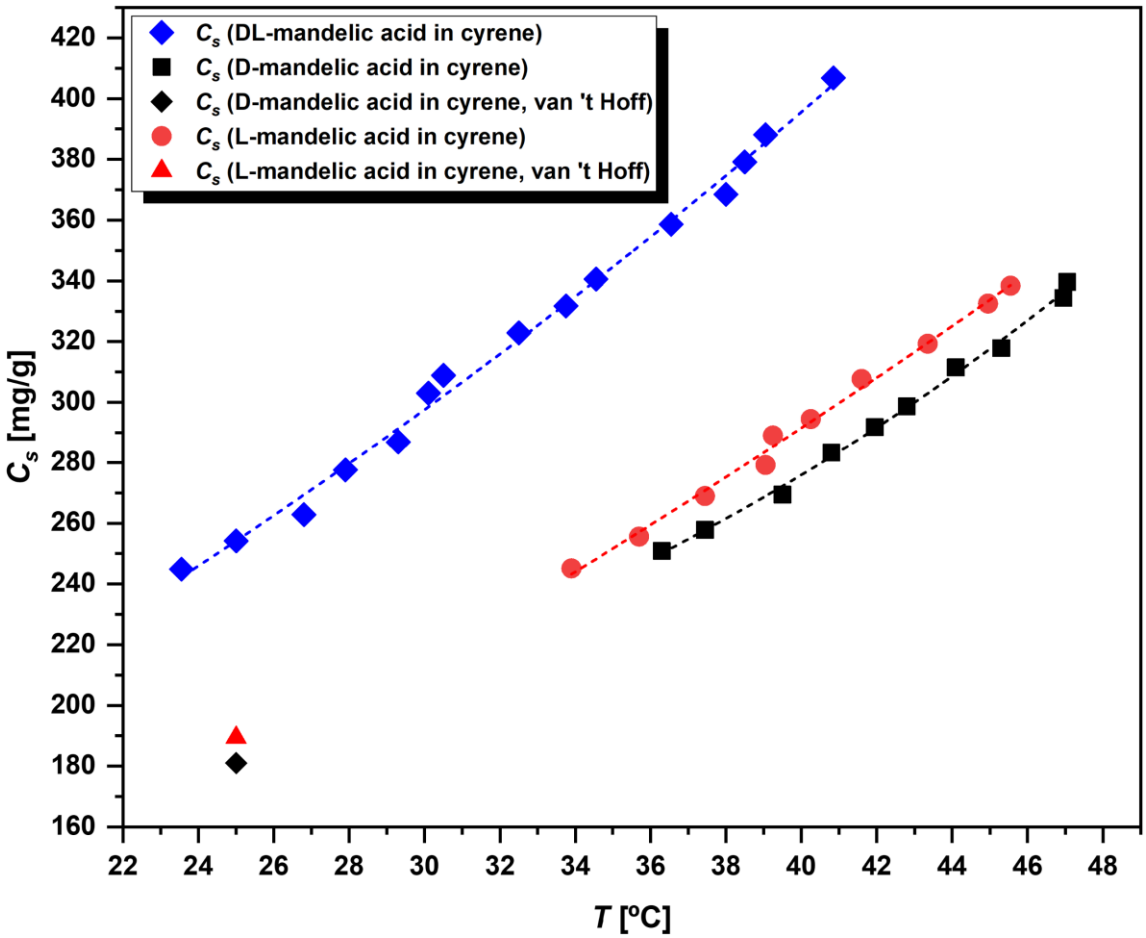

Fig. 13. Solubility curves of DL-, D-, and L-mandelic acid in cyrene. The solubility predictions for the two enantiomers at 25ºC are carried out by fitting the experimental data points with the van 't Hoff model equation (3) [4,32,33] and extrapolating to 25ºC. Dashed lines drawn as a guide to the eye.

Similar to the estimation of the ratio of solubilities $\alpha_{s,D\text{-}L}$ (2) performed with mandelic acid chiral species in water, now we apply the same study in order to compare the solubility results obtained from the UV-Vis spectroscopy and TV method (Table 6). For that, we assume the same molar extinction coefficient ε for all the chiral species of mandelic acid in the UV-Vis measurements. As the UV-Vis results are at 25ºC (Fig. 12), we then estimate the solubilities for D- and L-mandelic acid at 25ºC by means of an extrapolation from the solubility data points determined (Fig. 13). We did this by applying the following van 't Hoff model fitting equation that correlates mole fraction x_s of solute's solubility with temperature T [K] [4,32,33]:

$$\ln x_s = a + \frac{b}{T} \quad (3)$$

where subscript *s* refers to solubility and *a* and *b* are parameters obtained by regression of the solubility data.

Table 6. Absorbances *A*, solubilities C_s, and calculated solubility ratios $\alpha_{s,D\text{-}L}$ (2) for mandelic acid in cyrene from UV-Vis spectroscopy (Fig. 12) and TV method (Fig. 13) data, at 25ºC. C_s (TV) values for the two enantiomers at 25ºC obtained with Eq. (3). *A* and $\alpha_{s,D\text{-}L}$ obtained at λ_{max}. *A* and $\alpha_{s,D\text{-}L}$ obtained at λ_{max} (main band). *A* includes solvent correction.

Solute	Solvent	λ_{max} [nm]	*A*	$\alpha_{s,D\text{-}L}$ (UV-Vis)	C_s (TV) [mg/g]	$\alpha_{s,D\text{-}L}$ (TV)
DL-mandelic acid	Cyrene	226	2.61	-	254.24	-
D-mandelic acid		221	1.94	0.84	180.99	0.96
L-mandelic acid		223	2.30		189.40	

We determine that the ratio of solubilities of D- and L-mandelic acid $\alpha_{s,D\text{-}L}$ is lower than 1.00 (value indicating no chiral discrimination) in the TV method (0.96) and in the UV-Vis spectroscopy (0.84) at the λ_{max} of the main band observed (Fig. 12a, Table 6), but also for all the wavelengths registered (Fig. 12b), at 25ºC. These data quantify the chiral discrimination of mandelic acid enantiomers exerted by the chiral solvent cyrene. Note that, in cyrene, we do not obtain the same values of the ratios of solubilities $\alpha_{s,D\text{-}L}$ in both techniques as in the case of water (1.00, Table 4). This difference in the $\alpha_{s,D\text{-}L}$ values between the UV-Vis spectroscopy and TV method is due to the assumption of taking the same molar extinction coefficient ε for the two enantiopure compounds of mandelic acid in UV-Vis spectroscopy. In fact, we observed clearly that the UV bands for the three species of mandelic acid vary in both absorbance and wavelength (Fig. 12, Table 6), indicating then also that a different molar extinction coefficient ε applies for each chiral species of mandelic acid in cyrene. Note that as some of the absorbance values obtained are high (A >1.00; Fig. 12a, Table 6), the response (absorbance) may not be linear with the concentration at these values [22,25–27]. The latter could lead to errors in the calculation of the ratio of solubilities, which could contribute with additional differences in the $\alpha_{s,D\text{-}L}$ values between the UV-Vis spectroscopy and TV method.

We also see that the racemic compound shows a higher solubility than both enantiopure forms of mandelic acid in both UV-Vis spectroscopy (Fig. 12a) and TV method (Fig. 13). In Table 6, the difference in absorbance between the racemic compound of mandelic acid (A = 2.61) and its two enantiomers (A = 1.94 and 2.30 for enantiomers D and L, respectively) at the λ_{max} of the main band follows the same pattern with the difference in solubilities found in the TV method for the racemic compound (C_s = 254.24 mg/g) and both enantiomers (C_s = 180.99 and 189.40 mg/g for enantiomers D and L, respectively) at 25ºC. This difference in solubility between the racemic compound of mandelic acid and its two enantiomers in cyrene is related to their different crystal structures, which is similar to the behaviour observed with mandelic acid in water (see section 5.3.3.1.1.).

5.4. Discussion

The subtle differences observed in wave number/Raman shift and absorbance/intensity of peaks in the FTIR and Raman measurements of undersaturated solutions of the chiral species of mandelic acid and naproxen in optically active solvent cyrene (Figs. 4-9, Table 1) suggest certain enantiomeric discrimination effect of cyrene. These differences are larger in mandelic acid (Figs. 5 and 8) than in naproxen (Figs. 6 and 9). In general, FTIR spectroscopy (Figs. 4-6) seems to detect better these variations than Raman spectroscopy (Figs. 7-9). The FTIR and Raman signals indicate that the solute molecules mandelic acid and naproxen interact with cyrene through the polar functional groups (alcohol, ether, ketone, and carboxyl), suggesting the presence of intermolecular forces such as hydrogen bonding.

The solubility measurements with UV-Vis spectroscopy of the chiral species of mandelic acid in the chiral solvent cyrene and achiral solvent water do sufficiently indicate the enantiomeric discrimination effect exercised by cyrene (Figs. 11-12, Tables 3 and 5). This enantiomeric differential behaviour is also observed when quantifying different solubilities for the two enantiopure compounds of mandelic acid in cyrene by means of the TV method (Fig. 13). The determination of the ratios of solubilities $\alpha_{s,D\text{-}L}$ enable the

comparison of the solubility data between UV-Vis spectroscopy, TV method, and literature. We find that this ratio of solubilities is the same for mandelic acid in water by both UV-Vis spectroscopy and in the literature and constantly equal to 1.00 (Fig. 11, Table 4) whereas it differs when mandelic acid is dissolved in cyrene between the UV-Vis and TV method with values lower than 1.00 (Figs. 12-13, Table 6). Additionally, in the latter case with cyrene, the ratio of solubilities is not kept constant and decreases from 0.88 at 200 nm to 0 at 339 nm. These data confirm the enantiomeric discrimination effect of cyrene on the two enantiomers of mandelic acid. Cyrene shows preference for L-mandelic acid since its solubility is higher than the D-mandelic acid one, which is related to the formation of stronger intermolecular forces with L-mandelic acid than with D-mandelic acid.

Despite cyrene feasibility for the chiral resolution by enantioselective liquid-liquid extraction of DL-mandelic acid has been found to not be possible here because of the impossibility to find and ideal achiral solvent to form and heterogeneous liquid mixture with cyrene, this relatively new chiral solvent does show application potential for chiral resolution via crystallisation and also via extraction techniques under different conditions other than the ones studied here. In crystallisation, from a thermodynamics point of view, the distinct solubilities registered for D- and L-mandelic acid by means of UV-Vis spectroscopy and TV method (Figs. 12-13, Tables 5-6) indicate that the ternary phase diagram of both mandelic acid enantiomers in cyrene is not symmetric [1,4]. In addition, previous works described in the literature show that some chiral solvents can affect differently the crystal nucleation and growth of both enantiomers [7,11–13]. In particular, different induction times were encountered for both chiral forms of some compounds in the presence of a chiral solvent [7,11,13]. This could be also the case for certain chiral solutes, such as mandelic acid enantiomers, in cyrene. On the other hand, we find that the potential chiral resolution via extraction using cyrene as a chiral selective solvent has the requirement to find an ideal target chiral solute which could employ cyrene and non-polar solvents, the only ones that could present the desired heterogeneous mixtures for the separation process. Apart from this, the same chiral resolution extracting application could

be investigated with other chiral solvents which present better immiscibility with a broader spectrum of achiral solvents which, at the same time, might enlarge the chiral solute possibilities to be separated.

5.5. Conclusions

We find that the green optically active solvent cyrene presents a chiral recognition power when analysing the undersaturated solutions of mandelic acid and naproxen through FTIR and Raman spectroscopies. A further confirmation of this enantioselective solvent effect is found when examining the solubility of mandelic acid in the achiral solvent water and the chiral solvent cyrene by means of UV-Vis spectroscopy. UV-Vis spectra from the former case shows no distinction between enantiomers whereas spectra from the latter case shows clear band shifts and even distinct absorbances between the two enantiomers. Additionally, the ratios of solubilities of the two enantiomers of mandelic acid in water using UV-Vis spectral and literature data are found identical and equal to 1.00 whereas the same ratios in cyrene, using UV-Vis spectroscopy and TV method data, are significantly different for the two chiral forms and lower than 1.00. All of this provides enough evidences to confirm the enantiomeric discrimination effect of cyrene, at least with certain chiral solutes. On the other hand, the miscibility study of cyrene shows that it is miscible with most organic solvents, except those most non-polar ones such as cyclohexane, *n*-heptane, and *n*-hexane. It is also completely miscible with the inorganic solvent water. The chiral resolution of DL-mandelic acid by means of enantioselective liquid-liquid extraction with cyrene is not feasible due to the appearance of only one homogeneous liquid phase when mixing the solutions to be extracted (1-nonanol and 1-octanol solutions of DL-mandelic acid) with the extracting chiral solvent cyrene. We think that the potential chiral resolution via enantioselective liquid-liquid extraction using cyrene as chiral selective solvent has the requirement to find an ideal target chiral solute which could employ cyrene and non-polar solvents. Finally, we would like to remark the potential of cyrene to show its chiral discrimination ability when using crystallisation technologies. We believe that further work could be done focusing on the design of chiral

resolution procedures based on either thermodynamics or kinetics aspects, or the combination of both.

5.6. References

[1] E.L. Eliel, S.H. Wilen, Stereochemistry of organic compounds, John Wiley & Sons, 2014.

[2] J. McConathy, M.J. Owens, Stereochemistry in drug action, Prim. Care Companion J. Clin. Psychiatry. 05 (2003) 70–73.

[3] L.A. Nguyen, H. He, C. Pham-Huy, Chiral drugs: an overview, Int. J. Biomed. Sci. 2 (2006) 85–100.

[4] J. Jacques, A. Collet, Enantiomers, racemates and resolutions, John Wiley & Sons, 1981.

[5] H. Lorenz, A. Seidel-Morgenstern, Processes to separate enantiomers, Angew. Chemie - Int. Ed. 53 (2014) 1218–1250.

[6] J.E. Rekoske, Chiral separations, AIChE J. 47 (2001) 2–5.

[7] S.K. Tulashie, The potential of chiral solvents in enantioselective crystallization, Otto-von-Guericke-Universität Magdeburg, 2010.

[8] B. Schuur, B.J.V. Verkuijl, A.J. Minnaard, J.G. de Vries, H.J. Heeres, B.L. Feringa, Chiral separation by enantioselective liquid-liquid extraction, Org. Biomol. Chem. 9 (2011) 36–51.

[9] B. Schuur, J. Floure, A.J. Hallett, J.G.M. Winkelman, J.G. de Vries, H.J. Heeres, Continuous chiral separation of amino acid derivatives by enantioselective liquid-liquid extraction in centrifugal contactor separators, Org. Process Res. Dev. 12 (2008) 950–955.

[10] F. Tang, Q. Zhang, D. Ren, Z. Nie, Q. Liu, S. Yao, Functional amino acid ionic

liquids as solvent and selector in chiral extraction, J. Chromatogr. A. 1217 (2010) 4669–4674.

[11] S.K. Tulashie, H. Lorenz, L. Hilfert, F.T. Edelmann, A. Seidel-Morgenstern, Potential of chiral solvents for enantioselective crystallization. 1. Evaluation of thermodynamic effects, Cryst. Growth Des. 8 (2008) 3408–3414.

[12] S.K. Tulashie, J. Von Langermann, H. Lorenz, A. Seidel-Morgenstern, Chiral task-specific solvents for mandelic acid and their impact on solution thermodynamics and crystallization kinetics, Cryst. Growth Des. 11 (2011) 240–246.

[13] S.K. Tulashie, H. Lorenz, A. Seidel-Morgenstern, Potential of chiral solvents for enantioselective crystallization. 2. Evaluation of kinetic effects, Cryst. Growth Des. 9 (2009) 2387–2392.

[14] Cyrene. Circa Group Pty Ltd., (2020). www.circagroup.com.au/cyrene (accessed January 4, 2020).

[15] Merck, Greener solvent alternatives, (2020). https://www.sigmaaldrich.com/chemistry/solvents/products.html?TablePage=19919482 (accessed September 10, 2020).

[16] Merck, The future of solvents: biorenewable, Sigma-Aldrich. (2019). https://www.sigmaaldrich.com/content/dam/sigma-aldrich/docs/Sigma-Aldrich/General_Information/1/greener-solvents-br-mk.PDF (accessed September 10, 2020).

[17] P.T. Anastas, J.C. Warner, Green chemistry: theory and practice, Oxford University Press, New York, 1998.

[18] J. Sherwood, M. de Bruyn, A. Constantinou, L. Moity, C.R. McElroy, T.J. Farmer, T. Duncan, W. Raverty, A.J. Hunt, J.H. Clark, Dihydrolevoglucosenone (cyrene) as a bio-based alternative for dipolar aprotic solvents, Chem. Commun. 50 (2014) 9650–9652.

[19] Merck, Cyrene, Sigma-Aldrich. (2020). www.sigmaaldrich.com/catalog/product/sial/807796?lang=en&region=GB (accessed January 4, 2020).

[20] C.J. Clarke, W.C. Tu, O. Levers, A. Bröhl, J.P. Hallett, Green and sustainable solvents in chemical processes, Chem. Rev. 118 (2018) 747–800.

[21] M.A. Reus, A.E.D.M. van der Heijden, J.H. ter Horst, Solubility determination from clear points upon solvent addition, Org. Process Res. Dev. 19 (2015) 1004–1011.

[22] P.Y. Bruice, Organic chemistry, 5th ed., Pearson Prentice Hall, 2008.

[23] L.D. Field, S. Sternhell, J.R. Kalman, Organic structures from spectra, 5th ed., John Wiley & Sons, 2013.

[24] E. Pretsch, P. Bühlmann, M. Badertscher, Structure determination of organic compounds. Tables of spectral data, 4th ed., Springer, 2009.

[25] J.H. Lambert, Photometria sive de mensura et gradibus luminis, colorum et umbrae, Augustae Vindelicorum, Torino, 1760.

[26] Beer, Bestimmung der Absorption des rothen Lichts in farbigen Flüssigkeiten, Ann. Der Phys. Und Chemie. 162 (1852) 78–88.

[27] H.-H. Perkampus, UV-Vis spectroscopy and its applications. Springer lab manuals., Springer, Berlin, Heidelberg, 1992.

[28] R. Mohan, H. Lorenz, A.S. Myerson, Solubility measurement using differential scanning calorimetry, Ind. Eng. Chem. Res. 41 (2002) 4854–4862.

[29] W.R. Angus, R.P. Owen, Aqueous solubilities of r- and l-mandelic acids and three o-acyl-r-mandelic acids, J. Chem. Soc. (1943) 231.

[30] H. Lorenz, D. Sapoundjiev, A. Seidel-Morgenstern, Enantiomeric mandelic acid system-melting point phase diagram and solubility in water, J. Chem. Eng. Data.

47 (2002) 1280–1284. doi:10.1021/je0200620.

[31] H. Lorenz, A. Seidel-Morgenstern, A contribution to the mandelic acid phase diagram, Thermochim. Acta. 415 (2004) 55–61.

[32] F. Zhang, Y. Tang, L. Wang, L. Xu, G. Liu, Solubility determination and thermodynamic models for 2-methylnaphthalene in different solvents from T = (278.15 to 303.15) K, J. Chem. Eng. Data. 60 (2015) 1699–1705.

[33] J.M. Prausnitz, R.N. Lichtenthaler, E.G. de Azedo, Molecular thermodynamics of fluid-phase equilibria, 3rd ed., Prentice-Hall, New Jersey, 1999.

CHAPTER 6

6. Conclusions

The aim of this thesis was to develop new procedures to perform the chiral resolution of racemic solutions of fine chemicals by means of separation techniques, such as crystallisation, membrane filtration, and extraction. A wide variety of techniques to obtain enantiomerically pure compounds have been developed in the past based on two pathways: asymmetric synthesis and non-selective synthesis with resolution of racemates. Some of these techniques mimic the way biological systems distinguish chirality, others exploit minor differences in physical properties or interactions with other chemical entities. The design of chiral separation processes can have a tremendous impact on the pharmaceutical, pesticides, food, and cosmetics industries. The saving obtained in process cost metrics, such as time- and cost-to-process, provide a convincing argument for combining traditional racemic chemical synthesis with chiral separations for attaining a high enantiomeric excess. Therefore, the high potential of the chiral separation processes, in terms of time-to-market, overall process economics, and product quality; explains the importance in developing and exploring new chiral resolution methodologies and techniques.

In chapter 3, we determined the solubility of the amino acids alanine, phenylalanine, and valine in aqueous media by means of the temperature variation (TV) and equilibrium concentration (EqC) methods. The faster TV method was suitable for those cases which do not present fouling-related phenomena during crystallisation. For all other cases, the more laborious EqC method led to reliable results. The amino acid systems showed temperature- and pH-dependent solubilities, with the highest solubility values being obtained at high temperature and at extreme pH values. These effects of temperature and pH on solubility were observed in binary, pseudo-binary, and ternary phase diagrams. The temperature effect on solubility was explained by means of a van ’t Hoff-type model and

the pH effect due to the acid-base dissociation equilibria. The chemical structure of the amino acids was responsible of the differences observed in solubility among them, when considering similar solid characteristics for the three hydrophobic amino acids. The larger and more hydrophobic their side chain, the lower polarity and therefore their solubility. The different crystal lattice between the racemate and enantiopure compound explained their different solubilities, noting the effect of one enantiomer on the counter enantiomer's solubility in the racemic solution equilibrated with the racemic solid compared to the equilibrated solution with the enantiopure solid. We proposed the use of pseudo-binary phase diagrams, obtained through TV and EqC-HPLC methods, as a fast methodology to accurately estimate eutectic points and ternary phase diagrams of racemic compounds. Finally, we recommend a workflow process for an accurate determination of the eutectic points and ternary phase diagrams of racemic compound-forming systems, which are required in several chiral resolution applications focused on crystallisation techniques.

In chapter 4, we modelled and optimised a continuous chiral resolution process which integrates membrane filtration and crystallisation techniques. We found that the one-site competition model is widely applicable to explain the complexation interaction between the chiral selector BSA and hydrophobic amino acids (alanine, phenylalanine, and valine) in aqueous media. We also observed that there exists a trade-off between purity and recovery in the membrane ultrafiltration step. In terms of purity, the model predicted that a single-stage membrane ultrafiltration was enough for the valine system to obtain sufficient enantiomeric enrichment to surpass the eutectic point composition to be able to continuously crystallise a pure enantiomer, starting from its racemic mixture. Instead, for those systems with a more demanding eutectic point composition, such as phenylalanine and alanine, a second membrane stage was predicted necessary for the process. The complexation and chiral selector acid-base dissociation constants sensitivity studies predicted that an ideal BSA-similar chiral selector for the process should bear an unprotonated binding site for a large pH range and very different complexation constants. We used therefore the thermodynamic one-site competition model in order to predict the outcome of the membrane ultrafiltration step, which can be coupled to both concentration

and selective cooling crystallisation steps to establish a novel chiral resolution process for racemic solutions of racemic compound-forming systems. The overall process was predicted to obtain the best outcome, in terms of recovery, when the concentration gap is saved or small and for those systems which only require one membrane stage in the ultrafiltration step and have solubilities with a strong temperature dependence. Thus, we foresee that the sensitivity study of other chiral selectors and its optimisation in a similar manner described here will permit, along with the introduction of a recycling step in the process, to increase the overall process recovery for several chiral systems.

In chapter 5, we explored the potential of the chiral solvent cyrene for enantiomer recognition to be applied in chiral resolution processes through liquid-liquid extraction and crystallisation techniques. We observed this chiral discrimination power by FTIR and Raman spectroscopies of the undersaturated solutions of mandelic acid and naproxen. The examination of the saturated solutions of the chiral species of mandelic acid in the chiral solvent cyrene and the achiral solvent water by means of UV-Vis spectroscopy also revealed the chiral discrimination effect exercised by cyrene. The UV-Vis spectra showed different solubilities for both enantiomers in cyrene and a hypsochromic shift was detected at λ_{max} of the UV-Vis bands of the two enantiomers of mandelic acid. Instead, the same analysis in the achiral solvent water showed the same spectral response and thus the same solubility for the two mandelic acid enantiomers. These findings were related to the different interaction of each enantiomer with the chiral solvent. This observation was confirmed by quantifying different solubilities for the two enantiomers of mandelic acid in cyrene with the TV method. Furthermore, the ratios of solubilities of the two enantiomers of mandelic acid in water using UV-Vis spectral and literature data were found identical and equal to 1.00 whereas the same ratios in cyrene, using UV-Vis spectroscopy and TV method data, were significantly different for the two chiral forms and lower than 1.00. All of this provided sufficient evidences to validate the enantiomeric discrimination effect of cyrene, at least with the chiral solutes tested. Apart from this, the miscibility study of cyrene showed that it is miscible with water and most organic solvents, except those most non-polar ones such as cyclohexane, *n*-heptane, and *n*-hexane.

The chiral resolution of racemic mandelic acid by means of enantioselective liquid-liquid extraction with cyrene was not feasible because of the appearance of only one homogeneous liquid phase when mixing the solutions to be extracted with cyrene. We believe that the potential chiral resolution via enantioselective liquid-liquid extraction using cyrene as the chiral selective solvent has the requirement to find an ideal target chiral solute which could make use of cyrene and non-polar solvents. Finally, we want to note the potential of cyrene to show its chiral discrimination ability when using crystallisation technologies. We think that further work could be performed focusing on the design of chiral resolution procedures based on either thermodynamics or kinetics aspects, or the combination of both.

The research presented in this thesis led to advancements in the determination of the class of chiral compound with a keen focus on the crystallisation of racemic compound-forming systems. A detailed workflow for the fast and accurate determination of ternary phase diagrams of this class of chiral systems was proposed from the measurement of pseudo-binary phase diagrams. An interesting future approach of this workflow process would be to test it for other non-hydrophobic amino acids in aqueous media, or even for different racemic compounds in several organic solvents. The data obtained from the ternary phase diagrams permitted to achieve the aim of this thesis in proposing a novel chiral resolution process founded on the combination of membrane ultrafiltration and crystallisation technologies. The simulations of the process proved its potential for crystallising pure enantiomers from a racemic feed solution. In the future, we recommend testing the new combined resolution process with other BSA-similar/different chiral selectors and for other racemic compounds in not only aqueous media but also in organic solvents or in their mixtures with water. In addition, apart from a cooling crystallisation, other types of crystallisation techniques could be assessed depending on the solubility behaviour of the enantiopure fine chemical product of interest. The aim of the thesis was also achieved when we found the potential of a new green chiral solvent for its application in the separation of enantiomers starting from a fine chemical racemate by means of enantioselective liquid-liquid extraction and crystallisation techniques. The most

promising future approach for the enantioselective liquid-liquid extraction with the chiral solvent cyrene would require testing chiral compounds that can be extracted correctly with cyrene along with other solvents, that is to say, obtaining at least two physically separated liquid phases. Besides, we recommend attempting similar extraction processes with other chiral solvents that can provide enantiomeric discrimination. The enantioselective crystallisation by using the optically active solvent cyrene presents high potential to play with both thermodynamics and kinetics aspects of the technique in the future. All the results presented in this document will facilitate the study, understanding, and characterisation of the chiral resolution processes based on enantioselective interactions in separation techniques, such as membrane filtration, crystallisation, and extraction; in a more comprehensive and efficient manner to address current and future challenges. Finally, this thesis serves as an example for the future exploration, discovery, design, development, and control of new physicochemical processes for the separation of enantiomers.